

Anis Koubaa *Editor*

Robot Operating System (ROS)

The Complete Reference (Volume 7)



Springer

Studies in Computational Intelligence

Volume 1051

Series Editor

Janusz Kacprzyk, Polish Academy of Sciences, Warsaw, Poland

The series “Studies in Computational Intelligence” (SCI) publishes new developments and advances in the various areas of computational intelligence—quickly and with a high quality. The intent is to cover the theory, applications, and design methods of computational intelligence, as embedded in the fields of engineering, computer science, physics and life sciences, as well as the methodologies behind them. The series contains monographs, lecture notes and edited volumes in computational intelligence spanning the areas of neural networks, connectionist systems, genetic algorithms, evolutionary computation, artificial intelligence, cellular automata, self-organizing systems, soft computing, fuzzy systems, and hybrid intelligent systems. Of particular value to both the contributors and the readership are the short publication timeframe and the world-wide distribution, which enable both wide and rapid dissemination of research output.

Indexed by SCOPUS, DBLP, WTI Frankfurt eG, zbMATH, SCImago.

All books published in the series are submitted for consideration in Web of Science.

Anis Koubaa
Editor

Robot Operating System (ROS)

The Complete Reference (Volume 7)



Springer

Editor

Anis Koubaa
College of Computer Science
and Information Systems
Prince Sultan University
Riyadh, Saudi Arabia

ISSN 1860-949X ISSN 1860-9503 (electronic)

Studies in Computational Intelligence

ISBN 978-3-031-09061-5 ISBN 978-3-031-09062-2 (eBook)

<https://doi.org/10.1007/978-3-031-09062-2>

© The Editor(s) (if applicable) and The Author(s), under exclusive license to Springer Nature Switzerland AG 2023

This work is subject to copyright. All rights are solely and exclusively licensed by the Publisher, whether the whole or part of the material is concerned, specifically the rights of translation, reprinting, reuse of illustrations, recitation, broadcasting, reproduction on microfilms or in any other physical way, and transmission or information storage and retrieval, electronic adaptation, computer software, or by similar or dissimilar methodology now known or hereafter developed.

The use of general descriptive names, registered names, trademarks, service marks, etc. in this publication does not imply, even in the absence of a specific statement, that such names are exempt from the relevant protective laws and regulations and therefore free for general use.

The publisher, the authors, and the editors are safe to assume that the advice and information in this book are believed to be true and accurate at the date of publication. Neither the publisher nor the authors or the editors give a warranty, expressed or implied, with respect to the material contained herein or for any errors or omissions that may have been made. The publisher remains neutral with regard to jurisdictional claims in published maps and institutional affiliations.

This Springer imprint is published by the registered company Springer Nature Switzerland AG
The registered company address is: Gewerbestrasse 11, 6330 Cham, Switzerland

Contents

ROS2

Micro-ROS	3
Kaiwalya Belsare, Antonio Cuadros Rodriguez, Pablo Garrido Sánchez, Juanjo Hierro, Tomasz Kołcon, Ralph Lange, Ingo Lütkebohle, Alexandre Malki, Jaime Martin Losa, Francisco Melendez, Maria Merlan Rodriguez, Arne Nordmann, Jan Staschulat, and Julian von Mendel	

A Tutorial to Use the MediaPipe Framework with ROS2	57
Dieisson Martinelli, Jonathan Cerbaro, Marco Antonio Simoes Teixeira, João Alberto Fabro, and André Schneider de Oliveira	

ROS Frameworks and Applications

Autonomous 3D Thermal Mapping of Disaster Environments for Victims Detection	83
Christyan Cruz Ulloa, Guido Torres Llerena, Antonio Barrientos, and Jaime del Cerro	

Lab-Scale Smart Factory Implementation Using ROS	119
Marwan Abdelatti and Manbir Sodhi	

Cooperation, Sensing and Control

RosDrive: An Open-Source ROS-Based Vehicular Simulator for STEM Control Systems Classes Tutorial	147
Enio Vasconcelos Filho, Jones Yudi, Mohamed Abdelkader, Anis Koubaa, and Eduardo Tovar	

Autonomous Laser-Induced Breakdown Spectroscopy System for Chemical and Mineralogical Designation of Interplanetary Materials	177
George Stavrinou, Elias Chatzitheodoridis, and Olga Sykoti	
High Fidelity IMU and Wheel Encoder Models for ROS Based AGV Simulations	227
Emre Ozdemir, Hakan Gokoglu, M. Koray Yilmaz, Umut Dumandag, Ismail Hakki Savci, and Haluk Bayram	

ROS2

Micro-ROS



Kaiwalya Belsare, Antonio Cuadros Rodriguez, Pablo Garrido Sánchez, Juanjo Hierro, Tomasz Kołcon, Ralph Lange, Ingo Lütkebohle, Alexandre Malki, Jaime Martin Losa, Francisco Melendez, Maria Merlan Rodriguez, Arne Nordmann, Jan Staschulat, and Julian von Mendel

Abstract The micro-ROS stack (micro.ros.org) integrates microcontrollers seamlessly with standard ROS 2 and brings all major ROS concepts such as nodes, publisher, subscriptions, parameters, and lifecycle onto deeply embedded systems. This enables accessing all software using the same ROS tools and APIs, regardless of the underlying computing hardware and operating system. Micro-ROS supports a broad spectrum of microcontroller families and the main open-source real-time operating systems like FreeRTOS, Zephyr, or NuttX. It supports various microcontroller- or RTOS-specific build systems and provides ROS-CLI-based build tooling. Micro-ROS is an open-source project that has been under development at github.com/micro-ROS since 2018. It was initiated by the EU-funded innovation activity OFERA. During the last two years, micro-ROS has been adopted by a relevant group of professional users inside the ROS community. In this chapter, we give a technical introduction to the micro-ROS stack including APIs and architecture,

Because of the large number of authors, the names have been sorted alphabetically by surname.

K. Belsare · R. Lange (✉) · I. Lütkebohle · A. Nordmann · J. Staschulat
Robert Bosch GmbH, Robert-Bosch-Campus 1, 71272 Renningen, Germany
e-mail: ralph.lange@de.bosch.com

K. Belsare
e-mail: kaiwalyakalyan.belsare@de.bosch.com

I. Lütkebohle
e-mail: ingo.luetkebohle@de.bosch.com

A. Nordmann
e-mail: arne.nordmann@de.bosch.com

J. Staschulat
e-mail: jan.staschulat@de.bosch.com

A. C. Rodriguez · P. G. Sánchez · J. M. Losa · M. M. Rodriguez
eProsimma, Plaza de la Encina 10-11, Nucleo 4, 2a Planta, 28760 Madrid, Tres Cantos, Spain
e-mail: antoniocuadros@eprosima.com

P. G. Sánchez
e-mail: pablogarrido@eprosima.com

as well as the corresponding middleware Micro XRCE-DDS. Furthermore, tutorials for a simple application with an ESP32 microcontroller are provided together with a report on three use-cases from industrial and research applications.

Keywords ROS 2 · Microcontroller · Micro-ROS · Embedded · Robotics

1 Introduction

The system architecture of a robot generally includes a network of one or more stronger microprocessors and multiple microcontrollers. The microcontrollers are used for accessing sensors and actuators, for low-latency control functions (e.g., force or torque control at $\gg 1$ kHz), for power saving (in particular in consumer applications), and for safety functions. Microcontrollers typically feature about 100 kB to 10 MB of RAM only and use highly resource-optimized real-time operating systems (RTOS).

Due to their relevance in robotic applications, the integration of microcontrollers has always been an important topic in ROS [1]. The most prominent integration framework for classical ROS is *rosserial* [2]. It can be characterized as a lightweight protocol for exchanging ROS messages between a Linux-based microprocessor and a microcontroller, but offers only very few other ROS concepts on the microcontroller side beyond communication. Rosserial supports Arduino-compatible boards, Mbed-compatible platforms, Embedded Linux, and various other platforms.

J. M. Losa
e-mail: jaimemartin@eprosima.com

M. M. Rodriguez
e-mail: mariamerlan@eprosima.com

T. Kołcon · A. Malki
Łukasiewicz Research Network, Industrial Research Institute for Automation and Measurements
PIAP, Al. Jerozolimskie 202, 02-486 Warsaw, Poland
e-mail: tkolcon@piap.pl

A. Malki
e-mail: amalki@piap.pl

J. Hierro · F. Melendez
FIWARE Foundation e.V., Franklinstraße 13A, 10587 Berlin, Germany
e-mail: juanjose.hierro@fiware.org

F. Melendez
e-mail: francisco.melendez@fiware.org

J. von Mendel
Bosch Rexroth AG, Robert-Bosch-Straße 2, 71701 Schwieberdingen, Germany
e-mail: julian.vonmendel@boschrexroth.de

Another solution for the integration of microcontrollers with classical ROS is *mROS*. It provides a basic implementation of the core ROS concepts directly on the embedded device [3]. This allows implementing multiple ROS nodes on the same microcontroller. For message exchange between those nodes, mROS features an efficient shared memory communication mechanism. For communication with remote ROS nodes, mROS uses the lightweight TCP/IP stack lwIP [4]. The mROS stack is based on the TOPPERS RTOS [5].

1.1 New Use-Case for ROS 2

For the design of ROS 2, six new use-cases were identified compared to classical ROS [6]. The second use-case is the support of “small embedded platforms”, including bare-metal microcontrollers, as “first-class participants in the ROS environment, instead of being segregated from ROS by a device driver”. Our understanding of this use-case implies that robotics software should be developed on microcontrollers using the same ROS concepts as on strong microprocessors. This includes the structuring by nodes, communication by topics, actions, and services, and many more concepts. Similarly, the software on the microcontroller should be accessible with the same developer tools for introspection, monitoring, runtime configuration, etc.

Device driver nodes that merely implement a ROS interface for the software on a microcontroller and that communicate with the microcontroller via their own protocol or communication technology are far from this idea.

The first undertaking to bring ROS 2 onto microcontrollers was the RIOT-ROS2 project [7, 8], in which the ROS 2 Client Support Library (rcl) and a tiny C client library were ported to the RIOT operating system [9]. For communication, RIOT-ROS2 used Named Data Networking (NDN) [10], unlike standard ROS 2, which uses the Data Distribution Service (DDS) [11].

Recently, *mROS 2* was published [12]. Analogously to mROS, it provides a basic implementation of the core ROS 2 concepts directly on the embedded device. EmbeddedRTPS [13, 14] is used for direct communication with the Data Distribution Service (DDS) [11] used in ROS 2. In addition to the TOPPERS RTOS, mROS 2 also supports Mbed OS [15].

1.2 Goals of Micro-ROS

The RIOT-ROS2 project and the preparation of a new standard *DDS For Extremely Resource Constrained Environments* (DDS-XRCE) [16] led to the foundation of the micro-ROS project, backed by the EU-funded research and innovation action OFERA [17]. The micro-ROS project was launched in 2018 with the following three goals:

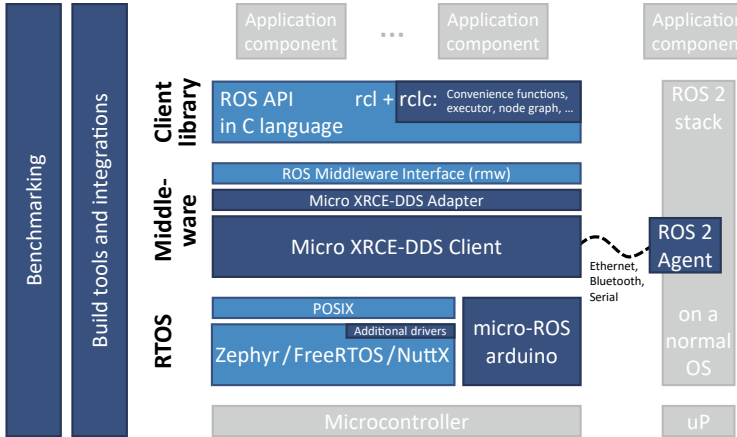


Fig. 1 Overview of micro-ROS architecture and tooling. Reused ROS 2 packages and other third-party open-source software are depicted in light blue. Dark blue colored components have been developed in the project

1. *Seamless integration of microcontrollers with ROS 2:* The robotic software on the microcontroller shall be accessible by standard ROS 2 interfaces and tools, which comprises not only topics and services, but also concepts like parameters and the new ROS 2 node lifecycle.
2. *Ease portability of ROS 2 code to microcontrollers:* The micro-ROS stack shall provide all core ROS concepts with compatible APIs to minimize the efforts for porting software from standard ROS 2 to micro-ROS. This specifically targets the gap observed with classic ROS between robotics research and product development: while research is typically conducted on Linux-based computers using ROS, product development for small embedded hardware platforms does not use ROS because these platforms are not adequately supported.
3. *Ensure long term maintenance of micro-ROS stack:* The micro-ROS stack and project shall be setup and developed in a way that the maintenance is ensured after the end of the EU-funded research and innovation action.

To achieve those goals, the founding partners of micro-ROS have designed a software stack that utilizes the layered architecture of the standard ROS 2 stack and integrates seamlessly with DDS. The micro-ROS stack reuses as many packages as possible of the standard ROS 2 stack, which is a key difference to the other approaches mentioned above. Relevant changes are contributed back to minimize the long-term maintenance costs of micro-ROS. Figure 1 shows the high-level architecture of the stack together with additional tooling.

The micro-ROS stack can be used with various open-source RTOS, including FreeRTOS [18], Zephyr [19], and NuttX [20], but also comes with support for bare-metal use-cases. On the middleware layer, it uses an open-source implementation of the DDS-XRCE standard by eProsima, named *Micro XRCE-DDS* [21]. It comes

with an agent that bridges between standard DDS and DDS-XRCE. On the client library layer, micro-ROS extends the rcl, which is implemented in the C programming language, by the rclc packages to form a feature-complete client library in C.

A substantial portion of the development effort has gone into build tooling. Micro-ROS provides tooling for the ROS 2 command line interface (CLI) as well as integrations with various microcontroller- and RTOS-specific build systems. Finally, micro-ROS is complemented by a generic benchmarking suite.

In addition to these technical measures, the partners successfully formed a global subcommunity to distribute the work on more shoulders, particularly by initiating a ROS Working Group named *Embedded Systems WG*, cf. [22].

1.3 Goals and Structure of This Chapter

The goals of this chapter are two-fold: First, to give a hands-on introduction and technical overview to micro-ROS and the corresponding tooling. Second, to inspire for practical use the micro-ROS stack by reporting on advanced use-cases from industrial applications and research.

This chapter is structured along those two goals. In Sect. 2, requirements and architecture are explained in detail as well as design decisions, followed by a tutorial for a first micro-ROS application with an ESP32 microcontroller in Sect. 3. In Sect. 4 an overview to the DDS-XRCE standard and the implementation by Micro XRCE-DDS is given. We also explain details on the use of Micro XRCE-DDS in micro-ROS and on its customization. Next, in Sect. 5, we present the client library with its implementation of common ROS concepts. Special focus is put on execution management. In Sect. 6, we present the integration of micro-ROS with different RTOS- or microcontroller-specific build tools as well as an own benchmarking tool. Thereafter, in Sect. 7, we report on practical use-cases of micro-ROS from industrial applications and research. The chapter is concluded in Sect. 8 with final remarks and a brief outlook.

2 Architecture Overview and Design Rationales

In this section, we first discuss fundamental requirements to micro-ROS. Then, we explain the micro-ROS stack layer by layer and compare it to the standard ROS 2 stack. Thereafter, we present major design decisions taken during the development. Finally, we list supported RTOS and microcontrollers and explain the relation to build tooling.

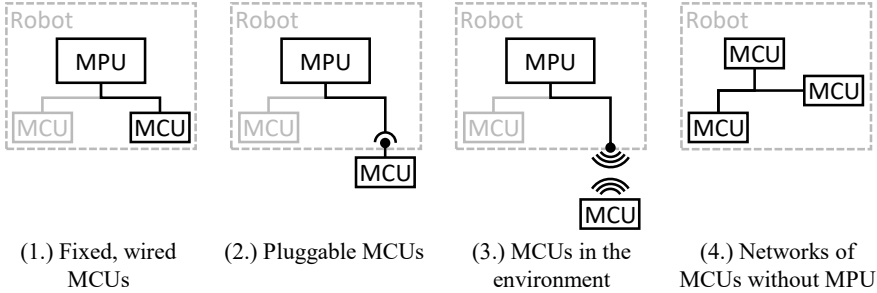


Fig. 2 Four typical computing and network system architectures used in robots

2.1 Requirements

In the first phase of the micro-ROS project, we analyzed a number use-cases and derived fundamental requirements. A key observation was the importance of the computing and network system architecture inside a robot. As indicated in the previous section, we distinguish between microprocessors with external RAM (typically $\gg 0.5$ GB), which are capable of running the standard ROS 2 stack on a desktop operating system like Linux, and systems-on-a-chip microcontrollers with integrated RAM, typically between 100 kB and 10 MB.

Throughout the rest of this chapter, we sometimes refer to a microprocessor as an *MPU* and a microcontroller as an *MCU*.

From the use-cases, we deduced four typical system architecture scenarios depicted in Fig. 2:

1. *Fixed, wired MCUs*: This is the most common scenario. The main software of the robot runs on one (or more) MPUs connected to a number of MCUs that interact with sensors and actuators, implement safety functions, or run low-latency real-time-critical control loops. Advanced sensor and actuators often come with integrated MCUs that have to be connected by UART, Ethernet, CAN, or similar standards.
2. *Pluggable MCUs*: In this scenario, the system architecture can be extended by pluggable devices. An example is an optional camera for a robot lawn mower that enhances the perception capabilities. Such devices can be either connected by a cable coupling or wirelessly.
3. *MCUs in the environment*: If sensors or actuators are deployed in the environment, they are not explicitly plugged and configured, but the robot has to discover them autonomously. An example is the wireless controller for a rolling shutter gate that a self-driving vehicle in a warehouse can open if it comes close to the gate.
4. *Networks of MCUs without MPU*: The last scenario comprises all robot system architectures without an MPU.

Table 1 Important requirements to the micro-ROS stack

Category	Requirement
Communication	<ol style="list-style-type: none"> 1. Support for 6LoWPAN or ZigBee, for Ethernet, and for serial protocols 2. Independent message serialization library 3. Dynamic discovery of participants without previous knowledge 4. Support for reliable communication 5. Efficient communication inside a microcontroller
Platform	<ol style="list-style-type: none"> 1. Support for Olimex LTD STM32-E407 and an STM-L1 board 2. Support for the RTOS NuttX 3. Portability to other RTOS, in particular if they follow the POSIX standard 4. Fit on microcontrollers with 192 kB SRAM
Runtime configuration	<ol style="list-style-type: none"> 1. Provisioning of ROS 2 node lifecycle 2. Mechanisms for deterministic start-up across microcontrollers and microprocessors. 3. Support of dynamic node parameters
Data model	<ol style="list-style-type: none"> 1. Usable with standard ROS message types for sensors, navigation, control, etc. 2. Support for custom message types
Diagnostics	<ol style="list-style-type: none"> 1. Tailored diagnostics mechanisms 2. Compatibility with ROS diagnostics
Time	<ol style="list-style-type: none"> 1. Quick boot 2. Time synchronization mechanism with <1 ms precision
Non-functional	<ol style="list-style-type: none"> 1. Compliance with ROS 2 2. Intuitive use for experienced ROS developers 3. Extensibility by modules/packages 4. Simple upgrade to new versions 5. Easy transfer of a standard ROS 2 node to micro-ROS and vice-versa

With the price of microprocessors dropping and algorithms becoming more sophisticated, we are expecting that the last scenario declines increasingly in importance. Therefore, it was ruled out for the time being.

In addition to providing support for the Scenarios 1 to 3, we derived a number of further requirements, which are explained in detail in a technical report [23]. The most important ones are given in Table 1. The current micro-ROS stack largely meets these requirements. In terms of supported microcontroller families, RTOS, and communication protocols, micro-ROS goes far beyond the original requirements as explained in the next subsections.

2.2 Layer-by-Layer Walkthrough

As mentioned in the previous section, micro-ROS utilizes and follows the layered architecture of ROS 2. This duality is depicted in Fig. 3.

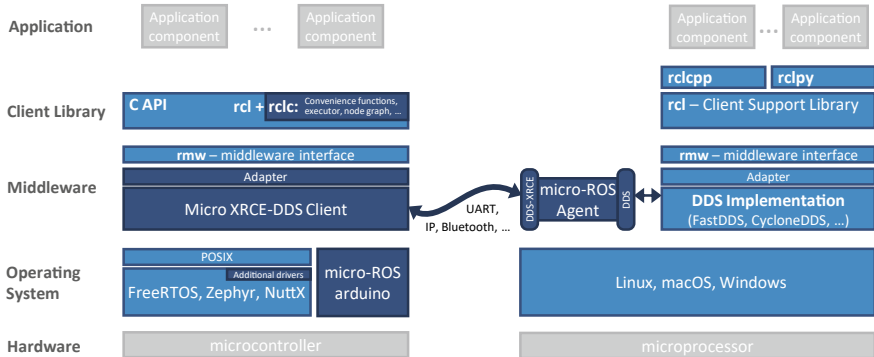


Fig. 3 Side-by-side comparison of micro-ROS stack (left) with standard ROS 2 (right)

2.2.1 The rcl and rmw Layers

The ROS 2 stack has been designed for high modularity and flexibility. The most important layers in terms of the software architecture are the *ROS Middleware Interface* (rmw) and the *ROS Client Support Library* (rcl).

The rmw defines a generic and slim interface to abstract from the underlying middleware being used for communication. It assumes three common concepts only: (1) naming of endpoints, (2) publish-subscribe communication, and (3) client-service (request-response) communication. These concepts are provided not only by implementations of the DDS standard but also by many other middlewares. To use a specific middleware, the interface defined by rmw has to be implemented in an adapter.

The rcl implements the most fundamental ROS concepts like node, publisher, subscription, client, service, and clock in the C programming language so that the high-level language client libraries (for C++, Python, etc.) can rely on the same implementation by binding rcl via native or foreign-function interfaces. This is a crucial difference to the architecture of classical ROS, where a custom middleware implementation is being used and the fundamental ROS concepts have been implemented independently for every programming language.

Both layers, rmw and rcl, are used as they are in the micro-ROS stack, with the exception that few features from rcl that are not available on a microcontroller are disabled (e.g., command line arguments). For this purpose, the micro-ROS project maintains a fork of the rcl repository¹ in which those features are disabled by one changeset applied after new releases of ROS 2. In addition, micro-ROS provides the rclc packages,² which extend rcl to make the combination rcl+rclc a feature-complete client library for the C programming language.

¹ <https://github.com/micro-ROS/rcl>.

² <https://github.com/ros2/rclc>.

2.2.2 Micro XRCE-DDS Middleware

The micro-ROS stack uses an implementation of the new DDS-XRCE standard provided by eProsimas open-source software under the name *Micro XRCE-DDS* [21]. The corresponding rmw adapter can be found in the micro-ROS organisation on GitHub.³ Micro XRCE-DDS is made up of two parts: The *Client* is a highly resource-optimized library in the C programming language for MCUs. The *Agent* is a standalone executable implemented in C++ for use on a microprocessor running Linux or Windows. The Agent bridges between DDS-XRCE and normal DDS. In particular, it performs the computationally intensive discovery tasks and quality-of-service mechanisms for the microcontroller. Serialization happens directly on the microcontroller in the *Common Data Representation* (CDR) format, which is also used by normal DDS. Hence, the Micro XRCE-DDS Agent can simply relay the binary messages in both directions.

The client-agent model of the XRCE-DDS standard fits very well to the typical hardware setup in robots as explained above in the scenarios 1 to 3 of computing and network system architectures.

Micro XRCE-DDS supports several *transports* for the connection between the microcontroller and the main microprocessor running the Agent. These transports include UDPv4, UDPv6, TCPv4, TCPv6, and serial. In addition, Micro XRCE-DDS comes with APIs for custom transports as explained in Sect. 4.

For efficient communication between micro-ROS nodes on the microcontroller, the middleware provides an optional *Shared Memory Transport* (SHM).

2.2.3 Real-Time Operating System

The ROS 2 stack has been developed for operating systems according to the *Portable Operating System Interface* (POSIX) standards [24]. In fact, ROS 2 only depends on a small subset of POSIX for process identification, clock, time, and filesystem operations. The use of POSIX is hidden by a thin abstraction layer implemented by the *rcutils* package and repository. This package also implements support for Windows and streamlines tiny differences between different Unix-like operating systems. Furthermore, *rcutils* implements an abstraction for atomic operations.

Micro-ROS adopts the assumption of POSIX but makes smaller changes to *rcutils*, using the same changeset mechanism as explained above for *rcl*: filesystem operations are disabled, dynamic memory allocations (in the context of error reporting) are prevented, and a user-level implementation of 64-bit atomic operations is provided.

³ https://github.com/micro-ROS/rmw_microxrcedds.

2.2.4 License

All middleware- and client-library-related packages created in the micro-ROS project are provided under the Apache 2.0 license, like the standard ROS 2 stack. Also, Micro XRCE-DDS is provided under Apache 2.0.

Things get interesting at the RTOS level: The micro-ROS build tool and the modules for external build systems are provided under Apache 2.0 but use (or are combined with) very differently licensed RTOS and board support components. The fact that typical embedded toolchains build the whole software (RTOS, micro-ROS, and application) into one binary image makes the situation more complex compared to desktop operating systems with clear separation between executables and kernel. More information is provided in the overview section of the micro-ROS website.⁴

2.3 Major Feature Differences to ROS 2

Although micro-ROS aims at implementing all core features of ROS 2 for microcontrollers, there are several important differences to take into account when creating own applications:

- *Fixed-size message only*: To avoid dynamic memory allocations, micro-ROS supports fixed-size message types only, i.e., the definition of a message type has to specify a size or upper bound for all arrays/vectors. If necessary, messages have to be converted on the agent side to dynamically-sized types.
- *Flexible, callback-level executor*: To cope with the very different scheduling APIs and mechanisms of the underlying RTOS, the rclc layer provides a flexible Executor on the level of individual callbacks.
- *No launch system*: Again, due to the very different underlying RTOS mechanisms, micro-ROS does not provide a launch system like standard ROS 2, but leaves the start of the micro-ROS nodes up to the developer.
- *Build-time node composition only*: The composition mechanism of the ROS 2 C++ Client Library allows deciding at launch time about the distribution of nodes to processes. It even allows for dynamic loading of nodes into running processes. Such mechanisms are not provided by micro-ROS. If multiple micro-ROS nodes should be executed in the same process, the composition has to be performed at compile-time by creating the nodes in the same main function of an executable.⁵
- *No DDS-XRCE security*: While there is a dedicated security standard for normal DDS [25], the DDS-XRCE standard does not define explicit security mechanisms but relies on such mechanisms of the underlying transport. If the underlying transport does not provide such mechanisms (e.g., plain UART) the connection is not

⁴ <https://micro.ros.org/docs/overview/license>.

⁵ Note that the concepts of *executables* and *processes* are not available in every RTOS.

encrypted, which is typically acceptable for wired connections inside a robot. Of course, the agent participates in the DDS and ROS 2 security mechanisms.

A continuously updated feature comparison between micro-ROS and ROS 2 can be found in the overview section of the micro-ROS website.⁶

2.4 *Design Rationales*

During the development of micro-ROS, we have made several important design decisions—starting with the use of DDS-XRCE, which has already been discussed above. In the following, we present and give reasons for four other major such decisions.

2.4.1 Reuse of Existing ROS 2 Layers

In the first months, we discussed two development strategies: First, developing a dedicated stack from scratch, similar to the rosserial client library of classical ROS. Second, developing micro-ROS based on existing ROS 2 packages and layers.

An important advantage of the first strategy would have been that the implementation could be optimized for microcontrollers from the very beginning, for example in terms of memory usage and execution management. However, due to our goal to bring all core ROS concepts on the microcontroller, we decided for the second strategy. The reuse of rmw and rcl ensures maximum compatibility and minimizes long-term maintenance costs.

2.4.2 Focus on POSIX-Based RTOS

Conceptual differences between RTOSes are much higher than between the dominating three desktop operating systems Windows, macOS, and Linux. Given the fact that ROS 2 was developed for POSIX-based OS and that there exist several open-source POSIX-based RTOS, we decided to focus on them first. In the other side, we avoided optimizing the micro-ROS stack for a specific RTOS. In the meanwhile, micro-ROS also supports bare-metal use. An example of a port for a non-POSIX RTOS is presented in Sect. 7.2.

⁶ https://micro.ros.org/docs/overview/ROS_2_feature_comparison.

2.4.3 Client Library by rcl+rclc

For the client library, we have discussed three options: An new implementation in C, a new implementation in C++ not requiring a full-fledged libstdc++, and a rework of the existing rclcpp package for use on microcontrollers. The third option was ruled out early, as rclcpp makes intensive use of dynamic memory allocations. In early 2019, we finally decided for the first option based on rcl and against the second option, to maximize compatibility with MCU-specific build tool chains. A detailed design decision paper⁷ from 2019 gives more details.

As of 2021, the second option has been reconsidered in the Embedded Systems WG as an additional client library for micro-ROS.

2.4.4 Tooling for ROS and Deeply Embedded Developers

During the requirements analysis, we identified two very different user groups for micro-ROS: First, ROS developers, who are used to Linux and the ROS concepts but have little experience with MCU or RTOS specific build tools, and, second, deeply embedded developers, who are used to specific MCU families and RTOS but likely new to ROS. To meet the needs of both groups, we decided to provide components or modules for different microcontroller and RTOS build tools as well as a generic build system named `micro_ros_setup` as a ROS 2 package and based on the ROS 2 CLI.

2.5 *Supported RTOS and Microcontrollers*

Micro-ROS comes with support for the three RTOS FreeRTOS [18], Zephyr [19], and NuttX [20] and a number of microcontrollers boards including Espressif ESP32, Renesas EK RA6M5, a couple of Arduino boards, Raspberry Pi Pico, and several boards by STMicroelectronics or with STM32 microcontrollers. There is also experimental support for bare metal use, the Arduino IDE, Mbed OS, and Azure RTOS.

The term “support” implies two aspects: First, microcontroller-specific extensions such as hardware drivers for the RTOS or micro-ROS stack. Second, provisioning of RTOS- and/or MCU-specific build tooling. At the same time both aspects are closely intertwined. Therefore, some of the extensions can be found in the generic `[NameOfRTOS]_apps` repositories of the micro-ROS organization at GitHub and some in microcontroller-specific repositories such as `micro_ros_espifdf_component`.

Section 6.1 gives details on the generic `micro_ros_setup` package and the provided integrations in RTOS- and microcontroller-specific build toolchains in form of components/modules.

⁷ https://micro.ros.org/download/client_library_decision_paper_2019.pdf.

Up-to-date lists of supported RTOS and microcontrollers can be found in the overview section of the micro-ROS website.^{8,9}

3 First Application Tutorial

In this section, we will guide you through all steps to build your own first micro-ROS application, which will implement a simple message ping-pong between a micro-ROS node and standard command line tools (CLI) under ROS 2 on a Linux host. All the build commands will be exemplified for the Espressif ESP32 microcontroller family, the Foxy distribution of ROS 2 and micro-ROS, and the real-time operating system FreeRTOS [18]. At very important commands, we will hint to other microcontrollers, distributions, and RTOSes. Complete tutorials with other microcontrollers and RTOSes can be found in the the tutorials section of the micro-ROS website.¹⁰

This section is organized in two parts: In the first subsection, we demonstrate the programming and build steps with the tooling from the `micro_ros_setup` package, which is based on the ROS 2 CLI tools. In the second subsection, we explain how to build the same application with micro-ROS component for the Espressif IoT Development Framework (ESP-IDF). More about build and development tools can be found in Sect. 6.1.

3.1 Ping-Pong Application with `micro_ros_setup`

First of all, install ROS 2 Foxy Fitzroy on your Ubuntu 20.04 LTS computer. Do so from binaries, via Debian packages. Alternatively, you can use a Docker container with a fresh ROS 2 Foxy installation. The one that serves the purpose is the container run by the command:

```
1 docker run -it --net=host -v /dev:/dev --privileged ros:foxy
```

Once you have a ROS 2 installation in the computer, follow these steps to download and build the `micro_ros_setup` package:

```
1 source /opt/ros/$ROS_DISTRO/setup.bash
2 mkdir microros_ws
3 cd microros_ws
4 git clone -b $ROS_DISTRO
    ↳ https://github.com/micro-ROS/micro_ros_setup.git
    ↳ src/micro_ros_setup
5 sudo apt update && rosdep update
6 rosdep install --from-path src --ignore-src -y
```

⁸ <https://micro.ros.org/docs/overview/rtos>.

⁹ <https://micro.ros.org/docs/overview/hardware>.

¹⁰ <https://micro.ros.org/docs/tutorials>.

```

7 sudo apt-get install python3-pip
8 colcon build
9 source install/local_setup.bash

```

These instructions will setup a workspace with a ready-to-use micro-ROS build system. The build system is in charge of downloading the required cross-compilation tools and building the apps for the required platforms. The build system's workflow is a four-step procedure:

1. *Create step*: This step is in charge of downloading all the required code repositories and cross-compilation toolchains for the specific hardware platform. Among these repositories, it will also download a collection of ready to use micro-ROS apps.
2. *Configure step*: In this step, the user can select which app is going to be cross-compiled by the toolchain. Some other options, such as transport, agent's IP address/port (for UDP transport) or device ID (for serial connections) will be also selected in this step.
3. *Build step*: Here is where the cross-compilation takes place and the platform-specific binaries are generated.
4. *Flash step*: The binaries generated in the previous step are flashed onto the hardware platform memory, in order to allow the execution of the micro-ROS app.

3.1.1 Creating a New Firmware Workspace

Once the build system is installed, create a firmware workspace that targets all the required code and tools for the ESP32 by:

```
1 ros2 run micro_ros_setup create_firmware_ws.sh freertos esp32
```

Once the command is executed, a folder named `firmware` must be present in your workspace.

This step is in charge, among other things, of downloading a set of micro-ROS apps for the specific platform you are addressing. In the case of FreERTOS, these are located at `firmware/freertos_apps/apps`. Each app is represented by a folder containing the following files:

- `app.c`: This C source file contains the logic of the application.
- `app-colcon.meta`: This file contains the micro-ROS app specific colcon configuration. Detailed info on how to configure the rmw via this file can be found in a dedicated tutorial in the micro-ROS website.¹¹

For creating a custom application, a folder `<my_app>` needs to be registered in this location, containing the two files just described.

¹¹ https://micro.ros.org/docs/tutorials/advanced/microxrcedds_rmw_configuration.

3.1.2 Configuring the Firmware

The configuration step will set up the main micro-ROS options and select the desired application. It can be executed with the following command:

```
ros2 run micro_ros_setup configure_firmware.sh [APP] [OPTIONS]
```

The options available for this configuration step are:

- 1 .--transport or -t: udp, serial or any hardware-specific transport label
- 2 .--dev or -d: agent string descriptor in a serial-like transport
- 3 .--ip or -i: agent IP in a network-like transport
- 4 .--port or -p: agent port in a network-like transport

In this tutorial, we will use a serial transport (labeled as `serial`) and focus on the out-of-the-box `ping_pong` application located at `firmware/freertos_apps/apps/ping_pong`. To execute this application with the chosen transport, run the configuration command above by specifying the `[APP]` and `[OPTIONS]` parameters as below:

```
ros2 run micro_ros_setup configure_firmware.sh ping_pong -t udp
    ↳ -i [LOCAL MACHINE ADDRESS] -p 8888
```

Then use the following command to set your wifi credentials for ESP32 to connect to your network:

```
ros2 run micro_ros_setup build_firmware.sh menuconfig
```

In the menuconfig window go to micro-ROS Transport Settings and then WiFi Configuration menu and fill your WiFi SSID and password. Save your changes, exit the window.

You can check the complete content of the `ping_pong` app in `apps/ping_pong/app.c` in the `freertos_apps` repository.¹²

This example showcases a micro-ROS node with two publisher-subscriber pairs associated with a topic named `ping` and a topic named `pong`, respectively. The node sends a message on `ping` with a unique identifier every two seconds. The `ping` subscriber receives all those messages, but sends a response on the `pong` topic only if the `ping` message comes from an external node.

To show that this micro-ROS node is functioning correctly, we implement communication with ROS 2 CLI tools that listen to the topics `ping` and `pong` published by the micro-ROS node and that publish a `fake_ping` message on `ping` that is received by the micro-ROS node. As a consequence, the `pong` publisher on the micro-ROS node will respond with a `pong` message to signal that it received the `fake_ping` message correctly.

The diagram shown in Fig. 4 clarifies the communication flow within the micro-ROS node and between this node and the ROS 2 CLI commands given below.

The contents of the application files can be found in `main.c` and `CMakeLists.txt` in the `micro-ROS-demos` repository.¹³

¹² https://github.com/micro-ROS/freertos_apps/tree/foxy/apps/ping_pong.

¹³ https://github.com/micro-ROS/micro-ROS-demos/blob/foxy/rclc/ping_pong.

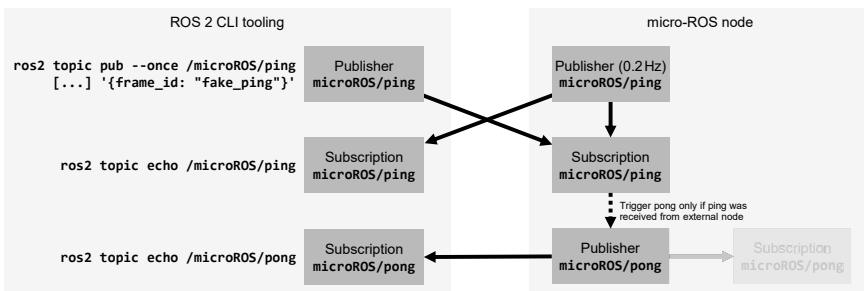


Fig. 4 Ping pong communication flow between micro-ROS application node and ROS 2 CLI tools

3.1.3 Building and Flashing the Application

When the configuring step ends, build the firmware by

```
1 ros2 run micro_ros_setup build_firmware.sh
```

Then, connect your ESP32 to the computer with a micro-USB cable and run:

```
1 ros2 run micro_ros_setup flash_firmware.sh
```

3.1.4 Creating the Agent

The micro-ROS app is now ready to be connected to a micro-ROS agent to start talking with the rest of the ROS 2 world. To do that, let's first of all create a micro-ROS agent:

```
1 ros2 run micro_ros_setup create_agent_ws.sh
```

Now, let's build the agent packages and, when this is done, source the installation by

```
1 ros2 run micro_ros_setup build_agent.sh
2 source install/local_setup.bash
```

A docker image is also available.

3.1.5 Running the Agent

At this point, you have both the client and the agent correctly installed in the ESP32 and in your host machine, respectively. To give micro-ROS access to the ROS 2 dataspace run the agent by

```
1 ros2 run micro_ros_agent micro_ros_agent udp4 --port 8888
```

or using docker by

```
1 docker run -it --rm --net=host microros/micro-ros-agent udp4
   ↳ --port 8888
```

3.1.6 Testing the Application

We now want to check that everything is working. Open a new command line. We are going to listen to the `ping` topic with ROS 2 to check whether the micro-ROS node is correctly publishing the expected pings:

```
1 source /opt/ros/$ROS_DISTRO/setup.bash
2 ros2 topic echo /microROS/ping
```

You should see the topic messages published by the Ping Pong node every five seconds:

```
1 user@user:~$ ros2 topic echo /microROS/ping
2 stamp:
3   sec: 20
4   nanosec: 867000000
5 frame_id: '1344887256_1085377743'
6 ---
7 stamp:
8   sec: 25
9   nanosec: 942000000
10 frame_id: '730417256_1085377743'
11 ---
```

At this point, we know that our app is publishing pings. Let's check if it also answers to someone else's pings. If this works, it'll publish a pong.

First, we subscribe with ROS 2 to the `pong` topic from a new shell (notice that initially we don't expect to receive any pong since none has been sent yet):

```
1 source /opt/ros/$ROS_DISTRO/setup.bash
2 ros2 topic echo /microROS/pong
```

And now, let's publish a `fake_ping` message on the `ping` topic with from yet another command line:

```
1 source /opt/ros/$ROS_DISTRO/setup.bash
2 ros2 topic pub --once /microROS/ping std_msgs/msg/Header
   ↳ '{frame_id: "fake_ping"}'
```

Now, we should see this `fake_ping` in the `ping` subscriber console, along with the micro-ROS pings:

```
1 user@user:~$ ros2 topic echo /microROS/ping
2 stamp:
3   sec: 0
4   nanosec: 0
5 frame_id: fake_ping
6 ---
7 stamp:
```

```

8     sec: 305
9     nanosec: 973000000
10    frame_id: '451230256_1085377743'
```

Also, we expect that, because of having received the `fake_ping`, the micro-ROS node on the ESP32 will answer with a pong:

```

1 user@user:~$ ros2 topic echo /microROS/pong
2 stamp:
3   sec: 0
4   nanosec: 0
5 frame_id: fake_ping
6 ---
```

3.2 Ping-Pong Application with Component for ESP-IDF

In this section, we explain how to build the above ping-pong with the micro-ROS Component for ESP-IDF. This has been tested in ESP-IDF v4.1, v4.2, and v4.3 with ESP32, ESP32-S2, and ESP32-C3.

3.2.1 Dependencies

This component needs `colcon` and other Python 3 packages inside the IDF virtual environment in order to build micro-ROS packages:

```

1 $IDF_PATH/install.sh
2 . $IDF_PATH/export.sh
3 pip3 install catkin_pkg lark-parser empy colcon-common-extentions
```

3.2.2 Usage

Clone the `micro_ros_espifdf_component` repository directly in the `components` folder of your project:

```

1 cd components
2 git clone
   ↳ https://github.com/micro-ROS/micro_ros_espifdf_component.git
```

If you encounter issues during the build process, ensure that you are running in a clean shell environment without the ROS 2 setup script sourced.

3.2.3 Example

In order to test a `ping_pong` example:

```

1 . $IDF_PATH/export.sh
2 cd examples/ping_pong
3 # Set target board [esp32/esp32s2/esp32c3]
4 idf.py set-target esp32
5 idf.py menuconfig
6 # Set configuration and WiFi credentials under micro-ROS settings
7 idf.py build
8 idf.py flash
9 idf.py monitor

```

To clean and rebuild all the micro-ROS library:

```
1 make -f libmicroros.mk clean
```

It is possible to use a micro-ROS Agent just with this Docker command:

```
1 docker run -it --rm --net=host microros/micro-ros-agent:galactic
   ↳ udp4 --port 8888 -v6
```

The other steps to test the application are the same is in Sect. 3.1.

3.3 Build with Docker Container

It is also possible to build the ping-pong application using a preconfigured Docker container. Docker is a good entry point in the case the tools are not available on the development machine by default. Execute this line to build an example app using Docker container:

```

1 docker run -it --rm --user espidf
   ↳ --volume="/etc/timezone:/etc/timezone:ro" -v
   ↳ $(pwd) :/micro_ros_espidf_component -v /dev:/dev
   ↳ --privileged --workdir /micro_ros_espidf_component
   ↳ microros/esp-idf-microros:latest /bin/bash -c "cd
   ↳ examples/ping_pong;idf.py menuconfig build flash monitor"

```

The Dockerfile for this container is provided in the ./docker directory and available in Dockerhub.

3.3.1 Using Serial Transport

By default, micro-ROS component uses UDP transport, but is possible to enable UART transport or any other custom transport by setting the colcon.meta like:

```

1 ...
2 "rmw_microrcdedds": {
3     "cmake-args": [
4         ...
5         "-DRMW_UXRCE_TRANSPORT=custom",
6         ...
7     ]
}

```

```
8 } ,  
9 ...
```

An example on how to implement such a transport is provided by the example of a custom serial transport in `examples/ping_pong_custom_transport`. Available ports are 0, 1, and 2 corresponding to `UART_NUM_0`, `UART_NUM_1`, and `UART_NUM_2`.

Again, it is possible to start the micro-ROS agent just with this Docker command:

```
1 docker run -it --rm -v /dev:/dev --privileged --net=host  
    ↳ microros/micro-ros-agent:galactic serial --dev [YOUR  
    ↳ BOARD PORT] -v6
```

4 Middleware Micro XRCE-DDS

In this section, we explain the DDS-XRCE standard, the implementation by Micro XRCE-DDS, and the integration in the micro-ROS stack. We also report memory profiling of Micro XRCE-DDS in connection with micro-ROS.

4.1 The DDS-XRCE Standard

The DDS standards are created and managed by the Object Management Group (OMG), where many distributed computing standards have been created by industry consortium members since 1989, being DDS-XRCE [16] one of them.

XRCE stands for *eXtremely Resource Constrained Environments* and refers to generally small devices with limited memory capacities. The DDS-XRCE protocol offers a way to communicate these constrained devices with full featured DDS systems. The DDS-XRCE protocol has been developed for devices and networks with the following characteristics:

- Operability over low-bandwidth networks (40–100 Kbps)
- Devices with sleep/wake cycles
- Support for specialized languages or frameworks
- Plug-and-play characteristics due to dynamic discovery
- Publish or subscribe to any *Interface Definition Language* (IDL) data types
- Support for data updates to multiple on the same or multiple DDS Topics
- Support for both reliably and best-effort communication streams
- Support for secure communication at the transport level
- Provides full read/write access
- Full implementation with less than 100 kB of code

The DDS-XRCE protocol allows the DDS-XRCE devices, called *clients*, to communicate with a server, called *agent*. This Micro XRCE-DDS Agent allows the devices to publish or subscribe to topics in the DDS domain, called *Global Data Space*. In

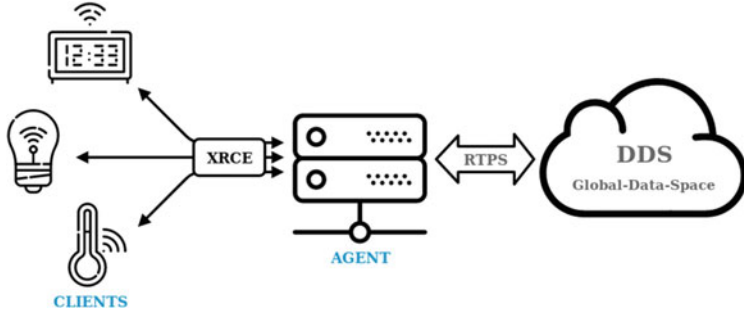


Fig. 5 Overview to architecture of DDS-XRCE standard

general, the DDS-XRCE standard describes a wire protocol that enables the XRCE clients to create and interact with DDS entities in the Micro XRCE-DDS Agent. Those DDS entities in the agent will act on behalf of the clients (Fig. 5).

As the DDS-XRCE protocol is applied on low-powered and resource-limited devices, the goal is not to embed the entire functionality of DDS into such a restricted environment but rather to allow them to act as participants in a larger DDS ecosystem.

4.2 Micro XRCE-DDS Architecture and Implementation

This section describes the most relevant features of Micro XRCE-DDS,^{14,15} the default middleware implementation for micro-ROS. Micro XRCE-DDS is the DDS-XRCE implementation of eProsima. It is fully open source and comes with an Apache 2.0 license.

As explained in Sect. 4.1, the XRCE standard follows a client-server architecture, which are the two main elements of Micro XRCE-DDS:

- *Micro XRCE-DDS Agent*: a C++11 out-of-the-box application which implements the agent functionality¹⁶
- *Micro XRCE-DDS Client*: a C99 library which implements the Micro XRCE-DDS Client side functionality¹⁷

In addition, the Micro XRCE-DDS suite offers two more components:

- *Micro CDR*: a CDR (Common Data Representation) compliant de-/serialization engine used in the Micro XRCE-DDS suite.¹⁸

¹⁴ <https://www.eprosima.com/index.php/products-all/eprosima-micro-xrce-dds>.

¹⁵ <https://micro-xrce-dds.docs.eprosima.com/en/latest>.

¹⁶ <https://github.com/eProsima/Micro-XRCE-DDS-Agent>.

¹⁷ <https://github.com/eProsima/Micro-XRCE-DDS-Client>.

¹⁸ <https://github.com/eProsima/Micro-CDR>.

- *Micro XRCE-DDS Gen*: a code generator tool used for generating Micro CDR de/serialization functions from IDL sources.¹⁹

4.2.1 Low Resource Consumption

Micro XRCE-DDS is focused on microcontroller applications. Therefore, the design and implementation of this middleware have been carried out taking into account the memory constraints of these kind of devices.

Given the limited memory resources offered by the systems targeted by the Micro XRCE-DDS Client library, the memory size manipulation is highly relevant and takes place at two different levels:

- *At configuration time*: To fix the size of the executable code size, the library can be compiled enabling or disabling several profiles. As described later, the client library follows a profile concept that enables to choose, add, or remove some features at configuration time, allowing the user to customize its size.
- *At runtime*: The client library is both dynamic and static memory free, implying that all memory footprint depends only on how the stack grows during the execution. The stack size is determined by the library functions, along with user configured parameters as the *Maximum Transmission Unit* (MTU) and the communication streams used:
 - The MTU is transport-dependent and can be configured by the user. The selected value represents the maximum message size that can be sent or received without fragmenting the message. The transport uses the MTU value to create an internal buffer, which is the memory block where the messages will be written to and stored in when interchanged.
 - As for the streams, the user can define a maximum of 127 best-effort streams and 128 reliable streams, but for the majority of purposes only one stream in either best-effort or reliable mode is needed. Moreover, reliable streams have a message history associated, whose size can be tailored to fit the specific requirements of the application. In this case, the size of the stream equals to the size of the configured MTU times the associated history. In the best-effort case, no history is stored and the memory reserved for the stream equals the size of the MTU.

Detailed information about the memory consumption as a function of message size, entity number, and internal memory management of the middleware library is provided in Sect. 4.4.

¹⁹ <https://github.com/eProsima/Micro-XRCE-DDS-Gen>.

4.2.2 Transport Agnosticity

The user can choose between several transport layers for the communication between the clients and the agent. In contrast to other IoT middlewares which support only one particular transport layer, XRCE supports multiple transport protocols natively. The latest version of Micro XRCE-DDS supports: UDPv4, UDPv6, TCPv4, TCPv6, and serial.

Apart from this, eProsima's Micro XRCE-DDS provides a custom transport API that allows the users to implement their own transport protocol in both the client and agent libraries. Thanks to this, the Micro XRCE-DDS wire protocol can be used over virtually any protocol, network, or communication mechanism. In order to do so, two general communication modes are provided:

- *Stream-oriented mode*: the communication mechanism implemented does not have the concept of a packet. Instead, *High-Level Data Link Control* (HDLC) framing²⁰ will be used.
- *Packet-oriented mode*: the communication mechanism implemented is able to send a whole packet that includes an XRCE-DDS message.

These two modes can be selected by activating and deactivating the `framing` parameter in both the micro-ROS client and the micro-ROS agent transport configuration.

4.2.3 Efficient Communication Inside a Microcontroller

Additionally, the Micro XRCE-DDS Client provides a *Shared Memory Transport* (SHM) for efficient communication between micro-ROS nodes within the same microcontroller memory space without the need of interacting with the micro-ROS agent. SHM provides clients with self-introspection capabilities to detect and communicate with compatible publishers, subscribers or any other DDS entities without the need to recur to the agent. The agent acknowledges the existence of those compatible entities within a client and avoids sending redundant information to the client. SHM can be activated by the flag `UCLIENT_PROFILE_SHARED_MEMORY` in the `colcon.meta` file of a micro-ROS application project.

4.2.4 Multi-Platform Support

Micro XRCE-DDS is portable to all low-mid range microcontrollers, to any RTOS, and bare metal. The only system requirements are timing functions that are usually provided by the RTOS or can be implemented easily in bare-metal systems. Up to date, the Micro XRCE-DDS Client supports FreeRTOS, Zephyr, NuttX, and Mbed OS as embedded RTOS. Moreover, it also runs on Windows and Linux. On the other hand, the Micro XRCE-DDS Agent supports Windows and Linux.

²⁰ See <https://micro-xrce-dds.docs.eprosima.com/en/latest/transport.html> for details.

4.2.5 QoS Support

The Micro XRCE-DDS Client library allows the user to use different approaches for creating DDS entities in the Micro XRCE-DDS Agent. This entity creation allows to define at the client side the required Quality of Services parameters of the DDS entities. The Micro XRCE-DDS suite allows to define the DDS entities using three modes: XML, references and binary encoded format.

4.2.6 Best-Effort Versus Reliable Operation

Micro XRCE-DDS messages flow between client and agent through streams. A stream represents an independently ordered flow of information, like a messaging queue. There are two kinds of streams: best-effort and reliable. Both streams have a raw buffer (`uint8_t` array) associated with them, but the layout is different. Best-effort streams handle a single message at a time, while reliable streams handle a sequence of messages using a message history with reception acknowledgment.

4.3 Micro XRCE-DDS in the Micro-ROS Stack

On the microcontroller, the micro-ROS stack uses the Micro XRCE-DDS Client by its default rmw adapter layer `rmw_microxrceddss`. In this layer, micro-ROS manages the memory for ROS 2 entities with a static pool approach. In general, `rmw_microxrceddss` has a defined struct for handling ROS 2 memory and one extra data structure for handling topics and services buffers.

When `rmw_microxrceddss` is initialized, it uses one static memory slot for handling a Micro XRCE-DDS session. For example, this session structure has handles for four XRCE-DDS streams: input reliable, input best-effort, output reliable, and output best-effort. The best-effort buffers will be MTU long and the reliable ones will have `RMW_UXRCE_STREAM_HISTORY` slots of MTU size each.

Similarly, the node, publisher, subscriber, and service entities will have their associated static memory items with all the required members for maintaining their states. The size of the static memory pools associated to the ROS 2 entities can be configured at build time with CMake variables, e.g., `RMW_UXRCE_MAX_NODES` for nodes.

There is one special static memory pool in `rmw_microxrceddss` named *Topic Handling Pool*. This static memory pool is used for storing the data received by the middleware when a “read data” operation is performed and before the “take data from middleware” operation retrieves the data. Its size is determined by `RMW_UXRCE_MAX_HISTORY` and each slot has `MTU × RMW_UXRCE_STREAM_HISTORY` because it is the biggest message size that the middleware can receive. The Topic Handling Pool is shared by all entities that receive data in a micro-ROS client.

Also, there are some build-time parameters related to client-to-agent connection (e.g., `CONFIG_RMW_DEFAULT_UDP_PORT`, `CONFIG_RMW_DEFAULT_UDP_IP`, and

`CONFIG_RMW_DEFAULT_SERIAL_DEVICE`) that can be configured either at build-time or at runtime. This means that they can be defined in the `client-host-colcon.meta` configuration file. Furthermore, some rmw and middleware parameters can be modified at run-time via a user configuration API.

Notice, that it is also possible to set the Micro XRCE-DDS `client_key`, which identifies a XRCE-DDS client and is set randomly by default. This feature is useful for reusing DDS entities already created on the agent side. Further information can be found in the `rmw-microxrcedds` repository.²¹

4.4 *Memory Profiling of Micro XRCE-DDS in Micro-ROS*

Micro-ROS and its middleware target low- and mid-range devices that do not have enough memory for running a full ROS 2 stack. Therefore, it is important to evaluate the memory usage of the different entities in the micro-ROS stack. A full memory profiling of the micro-ROS stack in terms of static, dynamic, and code memory is presented in the concepts section of the micro-ROS website.²² This webpage is updated with every major improvement on the micro-ROS memory management.

At the moment of writing this chapter, the memory usage of each entity in the micro-ROS stack is shown in Fig. 6. For example, a micro-ROS application that has only one publisher will use about 20 kB of memory. As the application increases the number of used entities, the memory usage of the application increases slightly. More complex entities, such as service servers or clients will require more memory than basic publishers or subscribers.

Note that most of the used memory is static memory assigned at build time. The dynamic memory usage in micro-ROS is guaranteed to be allocated during the entity creation stage and never during the entity operation. The stack usage in the benchmarking process has been measured as the peak stack used in a FreeRTOS-based system when creating the micro-ROS entity and using it for several minutes.

5 Client Library

This section describes the client library of micro-ROS, which implements the most fundamental ROS concepts in the C programming language by extending the ROS 2 Client support library `rcl` with the `rclc` packages.²³ The first subsection gives code snippets on how to use those concepts in user code. The second subsection explains execution management in micro-ROS, which is more customizable than in `rclcpp` or `rclpy` of standard ROS 2. The last three subsections give introductions to advanced

²¹ <https://github.com/micro-ROS/rmw-microxrcedds#rmw-micro-xrce-dds-implementation>.

²² https://micro.ros.org/docs/concepts/benchmarking/memo_prof.

²³ <https://github.com/ros2/rclc>.

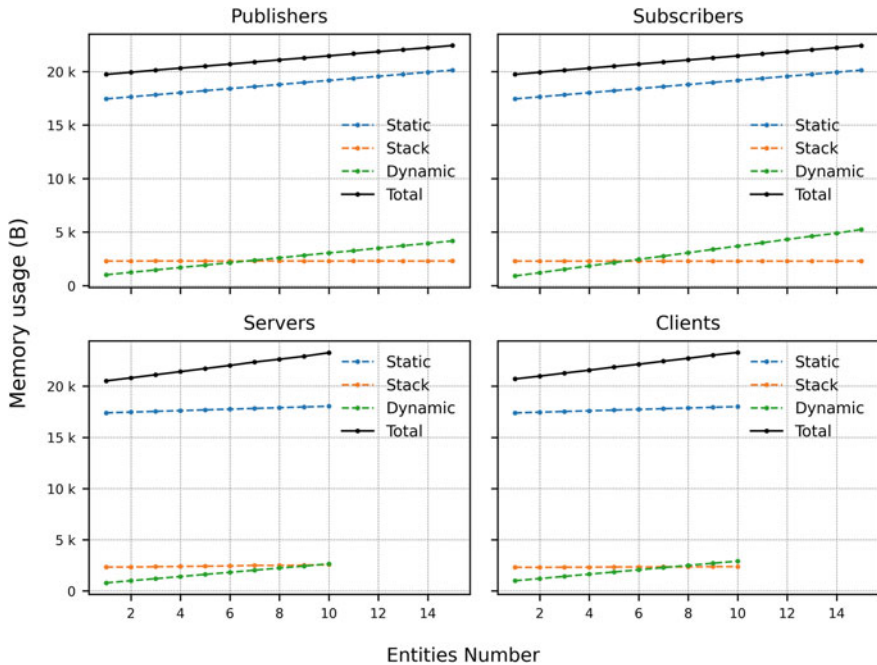


Fig. 6 Memory usage of micro-ROS entities

functionalities for querying the ROS graph, runtime lifecycle management, and diagnostics, which go beyond the core ROS concepts.

5.1 Programming with *rcl* and *rclc*

The *rclc* packages provide convenience functions to easily program a ROS application in the C programming language. The programming interface is demonstrated by a simple example: A publisher shall publish every second a message and a subscriber shall print out this message. First, a node can be created by specifying its name and namespace. Further more, memory allocation is organized by an *allocator* and the ROS context is initialized by using a *support* object:

```

1 rcl_node_t my_node;
2 rclc_support_t support;
3 rcl_allocator_t allocator = rcl_get_default_allocator();
4 rclc_support_init(&support, argc, argv, &allocator);
5 rclc_node_init_default(&my_node, "name", "namespace", &support);
```

A publisher is created with three parameters: node object, message type, and topic name. In this example, a string publisher with topic name `ping` is cre-

ated. A macro is available to convert message types familiar from ROS 2 (e.g., `std_msgs::msg::String`).

```

1 rcl_publisher_t my_pub;
2 const char * topic = "ping";
3 const rosidl_message_type_support_t * msg_type =
    ↪ ROSIDL_GET_MSG_TYPE_SUPPORT(std_msgs, msg, String);
4 rc = rclc_publisher_init_default(&my_pub, &my_node, msg_type,
    ↪ topic);
```

The memory of the string message that shall be published has to be allocated statically:

```

1 std_msgs__msg__String pub_msg;
2 std_msgs__msg__String__init(&pub_msg);
3 const unsigned int PUB_MSG_SIZE = 20;
4 char pub_string[PUB_MSG_SIZE];
5 snprintf(pub_string, 13, "%s", "Hello World!");
6 rosidl_generator_c__String__assignn(&pub_msg, pub_string,
    ↪ PUB_MSG_SIZE);
```

To publish this message, a timer is setup to call `rcl_publish` every second:

```

1 rcl_timer_t my_timer;
2 rclc_timer_init_default(&my_timer, &support, RCL_MS_TO_NS(1000), timer_cb);
3
4 void timer_cb(rcl_timer_t * timer, int64_t last_call_time)
5 {
6     if (timer != NULL) {
7         rcl_publish(&my_pub, &pub_msg, NULL);
8     }
9 }
```

Analogously, we create a subscriber that listens to the same string type and topic name:

```

1 rcl_subscription_t my_sub;
2 std_msgs__msg__String sub_msg;
3 std_msgs__msg__String__init(&sub_msg);
4 rclc_subscription_init_default(&my_sub, &my_node, msg_type,
    ↪ topic);
5
6 void sub_cb(const void * msgin)
7 {
8     const std_msgs__msg__String * msg =
        ↪ (const std_msgs__msg__String *)msgin;
9     if (msg != NULL) {
10         printf("I heard: %s\n", msg->data.data);
11     }
12 }
```

ROS 2 services is another communication mechanism between nodes. Services implement a client-server paradigm based on ROS 2 messages and types. A code example how to use services in micro-ROS can be found in the `rclc_examples` package.²⁴

²⁴ https://github.com/ros2/rclc/tree/master/rclc_examples.

A parameter is a configuration value of a ROS 2 node which can be dynamically reconfigured. Parameters can also be defined and used in rclc. A code example is again available in the `rclc_examples` package.

Guard conditions are objects that can be used to notify the Executor to wake up based on some external event similar to the concept of condition variables in multi-threaded C++ programs. Guard conditions are also available in rclc. They can also be used to react on hardware events.

After defining all objects, the `spin` method needs to be called, like in `rclcpp` or `rclpy`. As the ROS 2 Executors are implemented in the language-specific client libraries and not in rcl, the main rclc package provides its own Executor. This concept is explained in more detail in the next section.

The following code snippet completes the example by adding the timer and the subscription to an Executor instance. To avoid dynamic memory allocation at runtime, the user has to specify how many objects (handles) the Executor shall manage. Subscriptions and other objects can be added only until the maximum number of handles is reached. Handles can also be removed at runtime.

```

1 rclc_executor_t executor;
2 unsigned int num_handles = 2;
3 rclc_executor_init(&executor, &support.context, num_handles,
4   ↪ &allocator);
5 rclc_executor_add_timer(&executor, &my_timer);
6 rclc_executor_add_subscription(&executor, &my_sub, &sub_msg,
7   ↪ &sub_cb, ON_NEW_DATA);
8 rclc_executor_spin(&executor);

```

5.2 Execution Management with the rclc Executor

The development of an execution management mechanism for micro-ROS is based on an analysis of processing patterns commonly used in robotic applications.

The most basic pattern is the *sense-plan-act control loop* as depicted in Fig. 7. All callbacks of the *sense* phase, which usually comprise of sensor data acquisition, shall be processed before the *plan* phase to ensure that planning algorithms use the most recent sensor data information.

A second pattern is the synchronization of sensor data with different update rates. For example, an IMU has usually a very high update rate, while a laser sensor a low one. Synchronizing sensor data with different rates deterministically is difficult due to latency jitter and clock drift. An alternative pattern is to wait for a new laser input and then request available IMU data as shown in Fig. 8.

A third common pattern is the prioritization of certain processing paths, e.g., for safe obstacle avoidance.

The need for these patterns are often non-functional requirements that a robotic application must meet: bounded end-to-end latencies, low jitter of response times

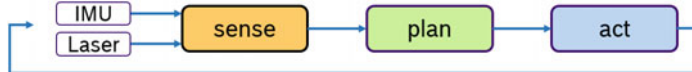
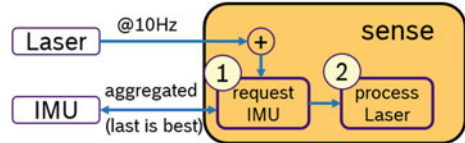


Fig. 7 Typical sense-plan-act control loop in robotics

Fig. 8 Sensor fusion of sensor data with different update rates



of cause-effect chains, deterministic processing, and quick response times even in overload situations.

Embedded real-time applications can be scheduled with different schemes. The most common is the periodic scheduling scheme, in which all functions are mapped to predefined periods, e.g., 1, 10, and 100 ms. This scheduling scheme is well supported by all real-time operating systems and formal performance analysis approaches are well known for decades.

In contrast, ROS 2 follows an event-driven approach. Messages are communicated between nodes using the publish and subscribe paradigm. It is the responsibility of an Executor to react upon new messages. In detail, this Executor coordinates the execution of callbacks issued by the participating nodes by checking the incoming messages from the DDS queue and dispatching them to the underlying threads for execution. Currently, the dispatching mechanism is very basic: the Executor looks up wait queues, which notifies it of any pending messages in the DDS queue.

If there are pending messages, the Executor executes the corresponding callbacks one after the other, which is also called round-robin to completion. In addition, the Executor also checks for events from application-level timers, which are always processed before messages. There is no further notion of prioritization or categorization of these callback calls. Moreover, the ROS 2 Executor from rclcpp in its current form does not leverage the real-time capabilities of the underlying operating system scheduler to have finer control on the execution order. The overall implication of this behavior is that time-critical callbacks could suffer possible deadline misses and degraded performance since they are serviced later than non-critical callbacks. Additionally, due to the round-robin mechanism and the resulting dependencies it causes on the execution time, it is difficult to determine usable bounds on the worst-case latency that each callback execution may incur [26].

To address the aforementioned common processing patterns found in robotic applications with the event-driven ROS 2 execution scheme, we have developed a very flexible approach in micro-ROS named *rclc Executor* [27].

It supports three main features: First, a *trigger condition* allows to define when the processing of a callback shall start. This is useful to implement sense-plan-act control loops or more complex processing structures with directed acyclic graphs. Second, a user can specify the *processing order* in which these callbacks will be

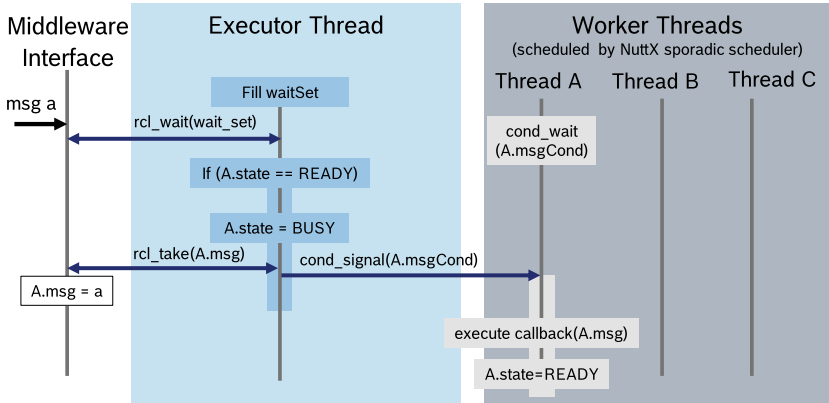


Fig. 9 Budget-based real-time Executor design

executed. With this feature, the pattern of sensor fusion with multiple rates, in which data is requested from a sensor based on the arrival of some other sensor, can be easily implemented. Third, the rclc Executor allows to set scheduling parameters (e.g., priorities) of the underlying operating system. With this feature, prioritized processing can be implemented.

By the example of NuttX, we even demonstrated how to use budget-based scheduling in micro-ROS [28]. Figure 9 shows the Executor design for this purpose: One Executor thread is responsible for checking for new data from the DDS queue. For every callback, a thread is spawned with the desired scheduling parameters of the operating system. The Executor thread dispatches new data to the corresponding callback functions, which are then executed based on the operating system scheduling parameters.

Last, but not least, since memory is very limited on microcontrollers, dynamic memory is only allocated at the configuration stage of the rclc Executor. This allows a safe execution on the microcontroller.

5.3 ROS Graph

A micro-ROS system is by definition a system where it is not possible to run a full featured DDS middleware. From ROS 2 Foxy, the ROS 2 graph discovery and handling is based on a hidden DDS topic named `ros_discovery_info`. This topic and its associated packages (such as `rmw_dds_common`) heavily rely on DDS identifiers such as GUIDs. This way, the node concept in ROS 2 is separated from the DDS participant.

The micro-ROS stack is not able to handle the ROS 2 graph in a fully compliant way because it does not have direct access to the DDS middleware but handles DDS

entities through DDS-XRCE (cf. Sect. 4). In order to have full support for ROS 2 graph in micro-ROS, the micro-ROS Agent implements a *graph manager*. This graph manager is in charge of two main functionalities related to the ROS 2 graph:

1. It announces all the micro-ROS participants, nodes, publisher, and subscribers in the `ros_discovery_info` topic, allowing ROS 2 nodes to discover the entities created by a micro-ROS application.
2. It retrieves the information from the `ros_discovery_info` topic from the ROS 2 nodes and prepares a memory-aware topic ready to be subscribed by micro-ROS nodes. This `ros_to_microros_graph` topic summarizes the ROS 2 graph information in a way that the micro-ROS stack can handle it while having the full information about the nodes names and associated topic names and types.

In the micro-ROS client part, the ROS 2 graph management tools are disabled by default. Users can enable them by setting a flag in the micro-ROS `colcon.meta` file. When the micro-ROS client graph manager is enabled, a subscription to `ros_to_microros_graph` will be configured and static and dynamic memory will be used in order to handle the ROS 2 graph data.

5.4 Advanced Runtime Lifecycle Management

The C++ ROS 2 client library `rclcpp` does not only provide abstractions for standard ROS nodes but also so-called *managed lifecycle nodes*, allowing greater control over the state of a ROS 2 system.²⁵ It allows to ensure that all components have been instantiated correctly before beginning executing its behavior, restarting, or replacing nodes. For this purpose, a standard lifecycle has been defined for all such nodes, see the gray and blue boxes in Fig. 10.

We took this concept as basis for advanced lifecycle management to enable sleep modes, power saving, etc., often required on resource-constrained devices. First, we ported managed lifecycle nodes to `rclc` in the `rclc_lifecycle` package for use on microcontrollers. Second, we extended the standard lifecycle by additional modes—termed *system modes*—that provide additional abstractions for easy (re-)configuration of nodes and entire (sub-)systems.²⁶

Based on a specification of a ROS 2 system in terms of its ROS 2 nodes, a hierarchy of nodes (sub-systems), and a definition of their system modes, a mode inference mechanism and a mode manager node enable easy (re-)configuration of entire ROS 2 systems. In detail, based on the current state and parameterization of the nodes, the system mode of the entire system can be inferred and switching an entire system to a specified system mode results in according state and parameterization of all contained ROS 2 nodes.

²⁵ See the ROS 2 design document at https://design.ros2.org/articles/node_lifecycle.html for details on the purpose of this concept.

²⁶ https://github.com/micro-ROS/system_modes.

As the mode inference mechanism and mode management node are quite complex, these are implemented on top of rclcpp and intended to run on a microprocessor. They manage standard ROS 2 rclcpp lifecycle nodes as well as rclc lifecycle nodes running on a microcontroller, see Fig. 11. The implementation of lifecycle nodes is not influenced by the system modes concept as the interface between the mode manager and lifecycle nodes purely relies on standard lifecycle messages and parameter events.

Nordmann et al. provide more information on the system modes concept and its application in [29].

5.5 Diagnostics

Core requirements for micro-ROS diagnostics were to (1) be slim and avoid dynamic memory allocation and (2) integrate with the ROS 2 diagnostics stack.

Requirement 1 cannot be met with standard ROS 2 diagnostics messages²⁷ because of the main message type `DiagnosticArray`: It is an array of arbitrary

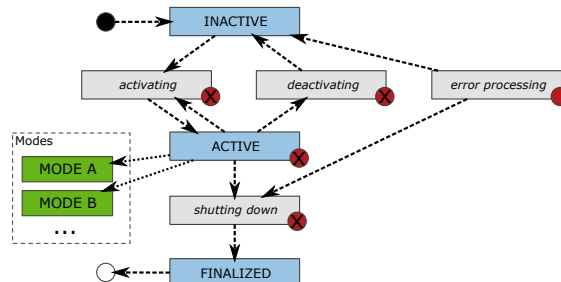


Fig. 10 Default node lifecycle (blue boxes for primary states, gray boxes for transition states) of ROS 2 and the extension by system modes (green boxes) developed with micro-ROS. Red dots indicate potential transitions to the error processing state

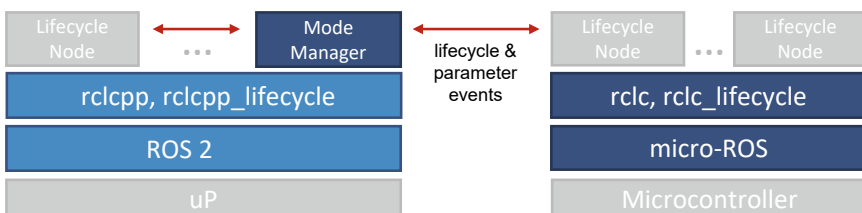


Fig. 11 System modes architecture: The mode inference and management runs in the mode manager on the microprocessor. It manages (re-)configuration of lifecycle nodes (and hierarchies of them) on the microprocessor itself as well as on connected microcontrollers

²⁷ Package `diagnostic_msgs` is part of ROS 2 common interfaces, cf. https://github.com/ros2/common_interfaces.

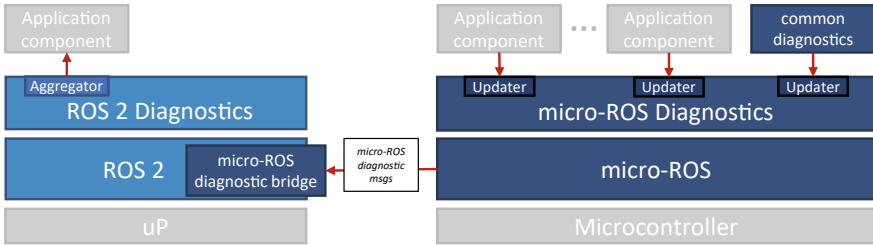


Fig. 12 micro-ROS diagnostics architecture, showing the diagnostics stack running on the microcontroller (right), sending optimized diagnostics messages to a ROS 2 bridge component that translates these messages to standard ROS 2 diagnostic messages

size, the array element `DiagnosticStatus` makes heavy use of strings, and it contains another array of arbitrary size of `KeyValue` messages. This constraint and Requirement 2 led to the micro-ROS diagnostics architecture²⁸ depicted in Fig. 12. The micro-ROS diagnostics packages do not provide any diagnostic aggregator as we assume that such aggregation takes place on a microprocessor running standard ROS 2.

First, micro-ROS diagnostics provides a specific `MicroROSDiagnosticStatus` message type that neither contains arrays nor contains strings. Instead, key and value of the diagnostic status as well as IDs of the hardware and updater are encoded with numeric values, referencing entries in a lookup table. Based on the lookup table, the *diagnostic bridge*, a standard ROS 2 component implemented with `rclcpp`, can translate `MicroROSDiagnosticStatus` into standard ROS 2 `DiagnosticStatus`.

Another part of micro-ROS diagnostics is an `rclc`-based library for diagnostic updaters. Each updater references a set of diagnostic tasks, i.e., c-functions that return a diagnostic value such as a boolean value, a numeric value (integer or double precision), or an ID that references a value entry in the lookup table. A diagnostic updater additionally holds IDs referencing a diagnostic key, an updater ID, and a hardware ID from the lookup table. Upon each execution of the updater, the diagnostic task is executed and a `MicroROSDiagnosticStatus` message is created and sent to a reserved topic `/diagnostics_uros`.

The diagnostic bridge, running on a microprocessor and instantiated with the lookup table, subscribes to `/diagnostics_uros`, translates `MicroROSDiagnosticStatus` messages into `DiagnosticStatus` messages, and publishes them to the standard `/diagnostics` topic. These messages are fully transparent, i.e., a standard ROS 2 diagnostic aggregator is able to treat the translated micro-ROS diagnostic messages in the same way it is treating diagnostic messages from standard ROS 2 components, hence fulfilling Requirement 2 stated above.

²⁸ https://github.com/micro-ROS/micro_ros_diagnostics.

6 Build and Development Tools

This section gives an overview to development tools for micro-ROS. The first part is focused on build tools, while the second part presents a generic benchmarking tool.

6.1 Build Tools

Micro-ROS provides multiple ways of building a library containing the whole micro-ROS stack. Usually those build systems generate a static library and a set of header files to be included and linked against the user application. Also, some of them integrate this library directly in a platform specific SDK.

6.1.1 `micro_ros_setup`²⁹

The principal package for creating micro-ROS apps is `micro_ros_setup`. It is provided as a ROS 2 package that can be included in a ROS 2 workspace and offers a set of utilities for creating, building, and flashing micro-ROS in an embedded target.

Using `micro_ros_setup`, a ROS 2 developer can use the same tooling to build and flash a micro-ROS applications without worrying about the underlying platform specific details such as: RTOS SDK, compiler version, additional platform configuration, etc.

It includes most of the micro-ROS supported platforms (e.g., Olimex STM32-E407, ST Nucleo boards, and ESP32) and RTOSes (including FreeRTOS, Zephyr, NuttX, and Mbed). Instructions about how to use it can be found in the tutorial section of the micro-ROS website.³⁰

The `micro_ros_setup` package also provides a tool for generating a standalone precompiled static library that can be copied and used in external projects or platforms. It is called *custom library generator*³¹ and works just providing the following files:

- CMake toolchain for defining the building target, flags and options
- `colcon.meta` file for configuring each layer of the micro-ROS stack

The `micro_ros_setup` package also allows building micro-ROS in a Linux environment for debugging and testing purposes.

²⁹ https://github.com/micro-ROS/micro_ros_setup.

³⁰ <https://micro.ros.org/docs/tutorials>.

³¹ https://micro.ros.org/docs/tutorials/advanced/create_custom_static_library.

6.1.2 Micro-ROS Component for ESP-IDF³²

This is a component that integrates micro-ROS in the Espressif ESP32 family: ESP32, ESP32-S2, and ESP32-C3. It builds and link a micro-ROS static library against an ESP-IDF application and provides serial, WiFi, and Ethernet transports.

6.1.3 Micro-ROS Module for Zephyr³³

This module integrates micro-ROS in the Zephyr RTOS build system. It builds and link a micro-ROS static library against a Zephyr application and provides Serial and UDP transports. It can be used to integrate micro-ROS in any of the Zephyr RTOS supported boards.³⁴

For debugging and testing purposes, this package allows building micro-ROS in a Linux environment using the *Zephyr Native POSIX port*.

6.1.4 Micro-ROS for Arduino³⁵

This support package is a special port of micro-ROS provided as a set of precompiled libraries for specific Arduino-enabled platforms. The main reason for this approach is that Arduino does not allow the build of a complex library such as micro-ROS, so by using this approach a ready-to-use solution is provided to the Arduino users.

Along with this package, there are detailed instructions for building the micro-ROS for Arduino library manually, for users that need to tune the default configuration.

6.1.5 Micro-ROS for STM32CubeMX and STM32CubeIDE³⁶

This package is a set of utilities which enables the seamless configuration, setup, and integration of micro-ROS into an STM32 controller based project. As such, it allows micro-ROS to be virtually supported by the full set of boards offered by STMicroelectronics.

Its usage is based on Dockers, via a prepared Dockerfile which eases micro-ROS library generation outside of a ROS 2 environment.

³² https://github.com/micro-ROS/micro_ros_espifd_component.

³³ https://github.com/micro-ROS/micro_ros_zephyr_module.

³⁴ <https://docs.zephyrproject.org/latest/boards>.

³⁵ https://github.com/micro-ROS/micro_ros_arduino.

³⁶ https://github.com/micro-ROS/micro_ros_stm32cubemx_utils.

6.1.6 Micro-ROS Module for Raspberry Pi Pico SDK³⁷

This module integrates micro-ROS in the Raspberry Pi Pico build system. It builds and links a micro-ROS static library ready to be used with serial transport in the Raspberry Pi Pico microcontroller.

6.1.7 Micro-ROS App for NuttX³⁸

This module integrates micro-ROS in the NuttX 10 build system. It builds and links a micro-ROS static library ready to be used with serial and networking transports virtually in any NuttX supported platform.³⁹

6.1.8 Micro-ROS for Mbed OS⁴⁰

This is a module that integrates micro-ROS in the ARM Mbed build system. It builds and link a micro-ROS static library ready to be used with serial transport.

6.1.9 Micro-ROS for Azure RTOS⁴¹

This repository provides a demo application that integrates micro-ROS in the Microsoft Azure RTOS build system. It builds and links a micro-ROS static library ready to be used with wireless transport.

6.2 *Benchmarking*

Developing a working and stable application from the scribbles to the final executing binary is a long and hard task. During this process developers may come across stability issues and performance issues. In addition to these issues, some specified QoS might be difficult to quantify. Solving those problems without the proper tools might be frustrating, tedious tasks leading to reduced developer efficiency. An adapted benchmarking tool can overcome important obstacles. There are different key performance indicators (KPIs) that developers might be interested. In the proposed benchmarking framework, the KPIs can be chosen freely by the developer. This way,

³⁷ https://github.com/micro-ROS/micro_ros_raspberrypi_pico_sdk.

³⁸ https://github.com/micro-ROS/micro_ros_nuttx_app.

³⁹ https://nuttx.apache.org/docs/latest/introduction/supported_platforms.html.

⁴⁰ https://github.com/micro-ROS/micro_ros_mbed.

⁴¹ https://github.com/micro-ROS/micro_ros_azure_rtos_app.

the benchmarking tool will remain flexible and allow the community to constantly add some support for a lot of different KPIs. The problems we want to tackle are:

- Out there, many benchmarking tools exist, each of targeting different KPIs
- Different platforms (Linux, RTOSes, bare metal)
- Too few time/resources to code benchmarking tool for each
- Avoid code overhead, i.e., keep code clarity
- Avoid execution overhead, i.e., do not make execution slower when benchmarking

6.2.1 Overview

The benchmarking tool under development is providing a framework to allow developers to create their own benchmarking tool. Each part a developer wants to benchmark can be added as a plugin using the provided framework. This way, plugins can be shared and this improves reusability as much as possible. The source code of the tool is provided in the micro-ROS organization on GitHub.⁴² The framework includes the features explained in the following paragraphs (Fig. 13).

6.2.2 Trace Framework Abstraction

The *Shadow Builder* alone only parses comments from the application and passes them along to the *Trace Framework Abstraction* (TFA) core. The TFA core is aware of the plugins that are available, all capabilities of the plugins, and of the platform target. The process goes as explained below:

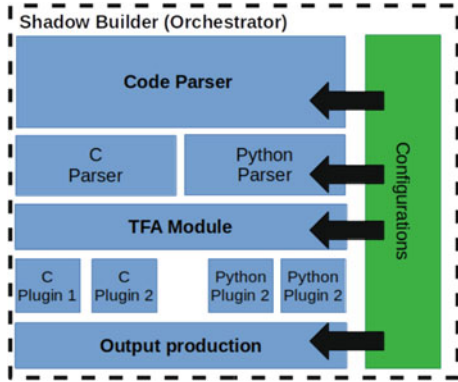
1. The line containing the functionality `Benchmarking::xx::yy` will be checked against all the available plugins.
2. Plugins that are capable of handling functionality will respond with a piece of code that will be replaced with a piece of code.
3. Then the output file will be added in a folder corresponding to the platform type and benchmarking type.

Being generic is the key for this benchmarking tool. The plugins, in contrast, will bring the specific implementation needed to benchmark a specific platform. Every plugin will provide information as requested by the parser:

- List of supported platforms
- List of functions that are handled
- Code snippets that will be added for benchmarking
- List of patches and/or patch code
- Optional end script to run and execute the benchmarks.

⁴² <https://github.com/micro-ROS/benchmarking>.

Fig. 13 Architecture of the micro-ROS benchmarking tool



6.2.3 Shadow Builder

The Shadow builder is a tool that will transparently instrument the code to benchmark and, if the benchmarking is not activated, it should be bypassed. The tools will be able to output an “instrumented code” that will be later be compiled as a normal code. The following steps describe what the shadow builder process flow:

1. Get *Benchmarking Configuration File* file from the user
2. Get appropriate sources
3. Execute Trace Framework Abstraction Configuration file
4. Parse the sources file needed Injecting code
5. Compile the targeted binary for different platform
6. If needed, depending on the type of benchmark being undertaken, compile another target binary.

6.2.4 Binary Generation for Instrumented Code

The binary generation is the process of compiling the source code. In order to benchmark, previously to compile the source code, it is necessary to instrument the code. The code will be instrumented in a transparent way for the developer/user. Therefore, a configuration file provided by the developer will be parsed and code injected as described in a configuration file. The two main steps in this process are:

1. *Receiving inputs:* The binary generation’s pipeline receives two inputs to work with the Configuration Benchmarking File and the source code to benchmark. In short, the configuration describes:
 - What is benchmarked (sources)
 - Where to benchmark
 - What type of benchmark
 - Optionally against what base line to compare (base line source)

2. *Parse and check:* Once the input received the Shadow Builder parses the configuration file. From the configuration file, the Shadow Builder obtains:
 - The different benchmarking to be achieved
 - The targeted platforms

In addition to parsing, the Shadow Builder is in charge of checking capabilities and consistency within the configuration file and the different TFA plugins registered in the TFA module.

6.2.5 TFA Execution

Once parsed and checked against the TFA module capabilities, the Shadow Builder will be in charge of translating configuration into source code. The translated sources will also be achieved in cooperation with the TFA module. At the end of this step, the TFA will generate the new forged source code ready for compilation. In addition to patched source code, the TFA will generate scripts that will complete the benchmarks.

6.2.6 Compilation

The compilation will happen for every kind of benchmark and target platform. Depending on the kind of benchmark that is being executed, there will be one or more binaries per benchmark session. The number of binary generated also depends on what plugins are provided by the user to the shadow builder. The shadow builder will retrieve capabilities of the plugins requested by the developer, match them, and generate software according to the matches.

6.2.7 Steps to Start Benchmarking

The Shadow Builder will be executed as follows:

1. Software sources are passed to the Shadow Builder.
2. The source are passed and upon comments containing `/Benchmarking::XX::YY/` (a tag) the code line is passed to the Trace Framework Abstraction module. Using comments is preferable, i.e., no includes are needed.
3. For all plugins that are registered with the TFA, the `Benchmarking::XX::YY` functionality will return a piece of code that will be added to the source.
4. Once all parsed, the Shadow Builder will compile for all the different platforms requested either by plugins or by user configuration.

6.2.8 Results

The list of benchmarking targets are:

- Communication performance
- Real-time performances
- Execution performances
- Function call count
- Static memory consumption
- Dynamic memory allocation consumption
- Power consumption

We used the benchmarking tool to measure the performance of the micro-ROS stack on a typical microcontroller with different communication technologies:

- Serial at 115200 baud 8 bits/No parity/1 stop
- Ethernet 100/10 Mbps link,
- 6LoWPAN over 802.15 link.

All the results, along with interpretations, are available on the micro-ROS website.⁴³

7 Use-Cases

In this section, we report on three use-cases of micro-ROS in industrial applications and research. The use-cases illustrate different usage scenarios: First, a pure sensing use-case. Second, the use for microcontrollers in an automated/robotic vehicle. Third, a highly automated environment with multiple autonomous robots and numerous additional fixed sensors.

7.1 *Micro-ROS-Enabled GNSS Module by Hydrasystem*

Hydrasystem is young and rapidly expanding enterprise created by experienced engineers on electronics and automation. The company provides state of the art positioning solutions for agricultural machines with work automation in mind. The main product is a system for precise localization based on real-time kinematic corrections, which enable field navigation with 1–2 cm precision. Starting with localization this system can be expanded with further modules, providing navigation and automated work functions.

The company offers several ROS-compatible modules, which are shown in Fig. 14. In this use-case the Hydra Box DGPS module is used (Fig. 15).

⁴³ <https://micro.ros.org/docs/concepts/benchmarking/results>.

	Hydra Box DGPS	Hydra Box	Hydra Twins	Hydra Base
micro-ROS	Yes	No	No	-
ROS	No	Yes	Yes	-
ROS2	No	Yes	Yes	-
other	Based on ESP32	Smart receiver with IMX6 based computer (Yocto Linux)	Two receivers solution for absolute heading	RTK base station for Hydra Box

Fig. 14 ROS-compatible GNSS products by Hydrasystem



Fig. 15 GNSS family parameters

7.1.1 Requirements

There are many applications in robotic systems where GNSS receivers are used for positioning. Usually, to connect a GNSS receiver to a ROS-based system, it is needed to connect it to the computer on which ROS is installed and create a dedicated node to support it. Hydrasystem has adapted a simple GNSS receiver to work with micro-ROS. In the case of Hydra Box DGPS, it is only needed to configure the network connection and the module itself starts the publishing standard NavSatFix⁴⁴ messages.

7.1.2 Technical Approach

The Hydra Box DGPS module (Fig. 16) is based on the ESP32. The module offers an absolute accuracy of approx. 1 m. The principle of operation is shown in Fig. 17.

The GPS receiver transmits data in the NMEA format to the ESP32 module via UART. The data is then parsed and converted into NavSatFix messages. This message is published by micro-ROS. In this case, WiFi has been selected for communication with the computer with ROS 2, but it can also be, for example, Bluetooth. The micro-ROS agent is running on the computer with ROS 2. The correct operation can be checked as follows:

```

1 ros2 topic echo /freertos_navsatfix_publisher
2 ---
3 header:

```

⁴⁴ See http://docs.ros.org/en/api/sensor_msgs/html/msg/NavSatFix.html for the message type definition.

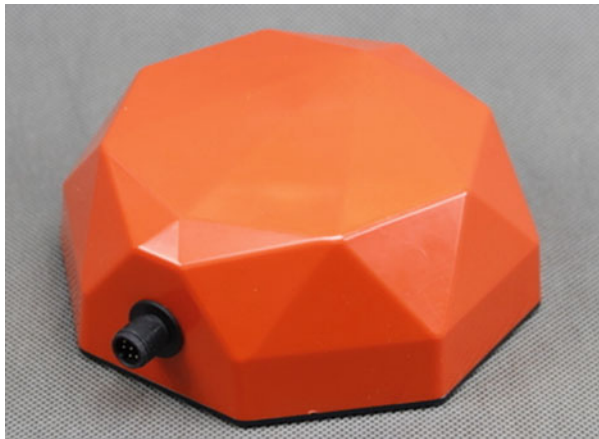


Fig. 16 Hydra Box DGPS module

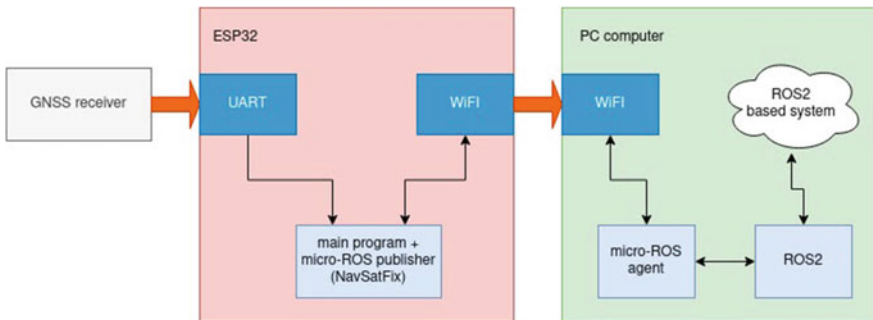


Fig. 17 Hydra Box DGPS diagram

```

4   stamp:
5     sec: -1515870811
6     nsecs: 2779096485
7   frame_id: ''
8   status:
9     status: -91
10    service: 42405
11  latitude: 52.19599914550781
12  longitude: 20.926616668701172
13  altitude: 0.0
14  position_covariance:
15    - 0.0
16    - 3.6720809936523438
17    - 5.30345388e-315
18    - 0.0
19  ...
20  position_covariance_type: 0

```



Fig. 18 The BODAS Controller RC40/5-6 (in the center) with an angle sensor and a pressure sensor (left side) as well as a speed sensor and a display (right side) from the BODAS hardware portfolio. (Photos by Bosch Rexroth.)

21 — — —

A video showing how Hydra Box DGPS works can be seen at YouTube.⁴⁵

The most important advantage of this solution is very simple integration with the ROS 2 system. Just plug in the power supply and configure the network connection.

7.1.3 Discussion and Outlook

The use-case shows that micro-ROS can be successfully used on resource-constrained devices where ROS/ROS 2 cannot be run. Thanks to the use of micro-ROS, it is possible to easily integrate various types of sensors or other types of IoT devices.

7.2 Off-Road Vehicle Control with Micro-ROS Interface by Bosch Rexroth

Bosch Rexroth is a company of the Bosch Group and one of the world's leading suppliers of drive and control technology for mobile applications, machinery applications, and factory automation. Bosch Rexroth has about 31,000 associates in over 80 countries.

BODAS is an open and scalable mobile electronics platform by Bosch Rexroth and intended in particular for safety-critical applications in mobile machinery, e.g., excavators, wheel loaders, and tractors. The BODAS hardware portfolio comprises sensors, joysticks, pedals, connectivity units, and displays, as illustrated in excerpts in Fig. 18. The heart of the platform are the BODAS Controllers with safety-rated microcontrollers in robust housings for off-road use and with a broad spectrum of interfaces including CAN, CAN FD, ISOBUS, and GPIOs.

⁴⁵ <https://youtu.be/hTEnTju1Qkg>.

The BODAS base software is built on the AUTOSAR Classic Platform [30] and can be tailored by a comprehensive cloud service named easyConfig. Application software can be implemented in C or IEC 61131-3 languages against a BODAS-specific API.

7.2.1 Requirements

In the mobile machinery market, we observe an increasing interest in ROS (and particularly ROS 2) for the development of advanced automation functions for construction and agriculture. While the main, computationally intensive algorithms are typically implemented on larger microprocessors, microcontroller platforms like BODAS Controllers are used to interact with the hardware, to realize low-latency control functions, and to implement safety mechanisms. To bridge the technological gap between those two classes of platforms, Bosch Rexroth and Bosch Research are porting micro-ROS to BODAS Controllers. The two top-level requirements for this endeavor are:

1. *Seamless integration with the BODAS API and AUTOSAR*: The micro-ROS stack shall be integrated in such a way that it does not interfere with non-ROS software. First of all, this means that micro-ROS has to fit into the scheduling model and memory management of AUTOSAR Classic, which again is based on the OSEK RTOS standard. Second, in the long term, freedom from interference in accordance with ISO 26262 shall be guaranteed.
2. *Transport over CAN*: The *Controller Area Network* (CAN) is the dominating vehicle bus system. For the communication between micro-ROS nodes on a BODAS Controller with the micro-ROS agent on a larger microprocessor, it is essential that CAN is supported as a transport of DDS-XRCE.

These requirements raise several technical challenges, three of which we will discuss next.

7.2.2 CAN Transport for DDS-XRCE

The DDS-XRCE standard [16] defines three transports—i.e., mappings to underlying protocols—namely to UDP, TCP, and serial (e.g., SPI, I2C, and RS-232). However, it is not limited to those ones. For this purpose, Section 11.1 of the standard defines a *transport model*, which consists of five requirements to an underlying transport.

CAN does not meet exactly one of the requirements, namely the capability to deliver messages of at least 64 bytes. The base frame format of CAN has a payload of 8 bytes only. In fact, Micro XRCE-DDS assumes 42 bytes only, but that is still too much. Therefore, we added mechanisms to packetize DDS-XRCE messages including checksum into 7 byte fragments and a sequence number on the sender side and to unpacketize them accordingly on the receiver side.

The transport model of DDS-XRCE also defines three functionalities that are explicitly not required: The transport does not need to provide reliability and ordering. It even does not need to provide notification of dropped messages. This simplifies the packetizing mechanism. If the unpacketizing routine detects a broken or incomplete DDS-XRCE message, it may simply drop it and rely on the error handling of DDS-XRCE.

7.2.3 Execution Management on Periodic Tasks

AUTOSAR Classic and the underlying OSEK RTOS use a scheduling model which is very different from POSIX. It consists of fixed periodic tasks (e.g., 50, 10, and 2 ms), whose priority is inverse to the period. Hence, the tasks may preempt each other in a strict ordering only. There may be multiple functions inside a task. In each iteration, these functions are executed in a fixed sequential order and run to completion. All data across iterations is stored in the global memory. Therefore, the whole system can be implemented by a single stack—unlike POSIX, where each thread has its own stack.

On the one hand, the periodic execution model does not fit at all to the event-based execution model of ROS and micro-ROS. On the other hand, we expect that many functionalities on the application level are in fact periodic. Many sensors provide their readings in a periodic fashion. Similarly, many actuators are controlled periodically.

Therefore, we decided to embed the micro-ROS execution model directly in this task scheme as depicted in Fig. 19. CAN frames are received by an interrupt service routine (ISR). A middleware interface function running in a high-frequency task (e.g., 1 ms) unpacketizes the CAN frames into DDS-XRCE messages. The Executor runs in the same or a slightly slower task and takes incoming DDS-XRCE message into ROS messages. Such a *take* does not imply that the corresponding application-level callback is invoked immediately but the callbacks are executed in *worker tasks*, often at much lower frequency. The assignment of callbacks to worker tasks has to

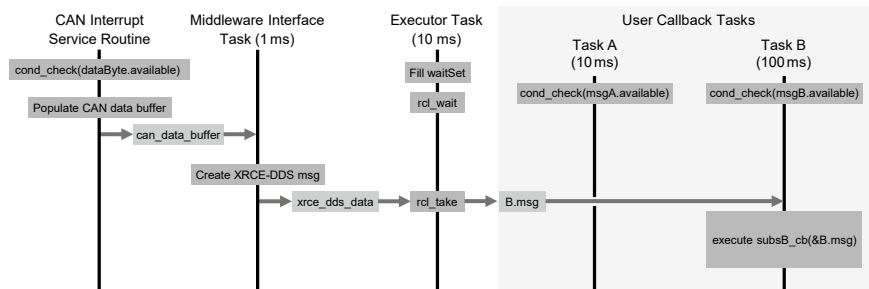


Fig. 19 Mapping of micro-ROS execution model to AUTOSAR Classic and OSEK task scheme

be implemented by the developer. The developer has to observe that the callback can run to completion in the period of the worker task.

7.2.4 Memory Management Without Explicit Heap

In the current version, micro-ROS avoids dynamic memory operations to a large extent, but cannot do without them entirely. Applications can be designed that allocations occur during some initialization phase only. In this case, micro-ROS performs some dynamic memory allocations but memory is only freed at shutdown. Conceptually, such use can be considered global/static variables, but technically `malloc` is called.

AUTOSAR Classic does not provide OS-level services for dynamic memory management at all, cf. Section 4.6.3 of [30], as such operations are generally considered harmful in safety-critical systems due to memory fragmentation. Therefore, we are currently designing a micro-ROS-specific allocation function backed by a static memory block whose size has to be determined by the developer.

7.2.5 Discussion and Outlook

The port of micro-ROS to the BODAS Controllers is still on-going. The CAN transport for Micro XRCE-DDS has been already implemented and tested successfully using the interface for custom transports. We have also implemented a first prototype of an Executor supporting worker tasks/threads, cf. Sect. 5.2. This implementation is currently integrated with AUTOSAR and the BODAS API.

The first release will not provide any freedom-from-interference mechanism but is mainly intended for prototyping.

7.3 Smart Warehouse Use-Case by Łukasiewicz-PIAP

Łukasiewicz-PIAP (PIAP) is a research institution with strong commercial branch, established in 1965. Currently it has approximately 300 employees, out of which more than 2/3 are scientists and/or engineers. PIAP is a part of Łukasiewicz Research Network. Activity topics include: Mobile robotics, Cyber-physical systems development, Industrial automation, Measurement devices, Rapid prototyping centre. PIAP is mainly Polish and one of the biggest European producers of IEDD/EOD/CBRN mobile robots and robotic accessories. PIAP is also a member of the EU-funded project OFERA [17], which has initiated the micro-ROS project.

The Smart warehouse is a complex use-case that intends to demonstrate that micro-ROS works well in a dynamic, distributed system of heterogeneous devices, including the low-power, microcontroller-based hardware and regular robots.

7.3.1 Requirements

In robotic or other automation systems there are many sensors or actuators that are based on microcontrollers where ROS/ROS 2 cannot be executed. Currently, it is required to connect such devices to a computer with ROS/ROS 2, containing custom implementation of their support and only then were they available in a ROS/ROS 2 system. Micro-ROS, which works with ROS 2, changes this dramatically as it can run directly on microcontrollers and other low resource devices. This allows for direct, convenient, and quick integration into the ROS 2 based system and also into classical ROS using the ROS bridge. In this use-case, a mobile platform roams around smart warehouse, doing scheduled tasks. These tasks will consist of reaching the sensors or actuators and interacting with these radio-controlled, micro-ROS enabled devices.

7.3.2 Technical Approach

A specially prepared laboratory simulates a smart warehouse. It contains all the devices needed to run the planned scenario, such as locating devices and several micro-ROS enabled devices. The layout of the warehouse is shown in Fig. 20. The warehouse is equipped with:

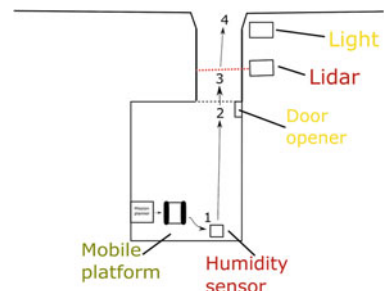
- Humidity and temperature sensor
- Laser scanner (distance measurements), shown in Fig. 22
- Door opener
- Final effector

The mobile robot platform, depicted in Fig. 21, is built on the basis of the standard Scout robot produced by Łukasiewicz-PIAP. The mobile robot platform has been equipped with

- an autonomy module (PC computer/lidar/indoor positioning/outdoor positioning),
- communication interfaces (6LoWPAN/WiFi), and
- other components, e.g., a wireless emergency stop.

The whole use-case is using a mixture of classical ROS, ROS 2, and micro-ROS environments. The autonomy of the mobile platform is based on ROS. The mobile

Fig. 20 Smart warehouse mission plan



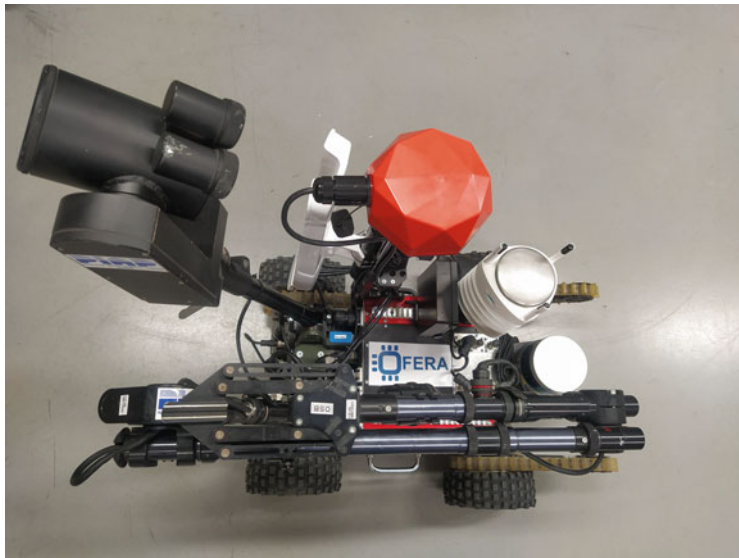


Fig. 21 Smart warehouse mobile platform



Fig. 22 Smart warehouse sensor example: distance sensor

platform's communication with sensors is based on ROS 2 and micro-ROS. The sensors and actuators use micro-ROS. A map of all those environments is shown on the Fig. 23.

The robot mobile platform is controlled by the autonomy module, but it is also possible to control it remotely using a standard joystick. The laptop (robot control unit) can provide information about the robot's states and its sensors' values. The

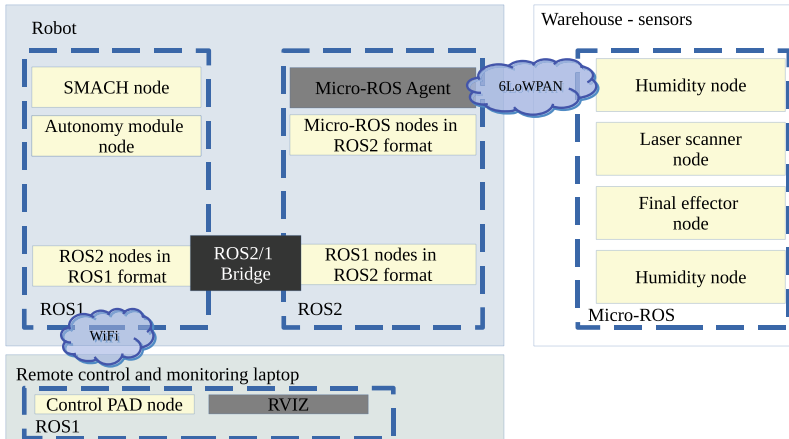


Fig. 23 Architecture of the smart warehouse use-case

ROS visualization tool rviz,⁴⁶ is used to give humans readable information. SMACH is used to design states machines to make missions steps.

The mobile platform will perform specific missions according to the developed scenario. The task for the robot is set in the mission planner. Missions are focused on presentation of micro-ROS features. One selected mission is described below.

The mission is performed according to the simplest scenario, taking into account communication with all sensors and actuators used in the use-case:

- approach the humidity sensor and obtain the measurement,
- go towards the warehouse gate and after communication with the door opener and their opening, the platform moves towards the road,
- the distance sensor next to the road provide information to the platform whether the road is empty and we can go,
- after crossing the road and reaching the lamp, the platform sends command to the lamp to switch it on,
- stop and wait for the next task.

This mission is focused on evaluating the communication and the correct operation of sensors and actuators. In the first task (approaching the humidity sensor), the robot mobile base moves near to the humidity sensor and tries to connect to it. After obtaining the connection, the measurement results are sent from the sensor to robot. Then robot mobile base goes towards the door. Like before, a connection is established with the door opener. After opening the door, we have to ensure that the exit is clear and there are no obstacles. This is checked by a distance sensor placed outside the warehouse. Now robot mobile base can go to the lamp, i.e., the final

⁴⁶ <http://wiki.ros.org/rviz>.

effector. After approaching final effector, it remotely lights the lamp. The video with the recorded mission is available on YouTube.⁴⁷

7.3.3 Discussion and Outlook

The warehouse use-case is a good demonstration of what is achievable in an industrial environment. This smart warehouse use-case also demonstrates that micro-ROS works well in a dynamic, distributed system of heterogeneous devices. In this case the focus was on the radio communication over 6LoWPAN. Showing that micro-ROS works in such conditions confirms the fulfillment of the micro-ROS project assumptions.

8 Final Remarks

After more than three years of active development and maintenance, micro-ROS is the first choice for integrating microcontrollers into ROS-2-based systems and for bringing ROS 2 itself onto microcontrollers. The micro-ROS stack turns ROS 2 into a great superset to cover an extended range of applications for new industrial deployments in Industry 4.0, IoT, and many other domains. The maturity of micro-ROS has been proven in several use-cases and projects from research to product development.

An important key factor to long-term success of the micro-ROS project is building a subcommunity inside the ROS community which takes over the maintenance of the micro-ROS stack. For this purpose we have initiated the ROS Embedded Systems Working Group (WG), held on a monthly basis [22], and we are happy about the large number of active participants.

Encouragingly, also major microcontroller vendors who are seeking good positioning in the robotics and autonomous systems market recognize the importance of micro-ROS. For example, in September 2021, Renesas Electronics Corporation integrated micro-ROS into the EK RA6M5 family and e2 studio.⁴⁸ The objective of this hardware and software combination is to provide a first to market comprehensive tool based on an Eclipse environment that covers the full development cycle. This will strongly impact on reducing the time to market of robotic solutions targeting a wide range of applications in logistics, security, agriculture, or healthcare.

Besides the support of further microcontroller families and RTOS, future technical topics are of course also on the micro-ROS roadmap. These topics include an embedded C++ client library and framework mechanisms for the use in wireless sensors (or even actuators) in the environment.

⁴⁷ https://youtu.be/XsUw1w_f8ks.

⁴⁸ See press release at <https://www.renesas.com/eu/en/about/press-room/renesas-and-eprosima-simplify-development-professional-robotics-applications-ra-mcus-micro-ros>.

Acknowledgements The development of micro-ROS was supported by the European Union's Horizon 2020 research and innovation programme under grant agreement No. 780785 in the project *Open Framework for Embedded Robot Applications* (OFERA) [17].

References

1. Bouchier, P.: Embedded ROS. *IEEE Robot. Autom. Mag.* **20**(2), 17–19 (2013)
2. Ferguson, M., Bouchier, P., Purvis, M.: rosserial Package Summary. <http://wiki.ros.org/rosserial>. Accessed 12 June 2021
3. Takase, H., Mori, T., Takagi, K., Takagi, N.: mROS: a lightweight runtime environment for robot software components onto embedded devices. In: Proceedings of the 10th International Symposium on Highly-Efficient Accelerators and Reconfigurable Technologies (HEART 2019), Nagasaki, Japan, ACM (2019)
4. Goldschmidt, S., Ziegelmeier, D.: lwIP - A Lightweight TCP/IP stack - Summary. <https://savannah.nongnu.org/projects/lwip/>. Accessed 12 June 2021
5. TOPPERS Project, Inc.: TOPPERS: Toyohashi OPen Platform for Embedded Real-time Systems. <https://www.toppers.jp/en/asp-kernel.html>. Accessed 12 June 2021
6. Gerkey, B.: Why ROS 2. http://design.ros2.org/articles/why_ros2.html. Accessed 12 June 2021
Accessed 12 June 2021
7. Dauphin, L., Baccelli, E., Adjih, C.: Riot-ros2: Low-cost robots in iot controlled via information-centric networking. In: 2018 IFIP/IEEE International Conference on Performance Evaluation and Modeling in Wired and Wireless Networks (PEMWN) (2018)
8. Dauphin, L., Vilches, V.M.: RIOT-ROS2 (Git Repository). <https://github.com/astralien3000/riot-ros2>. Accessed 12 June 2021
9. RIOT developers: RIOT Project Website. <https://www.riot-os.org/>. Accessed 12 June 2021
10. NDN Consortium: Named Data Networking (NDN) Project Website. <https://named-data.net/>. Accessed 12 June 2021
11. OMG and contributors: Data Distribution Service (DDS) 1.4. Standard, Object Management Group (OMG), Milford, MA, USA (2015)
12. Takase, H., et al.: mROS 2. <https://github.com/mROS-base/mros2>. Accessed 25 Nov 2021
13. Kampmann, A., Wüstenberg, A., Alrifaei, B., Kowalewski, S.: A portable implementation of the real-time publish-subscribe protocol for microcontrollers in distributed robotic applications. In: IEEE Intelligent Transportation Systems Conference (ITSC '19), pp. 443–448 (2019)
14. Kampmann, A., et al.: embeddedRTPS. <https://github.com/embedded-software-laboratory/embeddedRTPS>. Accessed 25 Nov 2021
15. ARM Limited: Mbed OS. <https://os.mbed.com/>. Accessed 25 Nov 2021
16. OMG and contributors: DDS For Extremely Resource Constrained Environments (DDS-XRCE) 1.0. Standard, Object Management Group (OMG), Milford, MA, USA (2020)
17. eProsima (project coordinator): OFERA Project: Open Framework for Embedded Robot Applications. <http://www.ofera.eu/>. Accessed 12 June 2021
18. Amazon Web Services, Inc.: FreeRTOS Project Website. <https://freertos.org/>. Accessed 12 June 2021
19. Linux Foundation: Zephyr Project Website. <https://www.zephyrproject.org/>. Accessed 12 June 2021
20. The Apache Software Foundation: Apache NuttX Project Website. <https://nuttx.apache.org/>. Accessed 12 June 2021
21. eProsima: eProsima Micro XRCE-DDS. <http://micro-xrce-dds.readthedocs.io/>. Accessed 12 June 2021
22. Open Robotics et al.: ROS 2 – Project Governance. <https://docs.ros.org/en/rolling/Governance.html>. Accessed 25 Nov 2021

23. Dabrowski, A., Lütkebohle, I., Lange, R., Losa, J.M., Gamarra, B.O., Goenaga, I.M., Vilches, V.M.: Reference Scenarios and Technical System Requirements Definition. H2020 project deliverable, OFERA Project (2018)
24. IEEE-SA Standards Board: IEEE/Open Group 1003.1-2017 - IEEE Standard for Information Technology–Portable Operating System Interface (POSIX(TM)) Base Specifications, Issue 7. Technical report, IEEE and Open Group (2017)
25. OMG and contributors: DDS Security (DDS-SECURITY) 1.1. Standard, Object Management Group (OMG), Milford, MA, USA (2018)
26. Casini, D., Blaß, T., Lütkebohle, I., Brandenburg, B.B.: Response-time analysis of ROS 2 processing chains under reservation-based scheduling (Artifact). Dagstuhl Artifacts Ser. **5**(1), 5:1–5:2 (2019)
27. Staschulat, J., Lütkebohle, I., Lange, R.: The rclc executor: Domain-specific deterministic scheduling mechanisms for ros applications on microcontrollers (work-in-progress). In: Proceedings of the International Conference on Embedded Software (EMSOFT), Virtual event, IEEE, pp. 18–19 (2020)
28. Staschulat, J., Lange, R., Dasari, D.N.: Budget-based real-time executor for micro-ros (2021)
29. Nordmann, A., Lange, R., Rico, F.M.: System modes - digestible system (re-)configuration for robotics. In: Proceedings of 3rd International Workshop on Robotics Software Engineering (RoSE), Virtual event (2021)
30. AUTOSAR Partners: AUTOSAR Classic Platform 4.4.0 – Specification of Operating System. Standard, AUTOSAR GbR, Munich, Germany (2018)

Kaiwalya Belsare holds a master's degree in information technology with specialization in embedded systems and microelectronics from the University of Stuttgart, Germany. During his tenure as a master thesis student at Bosch Research, he worked on integrating the micro-ROS stack on an AUTOSAR-based electronic control unit, especially regarding freedom from interference with existing safety-critical software functions. Currently, he works as an embedded software developer at Robert Bosch Power Tools GmbH, Germany.

Antonio Cuadros Rodriguez is a B.Eng. in Electronics, Robotics, and Mechatronics specialized in embedded systems. He is part of the micro-ROS team in eProsima, responsible for maintaining and evolving this framework to facilitate and enhance ROS 2 functionality in mid-range MCUs and embedded platforms with RTOS such as FreeRTOS, Zephyr or in bare metal.

Pablo Garrido-Sánchez is a M.Sc.Eng. Telecommunication Engineer specialized in embedded systems, digital hardware design, and low-level programming. He is the Technical Leader of micro-ROS in eProsima, responsible for maintaining and evolving this framework to facilitate and enhance ROS 2 functionality in mid-range MCUs and embedded platforms with RTOS such as FreeRTOS, Zephyr or in bare metal.

Juanjo Hierro is the CTO of the FIWARE Foundation. He obtained a degree in Computer Science in 1990 from the Universidad Politecnica de Madrid (UPM) and owns a certificate of research proficiency. Juanjo Hierro also plays the role of Chairman of the Technical Steering Committee of the FIWARE Open Source Community and is the Chief architect of the FIWARE platform, a growing open de-facto standard for the development of Smart Applications in multiple vertical sectors.

Tomasz Kołcon is a M.Sc.Eng. Electronics Engineer specialized in embedded systems, digital and analog hardware design, and low-level programming. He is the Project Manager of micro-ROS in Łukasiewicz-PIAP, responsible for managing the team dealing with the preparation of micro-ROS benchmark tools and one of the most complex use-cases in the project.

Ralph Lange joined Bosch Research in 2013 and is Chief Expert for Robotic Systems and Software Engineering. He was principal investigator in the EU-funded project OFERA, which has initiated the open-source project micro-ROS. Ralph actively follows and contributes to the development of ROS 2. Before joining Bosch, he worked as a software engineer for TRUMPF Machine Tools. He obtained his Ph.D. in computer science from the University of Stuttgart, Germany in 2010.

Ingo Lütkebohle (computer science Ph.D., Bielefeld University) is a software architect at Bosch Research, working on consumer robotics since 2014. He was co-PI for the EU-funded OFERA project, working on micro-ROS until early 2020, an active member of the ROS community since 2010 and worked on robot software integration and quality since 1995, in several publicly funded projects.

Alexandre Malki coming from a M.Sc.Eng. of Mechatronic specialized in microsystems. And working as software embedded developer engineer at Łukasiewicz-PIAP, in charge of developing micro-ROS benchmark tools and developing one of the most complex use-cases in the project.

Jaime Martin Losa is the eProsima CEO, with 21 years of experience in project management and software development focused on networking middleware and integration services. He is the Architect for all the company products, including eProsima Fast DDS and eProsima RPC over DDS. Jaime leads the eProsima OMG membership, and is the responsible of eProsima contribution to the DDS standards, as the Web-enabled DDS, DDS Security, RPC over DDS, OPC-UA DDS Bridge and DDS-XRCE.

Francisco Melendez is the FIWARE's Technical Expert in charge of the Robotics Roadmap. He is also one of the representatives of FIWARE in the Digital Twin Consortium and some international projects where FIWARE is developing its technical robotics roadmap. As a mobile robotics engineer and researcher with more than seven years of experience, his work focuses on the development of convenient interfaces between physical robots and digital twins in smart robotics applications.

Maria Merlan Rodriguez is Ph.D. Telecom Engineer by the University Pierre et Marie Curie. Solid scientific-technological background, specialized in the field of wireless communications. Her main field of research is documented in scientific publications focused on the field of Radio Frequency contactless techniques and machine learning techniques to monitor the hydro-mechanical properties of new materials. Maria holds 10 years of experience in Technical Projects and International Business Development.

Arne Nordmann joined Bosch Research in 2015 after obtaining his Ph.D. in model-driven engineering in robotics from the Bielefeld University, Germany. He is now focusing on dependable cyber-physical systems, such as robotics and highly-automated driving applications, and actively following and contributing to the development of ROS 2.

Jan Staschulat is Ph.D. Computer Scientist by Braunschweig Technical University in the field of performance analysis of real-time embedded systems. He joined Bosch Research in 2014 with main research focus on deterministic and real-time computing in robotics and autonomous driving. He actively contributes to the ROS 2 Real-Time Working Group.

Julian von Mendel joined Bosch Rexroth Mobile Electronics in 2018 and is project manager for safety-critical robotics controller software as well as for Rexroth's AUTOSAR cloud platform. Before joining Bosch Rexroth, he was CEO at an embedded electronics startup and worked as a software engineer at cibite AG, developing Linux and microcontroller solutions for optical inspection systems. He graduated 2014 in computer science (B.Sc.).

A Tutorial to Use the MediaPipe Framework with ROS2



**Dieisson Martinelli, Jonathan Cerbaro, Marco Antonio Simoes Teixeira,
João Alberto Fabro, and André Schneider de Oliveira**

Abstract This chapter presents a tutorial on the use of the MediaPipe package for ROS2, developed by the authors. Through the MediaPipe framework it is possible to collect data from the positions of the hand, face and body of an operator, using a webcam, and publish them in ROS2 topics, which can be used for various applications in robotics. A complete example application using this technology is also covered in this chapter. MediaPipe is used to collect data from the image of an operator's pose (hands, fingers, face and body positions), and this information is then used to control the navigation of a robot inside a simulated environment. The programming language used is Python and the only hardware needed for execution is a computer with Linux Ubuntu 20.04, ROS2 Galactic and a webcam. At the end of the chapter, the reader will be able to develop control strategies or other functionalities that use information about the movements of the operator, captured directly by the developed ROS2 package, through a webcam. All files used in this chapter can be accessed from the link https://github.com/dmartinelli1997/media_pipe_ros2, as well as the project videos. All code used in this project can be found in the following repository: https://github.com/dmartinelli1997/Script_ROSBOOK2021.git. (This project was partially funded by National Council of Technological and Scientific Development of Brazil (CNPq), and by Coordination for the Improvement of Higher Level

D. Martinelli (✉) · J. Cerbaro · M. A. S. Teixeira · J. A. Fabro · A. Schneider de Oliveira
Graduate Program in Electrical and Computer Engineering (CPGEI), Federal University of Technology, Paraná (UTFPR), Av. Sete de Setembro, Curitiba, PR 3165, Brazil
e-mail: dmartinelli@alunos.utfpr.edu.br

J. Cerbaro
e-mail: jonathancerbaro@alunos.utfpr.edu.br

J. A. Fabro
e-mail: andreoliveira@utfpr.edu.br

A. Schneider de Oliveira
e-mail: fabro@utfpr.edu.br
URL: <http://www.utfpr.edu.br/>

People (CAPES).) (This study was financed by the Human Resource Program of The Brazilian National Agency for Petroleum, Natural Gas, and Biofuels—PRH-ANP—FINEP Management, contractual instrument n° 0.1.19.0240.00, Ref 0431/19 - PRH21-UTFPR.)

Keywords MediaPipe · ROS2 · Teleoperation · Human-Robot interface

1 Introduction

The purpose of this tutorial is to present a tutorial on the use of a package developed to use the features of the MediaPipe framework for ROS2. This tutorial includes the installation and an example of application that uses the developed ROS2 package, by controlling the navigation of a mobile robot using gestures. The entire tutorial was developed in Ubuntu version 20.04.2 LTS, using Python 3, MediaPipe version 0.8.9 and the Galactic version of ROS2. Such computer must have a webcam installed, turned toward the operator. A computer without an accelerated video card was used to demonstrate that, even without great graphics processing capacity, MediaPipe can perform tasks that require a robust hardware in other technologies. This tutorial can serve as a base for creating other human-robot interaction techniques or other functionalities in robots equipped with ROS2.

For a case study, this tutorial will cover the installation of the MediaPipe framework, an example of the use of the without framework ROS2, installation and explanation of the developed MediaPipe ROS2 package, installation of the simulation environment of the mobile robot used in the example application, and the development of this application itself.

The simulated environment used for testing is composed of the Gazebo simulator version 11.5.1 with a TurtleBot3 robot.

This chapter is split in 5 sections: Introduction, MediaPipe Framework, MediaPipe for ROS2, Example Application and Conclusion. After this brief introduction (Sect. 1), Sect. 2 presents background information about the MediaPipe framework from Google, and the OpenPose library. In Sect. 3, the MediaPipe for ROS2 package is presented, covering installation of the package, and its integration with Python. Section 4 presents the complete development of an example application for ROS2 using the proposed package. Section 5 presents the conclusions and the final observations of the obtained results.

2 The MediaPipe Framework

This chapter is intended to present a package that allows for the use of the MediaPipe framework [1] in ROS2. MediaPipe is an open-source framework developed by Google for building applied, multimodal and cross-platform machine learning

Table 1 Table of solutions offered by MediaPipe for each platform

Solutions	Android	iOS	C++	Python	JS
Face detection	x	x	x	x	x
Face Mesh	x	x	x	x	x
Iris	x	x	x		
Hands	x	x	x	x	x
Pose	x	x	x	x	x
Holistic	x	x	x	x	x
Selfie segmentation	x	x	x	x	x
Hair segmentation	x		x		
Object detection	x	x	x		
Box tracking	x	x	x		
Instant motion tracking	x				
Objectron	x		x		
KNIFT	x				
AutoFlip			x		
MediaSequence			x		
YouTube 8M			x		

pipelines that supports IOS, Android, Python, Javascript and C++. MediaPipe offers several features, such as Face Mesh, Hands, Pose, and Holistic detection, which were the features used in the developed ROS2 package. The complete list of features provided by MediaPipe can be seen in Table 1.

In some works, techniques such as detection of hands or pose, connected to a ROS network, are used to control mobile robots [2–4]. For this end it is common to use a library called OpenPose, that is the first real-time multi-person system to detect points of interest in the human body, hands, face and feet, providing a total of 135 points for each image processed [5].

The MediaPipe framework has as its main advantage over OpenPose the possibility of a faster processing time, spending less processing resources. The main objective of this chapter is present the MediaPipe ROS2 package, that was developed specifically to allow the development of applications using some of the MediaPipe framework features directly in ROS2.

3 MediaPipe ROS2 Package

This section presents the features that were implemented in the **MediaPipe for ROS2** package. This section will provide installation instructions for this package, as well as a detailed description of each of the features implemented, that were selected by being the most relevant for robotics applications:

- **Hands Detector:** Responsible for detecting both hands of the operator informing the respective points for each one.
- **Pose Detector:** Detects the operator's body points such as torso, arms, legs and feet.
- **Face Mesh:** Maps all respective points on the operator's face.
- **Holistic:** A combination of all the above functionalities at the same time, having a complete profile of the operator points.

3.1 MediaPipe ROS2 Installation

To use the ROS package, first it is necessary to install MediaPipe. In this work it is used the Python language version 3.8.10 in Ubuntu 20.04.2 LTS. MediaPipe offers built-in and customizable Python solutions and is available on PyPI for Linux, macOS and Windows.

To install MediaPipe, first you need to install OpenCV, as it is a dependency. To do this, run the following command:

```
$ pip install opencv-python
```

OpenCV (Open Source Computer Vision Library) is an open-source, cross-platform computer vision library. It was developed in the mid 2000s by Intel [6]. It brings together all the resources necessary run the most varied computer vision applications, such as MediaPipe.

After installing OpenCV, run the following command to install MediaPipe:

```
$ pip install mediapipe
```

Now the package is ready to use. You can quickly validate the installation using one of the examples provided by the documentation itself, such as the hands detector.

Create a folder called MediaPipe and a file called hands.py inside it:

```
$ mkdir mediapipe && cd mediapipe
$ gedit hands.py
```

Inside this file, add the following code, which can be found in the hands.py file in the following repository: https://github.com/dmartinelli1997/Script_ROSBOOK2021.

```

import cv2
import mediapipe as mp
mp_drawing = mp.solutions.drawing_utils
mp_hands = mp.solutions.hands
drawing_styles = mp.solutions.drawing_styles

cap = cv2.VideoCapture(0)
with mp_hands.Hands(
    min_detection_confidence=0.5,
    min_tracking_confidence=0.5) as hands:
    while cap.isOpened():
        success, image = cap.read()
        if not success:
            print("Ignoring empty camera frame.")
            # If loading a video, use 'break' instead of 'continue'.
            continue

        # Flip the image horizontally for a later selfie-view display,
        # and convert the BGR image to RGB.
        image = cv2.cvtColor(cv2.flip(image, 1), cv2.COLOR_BGR2RGB)
        # To improve performance, optionally mark the image as not writeable to
        # pass by reference.
        image.flags.writeable = False
        results = hands.process(image)

        # Draw the hand annotations on the image.
        image.flags.writeable = True
        image = cv2.cvtColor(image, cv2.COLOR_RGB2BGR)
        if results.multi_hand_landmarks:
            for hand_landmarks in results.multi_hand_landmarks:
                mp_drawing.draw_landmarks(
                    image, hand_landmarks, mp_hands.HAND_CONNECTIONS,
                    drawing_styles.get_default_hand_landmark_style(),
                    drawing_styles.get_default_hand_connection_style())
        cv2.imshow('MediaPipe Hands', image)
        if cv2.waitKey(5) & 0xFF == 27:
            break
cap.release()

```

Make sure your webcam is connected and its reference name is correctly indicated in the above code (in this case, the camera was connected to dev video0):

```
cap = cv2.VideoCapture("number of your webcam in \dev\video")
```

After that, a window with the camera image will open and it will be possible to observe the MediaPipe working (as can be seen in Fig. 1) when you show your hands, validating the installation of MediaPipe on your machine. Other examples of implementations such as pose, face and object detection can be followed in MediaPipe's webpage [7].

At this point, MediaPipe is working but it is not communicating with ROS yet, so now you need to install the package developed for this chapter. The package is found in the media_pipe_ros2 repository on Github [7]. Just clone the repository into your ROS2 workspace /src directory and then run the build command from your ROS2 workspace:

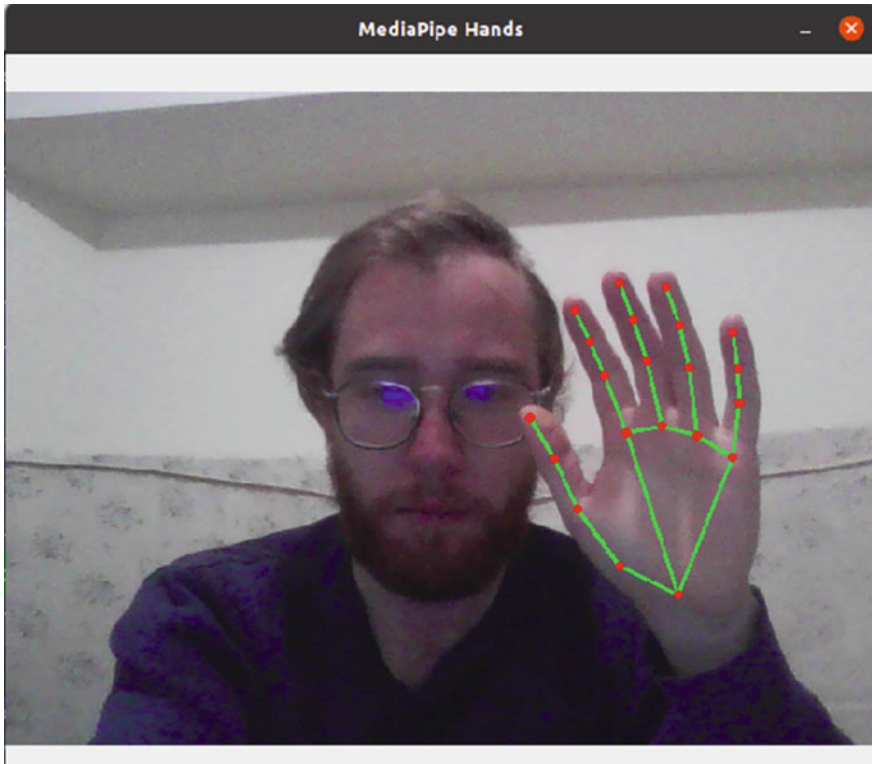


Fig. 1 Image representing the MediaPipe Hands output

```
$cd ros2_workspace/src  
$git clone \url{https://github.com/dmartinelli1997/media_pipe_ros2}  
$cd ..  
$colcon build
```

The MediaPipe package for ROS2 is now installed and ready to use. It is currently possible to use four functionalities: Pose detection, Hands Detection, Face Mesh and Holistic. Each of these features will be covered in the next subsections.

Development of the MediaPipe ROS2 package was all done in Python3. MediaPipe's own framework offers the position information of each point on the human body through an RGB image. This information was captured and sent to an outline for use through ROS2.

In order for all this to work, some ROS messages were created. Messages are the data read and written. When posting or subscribing to a topic, you must specify which type of message will be used, that is, which type of data will be written or read. For our development it was only necessary the information of x, y and z of the position of the points and an identification name of the point. Then the messages, HandPoint,

Table 2 Example of message created for writing and reading in MediaPipe package for ROS2

HandPoint.msg

String	Name
Float64	x
Float64	y
Float64	z

Table 3 Using example from previous message as a list in another message

MediaPipeHumanHand.msg

HandPoint [21]	right_hand_key_points
HandPoint [21]	left_hand_key_points

FaceMeshPoint and PosePoint were created, representing each of the points of its segment. An example of one of these messages can be seen in the Table 2.

Other messages like MediaPipeHumanHandList.msg were created to have a complete list of all the points in one of the segments, for example, from the operator's hand, facilitating its use in a ROS2 node. Its structure can be seen in Table 3.

Then, MediaPipe's ROS2 package uses the position data of a segment's points (operator's hands), creates a topic with the message type referring to that segment (MediaPipeHumanHandList.msg), and publishes the information of the points in it. Now, we can create a node in ROS2 capable of reading this topic and using these points for some application.

3.2 MediaPipe ROS2 Hands Detector

Hands Detector is the node responsible for collecting data from the operator's hand and sending it to a ROS topic.

MediaPipe Hands is a high fidelity hand and finger tracking solution. It employs machine learning to infer 21 3D points of each hand from just a single frame, as seen in Fig. 2.

To execute this node, run the following commands:

```
$ source ros2_workspace/install/setup.bash
$ ros2 run media_pipe_ros2 hands_detector
```

A window will open showing the image of your webcam with the MediaPipe Hands already working, as in Fig. 3.

You can view the topic responsible for the messages sent from the hands_detector node. To do this open another bash and run:

```
$ source ros2_workspace/install/setup.bash
$ ros2 topic list
```

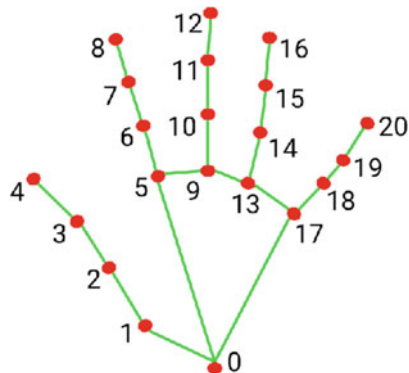


Fig. 2 Representation of 21 points of hands landmark. *Source* MediaPipe [1]

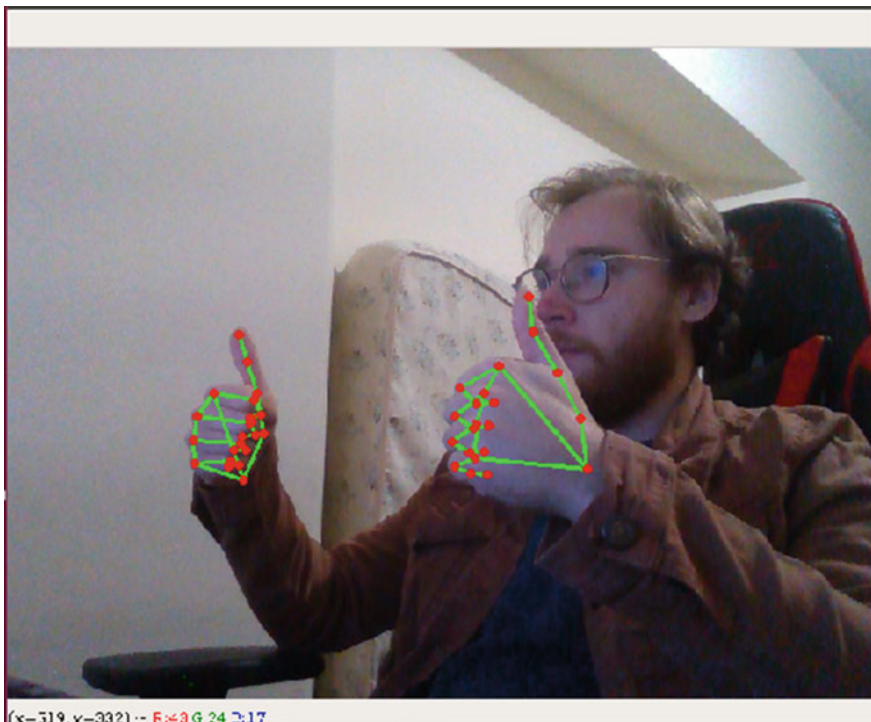


Fig. 3 Image representing the ROS2 MediaPipe Hands image output

The topic that should appear is “mediapipe/human_hand_list”. In this message there is a field responsible for informing the number of people on the image, which is manually defined by default as always being one person, and a hand list for right and left hands.

Each hand descriptor has 21 points in total, containing the point name and values for x , y , and z positions. The values for x and y are normalized to the interval $[0.0, 1.0]$ with respect to the width and height of the camera image. The value for z represents the depth of the reference point at the wrist, and the smaller the value, the closer the reference point is to the camera. The magnitude of z uses approximately the same scale as x . If hands are not identified, the fields will have the value 0.

3.3 MediaPipe ROS2 Pose Detector

Pose Detector is the node responsible for collecting data from the operator’s body and sending it to a ROS topic. MediaPipe Pose is an ML solution for high-fidelity full-body pose tracking, inferring 33 3D reference points across the entire body, as seen in Fig. 4.

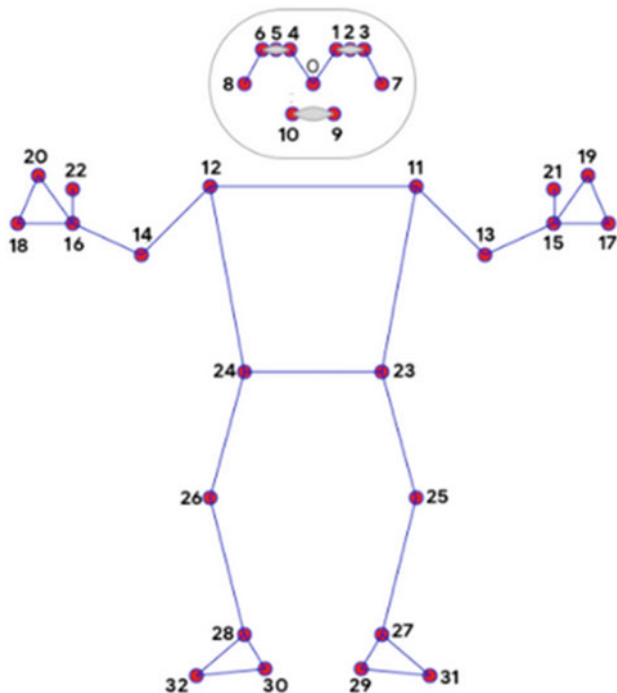


Fig. 4 The 33 pose landmarks

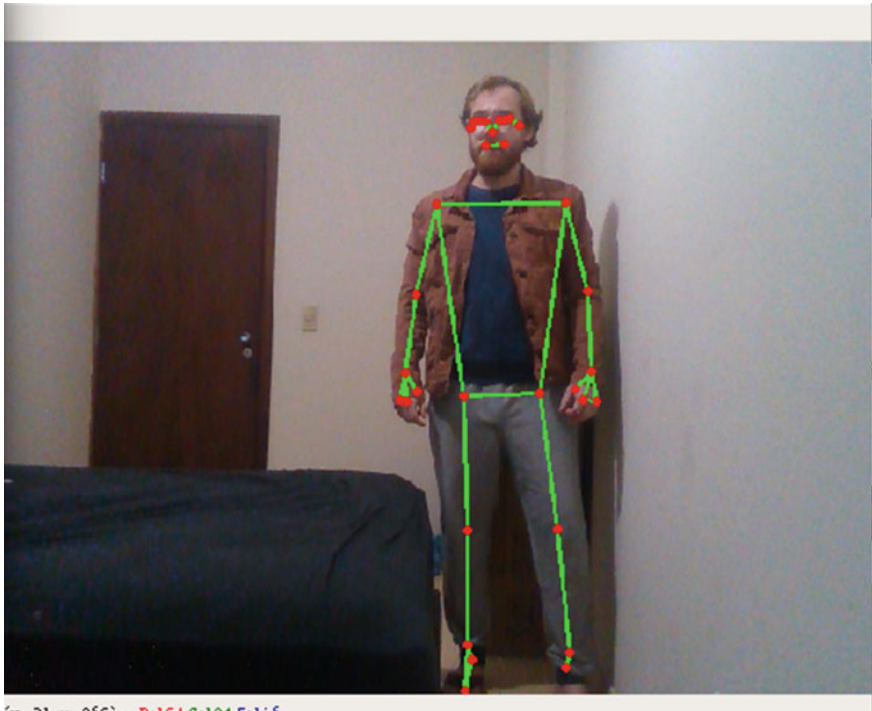


Fig. 5 Image representing the MediaPipe Pose output

The execution of this node is similar to the previous one, just run the following commands:

```
$ source ros2_workspace/install/setup.bash
$ ros2 run media_pipe_ros2 pose_detector
```

A window will open showing the image of your webcam with MediaPipe Pose already running, as in Fig. 5.

It is possible to view the topic responsible for the messages of the node pose_detector. To do this, open another bash and run:

```
$ source ros2_workspace/install/setup.bash
$ ros2 topic list
```

The topic that will appear now is “mediapipe/human_pose_list”. The message structure of this topic is composed of a field responsible for informing the number of people on the image and a list of body points. It has 33 points in total, containing the name of the point and the x , y and z values, following the same pattern as the previous topic.

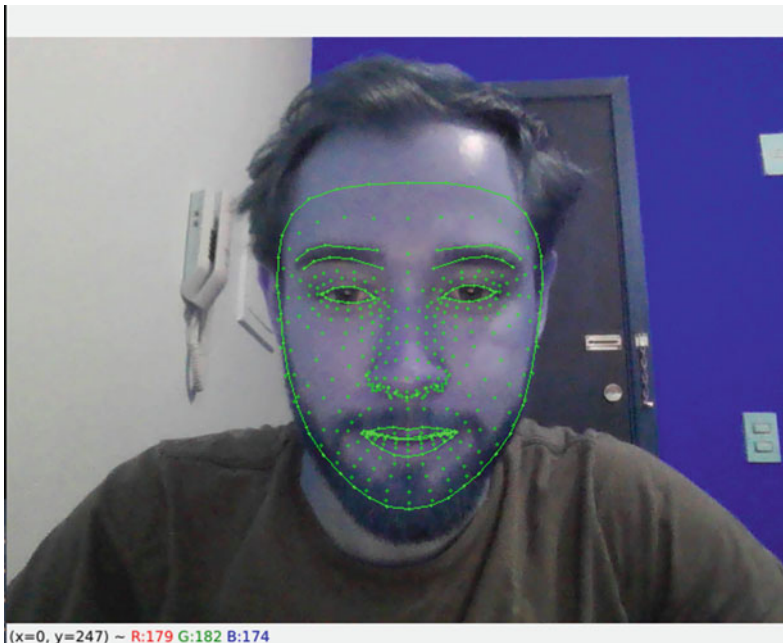


Fig. 6 Image representing the MediaPipe Face Mesh output

3.4 MediaPipe ROS2 Face Mesh

Face Mesh is the node responsible for collecting data from the operator's face and sending it to a ROS topic. MediaPipe Face Mesh is a facial geometry solution that estimates 468 3D reference points. It employs machine learning to infer 3D surface geometry, not requiring a depth sensor.

The execution is done through the following commands:

```
$ source ros2_workspace/install/setup.bash
$ ros2 run media_pipe_ros2 face_mesh_detector
```

As before, a window will open showing the image of your webcam with the MediaPipe Face Mesh already working, as in Fig. 6.

It is possible to view the topic responsible for the messages of the node `face_mesh_detector`. To do this, open another bash terminal and run:

```
$ source ros2_workspace/install/setup.bash
$ ros2 topic list
```

The topic that will appear this time is “`mediapipe/human_face_mesh_list`”. The message structure of this topic is composed of a field responsible for informing the number of people on the image and a list of face points. It has 468 points in total, containing values of x , y and z .

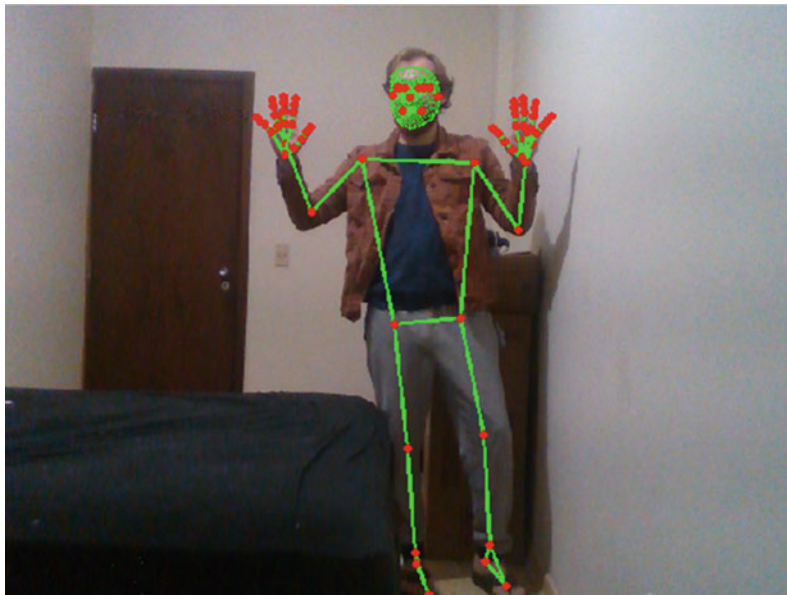


Fig. 7 Image representing the MediaPipe Holistic output

3.5 MediaPipe ROS2 Holistic

Holistic is the node responsible for collecting the operator's hand, face and pose data and sending them to a ROS topic. MediaPipe Holistic is the combination of the three features previously explained. It has a total of 543 points. MediaPipe's holistic pipeline integrates separate models for pose, face and hand components, each optimized for its specific domain.

The execution is done through the following commands:

```
$ source ros2_workspace/install/setup.bash
$ ros2 run media_pipe_ros2 holistic_detector
```

A window will open this time showing the image of your webcam with MediaPipe Holistic already running, as shown in Fig. 7.

At this point, all functionalities are running simultaneously and working without problems. It is possible to view the topic responsible for the messages of the holistic_detector node. To do this open another bash terminal and run:

```
$ source ros2_workspace/install/setup.bash
$ ros2 topic list
```

The topic that will appear this time is “mediapipe/human_holistic_list”. The message structure of this topic is composed of a field responsible for informing the number of people on the image and a list of points on the face, body and a list of

hands containing right and left hands, containing values of x , y and z , and name of the points for each of the cases.

4 Example Application

With the MediaPipe ROS package it is possible to run several applications, from autonomous robot control to security applications, such as solutions for human behaviour understanding [8]. For validation, the functionality of Hands Detector will be used to control a mobile robot. All development will be explained in this section. An application that uses OpenPose to control a mobile robot is used as a reference for the development, which in the end should work similarly.

4.1 Mobile Robot

In order to perform this task, you will first need a mobile robot. For this, a simulation in Gazebo can be used. In order to test the application, the TurtleBot 3 simulated robot was chosen, since it has what it takes to develop this challenge. Gazebo [9] is a powerful robotics simulator that calculates physics, generates sensor data and provides convenient interfaces to ROS2.

To install and run the gazebo simulator, just run the following commands and the simulator window should appear, as shown in Fig. 8:

```
$ sudo apt install ros-<distro>-gazebo-ros-pkgs
$ gazebo
```

In our installation, we replaced $<distro>$ by *galactic*.

Now let's install TurtleBot 3. TurtleBot is a standard ROS platform robot. It is a small, affordable, programmable mobile robot for use in education and research [10].

For its installation we will have to download the source files, compile and install the software:

```
$ sudo apt install ros-(distro)-turtlebot3 -*
$ mkdir -p ~/turtlebot3_ws/src
$ cd ~/turtlebot3_ws/src
$ git clone -b galactic-devel https://github.com/ROBOTIS-GIT/
    turtlebot3_simulations.git
```

Now that the source code has been downloaded from the repository, compile it and provide the ROS configuration file to add the newly installed executables to the environment:

```
$cd
$cd turtlebot3_ws/
$colcon build
$echo 'source ~/turtlebot3_ws/install/setup.bash' >> ~/.bashrc
```

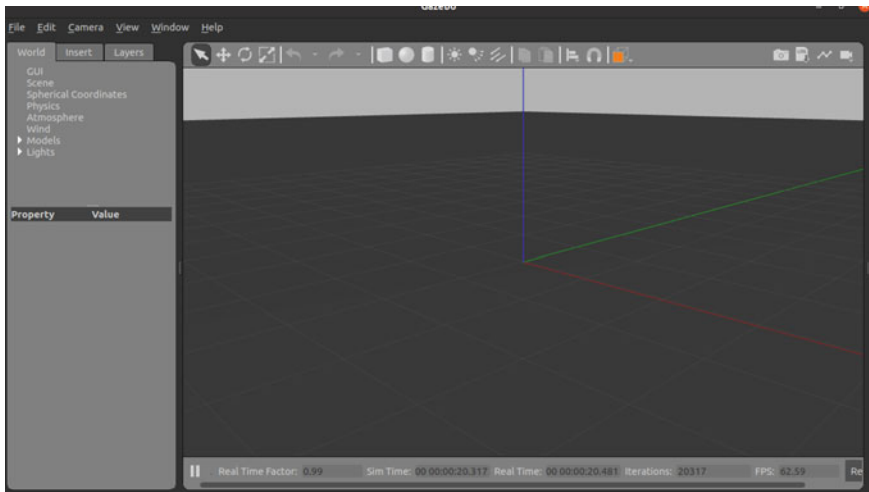


Fig. 8 Gazebo simulator graphical interface

Two environment variables must also be set. GAZEBO_MODEL_PATH variable to allow Gazebo to find TurtleBot model definition files and TURTLEBOT3_MODEL as waffle_pi to simulate TurtleBot3 Waffle Pi. After adding these lines to the .bashrc file, create the source file.

```
$echo 'export GAZEBO_MODEL_PATH=$GAZEBO_MODEL_PATH:~/turtlebot3_ws/src/turtlebot3/turtlebot3_simulations/turtlebot3_gazebo/models' >> ~/.bashrc
$echo 'export TURTLEBOT3_MODEL=waffle_pi' >> ~/.bashrc
$source ~/.bashrc
```

Now, all the software is installed and configured and everything is ready to run the simulation. Just open a terminal and run:

```
$ ros2 launch turtlebot3_gazebo empty_world.launch.py
```

The Gazebo simulator should open with the TurtleBot3 simulated model, as shown in Fig. 9, and we will have access to all the mobile robot control topics.

For our application, the ROS topic of interest is “/cmd_vel”. This topic is responsible for sending angular and linear velocities to the robot. You can test the operation using the following command:

```
$ ros2 topic pub --once /cmd_vel geometry_msgs/msg/Twist "{
    linear: {x: 2.0, y: 0.0, z: 0.0}, angular: {x: 0.0, y: 0.0, z: 1.8})"
```

In Gazebo, you can see TurtleBot moving in a circle. Now with everything set up and running it is possible to develop the control strategy.

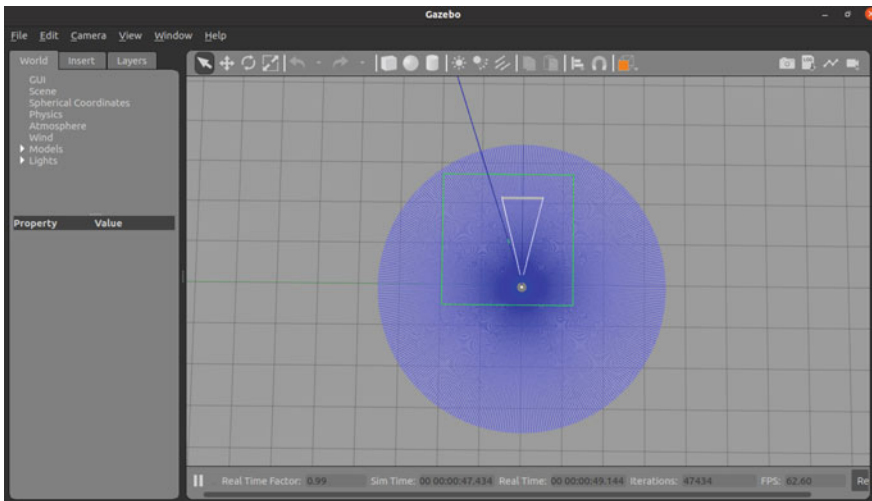


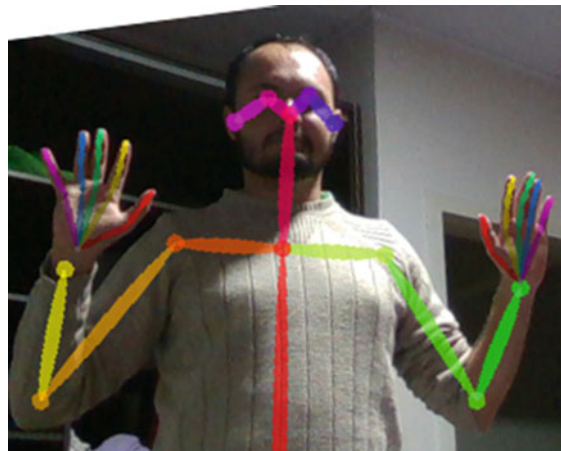
Fig. 9 TurtleBot3 simulated on Gazebo

4.2 Control Strategy

The strategy will use the hand detector functionality for this example. The control idea is based on the work of Martinelli [4], in which the authors use OpenPose to obtain data from the operator's hand, as can be seen in Fig. 10.

The strategy addressed by the authors is to use the right hand to control linear velocity and the left hand to control angular velocity. For this, it is calculated the angle difference between the points six and eight of the index finger on both left and right hand. Whenever the finger is moved, an angle between the two points is generated

Fig. 10 Image resulting from applying OpenPose to an RGB image. *Source* Martinelli [4]



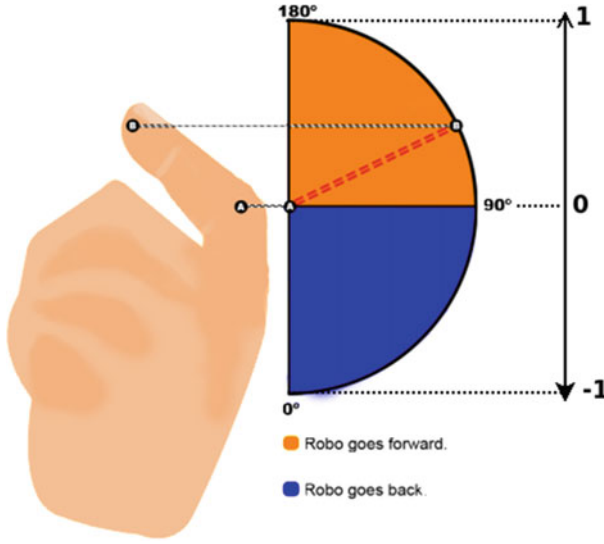


Fig. 11 Left hand, used for linear velocity control. The velocity is proportional to the angle, the closer to 180 degrees, the closer to 1 m/s the velocity will be. The closer to 0 degrees, the closer to -1 m/s the velocity will be. *Source* Martinelli [4]

and a linear and/or angular velocity is sent. The angular difference is calculated by the function atan2. Equation 1 represents the use of the function to obtain the angular difference between points six and eight.

$$\alpha = \text{atan2}((P[6]_i - p[8]_i), (P[6]_j - p[8]_j)) \quad (1)$$

As can be seen in Fig. 11, when the difference in the left hand is greater than 90 degrees the linear velocity will be positive, if it is smaller, it will be negative. The same is true for the right hand, but the angular velocity is controlled.

It was also implemented a control system to proportionally change the velocity as the angle difference changes. Equation 2 represents the decision taken by this control system:

$$vel = \begin{cases} 1.5 * \Delta_\alpha / 90, & \text{if } \Delta_\alpha \geq 95 \\ -1.5 * \Delta_\alpha / 90, & \text{if } \Delta_\alpha \leq 85 \\ 0, & \text{else} \end{cases} \quad (2)$$

Figure 12 represents the control strategy developed by the authors, in a flowchart format.

Following these criteria, the operator's finger movement will move the robot as in the work mentioned above, but using the MediaPipe for ROS2 package as a way to capture points in the operator's hands.

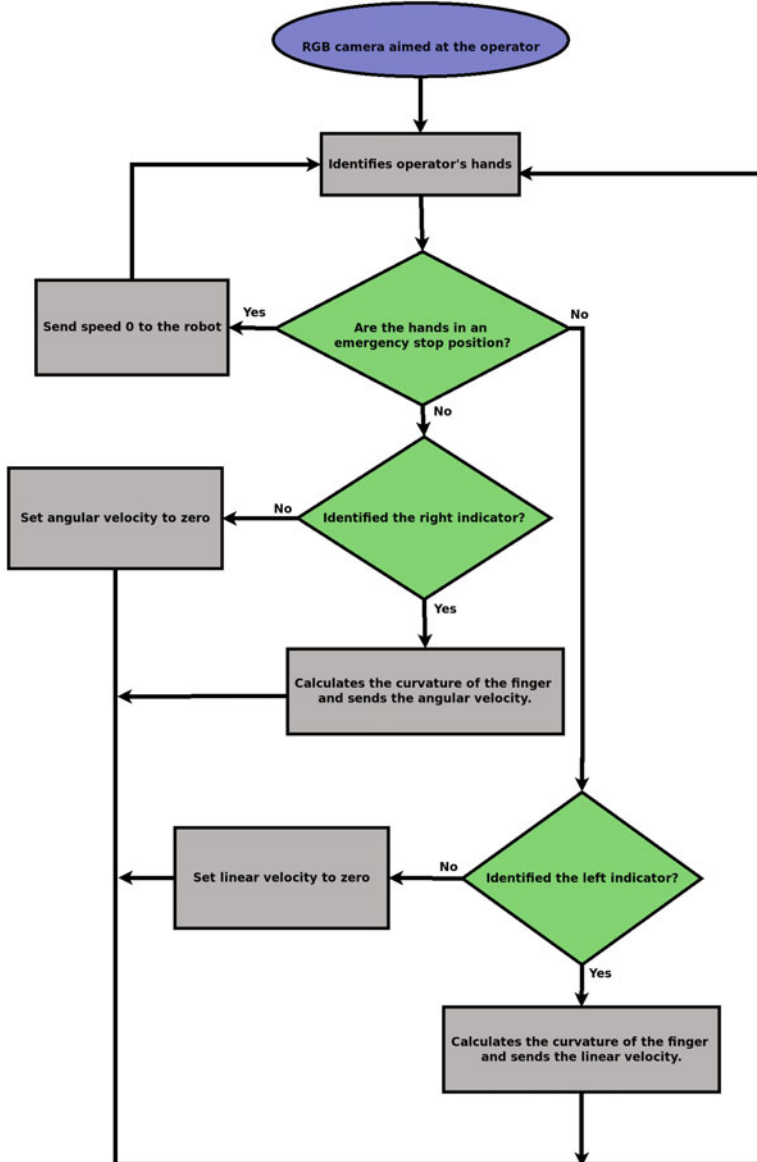


Fig. 12 Flowchart representing the control strategy adopted. *Source* Martinelli [4]

4.3 Execution and Results

Following the definitions discussed in the previous subsection, the code developed is as follows, and can be found in the control_logic.py file in the following repository: https://github.com/dmartinelli1997/Script_ROSBOOK2021.

```

        if (angle>=95):
            angular = (angle/90)*0.5
        elif(angle < 85 and angle != 0.0):
            angular = (angle/90)*-1*1.5
        elif(angle == 0.0):
            angular = 0.0
    else:
        angular = 0.0

    cmd_vel.linear.x = linear
    cmd_vel.angular.z = angular
    self.publisher_.publish(cmd_vel)

def CalcAngularDiff(data):
    difAngular = math.atan2(data[1][0]-data[0][0], data[1][1]-data[0][1])
    difAngular = abs(math.degrees(difAngular))
    return (difAngular)

def main(args=None):
    rclpy.init(args=args)

    cmd_sub = CmdSub()

    rclpy.spin(cmd_sub)

    cmd_sub.destroy_node()
    rclpy.shutdown()

if __name__ == '__main__':
    main()

```

For better understanding, each part of the code will be explained separately. The first few lines of code import `rclpy` so its `Node` class can be used.

```

import rclpy
from rclpy.node import Node

```

The next line imports the `math` library that provides the *atan2* function.

```

import math

```

Then, the structure of the node that will read the hand points is imported. The *Twist* message, where the velocity commands for the robot will be published, is also imported.

```

from media_pipe_ros2_msg.msg import MediaPipeHumanHandList
from geometry_msgs.msg import Twist

```

Next, the `CmdSub` class is created, which inherits from (or is a subclass of) `Node`.

```

class CmdSub(Node):

```

Inside the `CmdSub` class, a publisher (`cmd_vel`) and a subscriber (`/mediapipe/human_hand_list`) are created. The subscriber has as a callback function `listener_callback` where all the control strategy is developed, and the resulting command to the robot is published in the `cmd_vel` topic.

```

def __init__(self):
    super().__init__('sends_command')
    self.publisher_ = self.create_publisher(Twist, '/cmd_vel', 10)
    self.subscription = self.create_subscription(
        MediaPipeHumanHandList,
        '/mediapipe/human_hand_list',
        self.listener_callback,
        10)
    self.subscription

def listener_callback(self, msg):
    global linear
    global angular
    handLeft = []
    handRigth = []
    cmd_vel = Twist()
    if (msg.human_hand_list):
        if (msg.human_hand_list.left_hand_key_points):
            for i in range(0, len(msg.human_hand_list.left_hand_key_points)):
                handLeft.append(msg.human_hand_list.left_hand_key_points[i])

        if (msg.human_hand_list.right_hand_key_points):
            for i in range(0, len(msg.human_hand_list.right_hand_key_points)):
                handRigth.append(msg.human_hand_list.right_hand_key_points[i])

    if (len(handLeft)>0):
        if (handLeft[5]):
            angle = CalcAngularDiff([[handLeft[5].x, handLeft[5].y], [handLeft[8].x, handLeft[8].y]])
            if (angle>=95):
                linear = (angle/90)*0.5
            elif(angle < 85 and angle != 0.0):
                linear = (angle/90)*-1*1.5
            elif(angle == 0.0):
                linear = 0.0
        else:
            linear = 0.0

    if (len(handRigth)>0):
        if (handRigth[5]):
            angle = CalcAngularDiff([[handRigth[5].x, handRigth[5].y], [handRigth[8].x, handRigth[8].y]])
            if (angle>=95):
                angular = (angle/90)*0.5
            elif(angle < 85 and angle != 0.0):
                angular = (angle/90)*-1*1.5
            elif(angle == 0.0):
                angular = 0.0
        else:
            angular = 0.0

    cmd_vel.linear.x = linear
    cmd_vel.angular.z = angular
    self.publisher_.publish(cmd_vel)

```

The angular difference calculation uses the *atan2* function to be computed and uses the *abs* function to return the absolute result.

```
def CalcAngularDif(dados):
    difAngular = math.atan2(dados[1][0]-dados[0][0], dados[1][1]-dados[0][1])
    difAngular = abs(math.degrees(difAngular))
return (difAngular)
```

Just add this code in a file called *control_hands_strategy.py*, for example, and as soon as you run it will be possible to move the simulated robot.

With the logic developed, simulator installed and MediaPipe ROS2 package configured, it is possible to run all together and get the final result.

```
bash1:
$ ros2 launch turtlebot3_gazebo empty_world.launch.py
```

```
bash2:
$ ros2 run media_pipe_ros2 hands_detector
```

```
bash3:
$ python3 control_hands_strategy.py
```

A workspace similar to Fig. 13 will appear. When moving the fingers, the simulated robot will receive linear and angular velocity commands, causing it to move through the scenario.

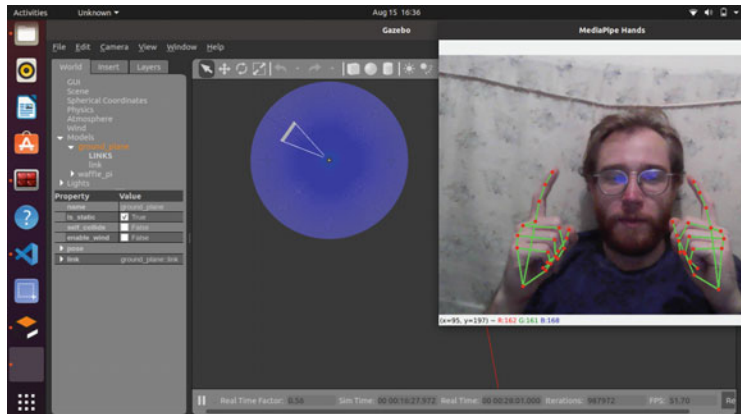


Fig. 13 Final workspace with MediaPipe and Gazebo in operation

5 Conclusion

The objective of this chapter is to present the MediaPipe for ROS2 package, that is developed in order to allow the use of the features offered by MediaPipe framework on ROS2. By presenting a brief tutorial, the use of this package is detailed, with a complete example application for a simulated mobile robot in Gazebo.

By developing the example application, it is possible to verify that any operator would be able to control the movements of any robot by simply moving the hands/fingers. In the developed application, it is shown how to control the movement of a mobile robot in an simulated scenario using the MediaPipe package, using only body recognition and no need for additional hardware, such as accelerated graphics cards.

Compared to the similar technology of OpenPose, MediaPipe shows an advantage due to its processing speed. The entire process was performed on a Core i5 notebook without an accelerated graphics card. In order to get the same results with OpenPose and its holistic detector, it is necessary an accelerated graphics card with at least 1.5 GB of RAM [11].

This tutorial presented the MediaPipe for ROS2 package, that makes it easy to create applications for interfacing with robots by using hand, body or face movements. All open-source code for this work is available in https://github.com/dmartinelli1997/media_pipe_ros2. The example application in https://github.com/dmartinelli1997/Script_ROSBOOK2021.git.

References

1. LLC, G.: Mediapipe (2020). <https://google.github.io/mediapipe/>
2. Yam-Viramontes, B.A., Mercado-Ravell, D.: Implementation of a natural user interface to command a drone. In: 2020 International Conference on Unmanned Aircraft Systems (ICUAS), pp. 1139–1144. IEEE (2020)
3. Vighneshwara, C., Kini, M.S., Shenoy, K.P.: Robot motion control using openpose. In: Smart Sensors Measurements and Instrumentation, pp. 49–57. Springer (2021)
4. Martinelli, D., Sousa, A.L., Augusto, M.E., Kalempa, V.C., de Oliveira, A.S., Rohrich, R.F., Teixeira, M.A.: Remote control for mobile robots using gestures captured by the rgb camera and recognized by deep learning techniques. In: Latin American Robotics Symposium (LARS), 2019 Brazilian Symposium on Robotics (SBR) and 2019 Workshop on Robotics in Education (WRE), pp. 98–103. IEEE (2019)
5. Cao, Z., Hidalgo, G., Simon, T., Wei, S.-E., Sheikh, Y.: Openpose: realtime multi-person 2d pose estimation using part affinity fields. IEEE Trans. Pattern Anal. Mach. Intell. **43**(1), 172–186 (2019)
6. Team, O.: Opencv (2021). <https://opencv.org/>
7. LLC, G.: Mediapipe (2020). https://google.github.io/mediapipe/getting_started/getting_started.html
8. da Silva Neto, J.G., Teixeira, J.M.X.N., Teichrieb, V.: Analyzing embedded pose estimation solutions for human behaviour understanding. In: Anais Estendidos do XXII Simpósio de Realidade Virtual e Aumentada, pp. 30–34. SBC (2020)
9. Foundation, O.S.R.: Gazebosim (2014). <http://gazebosim.org/>

10. Foundation, O.S.R: GazeboSim (2014). <https://www.turtlebot.com/>
11. Team, O.: Openposedoc (2021). <https://github.com/tramper2/openpose/blob/master/doc/installation.md>

Dieisson Martinelli Received the M.Sc. degree in electrical engineering, concentrate on teleoperation techniques through gesture recognition, from the Federal University of Technology - Paraná (UTFPR) in 2022, where is today a Ph.D. degree candidate. Bachelor's degree in Information Systems from the State University of Santa Catarina (UDESC). His research focuses on using deep learning techniques for teleoperated controls and mobile robotics.

Jonathan Cerbaro Received the M.Sc. degree in electrical engineering, concentrate on manipulator kinematics techniques, from the Federal University of Technology - Paraná (UTFPR) in 2022, where is today a Ph.D. degree candidate. Electronic Engineer graduated from University of Caxias do Sul (UCS) in 2020. His area of expertise encompasses control and automation, mobile robotics and industrial manipulators, with a focus on kinematics and Clifford's Algebra.

Marco Antonio Simoes received the M.Sc. and D.Sc. degree in Electrical and Computer Engineering from the Federal University of Technology—Parana, Brazil. His research interests comprise mobile robots in the areas of perception and intelligent systems, computervision, navigation, mapping, and applied AI.

João Alberto Fabro holds a degree in Informatics (bachelor's degree) from the Federal University of Paraná (UFPR-1994), a master's degree in Electrical Engineering from the State University of Campinas (UNICAMP-1996), a doctorate in Electrical Engineering and Industrial Informatics from the Federal Technological University of Paraná (UTFPR-2003). He was a professor at UNIOESTE (State University of Western Paraná) from 1998 to 2007. Since 2008, he is a professor at the Federal University of Technology - Paraná, based in the Department of Informatics - Curitiba. He is an Associate Professor. From 2012 to 2013, he was the Head of the M.Sc. course on Applied Computing of UTFPR. In 2014, Prof. Dr. Fabro was visiting fellow at the Faculty of Engineering of the University of Porto, Portugal. Has experience in Computer Science, focusing on Artificial Intelligence, researching the following subjects: Autonomous Mobile Robotics, Computational Intelligence (Neural Networks, Fuzzy Systems, Evolutionary Computing) and Educational Robotics. Is the coordinator of Research Groups on Computational Intelligence and the LASER-Advanced Laboratory of Embedded Systems and Robotics (<http://laser.dainf.ct.utfpr.edu.br>), at UTFPR. Is a collaborator of LIACC-Laboratory of Artificial Intelligence and Computer Science, University of Porto, Portugal (<https://liacc.fe.up.pt>). Since 2009, he has participated in several national, Latin American and international robotics championships (Robocup), in robot soccer and service robot categories (Robocup@Home), both as competitor and organizer.

André Schneider de Oliveira (Member, IEEE) received the M.Sc. degree in mechanical engineering, concentrate in force control of rigid ma-nipulators from the Federal University of Santa-Catarina (UFSC) in 2007 and the Ph.D. de-gree in engineering of automation and systemsin 2011. His Ph.D. thesis was on differentialkinematics through dual-quaternions for vehicle-manipulator systems. He is an Associate Pro-fessor with the Federal University of Technology-Parana (UTFPR) and a member of Ad-vanced Laboratory of Robotics and Embedded Systems (LASER) andLaboratory of Automation and Advanced Control Systems (LASCA). Hisresearch interests lie in the areas of robotics, mechatronics and automa-tion with particular focus in navigation and localization of mobile robots,autonomous and intelligent systems, perception and environment iden-tification, cognition, and deliberative decisions, human-interaction, andnavigation control.

ROS Frameworks and Applications

Autonomous 3D Thermal Mapping of Disaster Environments for Victims Detection



Christyan Cruz Ulloa, Guido Torres Llerena, Antonio Barrientos, and Jaime del Cerro

Abstract Early detection of victims in post-disaster environments is an essential task for rescue teams, and effective victim identification will save the greatest number of lives. One of the most significant challenges to carry out these tasks lies mainly in the harsh conditions typical of post-disaster environments such as low light, victims trapped both in rubble and by some materials that make their location difficult (blankets, wood, glass, Etc.) by simple visual inspection. To face this problem, this Chapter describes a robust method for identifying victims and their location within a heat map of the analyzed environment, using specific equipment (Thermal Camera Optris PI640, Microsoft Kinect, and Robot Dr. Jaguar). For this task development, a novel method developed in ROS is proposed based on the processing of thermal and depth images, in such a way that the first ones are used to detect victims through a Convolutional Neural Network and to generate Thermal Local Point Clouds of the environments in combination with depth images. Iterative Closest Point algorithms were used for a subsequent complete thermal map concatenation of the 3D environment using Point Clouds (Thermal Global Point Clouds). The tests to validate this method were carried out indoors (CAR Arena at Centre for Automation and Robotics) and outdoors (Robotics and Cybernetic Laboratory), recreating environments with post-disaster conditions. The main results show an average of 89% in concatenation efficiency to generate Thermal Global Point Clouds. For different scenarios. On the other hand, the detection of victims was carried out with an efficiency greater than 90% for the different proposed scenarios.

C. C. Ulloa (✉) · G. T. Llerena · A. Barrientos · J. del Cerro
Centro de Automatica y Robotica (UPM-CSIC), Universidad Politecnica de Madrid,
28006 Madrid, Spain
e-mail: christyan.cruz.ulloa@upm.es

G. T. Llerena
e-mail: guido.torres.rafael@alumnos.upm.es

A. Barrientos
e-mail: antonio.barrientos@upm.es

J. del Cerro
e-mail: j.cerro@upm.es
URL: <https://www.car.upm-csic.es/>

Keywords ROS · Thermal image · Point Clouds · Victim identification · 3D thermal mapping

1 Introduction

Search and rescue robots have had great relevance in recent years because a robot can enter where a rescuer or a dog cannot and gather valuable information from its environment to help in rescue tasks. Post-disaster scenarios result from natural events such as earthquakes, hurricanes, or attacks, completely devastated areas or cities with totally or partially collapsed buildings, rubble, Etc. They also produce high economic losses and, above all, the death of people trapped by the structures and debris generated by these disasters. The confined access spaces generated as tunnels and structures at risk of collapse pose a very high risk to rescue teams and front-line equipment during search and rescue missions in post-disaster environments.

Figure 1 shows the increase in publications in the Web Of Science (WOS) with topics related to search and rescue robotics, from 1999 to 2020, having an increase of 36% between each year.

Being a topic with great relevance, several competitions seek to reward the best search and rescue methods through collaborative or individual robots, through a series of cameras and sensors, to have extensive information on the environment to be searched. One of the main competitions is the DARPA (Defense Advanced Research Projects Agency) Subterranean Challenge, Rescue Robot Competitions at the AAAI (American Association for Artificial Intelligence) and the IJCAI (International Joint Conference on Artificial Intelligence). The competition scenarios are regulated by the NIST (National Institute of Standards and Technology) [1]. Where a group of robots or robots goes into a cave to locate victims in the environment to be scanned.

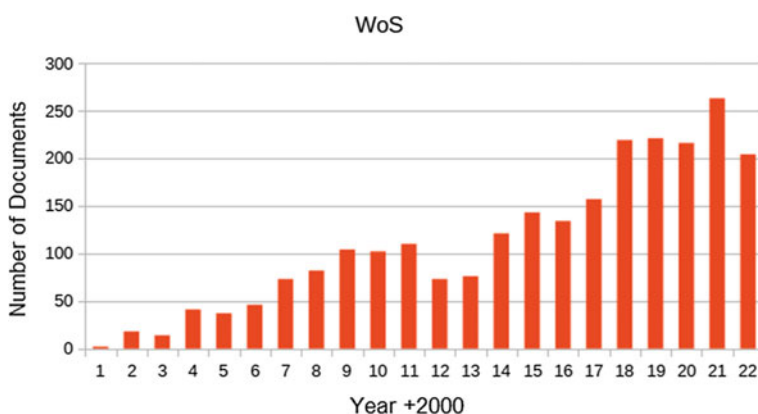


Fig. 1 Number of publications per year on the web of science WOS. *Source Authors*

The mapping of catastrophic environments is a great advantage for the different rescue groups to locate the different victims, and with this, it is possible to adapt different types of sensors or cameras, such as RGB, Thermal, Laser cameras, Etc. The coupling of different sensors and cameras gives better results to know the state of people. The mapping with thermal cameras has an advantage over the others because they do not depend on artificial and natural light, and they have different types of pallets to use in different applications. Different works within the state-of-the-art highlight the advantages of working with thermal images in search and rescue tasks [2–5].

This chapter describes the method used to locate victims in disaster areas and its 3D thermal mapping. For this purpose, an infrared Kinect sensor has been used, it is capable of projecting infrared structured light and capturing environmental distance information in the form of depth images, which, based on a normalization of parameters, have been transformed into Point Clouds. Each point within the cloud corresponds to the point distance of the object concerning the position of the sensor [6–9].

This sensor has been used mainly in indoor areas for extensive mapping areas. A 3D reconstruction of the environment was carried out using Point Clouds through thermal images (Th-Im) and depth images (Dp-Im).

A Convolutional Neural Network (CNN) was trained for victims location, carried out with a datasheet of several disaster areas such as exteriors and interiors to obtain a better result.

Thermal imaging is performed using an OPTRIS PI690 thermal camera and a Kinect V1 sensor, mounted on a Dr. JAGUAR V4 mobile robot, said an operator remotely manipulated robot.

The treatment and generation of the Thermal Local Point Clouds (T-LPC) are done offline; after a complete scan of the area, the images are processed to generate the Thermal Global Point Clouds (T-GPC) using Iterative Closest Point (ICP) algorithms. Once the 3D map has been prepared, and with the data acquired from the neural network training using thermal images, we obtain the location of the victim and her representation on the map.

The development of this method involves integrating different fields described within the state-of-the-art, which involve: 3D mapping, digital processing of thermal images, victim detection, neural networks, and search and rescue robotics. The main developments respectively within these fields are highlighted below.

Among the main developments in the processing of neural networks and thermal images, the approaches in detection of intruders in night environments stand out [10], comparison of the detection of people indoors and outdoors [11], the influence of atmospheric weather in the detection of people [12]. On the other hand, other methods focus on the detection of people using neural networks with images of low results both thermal and RGB [13–16], together with some developments that they use drones for this purpose [17].

On the other hand, the mapping techniques commonly used are based on representing Point Clouds in false color using grayscales or RGB images [18–20, 20, 21]. By processing the captured data, applying surface smoothing techniques [22], ICP

[23], and visual odometry [24]. However, developments within the state-of-the-art related directly to the proposed method are limited to equipment calibration [25, 26] and building thermal maps [27–30], but not in generating an integral system that generates support. For rescue teams in disaster areas, as is done in this chapter.

This chapter is structured as follows. In the first instance, there is the system overview and the background of the proposed method, to later describe the configuration of the ROS environment, to finally show the results, discussion, conclusions, and future work.

2 System Overview

One of the main contributions of this chapter stands out in the capability to generate thermal maps of a disaster environment, detect and locate (locate them in the T-GPC) victims in a disaster environment. Through thermal images and a previously trained network, through of the environmental inspection using a robot in the field capable of transmitting images to a remote station (ERO—Remote Operator Station), the Robot in this phase of experimentation of the system is teleoperated from a remote station by an operator or rescuer previously capable.

The transmission of images and processing are carried out in real-time in the ERO, so that the operator or rescuer can know a priori if there is a victim (which could be an unconscious person or trapped in rubble) who needs primary assistance). Furthermore, its location within the environment is based on the position of the Robot.

This implementation has been completely developed in ROS, which has been used for its great versatility and ability to integrate different sensory systems, robots and carry out processes on multiple computers through its node and topic communications architecture.

The Robot used for exploration in the disaster environment has been the Jaguar V4, equipped with a thermal camera and a Kinect sensor, the following components are mounted on the Robot and whose Hardware structure is shown in the Fig. 2:

- Computer Lenovo Flex 5.
- Thermal Camera Optris 640
- Sensor kinect V1

The robot's movement control in the environment is executed by publishing linear and angular velocity commands, through the topic /cmd_vel, for its part, the robot transmits its position within the environment through the topic /position. The flow of these data is shown in the Fig. 3. The structure of the published topics is:

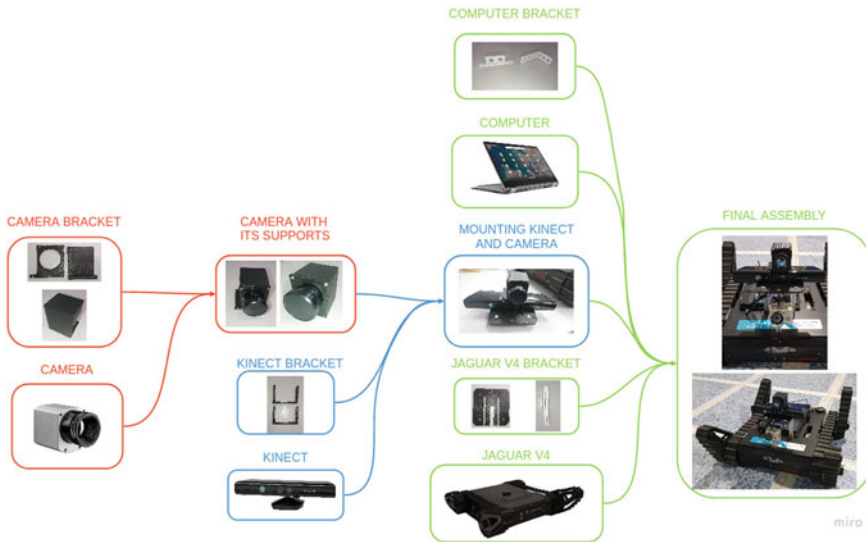


Fig. 2 Thermal camera and kinect assembly in Robot Jaguar V4

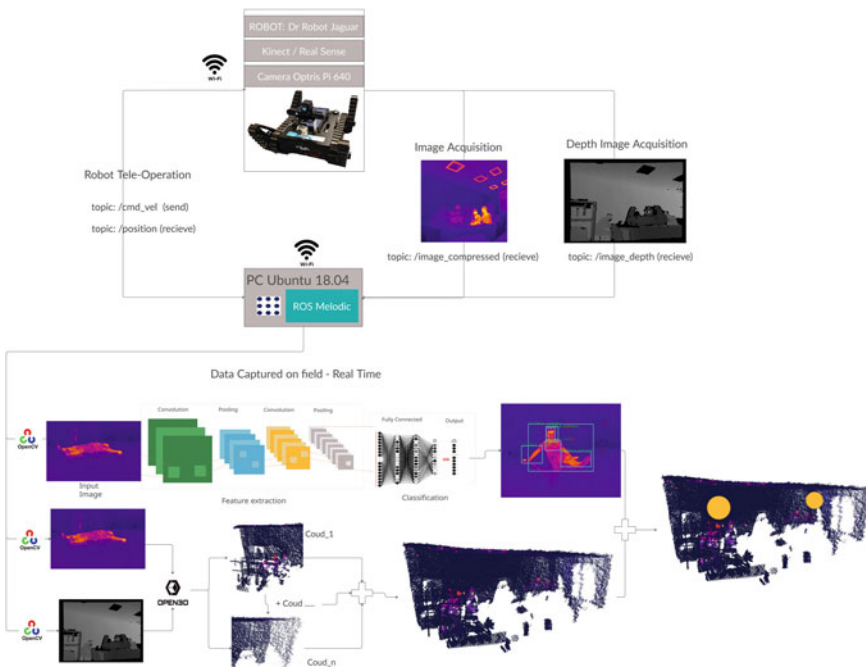


Fig. 3 Diagram of interconnections of the systems using ROS, used for the detection of victims and automatic generation of 3D thermal maps

- Speed command transmission to the robot:

```
/cmd_vel (geometry_msgs/Twist)
linear:
x: 0.1 (vel_lin)
y: 0.0
z: 0.0

angular:
x: 0.0
y: 0.0
z: 0.1 (vel_ang)
```

- Robot position reception:

```
/pose (geometry_msgs/Twist)
geometry_msgs/Vector3 linear
float64 x (Position x)
float64 y (Position y)
float64 z

geometry_msgs/Vector3 angular float64 x
float64 y
float64 z (Orientation)
```

For the capture and subsequent transmission of thermal and depth images from the Kinect camera and sensor integrated into the robot, drivers for ROS (in the Lenovo Flex computer) have been installed, developed by the manufacturer, and available at http://wiki.ros.org/optris_drivers.

The image is transmitted through the topic /image_compressed. The compressed image has been used, because it increases the fps transmission rate, and the loss of information is not significant for the development of the process.

The structure of the thermal image topic is:

- Thermal image reception:

```
/image_compressed (sensor_msgs/Image Message)
uint32 height uint32 width
string encoding (Contains the pixels and channels of the image)
uint8 is_bigendian
uint32 step
uint8[ ] data
```

For the real-time processing of the image received in the ERO, ROS packets have been previously installed in the anaconda environment in such a way that with the

network already trained, inference and detection of people within the received image can be carried out. as shown in Fig. 3.

An algorithm in python has been developed for artificial vision processing. It receives as input the image transmitted by the robot through the subscription to the related topic of ROS. It is processed using OpenCV libraries to apply the respective corrections to the image, erosion operations, dilation, and noise elimination, to pass as data to the neural network next stage.

Figure 3 shows in the lower part the CNN architecture, taking the image as input, features extraction phase is applied through convolutions and pooling phases. At the end, in the classification phase, the result of the fully connected layers is the victim location(s), the bounding box for each victim, and the accuracy percentage for each recognition.

The first convolution stage finds characteristics in the thermal image using detectors. The pooling layer reduces the characteristic maps size, in this phase more relevant characteristics are preserved.

After a sets of convolution-pooling phases, a flattening operation is applied, converting into a 1D vector the pooling result per thermal image. This new vector serves as final fully connected layers input, where internal weights are established through back propagation.

Finally, the inference is made with the trained network, and it is established whether or not there is a victim or a rescuer in the inspected area. This process runs cyclically throughout the environment inspection.

The detection algorithm for thermal images victim detection has been implemented in Python, a bounding box mark was established to detected victims and rescuers on the original image.

Simultaneously the thermal images received are processed together with the depth images captured by the Kinect, forming several T-LPCs. As the robot moves in the environment, the T-LPCs are concatenated to form the T-GPCs and locate victims on the global map, allowing rescuers to know the position of a possible victim within the environment.

3 Background, Sensors and ROS Configuration

3.1 ROS Packages, Configuration and Data Acquisition

3.1.1 Packages for Thermal Images—Compressed Image

The thermal camera used for this development was the Optris PI640 http://wiki.ros.org/optris_drivers. The files used for the configuration of the thermal camera used can be downloaded from the GitHub repository (<https://github.com/ChristyanCruz11/Thermal-3DMapping.git>). The same ones that have the structure shown in the Fig. 4



Fig. 4 Calibration and configuration files for the thermal chamber

The following steps must be followed for the installation and launch of the thermal chamber nodes:

1. sudo apt-get install cmake freeglut3-dev libusb-1.0-0-dev
2. In /src folder: git clone https://github.com/evocortex/optris_drivers
3. catkin_make
4. sudo ir_download_calibration
5. ir_download_calibration -t /tmp -d 18072067.xml

Subsequently its execution is carried out by means of the commands:

1. sudo rmmod uvcvideo
2. sudo modprobe uvcvideo nodrop=1
3. rosrn optris_drivers optris_imager_node_xmlConfig:=/home/explorador/catkin_ws/src/optris_drivers/config/generic.xml
4. rosrn optris_drivers optris_colorconvert_node _palette:=6 _paletteScaling:=1 _temperatureMin:=20 _temperatureMax:=40

The palette scaling should be considered because it will adapt to the maximum temperature existing in the environment to maximize the tones and adapt them to it. The Fig. 5 shows the difference between a uniform pallet through temperature values (Param: _paletteScaling:=1), with respect to a non-uniform pallet that adapts to the maximum temperature value (Param: _paletteScaling:=2).

The topics generated after launching these nodes are shown in the Fig. 6, of which we will work mainly with the compressed image to optimize processing times.

- /thermal_image_view/compressed.

3.1.2 Packages for Kinect—Depth Images

To work with depth images of the Kinect, the Freenect libraries have been used, the installation and execution of which are detailed below:

1. In /src: git clone <https://github.com/OpenKinect/libfreenect.git>
2. cd libfreenect

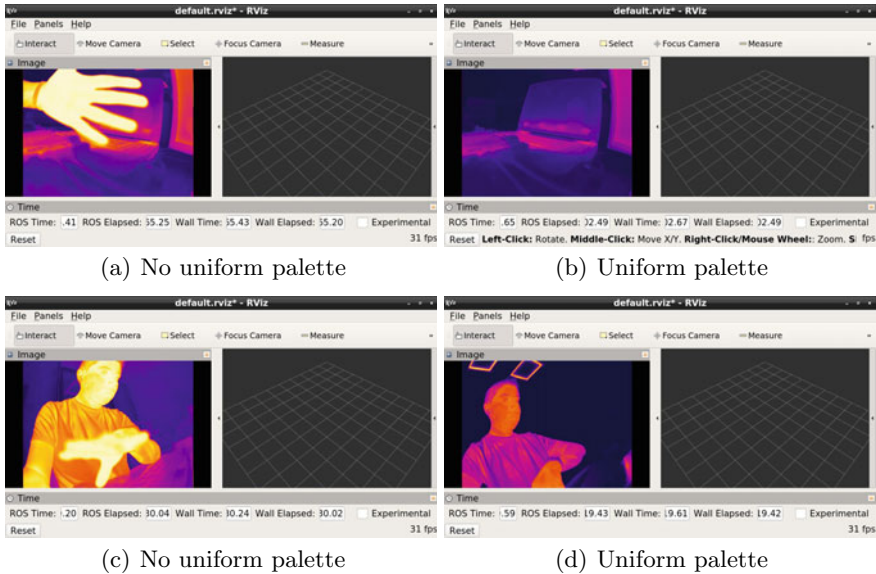


Fig. 5 Differences between uniform and non-uniform temperature pallet

3. `mkdir build`
4. `cd build`
5. `cmake -L ..`
6. `make`
7. `sudo make install`
8. `sudo apt-get install ros-melodic-freenect-launch`
9. `roslaunch freenect_launch freenect.launch`

3.1.3 Packages for Robot Dr. Jaguar

The files used to launch the .launch file to command the robot are located in the “Robot Dr. Robot Jaguar Files” folder at: <https://github.com/ChristyanCruz11/Thermal-3DMapping.git>. To launch the nodes, execute the commands from the robot’s computer:

1. `roscore`
2. `roslaunch jaguar jaguar`

The Fig. 7 shows the topics obtained when launching the .launch file; these topics will be used to command the robot based on linear and angular speeds, as well as to move the front and rear fliers through a joystick in a remote station.

```
explorador@explorador-desktop:~$ rostopic list
/camera_info
/clicked_point
/flag_state
/image_raw
/image_raw/compressed
/image_raw/compressed/parameter_descriptions
/image_raw/compressed/parameter_updates
/initialpose
/internal_temperature
/move_base_simple/goal
/optris_timer
/rosout
/rosout_agg
/tf
/tf_static
/thermal_image
/thermal_image/compressed
/thermal_image/compressed/parameter_descriptions
/thermal_image/compressed/parameter_updates
/thermal_image_view
/thermal_image_view/compressed
/thermal_image_view/compressed/parameter_descriptions
/thermal_image_view/compressed/parameter_updates
/visible_image
/visible_image_view
/visible_image_view/compressed
/visible_image_view/compressed/parameter_descriptions
/visible_image_view/compressed/parameter_updates
explorador@explorador-desktop:~$
```

Fig. 6 Topics for thermal imaging

Fig. 7 Thermal camera calibration

```
pioneer@pioneer-H110N: ~
pioneer@pioneer-H110N:~$ rostopic list
/cmd_flipper
/cmd_vel
/drrobot_jaguar_v6_gps_sensor
/drrobot_jaguar_v6_imu_sensor
/drrobot_jaguar_v6_motor_sensor
/drrobot_jaguar_v6_motorboard_sensor
/joint_states
/joy
/rosout
/rosout_agg
pioneer@pioneer-H110N:~$
```

Fig. 8 Master configuration

```
# MASTER
export ROS_MASTER_URI=http://192.168.43.204:11311
export ROS_IP=192.168.43.204
export ROS_HOSTNAME=192.168.43.204
```

Fig. 9 Slave configuration

```
# SLAVE
export ROS_MASTER_URI=http://192.168.43.203:11311
export ROS_IP=192.168.43.204
|export ROS_HOSTNAME=192.168.43.204
```

3.1.4 Master—Slave Communication

Master-Slave does the configuration of the system for information management. In such a way that the most powerful computer that receives all the information and sends speed commands is configured as a master. By the other hand the robot is configured as a slave. Figures 8 and 9 show respectively the IP addresses of the master and slave.

3.2 Equipment Calibration

3.2.1 Thermal Camera

Some cameras introduce significant distortion to images. Two main types of radial distortion and tangential distortion, Eqs. 1 and 2.

Radial distortion makes straight lines appear curved. Radial distortion increases as points move away from the center of the image.

$$x_{distortion} = x(1 + k_1r^2 + k_2r^4 + k_3r^6) \quad (1)$$

$$y_{distortion} = y(1 + k_1r^2 + k_2r^4 + k_3r^6) \quad (2)$$

Similarly, tangential distortion occurs because the imaging lens is not aligned perfectly parallel to the image plane. Therefore, some areas of the image may appear closer than expected. The amount of tangential distortion can be represented by the Eqs. 3 and 4:

$$x_{distortion} = x + [2p_1xy + p_2(r^2 + 2x^2)] \quad (3)$$

$$y_{distortion} = y + [p_1(r^2 + 2x^2) + 2p_2xy] \quad (4)$$

In summary, we need to find five parameters, known as distortion coefficients, given by the Eq. 5:

$$Distortion\ coefficients = (k1, k2, p1, p2, k3) \quad (5)$$

Besides this, we need some other information, such as the intrinsic and extrinsic parameters of the camera (Eq. 6). Intrinsic parameters are specific to a camera. They include focal length (f_x , f_y) and optical centers (c_x , c_y). The focal length and optical centers can be used to create a camera array, which can be used to eliminate distortion due to the lenses of a specific camera. The camera matrix is unique to a specific camera, so once calculated, it can be reused in other images taken by the same camera. It is expressed as a 3×3 matrix:

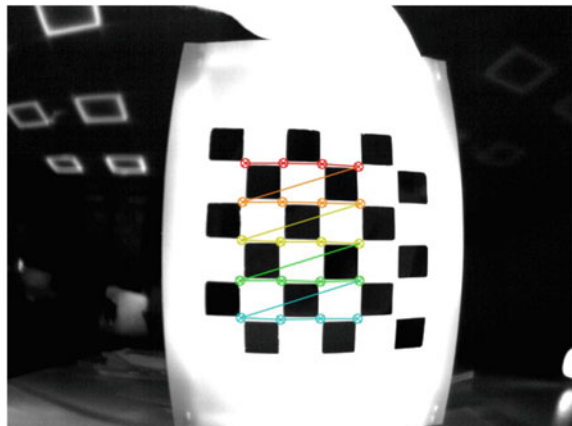
$$\begin{bmatrix} f_x & 0 & c_x \\ 0 & f_y & c_y \\ 0 & 0 & 1 \end{bmatrix} \quad (6)$$

The calibration of the Optris thermal camera uses the [31] method. It consists of registering the corners of a chessboard and using code, obtaining the fundamental matrix variables (Eq. 6), vectors of translation and rotation Eq. 5, previously explained. For this, some sheets of paper with checkerboard-shaped perforations were heated, and the thermal camera was adjusted on the White-Hot pallet to record the characteristic points from each corner of the chessboard. Once the calibration code has been developed, we obtain the desired values, the Fig. 10 shows the edges of the object to be calibrated (checkerboard), the fundamental matrix of the thermal chamber (7), distortion vector (8), rotation matrix (9), and the translation matrix (10) said calibration, a distortion error of 0.38487294716991416.

$$\begin{bmatrix} f_x = 458.41626958 & 0 & c_x = 327.15150492 \\ 0 & f_y = 457.27416629 & c_y = 213.86162691 \\ 0 & 0 & 1 \end{bmatrix} \quad (7)$$

$$[-0.63118568 \ 0.89263329 \ 0.02207553 \ -0.00361449 \ -1.11144398] \quad (8)$$

Fig. 10 Thermal camera calibration



$$\begin{bmatrix} \begin{bmatrix} -0.01884591 \\ 0.05737353 \\ -0.40815257 \end{bmatrix} & \begin{bmatrix} -0.14199782 \\ -0.02233268 \\ 0.02366859 \end{bmatrix} \end{bmatrix} \quad (9)$$

$$\begin{bmatrix} \begin{bmatrix} -2.68330769 \\ -1.10260326 \\ 12.13103857 \end{bmatrix} & \begin{bmatrix} -0.92708789 \\ -1.36752316 \\ 9.63877082 \end{bmatrix} \end{bmatrix} \quad (10)$$

3.2.2 Image Rectification

After obtaining the fundamental matrix, distortion vector, translation, and correction, we obtain the new correction matrix with the cv2.getOptimalNewCameraMatrix library. From this process, we extract the distortion map for rectification of the image with cv2.initUndistortRectifyMap with the new rectification matrix and fundamental matrix of calibration. Once the distortion map is obtained, we project said map with a test image with cv2.remap (Fig. 11).

3.2.3 Image Preprocessing

Erosion and dilation operations have been applied to pre-process the image transmitted by the robot in the field. These morphological operations have been applied sequentially. In the first instance, erosion has been applied to erode the limits of the object in the foreground, eliminating tiny objects that are not of interest and eliminating white noise; later, a dilation is applied, which Brings together the broken parts of an object and accentuates the characteristics of the objects in the image. The selection of the parameters used was: Erosion (kernel = 5; iterations = 1), Dilation (kernel = 3; iterations = 1).

3.3 *Thermal Image Processing and Transmission Using OpenCV and ROS*

- Installing ROS and optris drivers and plugins
- Generation of initial parameters generiz.xml
- Enable usb port for sudo rmmod uvcvideo thermal camera; sudo modprobe uvcvideo nodrop = 1
- Launch node with generic parameters rosrun optris drivers optris_imager node xmlConfig:=/home/guido/catkin_ws/src/optris_drivers/config/generic.xml
- Obtaining thermal camera video with Palette Hot heat, without temperature self-regulation, minimum temperature of 20 and maximum of 40 (rosrun optris drivers

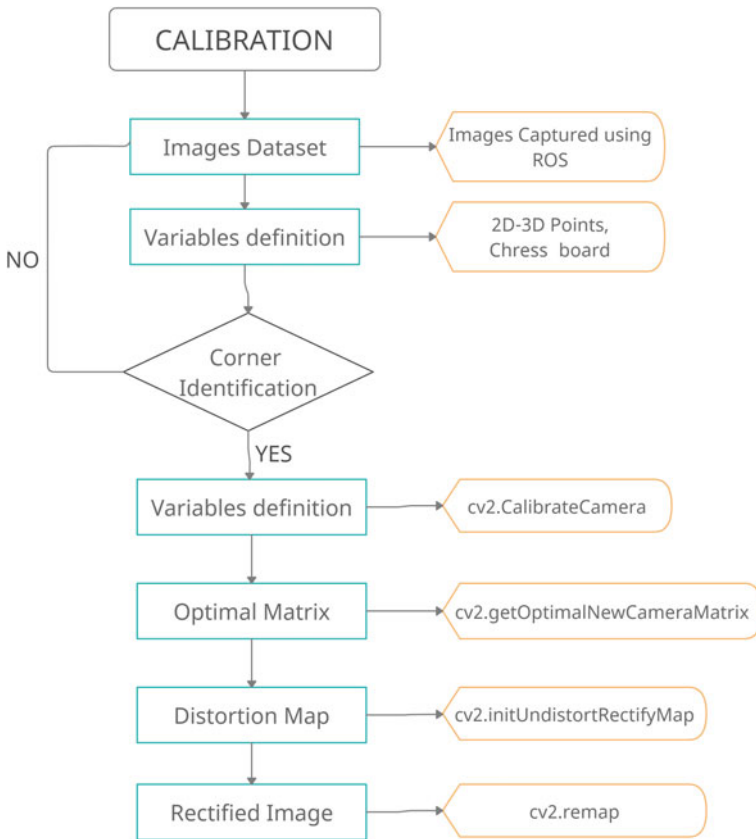


Fig. 11 Calibration process

```
optris colorconvert node palette:=6 paletteScaling:=1 temperatureMin:=20 temperatureMax:=40)
```

Figure 12 shows the acquisition of thermal images.

3.4 Integration of Thermal and Depth Camera with ROS

The acquisition of images for the creation of Point Clouds was executed using ROS. The process to develop this task is detailed below:

Fig. 12 Thermal image acquisition



Launch of Nodes for Thermal Camera

1. `sudo rmmod uvcvideo; sudo modprobe uvcvideo nodrop=1`
Subscribe the thermal camera serial port to COM 1
2. `rosrun optris.drivers optris.imager.node .xmlConfig:= /home/guido/catkin.ws/src/optris.drivers/config/generic.xml`
Execute the generic calibration parameters of the thermal chamber generated in the installation generic.xml
3. `rosrun optris.drivers optris.colorconvert.node .palette:=6 .paletteScaling:=1 .temperatureMin:=20 .temperatureMax:=40` Execute the thermal chamber node with palette 6 (Iron heat), deactivating the temperature auto scaling (paletteScaling: = 1), minimum temperature of 20 (.temperatureMin: = 20) and maximum temperature of 40 (.temperatureMax: = 40)

Kinect Sensor Releases

- `roslaunch freenect.launch freenect.launch depth.registration:=true`
We launch the freenect node of the Kinect sensor and activate the different registers for depth image.

Image Acquisition

1. **Node subscription:**
`rospy.wait_for_message ('/thermal.image.view', Image)` thermal camera node
`rospy.wait_for_message('/camera/depth.registered/hw.registered/image.rect.raw', Image)` rectified depth chamber node.
2. **CV.BRIDGE:**
For the bridge between ROS and image processing we use cv.bridge, for thermal images we use RGB format and for depth images passthrough (No image conversion).

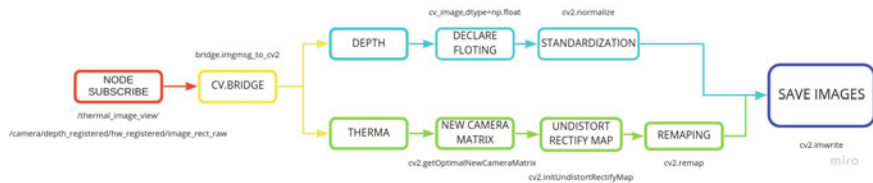


Fig. 13 Thermal and depth image

3. Depth Image Processing:

- **Image declaration as floating**

We declare the acquired images as floating for post processing (np.array (Imagen.profundidad, dtype=np.float)).

- **Depth image normalization**

We normalize the images from 0 to 255 for the generation of Point Clouds cv2.normalize(image.profundidad, image.profundidad, 0,255, cv2.NORM_MINMAX).

4. Thermal Image Processing:

- **New Camera Matrix**

Obtain a new optimal thermal camera matrix, using the fundamental matrix and rotation of the thermal camera, obtained these values in the calibration of the camera and the dimensions of the image (width and height), cv2.getOptimalNewCameraMatrix.

- **Rectified map without distortion**

The new map without distortion is obtained through cv2.initUndistort_ RectifyMap, through the old fundamental matrix and the new matrix obtained previously. The same process is carried out with the rotation vector.

- **Remapping the image**

Projection of the rectified image using the rectified map without distortion (cv2.remap). The interpolation technique used has been of type Linear through the python module cv2.INTER_LINEAR.

5. Save Images:

We save the processed images from a thermal camera and a depth camera, using cv2.imwrite (location where to save the images, the type of image to save) (Fig. 13)

3.5 Neural Network for Victims Identification

A Convolutional Neural Network has been trained to detect victims within the explored environment, using as input the thermal images transmitted by the robot. This subsection details the process carried out for automatic victim detection.

3.5.1 Datasets Generation

The dataset generation has been carried out by extracting video frames captured from the environment with the robot in a previous stage, choosing the images where there are victims and rescuers. The robot moves in a teleoperated way, in different scenarios, capturing the videos. The result of the extracted images is $1280 \times 720\text{ px}$.

The training database is 1747 images, with 7 labels:

1. Rescuer body
2. Rescuer legs
3. Victim body
4. Victim arm
5. Victim torso
6. Victim legs
7. Victim head

The validation of the network was given using a series of images taken after the network's training, with 2000 images.

3.5.2 Data Augmentation to Increase the Neural Network Robustness

To increase the neural network robustness, a series of treatments were applied to these images such as Increase in brightness, Horizontal Reflection and Increase in contrast, Gaussian Noise, as shown in the Figs. 14 and 15. Specific parameters used for Data Augmentation in Gaussian Noise are:

- $\text{gauss} = np.random.normal(\text{mean}, \text{sigma}, (\text{row}_\text{img}, \text{col}_\text{img}, \text{ch}_\text{img}))$
- $\text{gauss} = np.random.normal(0, 0.1, (720, 1280, 3))$

Thus we increased our database, and the Recognition of victims can be in environments with different environments. This image was taken at the Robotics and Cybernetics (RobCib) Laboratory.

Figure 14 shows a couple of rescuers, for which the same image treatment procedure is performed to increase the database and thus improve the validation of the work in different environments.

3.5.3 Neural Network Training and Hyper-Parameters

The neural network architecture consists of 24 Convolutional layers and two fully connected layers, receives the image ($1280 \times 720\text{ px}$) transmitted by the robot remotely and has as output one of the raised labels, the detection percentage and the location bounding box. The training has been carried out for 130 epochs, each epoch with 290 batches with a batch size of 6 images, resulting in 37700 iterations.

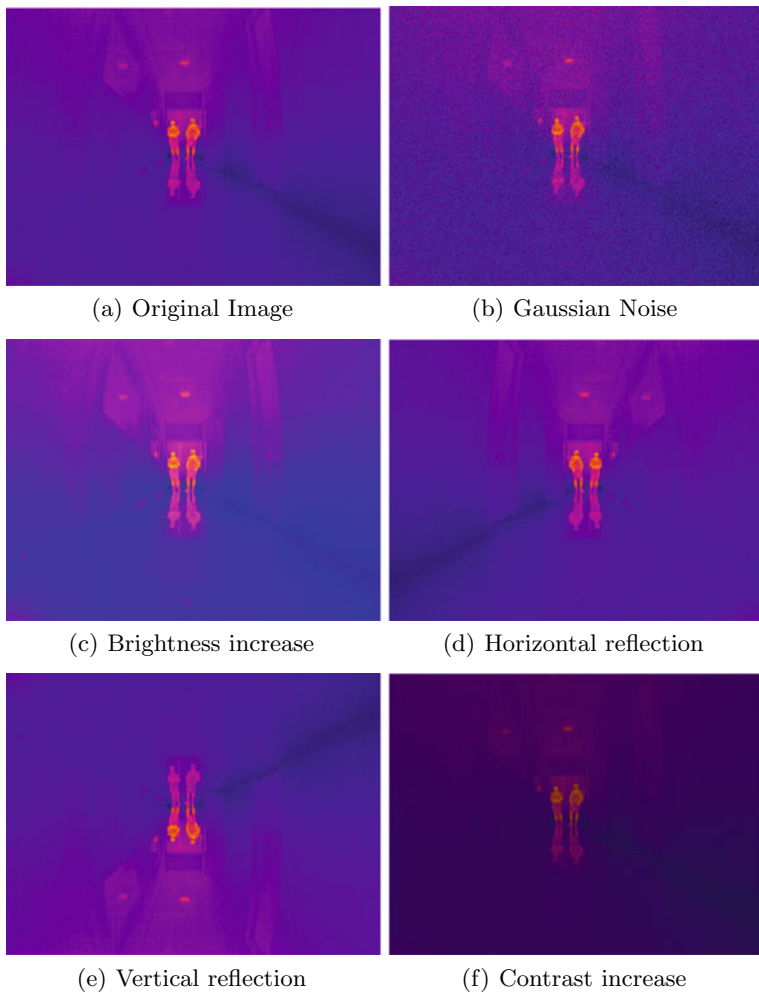


Fig. 14 Sample of the application of data augmentation to a thermal image of a rescuer

At the end of each training season, the adjustment weights of the network model are stored, so based on the analysis of the most optimal season, the final model of the network will be adjusted.

The neural network training has been carried out on a PC, MSI model, 16GB in RAM, 1660Ti GPU. The approximate time for training the network was 6h. TensorFlow libraries have been used for this section development.

The model's effectiveness has been analyzed in terms of Accuracy and Loss. The results of the training and validation of the neural network model are shown below.

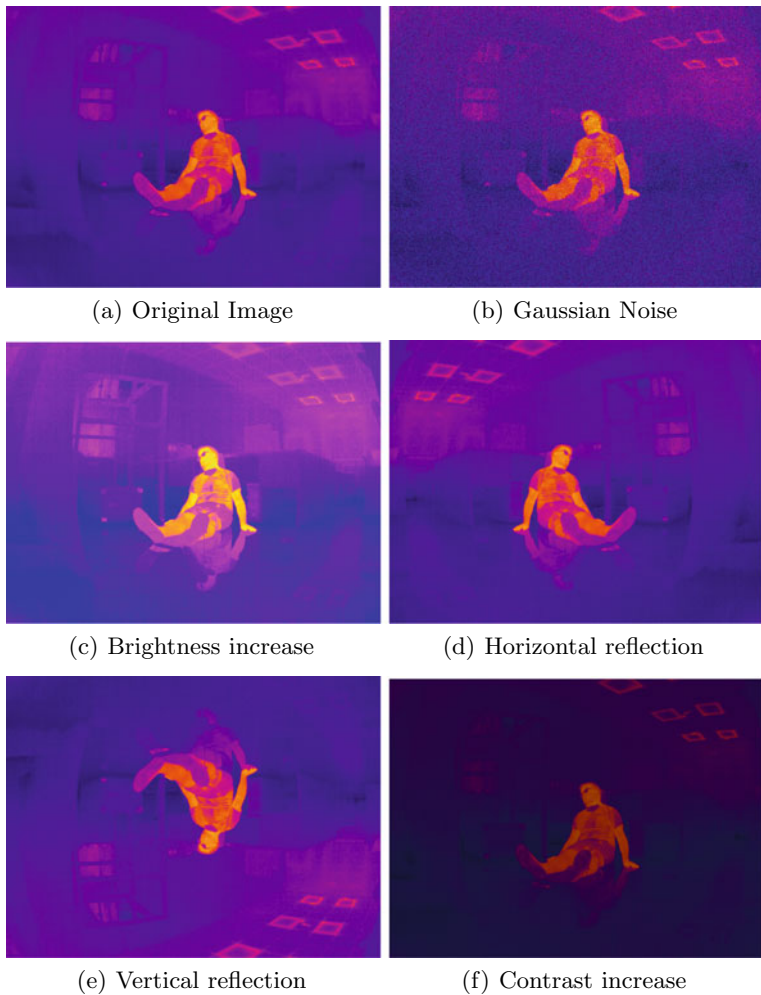


Fig. 15 Application of data augmentation to a victim thermal image

Figure 16 represents the Loss curve for training. This allows us to know how far apart are the predictions of a model and its labels. Each time it decreases, its performance improves. On the other hand, Fig. 17 shows the behaviour of the model during the validation stage. It is observed that the error decreases uniformly until time 107; from then on, there is no significant improvement, therefore which time has been considered optimal to adopt the adjustment weights of the CNN in the model.

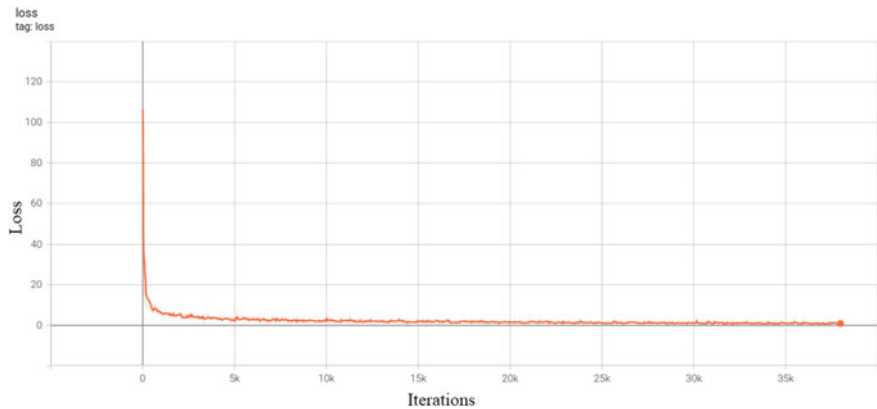


Fig. 16 Loss Training for 130 epochs (38 k Iterations). *Source Authors*

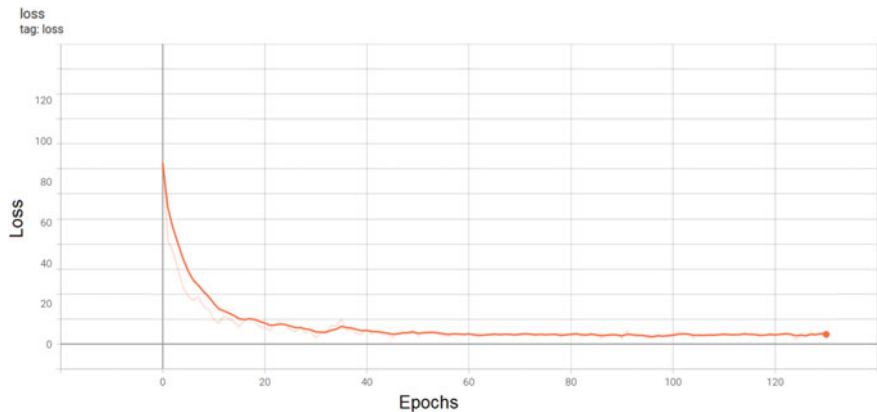


Fig. 17 Loss Validation Curve for 130 epochs. From epoch 107 on, the Loss value does not show a downward trend, therefore, at this time of training, the values for the model have been taken. *Source Authors*

Figure 18 shows the precision curve of our model, which increases as the training time continues. Figure 19 shows the validation of the network model after the end of each epoch. The curve shows that around epoch 107, there is no longer a significant improvement in the training result, so that It has been considered the best option to adjust the weights of the network based on those obtained at that time.

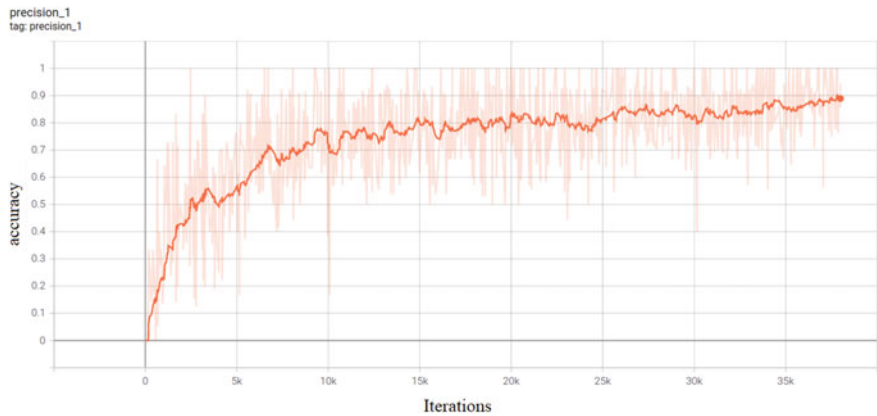


Fig. 18 Accuracy Training for 130 epochs (38 k Iterations). *Source Authors*

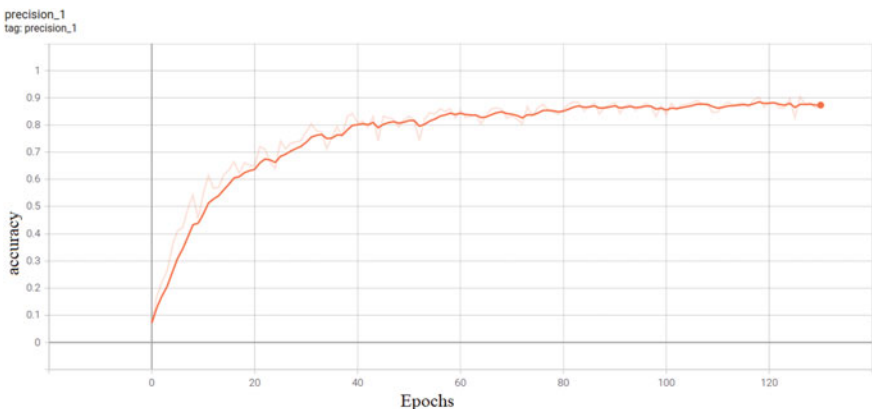


Fig. 19 Accuracy Validation Curve for 130 epochs. From epoch 107 on, the precision value does not show a growth trend, therefore, at this time of training, the values for the model have been taken. *Source Authors*

3.6 System Requirements for Execution

The following parameters are required To carry out the automatic mapping in order to be established in such a way that the error is minimized when generating local maps, and the global map, the requirements established based on experimentation are shown below:

3.6.1 Robot Mobility

The Table 1 describes the linear and angular velocity, and the angle of rotation in which the robot was moving

The minimum rotation angle of the robot is 30 degrees. In the Fig. 20 shown the acquisition of images from the thermal camera while the robot rotates.

Table 1 Robot mobility

Turning angle	Angular velocity (rad/sec)	Linear velocity (ms)
30	0.15	0.2

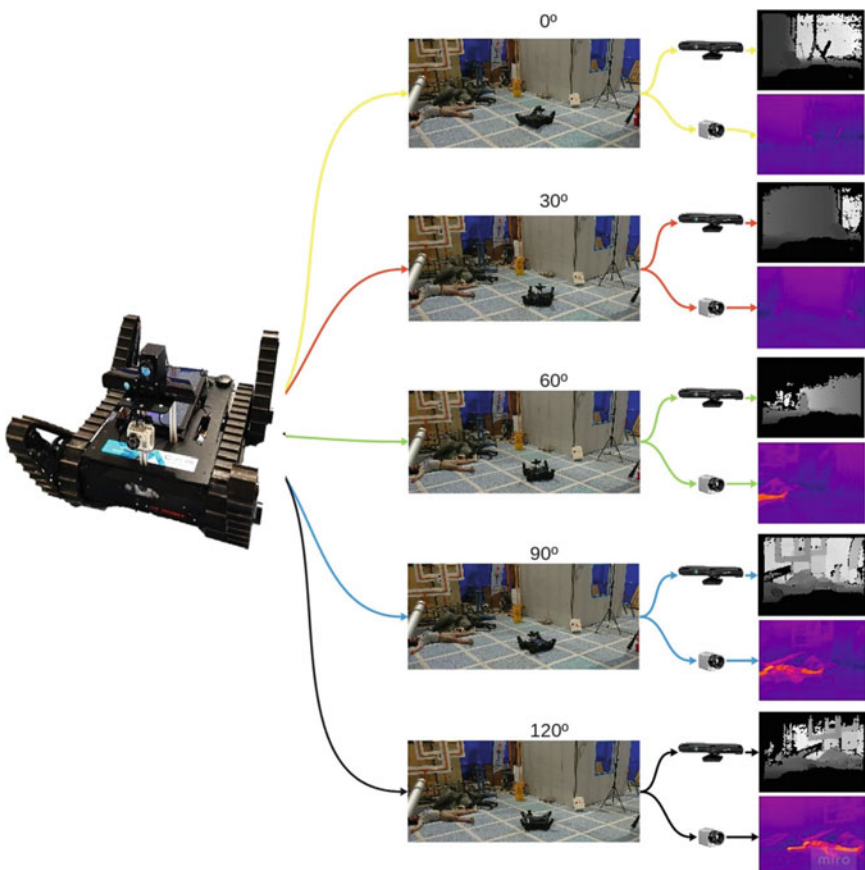


Fig. 20 Robot rotation to capture depth images and thermal images (CAR Arena)

3.6.2 Image Acquisition

The acquisition of depth images have certain limitations:

- Shooting speed
- Image loss
- Variation of images in different positions

The images were taken every second and it was normalized from 0 to 255, but due to the speed of image processing we have data loss in each image. The solution was to choose the best image for each position and process it to do the job.

4 Autonomous 3D Thermal Mapping and Victims Identification

4.1 Point Clouds Acquisition and Processing

The generation of Point Clouds is given through the open3d [32] library, with the intrinsic parameters obtained from the calibration of the thermal camera, the depth image of the Kinect v1 and the rectified image of the thermal camera.

Figure 21 shows the process of creation and processing of the Point Cloud. The basis is the rectified thermal image, the depth image, and the intrinsic parameters of the thermal camera.

Below we detail the steps in the Fig. 21:

1. Create from RGBD image:

The library to use is `open3d.geometry.RGBDImage.create.from.color.and.depth`, whose inputs are (depth image and thermal image)

2. Create from Point Cloud

The library to use is `o3d.camera.PinholeCameraIntrinsic`, whose inputs are (RGBD image and the internal parameters of the camera (fundamental matrix obtained from stereo calibration))

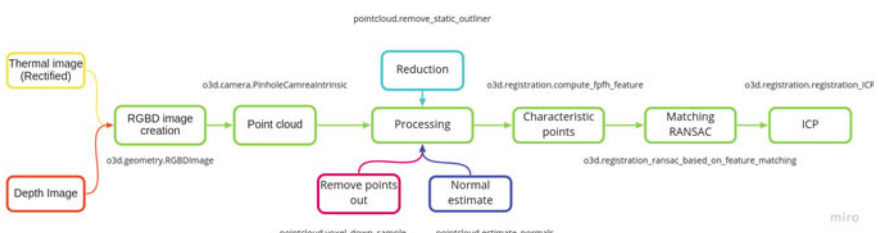


Fig. 21 Point cloud creation and processing

The steps above refer to the creation of the Point Cloud.
Next, we are going to detail the processing of these clouds and the process for ICP.

1. Remove points:

This process is to remove the points outside the Point Cloud using the point-cloud.remove.statical.outliner library, whose entries are (selection of close neighbors and a minimum radius)

2. Point Cloud reduction:

We reduce the Point Cloud to handle clouds of the same size, with point-cloud.voxel.down.sample with the input (the value to reduce the Point Cloud)

3. Estimation of normals:

We need to estimate the normals to obtain the characteristic points of each Point Cloud, for this, we use pointcloud.estimate.normals with the following inputs (the method to use in our case was

open3d.geometry.KDTreeSearchParamhhibrid (with which we name the search radius and the maximum number of neighbors to search))

4. Characteristic points:

We use the characteristic points to match with the RANSAC method and we occupy the library open3d.registration.compute.fpfh.feature with the inputs (Point Cloud, search radius and maximum neighbors)

5. Characteristic point matching:

For the matching of the characteristic points of two Point Clouds we use the RANSAC method for this we use the library

open3d.registration.registration.ransac.based.on.feature.matching with the following entries:

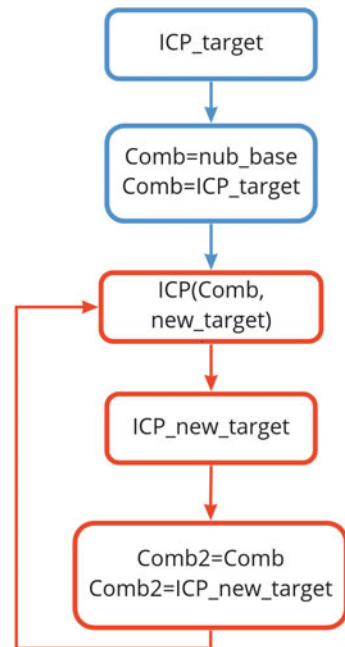
- Cloudbase.voxel.down reduced base cloud
- Cloudbase.fpfh base cloud feature points
- Nubetarget.voxel.down reduced target cloud or second cloud
- Cloudtarget.fpfh characteristic points of target cloud
- Threshold maximum distance between clouds
- Estimation method
- Fit.ransac
- Matching criteria (maximum.iteration and maximum.validation)

6. ICP:

We do the ICP with the open3d.registration.registration.ICP library with the following input parameters

- Base cloud
- Cloud to which we attach
- Threshold range of motion threshold
- Matrix resulting from pairing of characteristic points
- Type of estimate (PointtoPoint, PointtoPlane)

Fig. 22 Point Clouds concatenation



Point Clouds Concatenation

Figure 22 shows the Point Cloud concatenation process, which we describe below.

1. Once the ICP matrix is obtained, we apply transformation to the target cloud (`target.transformation`)
2. Store the new target points with ICP and the base cloud
3. Apply the previous steps for the processing of the new Comb Point Cloud and apply ICP between the Comb cloud and the new target
4. Apply the transformation matrix to the new target
5. Store the Comb cloud and transformed `new.target` in a new matrix, the process is repeated until the last Point Cloud to be obtained.

Figure 23 shows the integration of a depth image with a thermal image, by means of the open3d libraries.

4.2 Victims Detection

Figure 24 shows the detection of victims in exteriors is observed, with a precision of 90%.

Figure 25 shows a series of thermal images on the left and RGB images on the right, thus seeing the difference between RGB and thermal images. Thermal images have implemented the neural network for victim identification.

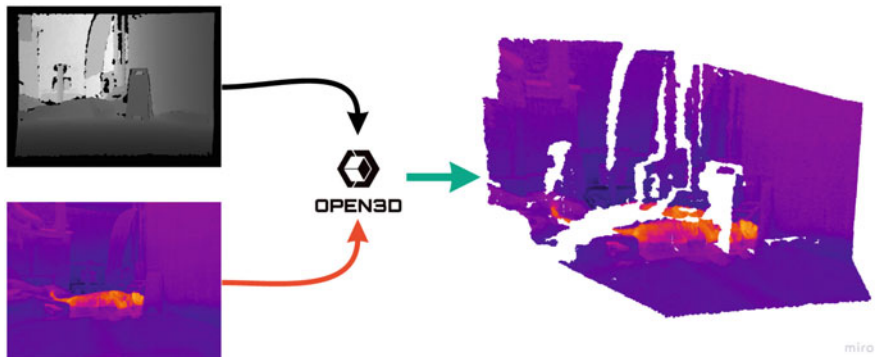


Fig. 23 Integration of thermal and depth image, to generate a Local 3d thermal map (Rob-Cib Lab)

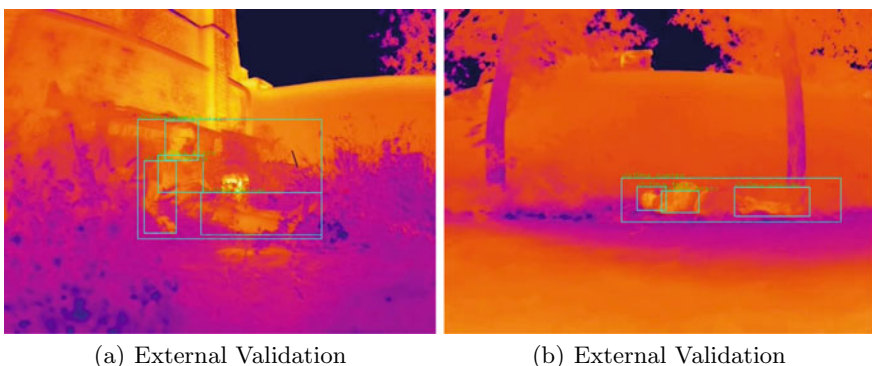


Fig. 24 External Validation

5 Results and Discussion

The proposed method has proven to be highly robust for the reconstruction of post-disaster environments and the provision of relevant information to rescuers during the execution of missions, thanks to cutting-edge techniques such as thermal image processing with neural networks. The main contributions lie above all in the provision of thermal information and location of the victim in the generated map, concerning conventional methods, which are limited to using RGB cameras for mapping or 3D reconstruction by laser.

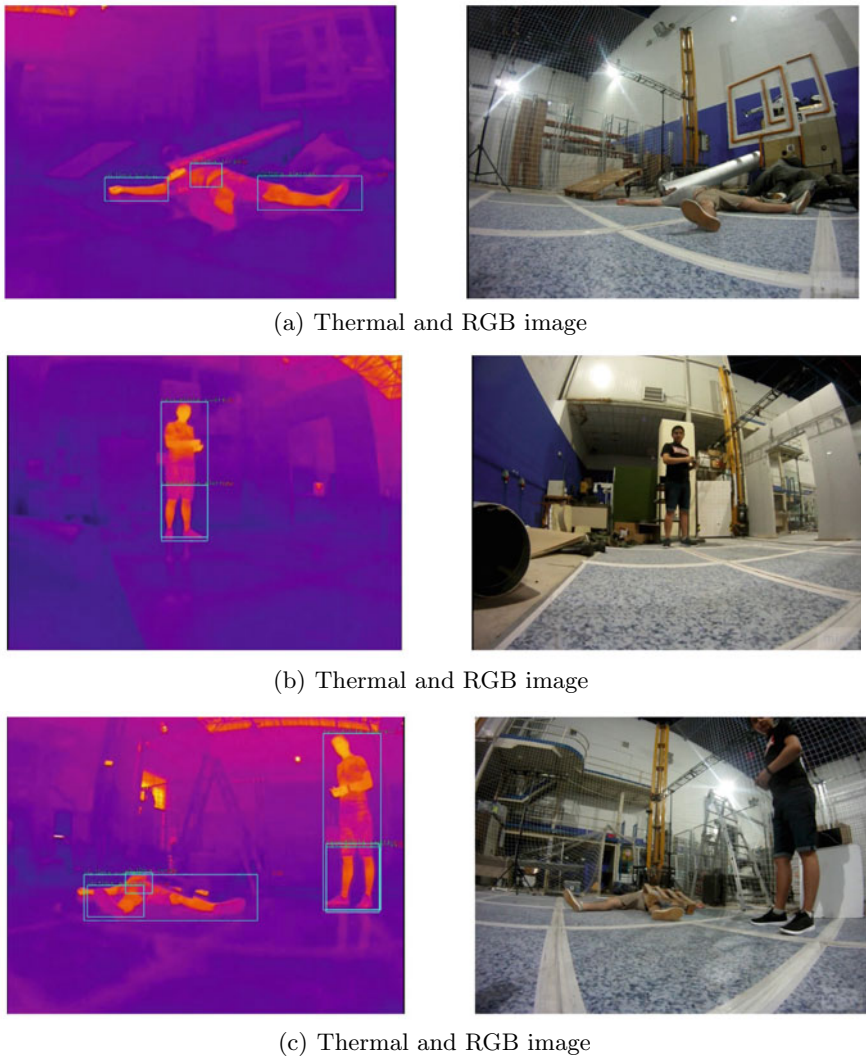


Fig. 25 Thermal and RGB image at different rotation angles of the robot

5.1 Victims Identification in Post-disaster Environments

Figure 26 shows the process carried out for generating a 3D map in the area of a corridor. Where there is a victim and a rescuer, the different views of the thermal map are shown. The subjects of interest are shown with a celestial mark; This information is very relevant to support the different brigades during a search and rescue

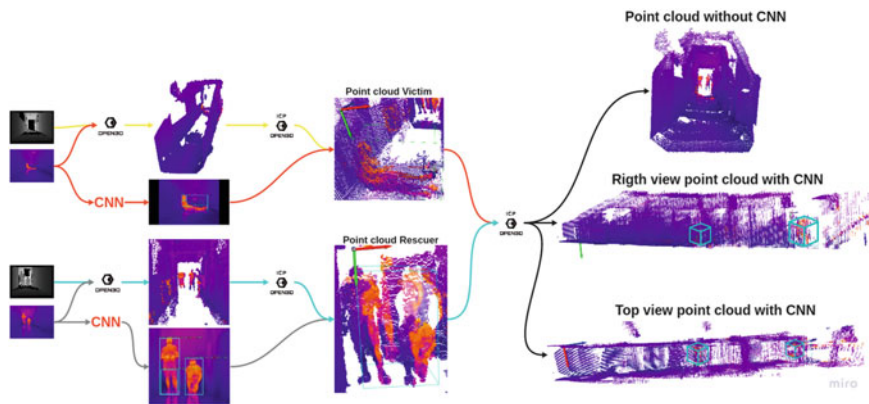


Fig. 26 Point cloud generation process in corridor

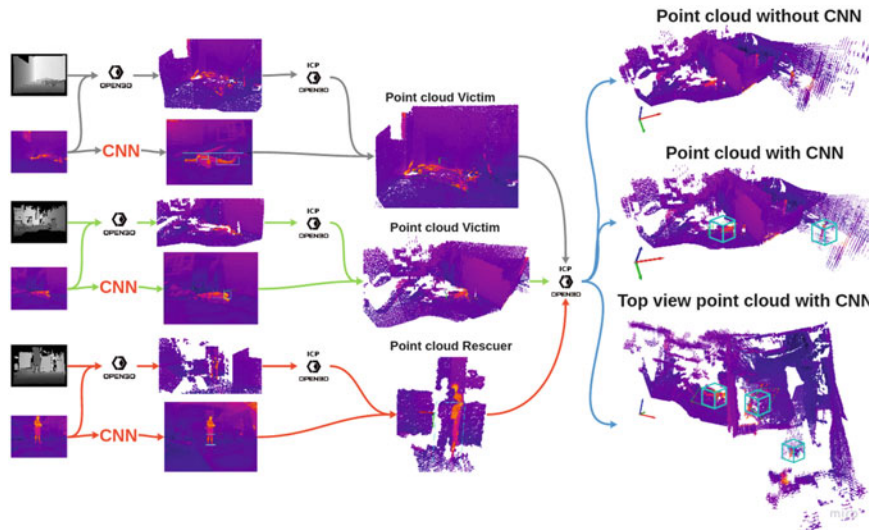


Fig. 27 Point Clouds generation process in CAR Arena

intervention. The approximate dimensions of the created point cloud are (2.01, 7.51, 2.17)[m].

Figure 27 shows the general and detailed process of the generation of the thermal map and the location of victims using the Convolutional Neural Network in the thermal images, in such a way that a marker can be placed in the map position. This information will serve the rescue teams to approach the different victims or areas directly and prioritize the time of each rescue.

Table 2 Ship total cloud data of CAR ARENA

Point cloud	Images	Points	% ICP	X, Y, Z (min, max)		
				$X_{*10}[m]$	$Y_{*10}[m]$	$Z_{*10}[m]$
1	2	432516	88.5	(-0.11567910, 0.31308051)	(-0.12189946, 0.04621907)	(0.04323747, 0.12711484)
2	3	609894	89.1	(-0.11567910, 0.31308051)	(-0.12189946, 0.04920207)	(0.02801179, 0.12711484)
3	4	846777	90.1	(-0.11567910, 0.31308051)	(-0.12769378, 0.04920207)	(0.01406533, 0.12910332)
4	5	1072094	91.3	(-0.11567910, 0.31308051)	(-0.12769378, 0.05085112)	(0.01174412, 0.12950451)
5	6	1307255	88.6	(-0.11567910, 0.31308051)	(-0.12769378, 0.05085112)	(0.01174412, 0.12950451)
6	7	1511905	87.8	(-0.11567910, 0.31308051)	(-0.12769378, 0.05085112)	(0.00853401, 0.12950451)
7	8	1683523	90.5	(-0.11567910, 0.31308051)	(-0.12769378, 0.05085112)	(0.00853401, 0.129504513)
8	9	1924684	92.7	(-0.11567910, 0.31308051)	(-0.12769378, 0.05085112)	(0.00853401, 0.12950451)
9	10	2161782	93.5	(-0.11567910, 0.31308051)	(-0.12769378, 0.05085112)	(0.00853401, 0.12950451)
10	11	2401940	94.8	(-0.11567910, 0.40739381)	(-0.12769378, 0.05085112)	(0.00853401, 0.12950451)
11	12	2645056	90.1	(-0.11567910, 0.40739381)	(-0.12769378, 0.05085112)	(0.00853401, 0.21950451)
12	13	2865852	87.9	(-0.11567910, 0.40739381)	(-0.14489141, 0.05085112)	(0.00853401, 0.21950451)
13	14	3095092	86.6	(-0.11567910, 0.40739381)	(-0.14489141, 0.05085112)	(0.00853401, 0.21112295)
14	15	3338212	87.5	(-0.11567910, 0.40739381)	(-0.14489141, 0.05085112)	(0.00853401, 0.21421589)
15	16	3581818	89.6	(-0.11567910, 0.43033820)	(-0.14489141, 0.05085112)	(0.00853401, 0.215866660)
16	17	3747882	90.3	(-0.11567910, 0.45019200)	(-0.14489141, 0.05085112)	(0.00853401, 0.213586666)
17	18	3982299	87.3	(-0.11567910, 0.50247442)	(-0.14489141, 0.05085112)	(0.00853401, 0.21661679)
18	19	4226592	90.4	(-0.11567910, 0.53304231)	(-0.14489141, 0.05085112)	(0.00853401, 0.21661679)
19	20	4441642	91.5	(-0.11567910, 0.59267616)	(-0.14489141, 0.05085112)	(-0.01253458, 0.21661679)
20	21	4642145	93.4	(-0.11567910, 0.62411952)	(-0.15411624, 0.05085112)	(-0.01867867, 0.21661679)
21	22	4813992	89.7	(-0.11567910, 0.66031938)	(-0.15411624, 0.05085112)	(-0.02061485, 0.21661679)

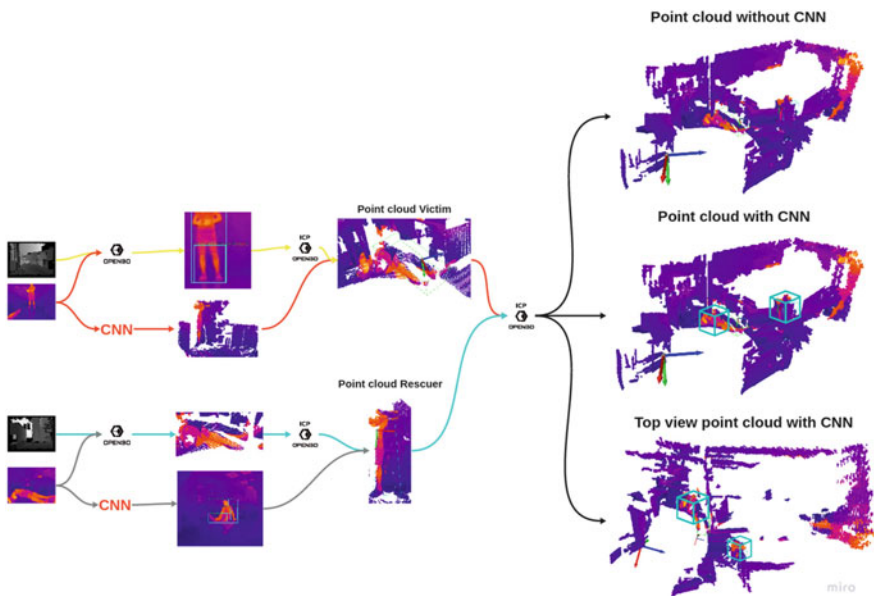


Fig. 28 Rob-Cib laboratory cloud generation process

The Fig. 27 shows the location of 2 victims in different positions and a rescuer. The map varies in terms of obtaining depth images since said Kinect sensor does not work properly outdoors.

The Table 2 describes the results in each T-LPC captured to form the T-GPC of Fig. 27, the percentage of ICP between each Point Cloud (Fig. 27) and the minimum and maximum distances of the X, Y, Z coordinates [meters] of each concatenation of Point Clouds. The first Point Cloud is the first ICP of two initial points.

Figure 28 shows the Rob-Cib laboratory on the first floor in which a victim and a rescuer are located in it, such an environment similar to the yellow sand of the Robo-Cup competition both due to its limited space and location.

Table 3 describes the results of the different T-LPCs captured to form the T-GPC of the Fig. 28, the percentage of ICP between each Point Cloud and the minimum and maximum of the X, Y, Z coordinates [meters] of each concatenation of Point Clouds, the first Point Cloud is the first ICP of two new initial points.

Table 3 Rob-Cib laboratory total cloud data

Point cloud	Images	Points	% ICP	X, Y, Z (min, max)		
				$X_{*10}[m]$	$Y_{*10}[m]$	$Z_{*10}[m]$
1	2	385868	85.74	(-0.22578875, 0.04596534)	(-0.10453029, 0.052261363)	(0.03945444, 0.21503266)
2	3	586889	92.1	(-0.2826026082, 0.04596534743)	(-0.1122396439, 0.05226136371)	(0.02035032, 0.21503266)
3	4	794060	90.2	(-0.2826026082, 0.0459653474)	(-0.11223964, 0.05437704)	(-0.043887581, 0.215032690)
4	5	1015257	93.5	(-0.282602608, 0.0459653474)	(-0.112239643, 0.054377041)	(-0.010153032, 0.215032690)
5	6	1218043	92.6	(-0.282602608, 0.045965347)	(-0.112239643, 0.054377041)	(-0.012963907, 0.21503269)
6	7	1431371	94.3	(-0.2826026082, 0.04596534743)	(-0.1122396439, 0.0543770417)	(-0.0129639074, 0.21503269)
7	8	1638043	95.4	(-0.282602608, 0.0459653474)	(-0.112239643, 0.054377041)	(-0.01351100, 0.21503269)
8	9	1846780	90.1	(-0.282602608, 0.0459653474)	(-0.112239643, 0.054377041)	(-0.01351100, 0.21503269)
9	10	2069730	94.6	(-0.282602608, 0.0527163445)	(-0.112239643, 0.054377041)	(-0.01351100, 0.21503269)
10	11	2264878	89.6	(-0.282602608, 0.0527163445)	(-0.112239643, 0.054377041)	(-0.01351100, 0.21503269)
11	12	2250620	87.4	(-0.282602608, 0.069837734)	(-0.112239643, 0.054377041)	(-0.01351100, 0.21503269)
12	13	2416492	93.2	(-0.282602608, 0.081097111)	(-0.112239643, 0.054377041)	(-0.01351100, 0.21503269)
13	14	2624830	95.4	(-0.282602608, 0.084412157)	(-0.112239643, 0.054377041)	(-0.01351100, 0.21503269)

6 Conclusion and Future Work

- An algorithm for automatic generation of 3D thermal maps and victim location was developed and implemented after analysis with Convolutional Neural Networks. Data was collected tele-operating a robot in the field, from a remote station in a post-disaster environment.
- The main aspects for the automatic 3D Point Cloud generation consider were the data collection (images), the normalization of depth images, the rectification of thermal images, and the thermal camera's intrinsic parameters obtained from the calibration of said camera.
- The Point Cloud processing started from the refinement of the same and the elimination of points outside a specific range (80 neighbors in a radius of 4), from we find the characteristic points of each new cloud and perform matching by the

RANSAC method. The previous process is called the registry of global variables, the result of this process is the rotation and translation matrix of each Point Cloud, which we apply to the ICP, and we obtain the integration of the Point Clouds.

- The training of the CNN neural network was given from creating an environment similar to the yellow and red zone of the Robo-Cup competition, which the NIST standardizes. In these environments, we acquired the images to create the data-set for the Point Cloud training. The accuracy of the network training was 98%, while in the validation, accuracies higher than 90% were obtained.
- The project's main objective was the location of victims in 3d disaster environments, for which the objective was fulfilled, but the limitations of the Kinect sensor, as it does not work in outdoor environments, give rise to proposing another type of sensor for the acquisition of images. Deep. Another alternative to generating Point Clouds would be to use 3d sensors such as lidar, Velodyne, Etc.
- Future works to continue the project's development are the localization of victims in disaster environments through deep learning with 3D laser sensors such as Lidar Velodyne, to contrast the proposed method.
- A next stage is proposed where the exploration of the robot in the unknown environment is developed autonomously. In this first approach, the problem has been addressed in an assisted way, where an operator in a remote area guides the robot through the environment, collecting information.

Acknowledgements This research has been possible thanks to the financing of Rob^oCity2030-DIH-CM, Madrid Robotics Digital Innovation Hub, S2018/NMT-4331, funded by “Programas de Actividades I+D en la Comunidad Madrid” and cofunded by Structural Funds of the EU and TASAR (Team of Advanced Search And Rescue Robots), funded by “Proyectos de I+D+i del Ministerio de Ciencia, Innovacion y Universidades”

References

1. Jaco, A., Messina, E., Weiss, B.A., Tadokoro, S., Nakagawa, Y.: Test arenas and performance metrics for urban search and rescue robots. In: Proceedings 2003 IEEE/RSJ International Conference on Intelligent Robots and Systems (IROS 2003) (Cat. No. 03CH37453), vol. 4, pp. 3396–3403 (2003)
2. Doulamis, N., Agrafiotis, P., Athanasiou, G., Amditis, A.: Human object detection using very low resolution thermal cameras for urban search and rescue. In: Proceedings of the 10th International Conference on PErvasive Technologies Related to Assistive Environments, pp. 311–318. Association for Computing Machinery, Island of Rhodes, Greece (2017). ISBN: 9781450352277. <https://doi.org/10.1145/3056540.3076201>
3. Portmann, J., Lynen, S., Chli, M., Siegwart, R.: People detection and tracking from aerial thermal views. In: 2014 IEEE International Conference on Robotics and Automation (ICRA), pp. 1794–1800 (2014)
4. Rodin, C.D., et al.: Object classification in thermal images using convolutional neural networks for search and rescue missions with unmanned aerial systems. In: 2018 International Joint Conference on Neural Networks (IJCNN), pp. 1–8 (2018)
5. Cruz Ulloa, C., Prieto Sánchez, G., Barrientos, A., Del Cerro, J.: Autonomous thermal vision robotic system for victims recognition in search and rescue missions. Sensors **21**, 7346 (2021)

6. Turgut, K., Kaleci, B.: A PointNet application for semantic classification of ramps in search and rescue arenas. *Int. J. Intell. Syst. Appl. Eng.* **7**, 159–165 (2019)
7. Colas, F., Mahesh, S., Pomerleau, F., Liu, M., Siegwart, R.: 3D path planning and execution for search and rescue ground robots. In: 2013 IEEE/RSJ International Conference on Intelligent Robots and Systems, pp. 722–727 (2013)
8. Lauterbach, H.A., et al.: The Eins3D project — instantaneous UAV-based 3D mapping for search and rescue applications. In: 2019 IEEE International Symposium on Safety, Security, and Rescue Robotics (SSRR), pp. 1–6 (2019)
9. Cruz Ulloa, C., Krus, A., Barrientos, A., Del Cerro, J., Valero, C.: Robotic fertilisation using localisation systems based on point clouds in strip-cropping fields. *Agronomy* **11**, 11 (2021)
10. Park, J., Chen, J., Cho, Y.K., Kang, D.Y., Son, B.J.: CNN-based person detection using infrared images for night-time intrusion warning systems. *Sensors* **20**, 34 (2020)
11. Königs, A., Schulz, D.: Evaluation of thermal imaging for people detection in outdoor scenarios. In: 2012 IEEE International Symposium on Safety, Security, and Rescue Robotics (SSRR), pp. 1–6 (2012)
12. Krišto, M., Ivasic-Kos, M., Pobar, M.: Thermal object detection in difficult weather conditions using YOLO. *IEEE Access* (2020)
13. Cerutti, G., Prasad, R., Farella, E.: Convolutional neural network on embedded platform for people presence detection in low resolution thermal images. In: ICASSP 2019-2019 IEEE International Conference on Acoustics, Speech and Signal Processing (ICASSP) (2019)
14. Gomez, A., Conti, F., Benini, L.: Thermal image-based CNN's for ultralow power people recognition. In: Proceedings of the 15th ACM International Conference on Computing Frontiers, pp. 326–331 (2018)
15. Cerutti, G., Milošević, B., Farella, E.: Outdoor people detection in low resolution thermal images. In: 2018 3rd International Conference on Smart and Sustainable Technologies (SpliTech) (2018)
16. Jiménez-Bravo, D.M., Mutombo, P.M., Braem, B., Marquez-Barja, J.M.: Applying faster R-CNN in extremely low-resolution thermal images for people detection. In: 2020 IEEE/ACM 24th International Symposium on Distributed Simulation and Real Time Applications (DS-RT), pp. 1–4 (2020)
17. Perdana, M.I., Risnumawan, A., Sulistijono, I.A.: Automatic aerial victim detection on low-cost thermal camera using convolutional neural network. In: 2020 International Symposium on Community-centric Systems (CCS), pp. 1–5 (2020)
18. Chen, L., Yao, X., Xu, P., Moon, S.K., Bi, G.: Rapid surface defect identification for additive manufacturing with in-situ point cloud processing and machine learning. *Virtual Phys. Prototyp.* **16**, 50–67 (2021)
19. Guo, M.-H., et al.: PCT: point cloud transformer. *Comput. Vis. Media* 187–199 (2021)
20. Rusu, R.B.: Semantic 3D Object Maps for Everyday Robot Manipulation. Springer, Berlin (2013)
21. Rase, W.-D.: In: True-3D in Cartography, pp. 119–134. Springer, Berlin (2011)
22. Mineo, C., Pierce, S.G., Summan, R.: Novel algorithms for 3D surface point cloud boundary detection and edge reconstruction. *J. Comput. Design Eng.* **6**, 81–91 (2019)
23. Li, P., Wang, R., Wang, Y., Tao, W.: Evaluation of the ICP algorithm in 3D point cloud registration. *IEEE Access* **8**, 68030–68048 (2020)
24. Scaramuzza, D., Zhang, Z.: Visual-inertial odometry of aerial robots (2019). [arXiv:1906.03289](https://arxiv.org/abs/1906.03289)
25. Borrmann, D., Afzal, H., Elseberg, J., Nüchter, A.: Mutual calibration for 3D thermal mapping. In: IFAC Proceedings Volumes 45. 10th IFAC Symposium on Robot Control, pp. 605–610 (2012). ISSN: 1474-6670. <https://www.sciencedirect.com/science/article/pii/S147466701633676X>
26. Adamopoulos, E., et al.: 3D thermal mapping of architectural heritage in digital heritage. In: Ioannides, M., Fink, E., Cantoni, L., Champion, E. (eds.) Progress in Cultural Heritage: Documentation, Preservation, and Protection, pp. 26–37. Springer International Publishing, Cham (2021). ISBN: 978-3-030-73043-7

27. Adamopoulos, E., Volinia, M., Girotto, M., Rinaudo, F.: Three-dimensional thermal mapping from IRT images for rapid architectural heritage NDT. *Buildings* **10** (2020). ISSN: 2075-5309. <https://www.mdpi.com/2075-5309/10/10/187>
28. Vidas, S., Moghadam, P., Bosse, M.: 3D thermal mapping of building interiors using an RGB-D and thermal camera. In: 2013 IEEE International Conference on Robotics and Automation, pp. 2311–2318 (2013)
29. Schönauer, C., Vonach, E., Gerstweiler, G., Kaufmann, H.: 3D building reconstruction and thermal mapping in fire brigade operations. In: Proceedings of the 4th Augmented Human International Conference. Association for Computing Machinery, Stuttgart, Germany (2013), pp. 202–205. ISBN: 9781450319041. <https://doi.org/10.1145/2459236.2459271>
30. Borrman, D., Elseberg, J., Nüchter, A.: In: Lee, S., Cho, H., Yoon, K.-J., Lee, J. (eds.) Intelligent Autonomous Systems 12: Volume 1 Proceedings of the 12th International Conference IAS-12, held June 26–29, 2012, Jeju Island, Korea, pp. 173–182. Springer, Berlin, Heidelberg (2013). ISBN: 978-3-642-33926-4. https://doi.org/10.1007/978-3-642-33926-4_16
31. Zhang, S., et al.: Optimized calibration method for ultra-field dual bands cameras based on thermal radiation checkerboard. *Infrared Phys. & Technol.* **108**, 103346 (2020)
32. Yang, J., Cao, Z., Zhang, Q.: A fast and robust local descriptor for 3D point cloud registration. *Inf. Sci.* **346**, 163–179 (2016)

Christyan Cruz Ulloa received the M.Sc degree Robotics and Automation from the Polytechnic University of Madrid in 2019, currently is Ph.D. candidate in Robotics and Automation in the same University from 2019. In 2018–2019 he was Professor of the Army Forces University form Ecuador. Currently, he is researcher of the Robotics and Cybernetics research group of the Centre for Automatic and Robotic in the Technical University of Madrid–Spanish National Research Council. His main research activities are in the field of ground robotics and specific sensors for artificial vision systems, focused on Search and Rescue Robotics (TASAR National Project) and Robotics in Precision Agriculture (SUVEREV European Project). He has participated in international conferences as expositor is also autor and co-author of different international scientific papers in journals and conferences (<https://orcid.org/0000-0003-2824-6611>). He has an active participation as a reviewer for different journals as Sensors, Drones and Revista Iberoamericana de Automática e Informática Industrial.

Guido Torres Llerena received the title of M.Sc Robotics and Automation at the Polytechnic University of Madrid in 2021. In 2020–2021 Research Assistant at the Center for Automation and Robotics of the Polytechnic University of Madrid. His research activities have been developed in the handling of robots and specifically, in the handling of artificial vision systems with ROS, his publications are related to the design of machines and automation.

Antonio Barrientos received the M.Sc Engineer degree by Automatic and Electronic from the Polytechnic University of Madrid in 1982, and the Ph.D. in Robotics from the same University in 1986. In 2002 he obtained de M.Sc Degree in Biomedical Engineering by Universidad Nacional de Educación a Distancia. Since 1988 he is Professor of robotics, computers and control engineering at the Polytechnic University of Madrid. He has worked for more than 30 years in robotics, developing industrial and service robots for different areas. Currently, he is the head of the Robotics and Cybernetics research group of the Centre for Automatic and Robotic in UPM-CSIC. The main interests of his research group are in the field robotics (ground and aerial), seeking its application in two areas: agriculture and security, search and rescue scenarios. He is author of several textbooks in Robotics and Manufacturing automation and has participated as coauthor in the white books about the state of robotics and manufacturing in Spain. He is also co-author of about 200 scientific papers in journals and conferences (<https://orcid.org/0000-0003-1691-3907>). He has been a reviewer for several journals and is an Editorial Board Member of the International Journal of Advanced Robotic Systems and of the Revista Iberoamericana de Automática e Informática

Industrial. Also, he is member of the Board of directors of the Comite Español de Automática a senior member of the IEEE.

Jaime Del Cerro received his M.S. degree in Industrial Engineering and his Ph.D. degree in Robotics and Automation from UPM (Spain) 2007. He currently teaches Control Basics, Robotics, System Programming and Guidance Navigation and Control of Autonomous Vehicles at the ETSII-UPM. He collaborated with the Universidad Internacional de la Rioja in the posgrade program of Designing and Management of Technological projects and Universidad Europea de Madrid for several years. His main research activities are related to robotics (ground and aerial) and multi-robot systems applied to security and agriculture. He has worked on several national and European R&D projects as Researcher.

Lab-Scale Smart Factory Implementation Using ROS



Marwan Abdelatti and Manbir Sodhi

Abstract The central concepts underlying Industry 4.0 are the inter-connectivity between smart machines, production equipment, storage systems, algorithms with autonomous data exchange, action triggers, and, autonomous process controls. The goal of Industry 4.0 is to improve monitoring and control of manufacturing processes and systems, leading to high-quality parts, lower inventory, and reduced throughput times. However, the limitations and incompatibilities of legacy systems present significant challenges for the introduction of Industry 4.0. This use case chapter describes the implementation of a fully functioning, lab-scale, Industry 4.0 smart factory to demonstrate how legacy systems can be upgraded without major infrastructure changes. Using existing and proven frameworks and protocols such as robot operating system (ROS), and telemetry transport protocol (MQTT), Industry 4.0 features can be introduced to legacy systems by adding a single layer of hardware. Additionally, a supervisory control and data acquisition (SCADA) system is integrated with the IIoT to monitor and control the entire system processes and to provide analytical reports from the collected data. By utilizing ROS, the system has standardized functionalities including unified high-speed communication, hardware interfacing, and multi-thread handling, to name a few. We present the `ft_industry4_raspi` ROS Melodic package that handles all the distributed nodes over the multiple controllers in the factory. The reconfigured system is upgraded to demonstrate Smart Manufacturing, Cybersecurity, and Cloud-based Manufacturing. This system can function as a testbed for evaluating Cybersecurity, Cyber-Physical Systems concepts, and new IIoT hardware and SCADA software, as well as for embedding a variety of operations control approaches.

Keywords Industry 4.0 · Internet of Things · ROS · SCADA · Smart factory · Embedded systems

M. Abdelatti (✉) · M. Sodhi

Department of Industrial Engineering, University of Rhode Island, Kingston, RI 02881, USA
e-mail: mabdelrazik@uri.edu

M. Sodhi
e-mail: sodhi@uri.edu

1 Introduction

The factory of the future, as conceptualized in Industry 4.0, is an integrated system where production machines, material handling systems, part input and output processes, and humans interact within a framework of distributed and centralized controls [1, 2]. Machines exchange parts and data autonomously and algorithms act on this data to control processes and part movements. The data also gives insight into the condition of machines, and maintenance is invoked in a predictive manner. Much of this data is generated by components of the Internet of Things (IoT) [3, 4]. One of the challenges in implementing an Industry 4.0 system is assembling a collection of heterogeneous devices in a common framework. Using the architecture of Robot Operating System (ROS), it is possible to integrate the communications of a variety of production devices. In this application, ROS has the advantage that many of the material handling devices such as robots and other material transfer devices such as AGVs may already have been set up to operate with ROS, facilitating their integration expeditiously.

Small-scale factories or simplified physical models have been commonly used in research involving operations research and maintenance. The main purpose of using such systems is to generate representative data for modeling and testing since it is difficult to get this data from industrial settings by disrupting production, and furthermore, when available, it is not publicly accessible [5]. This cyber-physical approach has many benefits over using a virtual model of a factory or machine since it allows training in real environments and allows replication of details related to industrial practice that can be difficult to simulate virtually [6]. Another advantage of using lab-scale implementations is that these can be built using low cost, non-industrial components. There are several platforms available nowadays including the Smart-LEGO Factory, the Fischertechnik plant model for Industry 4.0 [7] a Fischertechnik punching workstation [8], the Festo Learning Factory [9] to name a few.

There is an increasing interest in the use of small-scale factories, especially for exploring Industry 4.0 concepts. Andersen et al. [10] show how a learning factory can be used in an engineering course on reconfigurable manufacturing in a blended and problem-based learning approach. Nardello et al. [11] present an in-house developed learning factory to meet various manufacturing requirements and proving their value in a production environment. A mechanism of how a generic client can access data generated from a workstation has been demonstrated in [8]. Three application cases from business process management (BPM) have been used in [12] to address challenges in Industry 4.0 using DFKI Smart Lego Factory. A physical Fischertechnik factory model equipped with several sensors has been introduced in [5] as an approach for the generation of predictive maintenance data. The development of an ontology to represent a Fischertechnik manufacturing simulation model by reusing existing ontologies has been investigated in [13]. A fully automated factory prototype built out of LEGO bricks has been introduced in [14] to demonstrate artificial

intelligence applications in Industry 4.0. However, these all use proprietary software that makes the process of expanding the factory challenging.

In this chapter, we present a laboratory-scale smart factory that can be assembled with off-the-shelf components and IoT devices. The system has been created to give students a facility to learn about Industry 4.0 concepts without the expense, complexity and risk of working in life-scale installations. Another intended use of this system is as a sand-box for testing different frameworks, such as ROS, with a variety of Manufacturing Execution Systems (MESs) to detect performance issues at low expense. A video showing the system in action can be viewed at: <https://youtu.be/mH5jlzI3Shw>. Our contributions in this work can be listed in the following aspects:

- We introduce the “University of Rhode Island Lab-scale Factory for Industry 4.0 Kit” (i.e., URILF4.0 for short) as an open-source system for manufacturing research. All proprietary interconnections including hardware, software, and protocols have been replaced by open-source components.
- We develop the `ft_industry4_raspi` ROS package to handle the industrial processes of the factory. This will give the learners the opportunity to get practical training on ROS for industrial applications.
- We efficiently developed a SCADA system to monitor and control industrial processes by mapping between MQTT and ROS topics.

This chapter is organized as follows, a detailed description of the factory kit is provided in Sect. 2 where various functioning modes are explained with diagrams and flowcharts. Section 4 discusses the proposed ROS package and details its key files and environment configurations, and other software architecture. The `ft_industry4_raspi` system is tested in Sect. 6. Section 5 discusses the SCADA system concept and the use of the bridge package to map between ROS and MQTT topics. Section 7 concludes this work with some remarks on possible future developments.

2 The Smart Factory Kit

The URILF4.0 is a physical simulation of a “smart factory” designed to familiarize students with Industry 4.0 concepts and to serve as a test-bed for exploration and experimentation. The current configuration uses the basic modules purchased from FischerTechnik as part of the Industry 4.0 Learning Factory, but all proprietary interconnections including hardware, software and protocols have been replaced by open components. URILF4.0 simulates the storing of raw materials, as well as product manufacturing and delivery according to the orders placed by customers. Figure 1 shows the different components of the kit, it consists of factory modules like automatic storage and retrieval station (ASRS), vacuum gripper robot (VGR), high-bay warehouse (HBW), multi-processing station with kiln (MPS), and a sorting line with color detection (SLD).

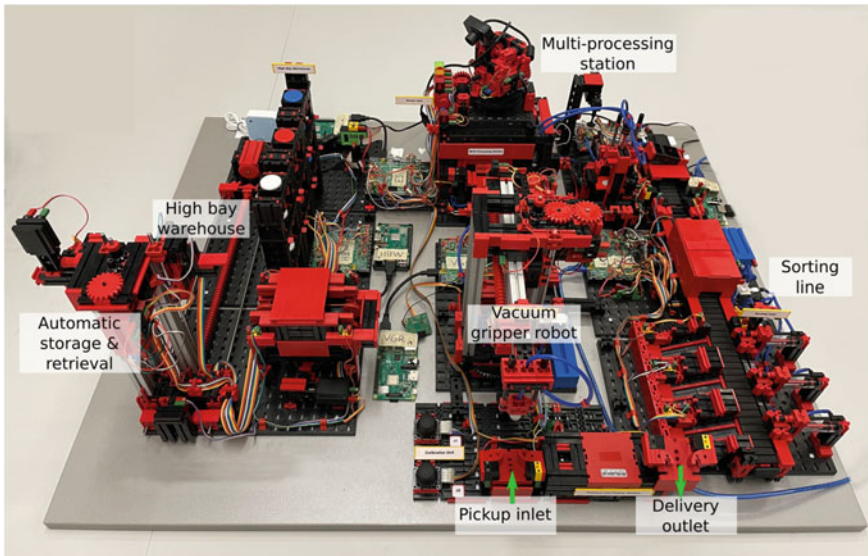
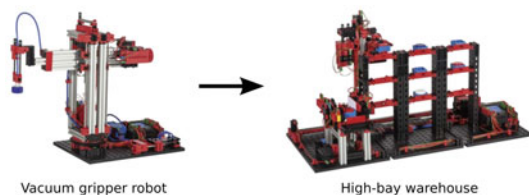


Fig. 1 The smart factory kit

Fig. 2 New material process flow



URILF4.0 supports two main processes: (i) Storing new (incoming) materials. When a part arrives at the pickup location, the VGR picks it and transports it to the ASRS. The ASRS checks for the first free location in the HBW and places the material accordingly. This is shown in Fig. 2. (ii) Processing new orders, as documented by Fig. 3. This process is activated by receiving an order from the SCADA system representing a customer request. The customer may request a part with one of three colors: red, white, or blue within a unique processing sequence. The ASRS checks for the first available material location in the HBW and moves to it then places the part where the VGR can pick it and transport it to the MPS. The material moves through the MPS and passes along a conveyor belt to the sorting line where it is processed according to its color. Finally, the VGR picks up the finished product and places it into the delivery outlet where it is ready for customer pick up. The discussion below details the functionalities of each unit component in the kit:

High-Bay Warehouse As shown in the flowchart in Fig. 4, there are two different processes associated with the HBW, namely, new material reception and new order processing. With regards to new material reception, an inventory piece is moved from

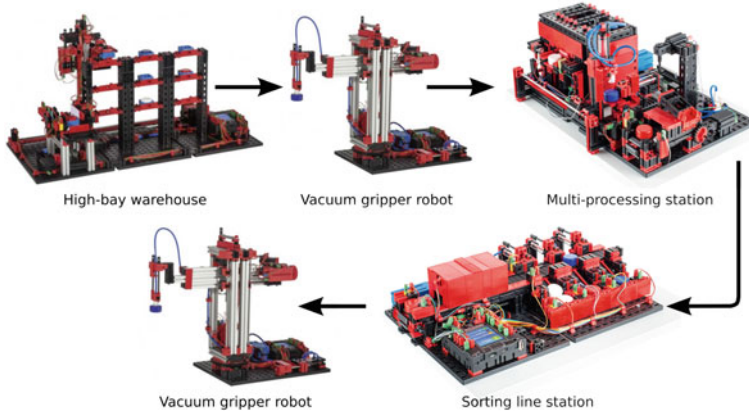


Fig. 3 New order process flow

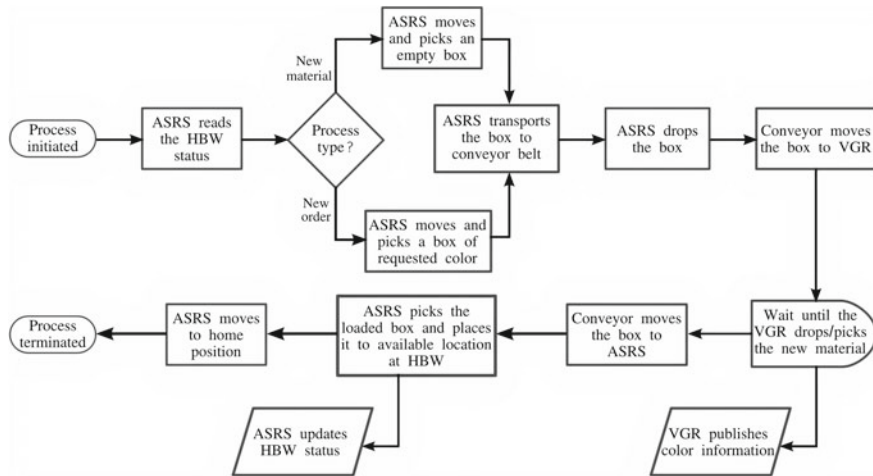


Fig. 4 The HBW flowchart

the vacuum gripper robot (VGR) into storage, whereas in the new order process an inventory piece is moved out of storage and back to the custody of the vacuum gripper robot. It is worth mentioning that the high-bay warehouse (HBW) communicates both location and inventory color information for access by both the SCADA and the VGR as will be detailed in the ROS section of this chapter.

Vacuum Gripper Robot The vacuum gripper robot (VGR) is equipped with a suction end to pick and move materials. The role of the VGR is to transport the materials between the different stations and can reach any station in the system. Figure 5 shows the flowchart for the actions performed by the VGR for the two main processes in the system. When a new part arrives at the pickup inlet, the photosensor sends a

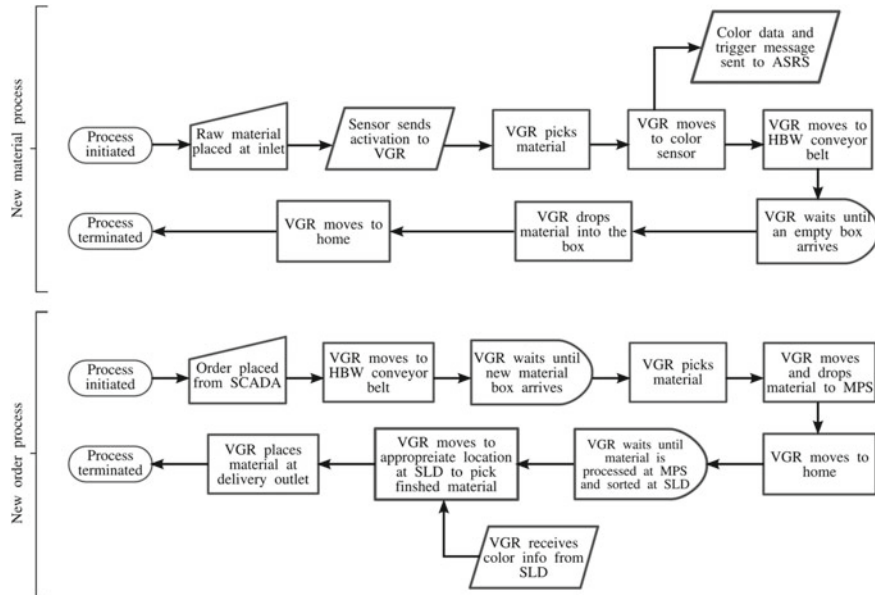


Fig. 5 The VGR flowchart

triggering flag to the VGR to initiate a pickup and subsequent placement at the color detection unit where the color data is created and published along with a triggering flag to the ASRS. The ASRS in turn reads HBW status then moves and picks up an empty box which is transported to the HBW conveyor belt to the VGR dropping side. Meanwhile, the VGR moves the material towards the HBW conveyor belt and waits for the arrival of the empty box where the VGR drops it.

The second process, which defines how parts are processed in the system, starts by placing a new order through the SCADA system. The customer can indicate the part color and the number of parts desired. The VGR moves to the HBW conveyor while the ASRS moves to the appropriate location at the HBW to pick a material and place it on the conveyor belt. The VGR then picks the material and transports it to the multi-processing station (MPS). The VGR waits at its home location until the material processing is completed and the sorting line (SLD) moves the material to its pickup location based on its color. Finally, the VGR picks the material from SLD to its delivery outlet.

Multi-Processing Station The Multi-Processing Station (MPS) includes multiple processing units like klin, and a milling machine. These units communicate through I2C protocol to simulate a legacy system. Various conveying techniques are used such as a conveyor belt, a turntable, and a vacuum suction gripper.

Sorting Line Station The sorting line (SLD) is responsible for sorting the completed parts by color. Its function lies in the new order process only where it is the last station before the finished product is picked up by the (VGR) and marked as ready

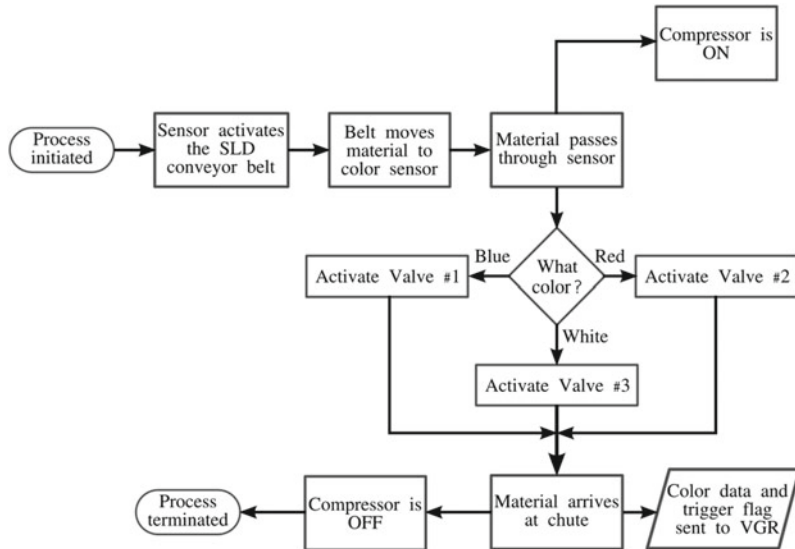


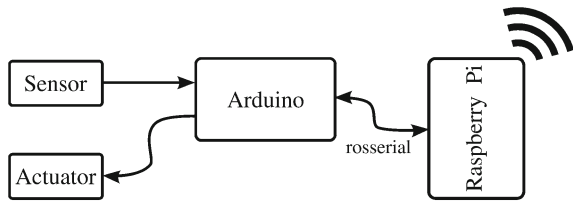
Fig. 6 The SLD flowchart

for delivery. The flowchart in Fig. 6 illustrates the SLD process which is activated once a finished material is dropped from the MPS station. A conveyor belt moves the material to a color detecting unit then one of three pneumatic valves is activated, according to the detected color, moving the processed part onto the corresponding chute. A trigger signal accompanied by the color is published to activate the VGR to transport the finished piece to the delivery outlet.

3 Legacy System Upgrade

The original Industry 4.0 kit is available from Fischertechnik company with multiple options such as basic running voltages of 9v or 24v, proprietary TXT control units or PLCs etc. Technical details about their product and the different purchasing options are available on their website: <https://www.fischertechnik.de/en/products/simulating/training-models>. The base kit used in this project is the 9v kit with TXT controllers. It was delivered pre-assembled and was equipped with proprietary controllers, and software accessible through the company's website. To increase the flexibility and to support expansion of the system using hardware from different suppliers without compatibility issues, the controllers were replaced by open-source models. We chose Arduinos and Raspberry Pis because of the large established user community, relatively low cost components, and free and broad ranges of libraries of codes. Furthermore, there is increasing interest in using ruggedized versions of these controllers in factory settings. Since the original system utilizes separate controllers

Fig. 7 Rosserial between Arduino and Raspberry Pi



for each processing unit, we follow the same principle in our upgrade and expand it into a distributed system that can: (1) provide the system with reliability and high fault tolerance so that a crash on one unit does not affect the others; (2) enable a scalability level so that more machines can be added in the future with a flexibility to install, implement and debug new services; and (3) reduce the computational load if central PCs are used.

To further support the open-source idea and facilitate reproducibility of the proposed system, ROS is adopted as the basic integration tool. Along with being general and new parts can be added easily in the system, ROS can be implemented with sparse storage and computational resources which makes it suitable for use on embedded computers. Additionally, there is a large library of community developed packages. For example, instead of writing an exclusive master-slave program to interface between the Raspberry Pi's and Arduino boards in our system, the `rosserial` package is used for the task, which reduces development and maintenance effort. Moreover, ROS is language agnostic which means that the system can run with parts of codes written in different languages, increasing the scalability of the system.

In order to support the idea of adding a single layer of software and hardware to the pre-built legacy system, the SCADA software interface was retained in its original condition without altering the communication protocol supporting it. This reduces the modifications needed to the original system. Since the SCADA software being used in the system uses the MQTT protocol and does not support ROS messaging, the ROS bridge package is used to map between the two protocols as explained in the sequel. MQTT itself was not utilized to interface to the embedded computers or in the sensor/actuator layer for the same reasons as discussed above. As illustrated by Fig. 7, the Arduino controller is used to perform low-level control such as reading inputs from sensors and sending outputs to motors and pneumatic valves, and handling I2C communication to other machine controllers. Whereas the Raspberry Pi takes care of the WiFi communication and integrates Arduino controllers in the network loop through USB connectivity and the `rosserial` package.

`rosserial` is a communication protocol to transfer data through a serial interface or network socket [15]. It's based on a client-server model where a `rosserial` service runs on a computer running ROS (the Raspberry Pi in our implementation) and a `rosserial` client on the Arduino side. Data is transferred in the form of ROS messages between them. `rosserial_client` package is available for sev-

eral microcontroller types including Arduino, STM32, Raspberry Pi to name a few. Rosserial packages are available for both Python or C++.

3.1 *ROS Components and Network*

Since our system mimics a real factory with multiple machines involved, the proposed ROS framework is based on a distributed package concept. ROS nodes are run on different machines and communicate over a network. Every machine is responsible for specific tasks, as explained earlier and, therefore, they respond to different ROS topics. The system has one PC functioning as a Human Machine Interface (HMI) with the SCADA system running on it.

Raspberry Pi 3 B+ boards were selected to handle the ROS communication between the local Arduino board as well as with the ROS core over WiFi. The 1.4 GHz processor, 1 GB RAM, and the installed Linux operating system (Ubuntu 18.04 server) were sufficient for this project. Four processing stations were interfaced to the Raspberry Pi's: three of them, called "unit Pis", take care of the ROS nodes of the factory units and necessary packages, and the fourth, called "main Pi", hosts the ROS core, MQTT server, and other configuration files necessary to the system. To be more specific, each unit Pi runs `rosserial_server` package to communicate with its Arduino board, and the proposed `ft_industry4_raspi` package to handle the factory tasks. In addition to these packages, the main Pi runs the ROS core, and the `mqtt_bridge` package to map between the ROS topics and the MQTT topics as detailed in the following sections as well as the Mosquitto MQTT server. The HMI PC has a SCADA software installed. The PC does not directly interact with ROS since the SCADA software supports MQTT rather than ROS, the mapping performed by the `mqtt_bridge` package installed on the main Pi is responsible for this PC interface.

The remainder of basic control operations that require direct physical link to sensors or actuator drivers like color detection, robot manipulation, and servo motor and solenoid control are performed on the Arduino boards. The board used is an Arduino-Leonardo compatible board called ftDuino. It has built in motor drivers, eight universal inputs that can be utilized for analog or digital readings, four counter inputs, and eight outputs in addition to I2C, and USB connections. More information about the board can be found in this link: <https://harbaum.github.io/ftduino/www/de/>. It fits perfectly into the Arduino ecosystem for handy development, as discussed in Sect. 3.2, but the lack of network connectivity in ftDuino was one of the motivators behind using Raspberry Pi as another board to grant network access. The communication network uses a router and all the devices are connected via WiFi. The formed network consists of one PC, four Raspberry Pis 3 B+, and six ftDinos. Every ftDuino is connected to one Raspberry Pi for ROS connectivity, the two additional ftDinos are for the local Multi-processing station that rely on sensor based detection and I2C master-slave communication for operation. The network components are detailed in the architecture given in Fig. 8 where the Raspberry Pis are connected

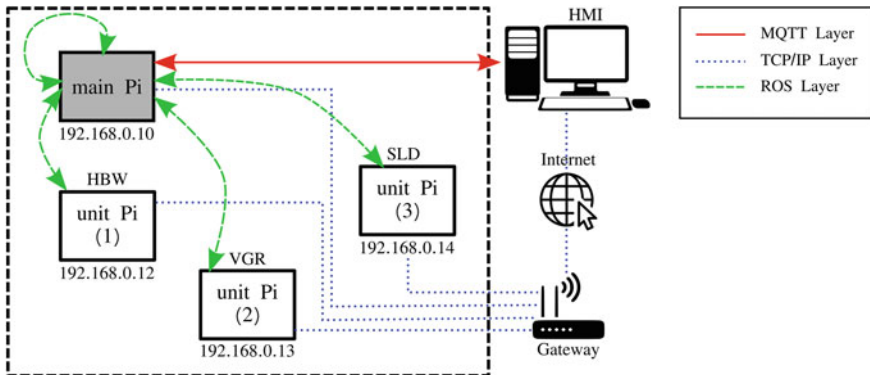


Fig. 8 Physical and logic layers in the system

to a WiFi router gateway with unique static IP addresses, the PC is remotely connected to the main Pi via internet. The main Pi functions as the ROS master that handles the communications between the factory components on one hand, and on the other hand acts like an MQTT broker that talks to the HMI PC to present data on the SCADA. The `mqtt_bridge` package on the main Pi simultaneously maps between the ROS messages and the MQTT messages in a bidirectional form. The MQTT communication is done through port 1883 since encrypted messages are not handled in this version of the system.

3.2 *ftDuino Integration into the Arduino IDE*

In order to access the ftDuino through the Arduino IDE, the following steps need to be followed: after connecting the ftDuino to the PC where the Arduino IDE is installed, the ftDuino board must be installed in the IDE. At the `File -> Preferences` menu, the following URL is added in the “Additional Boards Manager URLs:” field: https://harbaum.github.io/ftduino/package_ftduino_index.json. Then press “OK” as shown in the screenshot in Fig. 9.

Once the link is provided, the board package can be installed from the Boards Manager at `Tools -> Board: ... -> Boards Manager` as shown in Fig. 10. The ftDuino can now be selected by choosing ftDuino from `Tools -> Board: ... -> ftDuino Boards` as illustrated in Fig. 11. If the board is already connected to the PC, it can now be selected under `Tools -> Port` as in Fig. 12.

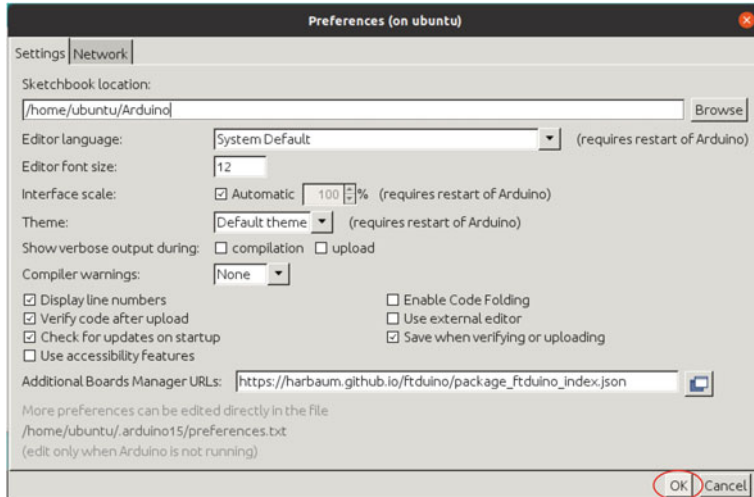


Fig. 9 Arduino IDE preferences

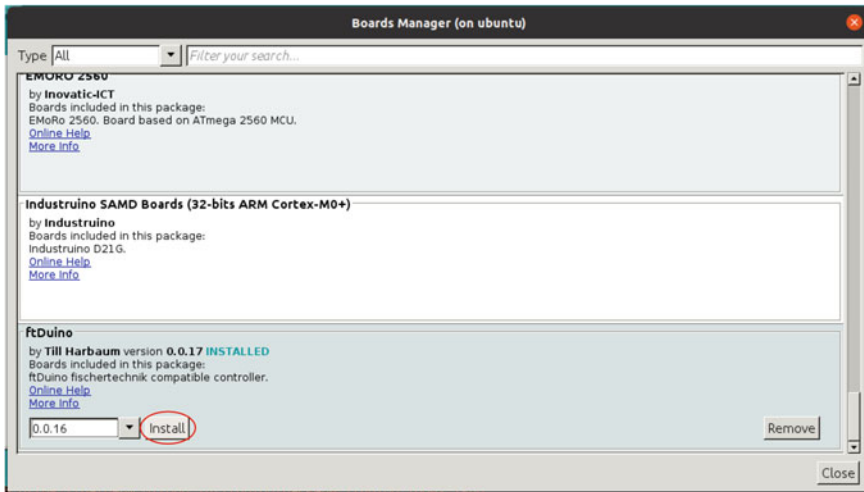


Fig. 10 Arduino IDE boards manager

4 ROS Environment Configuration

The ROS version used for this project is ROS Melodic on Ubuntu 18.04 server connected to four ROS machines that are running on a network with the same ROS master. All necessary files including the configuration, and the nodes as well as the launch files are available in the package repository in the following link:

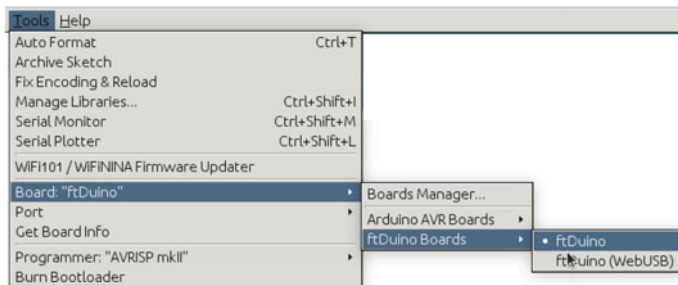
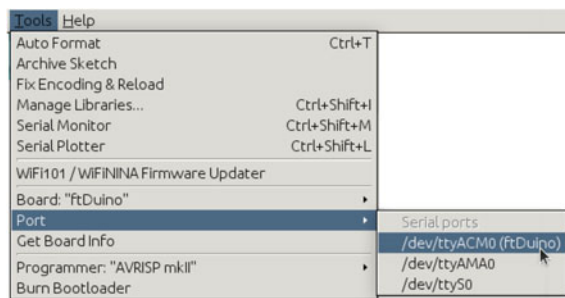


Fig. 11 Arduino IDE board selection

Fig. 12 Arduino IDE port selection



https://github.com/MarwanAbdelatti/ft_industry4_raspi

The package should be cloned inside the `src` folder in the `catkin_ws` workspace. The `src` folder inside the package includes five folders for the four system machines as well as the “main Pi”. Some of the key files inside this package are discussed below:

- Every unit Pi has a shell file to configure its launch processes and remote environment, namely, `env_hbw.sh`, `env_vgr.sh`, and `env_sld.sh`. The code below shows an example of these files:

```

1 #!/bin/bash
2
3 export ROS_MASTER_URI=http://192.168.0.10:11311
4 export ROS_HOSTNAME=192.168.0.12
5
6 source /opt/ros/melodic/setup.bash
7 source /home/ubuntu/catkin_ws/devel/setup.bash
8
9 exec "$@"

```

where the ROS master remote IP is defined in line 3 followed by the local host IP definition. The environment is configured in lines 6 and 7.

- `src/main/industry4.launch`: is the main launch file that initiates the nodes and sub-launch files for the system. The file can be divided into two parts: (1) the machine declaration, where the parameters of the “main Pi” and every “unit Pi” are defined; and (2) the node declaration, where every node required to run on the system is defined. The following code shows part of the file:

```

1 <launch>
2 <!-- Declaring Machines -->
3   <group>
4     <machine
5       name="main"
6       address="192.168.0.10"
7       env-loader="/home/ubuntu/catkin_ws/devel/setup.bash"
8       default="true"
9       user="ubuntu"
10      password="RandomPassword">
11    </machine>
12
13    <!-- Include Files -->
14    <include file="$(find ft_industry4_raspi)/src/main/
15      ft_industry4_params.launch" />
16  </group>
17
18  <machine
19    name="hbw"
20    address="192.168.0.12"
21    env-loader="/home/ubuntu/env_hbw.sh"
22    ....
23  </machine>
24
25  <!-- Declaring Nodes -->
26
27  <node machine="main" pkg="ft_industry4_raspi" name="
28    status_update" type="status_update.py">
29    <param name="port" value="/dev/ttyACM0"/>
30    <param name="baud" value="57600"/>
31  </node>
32
33  <node machine="hbw" pkg="rosserial_python" name="hbw_node"
34    type="serial_node.py">
35    <param name="port" value="/dev/ttyACM0"/>
36    <param name="baud" value="57600"/>
37  </node>
38  ....
39 </launch>
```

In this file, we start with a `<group>` tag since we are using multiple launch files in the “main” machine. Then, we define the machine parameters using the `<machine>` tag where we provide the machine name, its local IP, the bash environment loader file, and the username and password for the ssh remote connection. Although explicitly providing passwords in a readable file is a

security risk, we provide it here for clarification and simplicity. A secure version of the launch file utilizing public key authentications is detailed the text file https://github.com/MarwanAbdelatti/ft_industry4_raspi/blob/main/Secured-Approach-for-Launch-Files.md in the package repository link on Github. At line 14 in the file we currently discuss, another launch file is included. This file is responsible for launching the `mqtt_bridge` nodes that interface between MQTT and ROS messaging. The file includes node configurations, and the conversion map between ROS and MQTT topics which is available in the data file `ft_industry4_params.yaml`. Similarly, the other machines are declared such as the HBW in line 17 but there's no `<group>` tag used here since there are no sub-launch files to include, the other parameters are similar like the IP address, the environment loader file, and so on.

The second part of this file is the node declaration where we launch the `rosserial_python` node on each machine using the `<node machine>` tag to enable the communication between each Raspberry Pi and the ftDuino connected to it. The link is enabled on the USB port with ID `ttyACM0` and with communication speed 57600 bps. In addition to this, the `status_update` node is declared on the main Pi which is responsible for updating the HBW occupancy status of the shelves as well as the material color available. This data is saved in the `data.json` status file. The dots in lines 21 and 35 are to indicate that the file is clipped for the sake of space and that the clipped parts are similar.

- The rest of files contain Arduino codes (`.ino` files) that are meant to run on the ftDuino's of the units and contain the remainder of nodes that subscribe or publish to the different ROS topics in the system. The following is a sample of the VGR Arduino code:

```

1 // Use the following line if you have a Leonardo, FtDuino or MKR1000
2 #define USE_USBCON
3
4 #include <ros.h>
5 #include <std_msgs/String.h>
6 #include <std_msgs/Bool.h>
7 #include <Ftduino.h>
8
9 ros::NodeHandle nh;
10 std_msgs::String str_msg;
11 std_msgs::String str_loc_msg;
12
13 ros::Publisher vgr_new_material("vgr_new_material", &str_msg);
14 ros::Publisher provide_empty_loc("provide_empty_loc", &str_loc_msg);
15
16 char empty_loc_content[3] = "Z4";
17 char detected_color[6] = "NA";
18 bool move_cmd = true;
19 bool in_processing_object = false;
20
21 void messageCb_red(const std_msgs::Bool &payload_msg){
22
23     if (payload_msg.data && move_cmd){
24         nh.loginfo("VGR Received an Order at the RED Topic");
25         move_cmd = false;
26         //move to Sorting Line Drop-off area (red)
27 }
```

```
27     ftduino.motor_counter(Ftduino::M1, Ftduino::LEFT, Ftduino::MAX, 390);
28     while(ftduino.motor_counter_active(Ftduino::M1)); /*no-op*/
29
30 //pick up material (red)
31 ftduino.motor_counter(Ftduino::M3, Ftduino::LEFT, Ftduino::MAX, 450);
32 while(ftduino.motor_counter_active(Ftduino::M3)); /*no-op*/
33
34 ftduino.motor_counter(Ftduino::M2, Ftduino::LEFT, Ftduino::MAX, 850);
35 while(ftduino.motor_counter_active(Ftduino::M2)); /*no-op*/
36
37 ftduino.output_set(Ftduino::O7, Ftduino::HI, Ftduino::MAX);
38 ftduino.output_set(Ftduino::O8, Ftduino::HI, Ftduino::MAX);
39 delay(2000);
40
41 //move to end point
42
43 ....
44
45 //drop off material at end point
46 digitalWrite(LED_BUILTIN, HIGH);
47 dropMaterial();
48 delay(2000);
49 digitalWrite(LED_BUILTIN, LOW);
50
51 //move back home
52 goHome();
53 }
54 }
55
56 ros::Subscriber<std_msgs::Bool> vgr_blue_sub("sld_blue_pub",
57 &messageCb_blue);
58 ros::Subscriber<std_msgs::Bool> vgr_red_sub("sld_red_pub",
59 &messageCb_red);
60 ros::Subscriber<std_msgs::Bool> vgr_white_sub("sld_white_pub",
61 &messageCb_white);
62 ros::Subscriber<std_msgs::String> new_order_sub("new_order",
63 &material_processing);
64 ros::Subscriber<std_msgs::String> provide_empty_loc_sub("provide_empty_loc_back",
65 &empty_locCb);
66
67 void setup()
68 {
69     nh.initNode();
70     nh.subscribe(vgr_blue_sub);
71     nh.subscribe(vgr_red_sub);
72     nh.subscribe(vgr_white_sub);
73     nh.subscribe(new_order_sub);
74     nh.subscribe(provide_empty_loc_sub);
75
76     nh.advertise(provide_empty_loc);
77     nh.advertise(vgr_new_material);
78
79     pinMode(LED_BUILTIN, OUTPUT);
80
81     ftduino.init();
82 //Vertical motor inputs
83     ftduino.input_set_mode(Ftduino::I2, Ftduino::SWITCH);
84     ftduino.counter_set_mode(Ftduino::C2, Ftduino::C_EDGE_RISING);
85 //Horizontal motor inputs
86     ftduino.input_set_mode(Ftduino::I3, Ftduino::SWITCH);
87     ftduino.counter_set_mode(Ftduino::C3, Ftduino::C_EDGE_RISING);
88 //turn encoder
```

```

88     ftduino.input_set_mode(Ftduino::I1, Ftduino::SWITCH);
89     ftduino.counter_set_mode(Ftduino::C1, Ftduino::C_EDGE_RISING);
90     //in-processing sensor
91     ftduino.input_set_mode(Ftduino::I7, Ftduino::SWITCH);
92     //color sensor
93     ftduino.input_set_mode(Ftduino::I8, Ftduino::VOLTAGE);
94     //ending sensor
95     ftduino.input_set_mode(Ftduino::C4, Ftduino::SWITCH);
96 }
97
98 void loop()
99 {
100     while(move_cmd && ftduino.input_get(Ftduino::I7)) {
101         nh.spinOnce();
102         delay(250);
103     }
104
105     if (!ftduino.input_get(Ftduino::I7)) {
106         in_processing();
107     }
108 }
```

The first six lines are related to the `rosserial_arduino` package and enable the ftDuino to connect to ROS topics. Line 7 imports the `ftDuino` library to communicate with the IO ports to read sensors and control devices connected to it. Lines 9–14 declare the ROS node handle, message objects used in the code, and publisher objects to different topics. Some global variables are defined in lines 16–19. The `messageCb_red()` callback function is defined in lines 21–54 to be invoked when a red part is detected at the SLD chute, the dots in line 43 are to cut some text to save space. ROS subscriber objects are defined in lines 56–60 where the corresponding callback functions are tied to them. The node is initialized and ROS objects are connected to the topics by the `setup()` function declared in lines 62–92 where board-related I/O definitions are also defined. The main loop is defined in lines 94–104.

4.1 Prerequisite Packages

In order for the `ft_industry4_raspi` package to initiate and run successfully, some packages are necessary. The communication between each Raspberry Pi and the ftDuino board connected with requires the `rosserial` package to be available on each Raspberry Pi and ftDuino. To handle the communication between the main Pi and the SCADA HMI, an MQTT server and the `mqtt_bridge` package are required on the main Pi to exchange the messages between ROS and MQTT back and forth. Steps to properly install and configure these packages are summarized below:

The `rosserial` Package is a metapackage that references multiple packages required to handle the communication over the USB port in our system. This package includes `rosserial_arduino`, `rosserial_python`, `rosserial_msgs`,

and `rosserial_client`. More information can be found in ROS Wiki: <http://wiki.ros.org/rosserial>. To install the package on ROS Melodic for Arduino-compatible boards, the following steps should be followed:

These two commands install the packages on each Raspberry Pi:

```
$ sudo apt-get install ros-melodic-rosserial-arduino  
$ sudo apt-get install ros-melodic-rosserial
```

Now that the necessary libraries are installed on the Raspberry Pi, packages are built using `catkin_make` command. Header files and libraries necessary for Arduino programs to interact with ROS are built using the following commands:

```
$ cd ~/Arduino/libraries  
$ rm -rf ros_lib  
$ rosrun rosserial_arduino make_libraries.py .
```

The goal of the first two commands is to remove any old ROS libraries installed within the libraries folder, which exists inside the installation folder of the Arduino IDE. Then, ROS libraries are built with the third command which requires a target location for the libraries, and is specified by the last (dot) in the line.

The mqtt_bridge Package is a package that maps between ROS and MQTT messages in a bidirectional form. Messages from ROS are serialized by a messagepack json file for MQTT, and messages from MQTT are deserialized for ROS topic. More information is available in the ROS Wiki: http://wiki.ros.org/mqtt_bridge. The `mqtt_bridge` and its components are required on *the main Pi only*. First the MQTT broker (i.e., server) is installed:

```
$ sudo apt install mosquitto mosquitto-clients
```

Then the following commands install the rest of the prerequisites before installing the package:

```
$ sudo apt install python-rospkg  
$ pip install rospkg  
$ sudo apt install ros-melodic-rosbridge-library
```

The `mqtt_bridge` package is installed by the following command:

```
$ sudo apt install ros-melodic-mqtt-bridge
```

5 SCADA System

Supervisory Control and Data Acquisition (SCADA) system, as defined in [16], is:

A sub-class of industrial control systems (ICSSs) in which control is performed over multiple, distributed individual lower-level control systems (hence the word “supervisory”).

A typical SCADA control center monitors and manages automation processes across remote areas through smart controllers such as remote terminal units (RTUs) and intelligent electronic devices (IEDs). The system status is presented on human-machine interface (HMI) that represents the system graphically and displays events and alarms lists. In addition to status monitoring, human operators can send control commands via the HMI software to different ICS components. Such control commands include but are not limited to changing a set point of a motor speed, start/stop a compressor, or open/close valves. In order for a SCADA software to communicate with the remote site, appropriate communication drivers must be available in the software. The SCADA software in our proposed system supports MQTT data transmission and functions as an MQTT client connecting to the MQTT broker located in the main Pi.

5.1 *MQTT Protocol*

According to the official MQTT specifications in the OASIS standard [17], MQTT is defined as:

MQTT is a Client Server publish/subscribe messaging transport protocol. It is light weight, open, simple, and designed so as to be easy to implement. These characteristics make it ideal for use in many situations, including constrained environments such as for communication in Machine to Machine (M2M) and Internet of Things (IoT) contexts where a small code footprint is required and/or network bandwidth is at a premium.

MQTT was developed in 1999 by Andy Stanford-Clark (IBM) and Arlen Nipper (Arcom, now Cirrus Link) to connect to oil pipelines via satellite with minimal battery loss and minimal bandwidth. In contrast to client/server architecture where a client communicates directly with an endpoint (server) and the server responds back, MQTT adopts publish/subscribe architecture where there are three key components illustrated in Fig. 13 forming the communication process, i.e. the publisher, the subscriber and the broker. The broker decouples the client (the publisher) that sends a message from the client or clients (the subscribers) that receive the messages. The publishers and subscribers never have a direct contact to each other. The broker filters all incoming messages and ensures they are correctly distributed to subscribers [18].

MQTT has been gaining popularity along with the proliferation of the Internet of Things (IoT) that needs the capability to work with low-powered devices. According to ISO/IEC 20922, MQTT is an ideal communication protocol in Machine to Machine (M2M) communications and within the IoT. The publish/subscribe architecture showed more efficiency than the conventional client/server model for industry 4.0 systems. Therefore, many systems are adopting MQTT. The publish-subscribe architecture along with the quality of service (QoS), scalability, message filtering, as well as the last will and testament (LWT) features give more flexibility to the connection of low-bandwidth devices with limited CPUs and with very little overhead [19].

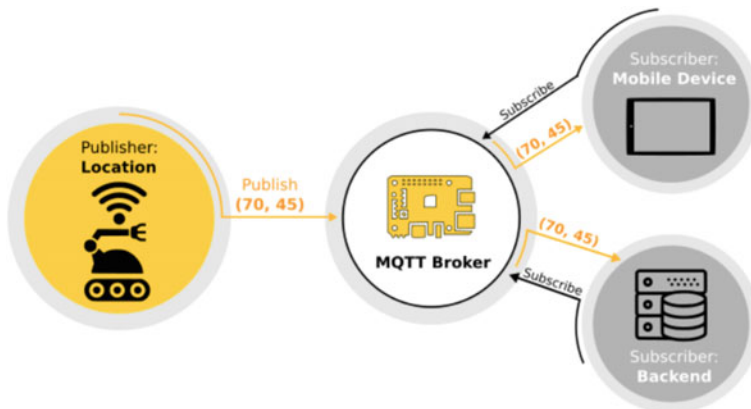


Fig. 13 MQTT main components

MQTT has already been successfully implemented in many smart applications like home automation, surveillance, healthcare, transportation, industry, and logistics.

5.2 ROS-MQTT Bridge Configuration

As discussed in Sect. 4, the file `ft_industry4_params.yaml` includes the MQTT configurations, and the conversion map between ROS and MQTT topics. The contents of the file are shown in the listing below which includes the mapping between different ROS and MQTT topics in both directions.

```

1 mqtt:
2   client:
3     protocol: 4 # MQTTv311
4   connection:
5     host: localhost
6     port: 1883
7     keepalive: 60
8     private_path: device/001
9   #serializer: json.dumps
10  #deserializer: json.loads
11 bridge:
12   # new_order
13   - factory: mqtt_bridge.bridge:MqttToRosBridge
14     msg_type: std_msgs.msg:String
15     topic_from: mq_new_order
16     topic_to: /new_order
17   # /vgr_new_material
18   - factory: mqtt_bridge.bridge:RosToMqttBridge
19     msg_type: std_msgs.msg:String
20     topic_from: /vgr_new_material

```

```

21   topic_to: mq_vgr_new_material
22   # /sld_blue_pub
23   - factory: mqtt_bridge.bridge:RosToMqttBridge
24     msg_type: std_msgs.msg:Bool
25     topic_from: /sld_blue_pub
26     topic_to: mq_sld_blue_pub
27   # /sld_red_pub
28   - factory: mqtt_bridge.bridge:RosToMqttBridge
29     msg_type: std_msgs.msg:Bool
30     topic_from: /sld_red_pub
31     topic_to: mq_sld_red_pub
32   # /sld_white_pub
33   - factory: mqtt_bridge.bridge:RosToMqttBridge
34     msg_type: std_msgs.msg:Bool
35     topic_from: /sld_white_pub
36     topic_to: mq_sld_white_pub

```

The lines 1–8 contain the MQTT connection configuration for the bridge including the broker name (here is localhost since the bridge and the broker are on the same machine), and the port number. The mapping bridge configurations start at line 11, the first block of configuration serves the order placing feature from the HMI which sends the order to an MQTT topic called `mq_new_order` then the bridge forwards it to the ROS topic `/new_order`. Line 13 tells the bridge to map from MQTT to ROS. Line 14 specifies the message type based on ROS message types. Lines 15 and 16 specifies the source and destination topics respectively. The same applies to the blocks at lines 17–36 but the difference is that the mapping is in the other direction (i.e., from ROS to MQTT), the source and destination topics, as well as the message type for the last three topics (lines 22–36).

6 Test of the System

In this section, steps for properly running the system are provided. A graph with the system nodes and topics is given for better understanding how the system works and the node running sequence. Also, an application video is linked at the end of this section.

The system is initiated by running the nodes in related packages through a single `.launch` file that also contains other `.launch` files for easy operation. The launch file is run by the following command:

```
$ roslaunch ft_industry4_raspi industry4.launch
```

where `ft_industry4_raspi` is the package name and `industry4.launch` is the launch file. By running this command on the main Pi, the ROS master connects to the different unit Pi machines through SSH connections and uses the environment configuration `.sh` files as shown in the first part of Fig. 14. The different `roslaunch` components including the nodes, machines, as well as the connection parameters of both `rosserial` and `mqtt_bridge` are listed in the summary part in the figure.

```

ubuntu@ubuntu:~$ roslaunch ft_Industry4_raspI industry4.launch
... logging to /home/ubuntu/.ros/log/bc93d9cc-d82a-11eb-920a-b827ebca68de/roslaunch-ubuntu-2709.log
Checking log directory for disk usage. This may take a while.
Press Ctrl-C to interrupt
Done checking log file disk usage. Usage is <1GB.

started roslaunch server http://192.168.0.10:39187/
remote[192.168.0.12-0]: starting roslaunch
launching remote rosnode child with command: [env ROS_MASTER_URI=http://192.168.0.10:11311 /home/ubuntu/env_hw.sh roslaun -c 192.168.0.12-0]
g http://192.168.0.10:39187/ --run_id bc93d9cc-d82a-11eb-920a-b827ebca68de]
remote[192.168.0.12-0]: ssh connection created
remote[192.168.0.14-1]: starting roslaunch
remote[192.168.0.14-1]: creating ssh connection to 192.168.0.14:22, user[ubuntu]
launching remote rosnode child with command: [env ROS_MASTER_URI=http://192.168.0.10:11311 /home/ubuntu/env_sld.sh roslaun -c 192.168.0.14-1]
1 -u http://192.168.0.10:39187/ --run_id bc93d9cc-d82a-11eb-920a-b827ebca68de]
remote[192.168.0.13-2]: ssh connection created
remote[192.168.0.13-2]: starting roslaunch
remote[192.168.0.13-2]: creating ssh connection to 192.168.0.13:22, user[ubuntu]
launching remote rosnode child with command: [env ROS_MASTER_URI=http://192.168.0.10:11311 /home/ubuntu/env_vgr.sh roslaun -c 192.168.0.13-2]
2 -u http://192.168.0.10:39187/ --run_id bc93d9cc-d82a-11eb-920a-b827ebca68de]
remote[192.168.0.13-2]: ssh connection created

SUMMARY
*****
PARAMETERS
* /hw_node/baud: 57600
* /hw_node/port: /dev/ttyACM0
* /mqtt_bridge/bridge/topic_from: '...
* /mqtt_bridge/client_id: client
* /mqtt_bridge/mqtt/connection/protocol: 4
* /mqtt_bridge/mqtt/connection/host: localhost
* /mqtt_bridge/mqtt/connection/keepalive: 60
* /mqtt_bridge/mqtt/connection/port: 1883
* /mqtt_bridge/mqtt/private_path: device/001
* /rosdistro: melodic
* /rosversion: 1.14.10
* /sld_node/baud: 57600
* /sld_node/port: /dev/ttyACM0
* /status_update/baud: 57600
* /status_update/port: /dev/ttyACM0
* /vgr_node/baud: 57600
* /vgr_node/port: /dev/ttyACM0

MACHINES
* hw
* main
* sld
* vgr

NODES
/
  hw_node (rosserial_python/serial_node.py)
  mqtt_bridge (mqtt_bridge/mqtt_bridge_node.py)
  sld_node (rosserial_python/serial_node.py)
  status_update (ft_Industry4_raspI/status_update.py)
  vgr_node (rosserial_python/serial_node.py)

auto-starting new master
process[master]: started with pid [2734]
ROS_MASTER_URI=http://192.168.0.10:11311

setting /run/_id to bc93d9cc-d82a-11eb-920a-b827ebca68de
process[rosout-1]: started with pid [2745]
status_update[status_update-2]: started with pid [2746]
process[mqtt_bridge-2]: started with pid [2748]
process[status_update-3]: started with pid [2749]
[192.168.0.12-0]: launching nodes...
[192.168.0.12-0]: ROS_MASTER_URI=http://192.168.0.10:11311
[192.168.0.12-0]: process[hw_node-1]: started with pid [2329]
[192.168.0.12-0]: ... done launching nodes
[192.168.0.14-1]: ROS_MASTER_URI=http://192.168.0.10:11311
[192.168.0.14-1]: process[sld_node-1]: started with pid [2683]
[192.168.0.14-1]: ... done launching nodes
[192.168.0.13-2]: launching nodes...
[192.168.0.13-2]: ROS_MASTER_URI=http://192.168.0.10:11311
[192.168.0.13-2]: process[vgr_node-1]: started with pid [2282]
[192.168.0.13-2]: ... done launching nodes
[INFO] [1624860397.871048]: MQTT connected

```

Fig. 14 Screenshot of the ROS master initiation

The last part in the figure shows the successful initiation of all the nodes in the system indicating that the system is up and ready to work.

Although part of the system we present works using the client/server mechanism in the `rosserial` package, the system mainly depends on the pub/sub mechanism of ROS. Most the node communications are based on topics that show up on the `$ rostopic list` command once the nodes are run. These topics are:

```
/back
/diagnostics
/echo
```

```

/new_order
/private/back
/private/echo
/provide_empty_loc
/provide_empty_loc_back
/sld_blue_pub
/sld_red_pub
/sld_white_pub
/vgr_new_material
/what_is_empty
/what_is_occupied

```

While some topics are feedback topics that return some information to nodes for processing, others are command topics that are intended to directly initiate an action in the system (e.g., moving the robot). The ROS graph in Fig. 15 depicts the system nodes (as ellipses) and their corresponding connections to the topics that are shown as rectangles. Now that the system is up and ready, we have two modes of operations as discussed earlier in Sect. 2, namely, (i) storing new part, and (ii) processing materials for new orders. Storing new material mode is automatically initiated once the system detects a new material at its pickup inlet by the photosensor connected to the ftDuino which runs the vgr_node. The vgr_node, as the graph shows, publishes an inquiring message to the /provide_empty_loc topic where the status_update node subscribes and checks the HBW shelf status i.e., data.json file for empty locations then returns this location back to the VGR through the /provide_empty_loc_back.

The VGR moves the material to the color detection station then publishes to the /vgr_new_material topic its color and the intended location to be placed in. The hbw_node which subscribes to this topic moves its ASRS robot to pick the material from the VGR and places it accordingly. Once the new material is placed successfully, the node publishes to the /what_is_occupied topic the updated location and color for the status_update node to update the shelf status file. The typical data.json file looks like the following, where A1, A2,...,C3 are pre-defined locations at the HBW:

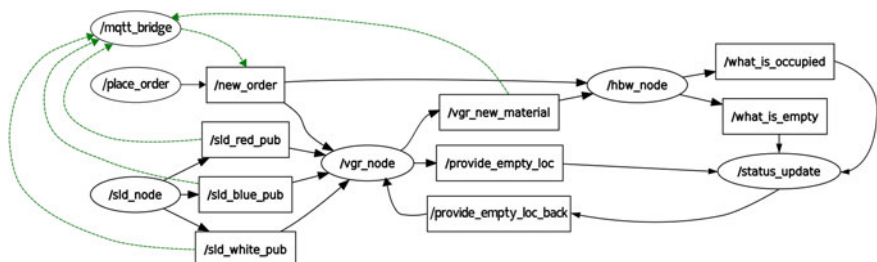


Fig. 15 ROS graph, nodes and topics connections

```

1  {
2  "A1 ":"white",
3  "A2 ":"red",
4  "A3 ":"blue",
5  "B1 ":"white",
6  "B2 ":"red",
7  "B3 ":"blue",
8  "C1 ":"white",
9  "C2 ":"red",
10 "C3 ":"blue"
11 }
```

The second operation mode, on the other hand, responds to new order request from customers. The mode is initiated by the following command from terminal or by the SCADA HMI:

```
$ rosrun ft_industry4_ftduino place_order.py red
```

The `rosrun` command runs the `place_order` node which takes the requested color as an argument, searches for an HBW location having a material with the corresponding color, then publishes this location to the topic `/new_order` as shown in the graph of Fig. 15. Both the `hbw_node` and `vgr_node` subscribe to this topic and respond to it at the same time such that the HBW ASRS robot moves to the target location, picks the material, and places it where the VGR robot can pick. The ASRS brings the empty box back to the HBW shelf and the `hbw_node` publishes to the `/what_is_empty` topic the empty location for the `status_update` node to update the shelf status file. Meanwhile, the VGR moves the material to the MPS station for processing and returns back home listening to the topics: `/sld_blue_pub`, `/sld_red_pub`, and `/sld_white_pub`. Once the material processing is done, it's kept at one of the three SLD locations based on its color where the `sld_node` publishes to one of the three above-mentioned topics so that the VGR can pick and place it at the delivery outlet.

In order for the SCADA to monitor the processes properly, the ROS node of name `mqtt_bridge` subscribes to relevant topics namely, `/vgr_new_material`, `/sld_blue_pub`, `/sld_red_pub`, and `/sld_white_pub` and publishes to `/new_order` as illustrated with green connections in Fig. 15. Future work will include other topics that provide manual override to VGR and ASRS robots to forcefully send them to their home positions in case of emergencies.

7 Conclusion

URILF4.0 is designed as a laboratory-scale manufacturing test-bed for exploring and experimenting with Industry 4.0 concepts. It is built with low cost, open-source controllers and software. The sensors interface to Arduinos, connected with Raspberry Pi 3 B+'s, which provide network communications and serve as ROS nodes. An additional Pi is used as the ROS master node. The ROS network is connected to a SCADA

system and a widely used protocol, MQTT, is used to link SCADA and ROS. The SCADA gives full access to the low level hardware and enables user inputs to initiate (and process) orders through the manufacturing test-bed and to receive and store materials in an ASRS. Work on expanding the manufacturing test-bed is ongoing. A digital twin of this system is also under development. The source code has been shared at https://github.com/MarwanAbdelatti/ft_industry4_raspi, and the authors can also be contacted directly for any additional information.

References

1. Kagermann, H., Lukas, W.-D., Wahlster, W.: Industrie 4.0: Mit dem internet der dinge auf dem weg zur 4. industriellen revolution. *VDI nachrichten* **13**(1), 2–3 (2011)
2. Lasi, H., Fettke, P., Kemper, H.-G., Feld, T., Hoffmann, M.: Industry 4.0. *Bus. & Inf. Syst. Eng.* **6**(4), 239–242 (2014)
3. Lee, J., Kao, H.-A., Yang, S.: Service innovation and smart analytics for industry 4.0 and big data environment. *Procedia Cirp* **16**, 3–8 (2014)
4. Thames, L., Schaefer, D.: *Cybersecurity for Industry 4.0*. Springer, Berlin (2017)
5. Klein, Patrick, Bergmann, Ralph: Generation of complex data for ai-based predictive maintenance research with a physical factory model. *ICINCO* **1**, 40–50 (2019)
6. Abele, Eberhard, Metternich, Joachim, Tisch, Michael, Chryssolouris, George, Sihn, Wilfried, ElMaraghy, Hoda, Hummel, Vera, Ranz, Fabian: Learning factories for research, education, and training. *Procedia CiRp* **32**, 1–6 (2015)
7. Lang, S., Reggelin, T., Jobran, M., Hofmann, W.: Towards a modular, decentralized and digital industry 4.0 learning factory. In: 2018 Sixth International Conference on Enterprise Systems (ES), pp. 123–128. IEEE (2018)
8. Angione, G., Barbosa, J., Gosewehr, F., Leitão, P., Massa, D., Matos, J., Peres, R.S., Rocha, A.D., Wermann, J.: Integration and deployment of a distributed and pluggable industrial architecture for the perform project. *Procedia Manuf.* **11**, 896–904 (2017)
9. Tisch, M., Abele, E., Metternich, J.: Overview on potentials and limitations of existing learning factory concept variations. In: *Learning Factories*, pp. 289–321. Springer (2019)
10. Andersen, A.-L., Brunoe, T.D., Nielsen, K.: Engineering education in changeable and reconfigurable manufacturing: using problem-based learning in a learning factory environment. *Procedia Cirp* **81**, 7–12 (2019)
11. Nardello, M., Madsen, O., Møller, C.: The smart production laboratory: a learning factory for industry 4.0 concepts. In: *CEUR Workshop Proceedings*, vol. 1898. CEUR Workshop Proceedings (2017)
12. Rehse, J.-R., Dadashnia, S., Fettke, P.: Business process management for industry 4.0—three application cases in the dfki-smart-lego-factory. *IT-Inf. Technol.* **60**(3), 133–141 (2018)
13. Klein, P., Malburg, L., Bergmann, R.: Fntonto: a domain ontology for a fischertechnik simulation production factory by reusing existing ontologies. In: *LWDA*, pp. 253–264 (2019)
14. Rehse, J.-R., Mehdiyev, N., Fettke, P.: Towards explainable process predictions for industry 4.0 in the dfki-smart-lego-factory. *KI-Künstliche Intelligenz* **33**(2), 181–187 (2019)
15. Michael Ferguson. rosserial package summary (2018)
16. Colbert, E.J.M., Kott, A.: *Cyber-security of SCADA and other industrial control systems*, vol. 66. Springer (2016)
17. OASIS Standard Incorporating Approved Errata. Mqtt version 3.1. 1 plus errata 01. (2015)
18. Hillar, G.C.: *MQTT Essentials-A lightweight IoT protocol*. Packt Publishing Ltd (2017)
19. The HiveMQ Team. Publish & subscribe - mqtt essentials: Part 2 (2015)

Marwan F. Abdelatti received the M.Sc. degree in Control Engineering from Cairo University, Egypt in 2010. He is currently a Ph.D candidate in the department of Industrial Engineering at the University of Rhode Island, USA. His current research focuses on smart manufacturing system, intelligent agents, and parallel GPU computing. Marwan is involved in research projects including GPU implementations of optimization algorithms for route-planning problems, and autonomous robots, specifically, ground vehicles.

Manbir S. Sodhi obtained his undergraduate degree from Jadavpur University, Kolkata, and graduate degrees from the University of Arizona. He is the Professor of Industrial and Manufacturing Engineering at the University of Rhode Island. He has published many engineering research articles involving manufacturing, sustainability, driving distractions and autonomy. For over a decade, he has hosted the Global Product Sustainability Systems Meeting in Rhode Island. He has also worked as a visiting scientist with NATO in Italy, and a visiting Professor at the Technical University of Braunschweig, Germany.

Cooperation, Sensing and Control

RosDrive: An Open-Source ROS-Based Vehicular Simulator for STEM Control Systems Classes Tutorial



Enio Vasconcelos Filho, Jones Yudi, Mohamed Abdelkader, Anis Koubaa, and Eduardo Tovar

Abstract The study of control systems in the engineering courses is quite complex, given the difficulty of some teachers in exemplifying and allowing the student to understand how such systems affect the environment. In this context, the STEM methodologies aim to fill this gap between the traditional classes and the student comprehension of the topic through the active learning process. Realistic open-source simulators can be interpreted as one solution for this STEM implementation, allowing students to test, modify and create different configurations and sensors with a low-cost environment. This work presents a flexible open-source 3D simulation framework, based on ROS, of a line follower vehicle, using an embedded PID controller, a camera for processing and detecting lines, and sonars for detecting and avoiding obstacles. This simulator integrates several controller systems, allowing the student to build consistent skills in control and related areas, analyze the impacts of models configurations, and extends its knowledge to new techniques.

Keywords Control systems · Education · Simulator · STEM · Open-Source · ROS

E. Vasconcelos Filho (✉) · A. Koubaa · E. Tovar
ISEP, CISTER Research Centre, Rua Alfredo Allen 535, 4200-135 Porto, Portugal
e-mail: enpvf@isep.ipp.pt

A. Koubaa
e-mail: akoubaa@psu.edu.sa

E. Tovar
e-mail: emt@isep.ipp.pt

J. Yudi
Automation and Control Group, University of Brasilia, Brasilia, Brazil
e-mail: jonesyudi@unb.br

M. Abdelkader · A. Koubaa
Prince Sultan University, Riyadh, Saudi Arabia
e-mail: mabdelkader@psu.edu.sa; mohamed.abdelkader@systemtrio.com

M. Abdelkader
Systemtrio Electronics L.L.C, Abu Dhabi, United Arab Emirates

1 Introduction

Control system techniques are one of the most significant challenges in several engineering courses. Since it requires extensive mathematical background, a theoretical load is quite extensive, requiring effort to learn by students and teachers. Moreover, there is still an inherent difficulty in transporting the studied theory to practice, making it challenging to retain learning [1]. Thus, alternative teaching techniques [2] can facilitate knowledge production and construction of the skills expected by the agents involved. In addition, [3] concludes in their work that the student's perception of applicability and the ability to construct different solutions is a motivator for the search for more knowledge.

This line of education development puts the student as a producer of dynamic and practical knowledge. It should be encouraged to take an active and autonomous attitude and not necessarily follow pre-established models [4]. So, the student can go further and propose new solutions to existing problems and even create different issues. Active student engagement in the learning process also helps to keep the motivation to research and learn [5], using Active Learning techniques. Thus, integrating different areas of knowledge, experimentation, and implementation allows the student to retain more excellent expertise and develop new skills. This integration of knowledge is called STEM—Science, Technology, Engineering, and Mathematics [6].

A standard solution in many universities is using pre-defined laboratory sessions, using commercial kits such as [7–9]. Although such solutions are attractive, efficient, and robust, they are often expensive and not flexible for experimenting and developing different solutions. Nevertheless, using Arduino development kits has shown promising results as a learning tool [10]. This study suggests the development of kits that can be used throughout the semesters, gradually increasing the project's difficulty [11] and even in specific dynamics and control systems projects [12].

In the same line of knowledge integration, other low-cost projects have been developed and implemented, giving students greater flexibility in experimenting with techniques and knowledge. For example, in [13], the authors proposed an educational line-following robot based on Arduino, allowing the implementation of low-level control techniques. A similar application is presented in [14], proposing an even lower cost robot with less flexibility. The increased complexity of possible control algorithms is achieved on other platforms, such as those seen in [15, 16]. However, such applications imply a significant increase in project costs. Thus, although Arduino-based solutions integrate the theoretical model and practice regarding control aspects, they present a limitation regarding the complexity of the algorithms, given the restriction of processing capacity and design flexibility, due to the need to purchase different sensors.

A solution that combines a low-cost implementation with flexibility and allows knowledge retention through experimentation and active learning is based on realistic open-source simulators. In STEM, a simulator represents a crucial stage of development and education, reducing the time to produce prototypes. Thus, emulating

a real scenario with physical interactions allows the development of safety tests in different environments and situations. As a result, it is possible to experiment with techniques, analyze results and propose solutions flexibly, with great speed and less cost.

The work done in [17] presents some of these tools, comparing simulators such as Webots [18], Gazebo, and ROS [19], using criteria such as supported operating systems, programming languages, documentation, tutorials, among others. In addition to these tools, others have been developed over time, such as the one presented in [20], where a virtual laboratory is designed so that students can experiment with models of line-following robots for competitions. However, such a simulator does not allow the 3D visualization of the models, allowing only the testing of the proposed algorithms. Another interesting simulator is proposed in [21], which presents CARLA, an open-source simulator aimed at autonomous-driving research in this work. It is a very realistic simulator with many items, with several physical interactions between the components. However, despite being an extensible platform for new developments, its vehicle control methods are limited to artificial intelligence learning models without control models.

The authors of [22] present a simulator that uses a competition model to teach robotics based on ROS. An autonomous robot capable of traveling a path is used in this simulator, following directions on the track. Such a simulator showed promising results when crossing the designated paths but presented the limitation of not using a realistic vehicle model or even different control models. It has also been used in competition simulation, which increases students' comprehension and stimulates self-learning [23, 24].

Seeking to use the advantages of a simulator capable of emulating realistic vehicles, RosDrive is presented. A flexible platform based on ROS and the 3D simulator, Gazebo, for studying different models of vehicle control. RosDrive uses an electric vehicle model [25], with several sensors capable of covering different routes and avoiding obstacles. Thus, the student will be able to implement additional control strategies, analyze the system's responses, and visualize the impacts of theoretical models and their variables on the simulated scenarios. In addition, the tool allows the use of different strategies in different vehicles, allowing the comparison between the adopted models. For instance, a line follower controller mode with obstacle avoidance will be implemented to exhibit the simulator results. The tool's flexibility allowed its extension for the study of communication models [26], the development of hardware in the loop (HIL) simulation [27], and the implementation of the same control model on a testbed platform [28]. As it is an open-source tool, the full code access is provided in Sect. 5, for general use, with all the necessary steps for its installation. The general simulator environment is illustrated in Fig. 1. The concrete contributions of this paper are presented below:

- Present RosDrive, a realistic open-source 3D vehicle simulator that allows the students to apply different control models techniques, improve their practical knowledge in the control area, and create new strategies to perform vehicle movements;

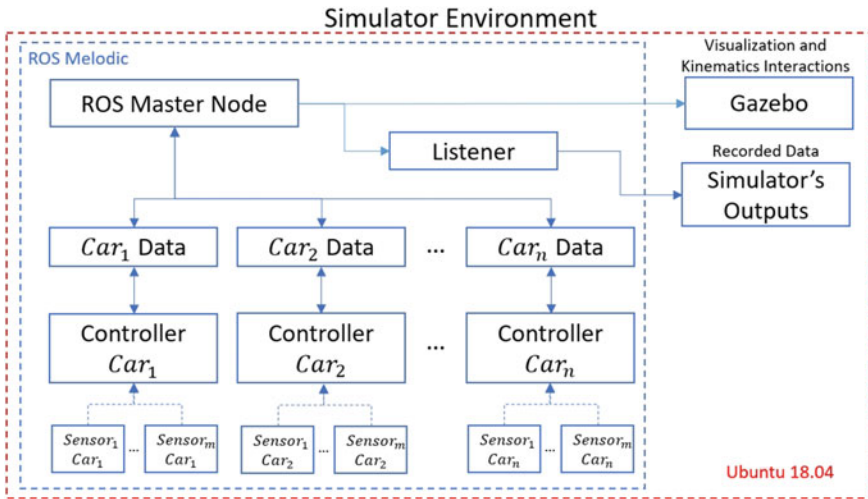


Fig. 1 General simulator architecture

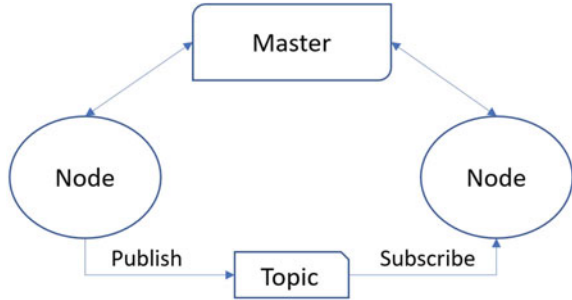
- Introduce a flexible simulator architecture, that allows modules exchange, parameters configurations, and system response analysis and visualization;
- Demonstrate the simulator flexibility due to the use of a camera and sonar sensors to perform a Line Follower algorithm, and an Obstacle Detection and Avoidance strategy integrated with a PID Cruise Controller model;

This paper is organized as follows: Sect. 2 shows the Simulator Architecture, the leading technologies, and the minimal system requirements. The control and perception modules including the speed control algorithm, the image processing module with the heading controller, and the collision avoidance module are introduced in Sect. 3. The results of designed scenarios are presented in Sect. 4, while the main conclusions are drawn in Sect. 5. Finally, the software installation and execution instructions are shown in Sect. 5.

2 Simulator Architecture

This section will introduce the simulator tools and their general architecture, providing details about the vehicle model and data analysis.

Fig. 2 Publish/subscribe model



2.1 Robot Operating System (ROS)

ROS is an open software developed by Open Source Robotics Foundation. It is a robotic middleware with many software frameworks for robot software development. It provides hardware abstraction, enabling users to avoid low-level problems, with profound device control, communication between nodes and processes, and packet management. ROS-based functions are realized in nodes that may post, receive and reproduce control features, sensor data, state of the node, or general messages. ROS is not a real-time framework or a Real-time Operating System (RTOS). This project will be used in ROS Melodic distribution.

The basic concepts of ROS are nodes, Master, messages, and topics. The Master node works as a central node of the system, storing data and information regarding the ROS Nodes. Nodes inform their registration information to the Master and then can receive data from other nodes. The Master is also responsible for reporting the nodes, using Callbacks, if new information or connections are made. The nodes exchanges messages using the publish/subscribe method, as described in Fig. 2.

Due to its flexibility, ROS has been used in several vehicular applications, such as ground [29], aerial [30], and water [31] and many other robotic platforms. As a consolidated open-source community, several new libraries are available and supported, at the same time that it is highly portable between platforms, including embedded platforms [32]. The extensive material allows a quick learning curve for the student, enabling a simple familiarization with the commands and interfaces and quickly creating new modules.

2.2 Gazebo

One of the critical aspects of a learning-oriented system is its ability to present the results of user interactions intuitively. Thus, the high capacity of ROS to integrate with other platforms shows itself to be a competitive advantage since its functionalities can be extended, expanding the experimentation horizon. For example, integration with a robotic simulation tool helps to visualize the iterations between objects simply,

aiding in learning [33]. One of the most used tools for robotic simulation in ROS is Gazebo. The Gazebo is an open-source 3D robotics simulator, for indoor and outdoor environments, with multi-robot support that allows a complete implementation of dynamic and kinematic physics and a pluggable physics engine. Furthermore, it provides a realistic rendering of backgrounds, including high-quality lighting, shadows, and textures. In addition, it can model sensors that “see” the simulated environment, such as laser range finders, cameras (including wide-angle), Kinect style sensors, among others.

The Gazebo present the same message interface as the rest of the ROS ecosystem. So, the development of ROS nodes is compatible with simulation, logged data, and hardware. Many projects integrate ROS with Gazebo, such as the QuadRotor presented in [34], the Humanoid implementation in [35], and the Ground Vehicle in [29]. As a powerful and very visual tool, Gazebo has also been used as the simulation environment for several technology challenges and competitions, such as NASA Space Robotics Challenge (SRC) [36], Agile Robotics for Industrial Automation Competition (ARIAC) [37], and Toyota Prius Challenge [38].

Gazebo is responsible for realistically mimicking the system’s fundamental dynamics, representing physical issues such as mass, inertia moment, friction, and even collisions. To ensure better representation, Gazebo supports four engines: Simbody [39], Bullet Physics [40], ODE [41], and DART [42]. Such engines guarantee a wide range of representations, bringing simulations closer to reality, offering the student a greater possibility of representing theoretical concepts practically.

Although some Gazebo components show some lag with new technologies, its overview still has more advantages than the alternatives presented. For example, Unity [43] has similarities in the implemented physics, but its integration with ROS is still complex. Furthermore, the Webbots recently developed a ROS integration but still do not have the same flexibility in implementing different physical models. Finally, the Coppelia [44] does not have the same rendering quality [45] as Gazebo, although it has similar flexibility and quality in physical representation.

2.3 Scenario and 3D Vehicle Model

The Gazebo allows the construction of several different scenarios, including as many objects as desired. Those objects can be static or dynamic and controlled in the simulation. For illustration, this work introduces the track presented in Fig. 3 with and without obstacles. Those obstacles can be removed or added by the user.

ROS applications have a launch file that allows the easy start of several applications with previously saved scenarios and desired configurations. In this project, the file *car_demo.launch* is responsible for starting the track, and the *cars.launch* defines the vehicle’s initial coordinates and model. The simulator flexibility allows different car models, including or removing sensors, modifying their positions and configurations. The sensors data can be real-time observed though the *RViz* software.

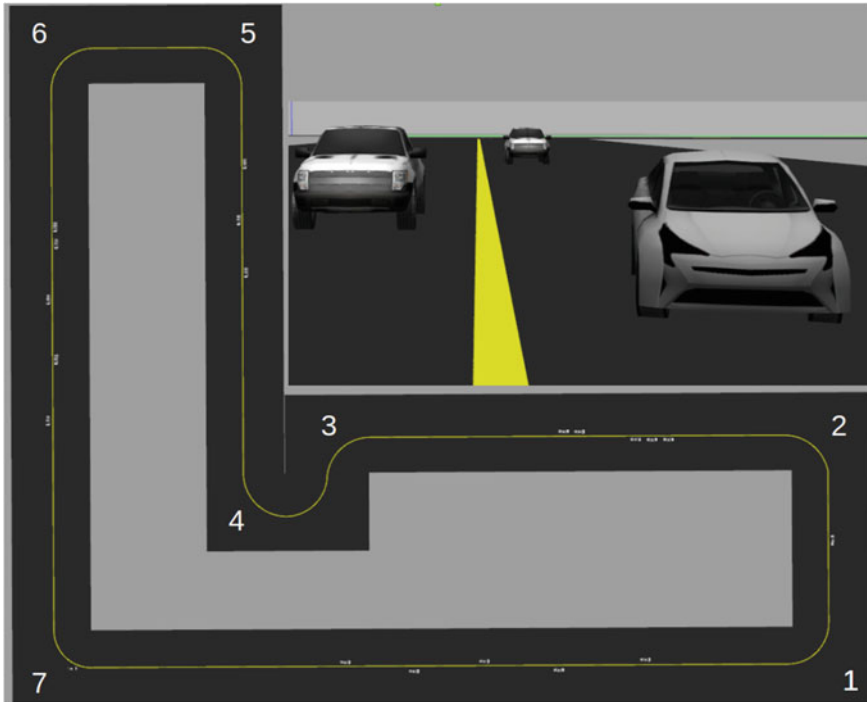


Fig. 3 Track model

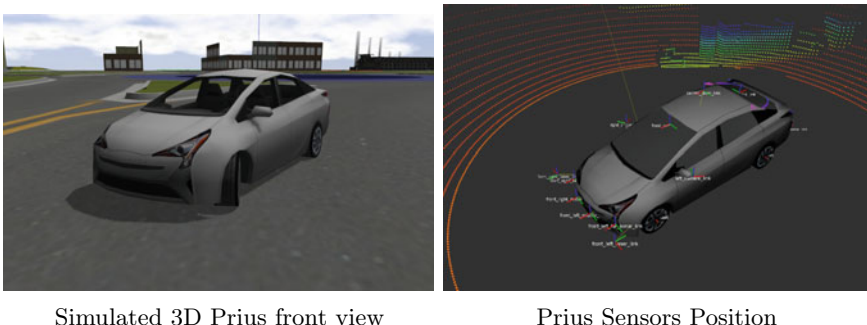


Fig. 4 Prius Gazebo model [25]

The 3D car model used in this work was presented in [25]. Figure 4 illustrates the Hybrid Prius 3D model's main details. Its fundamental dynamics are contained in the node *PriusHybridPlugin.cpp*, and the model's characteristics can be edited in *prius.urdf*.

The primary vehicle controllers, such as throttle, brake, steering, and gear, can be actuated by publishing to a ROS topic. Thus, the vehicle Powertrain will control

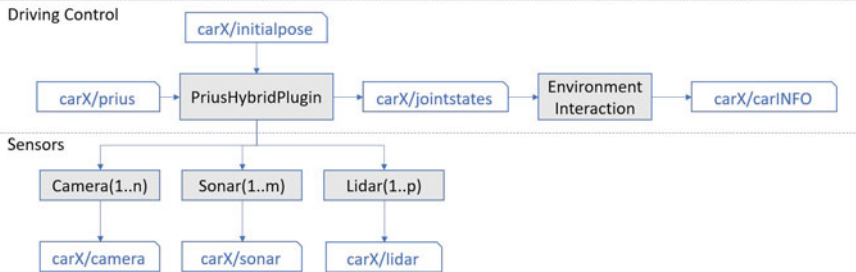


Fig. 5 Prius information structure

the gear control in this simulation. The simulated vehicle also has multiple sensors: 16-beam LIDAR on the roof, eight ultrasonic sensors, four cameras, and two planar LIDARs. However, adding or removing sensors is a simple task that allows adjustments, as necessary. Furthermore, implementing the vehicle with all the kinematics and basic controls enables the study of other project aspects, such as motion control, platooning, stability, and detection and avoidance models.

The vehicle information flowchart is illustrated in Fig. 5. All the vehicles have the same model, and the simulation is composed of $n \in \mathbb{N}$ vehicles. The full set of cars can be defined as $\text{car}_n = \{i \in \mathbb{N} | 0 \leq i \leq n\}$. The information provided by each module/node is:

- `cari/initialPose`: defines the vehicle's initial position
- `cari/prius`: new vehicle settings—throttle, break, steering
- `cari/jointstates`: conditions of each vehicle component—wheels and steering
- `cari/carINFO`: vehicle's current state—throttle, brake, speed, latitude, longitude, steering, heading, etc.
- `cari/camera`: vehicle's onboard cameras info
- `cari/sonar`: vehicle's onboard sonars info
- `cari/lidar`: vehicle's onboard LIDARs info
- `PriusHybridPlugin`: dynamics and vehicle model
- `Environment Interaction`: Gazebo calculation about interactions
- Camera (1 ... n), Sonar (1 ... m) and Lidar (1 ... p): sensor nodes

All the sensors can be added, removed, or modified in the file `prius.urdf`. The vehicle control is managed through the data sent to `cari/prius` topic, which works as the vehicle's input center, receiving throttle, brake, and steering. The throttle and brake have a limit from 0 to 1, and the steering has a range from -30° to $+30^\circ$. Its format is defined in the “Control.msg”. To better understand the text, the rest of this text will refer to a generic simulated vehicle identified by the “i” index, unless in cases where some differentiation is necessary.

2.4 System's Outputs

As a simulator for learning purposes, the system's outputs are essential. Moreover, as a STEM application, with many details, several analysis must be performed using a mathematical approach. The output data will allow the study and comparison of each simulation, allowing the student to evaluate the impact of slight differences in the system's response in each experiment. The system's outputs are provided in .csv files generated during the simulation. The module *listener.py* is responsible for collecting the desired vehicle's data in the related topics and exporting that to a .csv file.

During the simulation, the topic *car_i/carINFO* can be used to perform a Real-Time system evaluation, showing the vehicle's most important information, like coordinates, heading, speed, throttle, and brake conditions. The *listener.py* collects this data and adds some information to the simulation's output file, triggered by the car's movement or spent time. The output file contains the timestamp, coordinates, speed, speed error, throttle and brake percentage, heading, heading error, and sonar information, in this version.

3 Control Algorithms

This section will introduce the controller models used in this simulator. Then, it will discuss the Cruise Controller (CC), the Line Follower characteristics, and the Obstacle Avoidance Strategy. The Prius model simulates sensors that publish to the *car_i/carINFO* topic. This topic contains the main data about the vehicle, like latitude, longitude, altitude, heading, speed, direction, steering angle, acceleration pedal percentage, and brake pedal percentage. All the data is updated every 0.01 s.

3.1 Vehicle Model

The vehicle model used in this work is based on the two-degree-of-freedom bicycle system, as shown in Fig. 6. This model considers the car's rotation around the z-axis (θ) and its lateral velocity. Assuming x and y as the vehicle's frame coordinates, respectively, and θ its rotation in the z-axis, X , Y , and Θ are their absolute equivalents in the global frame. Thus, the vehicle frame can be expressed using the rotation angle θ in the global frame ($\Theta = \theta$). Finally, The steering angle, expressed in the vehicle's frame, is defined as δ and admits that both wheels turn the same value. By applying Euler–Newton equations [46], it is possible to simplify the vehicle's dynamics in the plane as:

$$m\ddot{x} = m\dot{y}\dot{\theta} + F_{x_F} + F_{x_R}, \quad (1a)$$

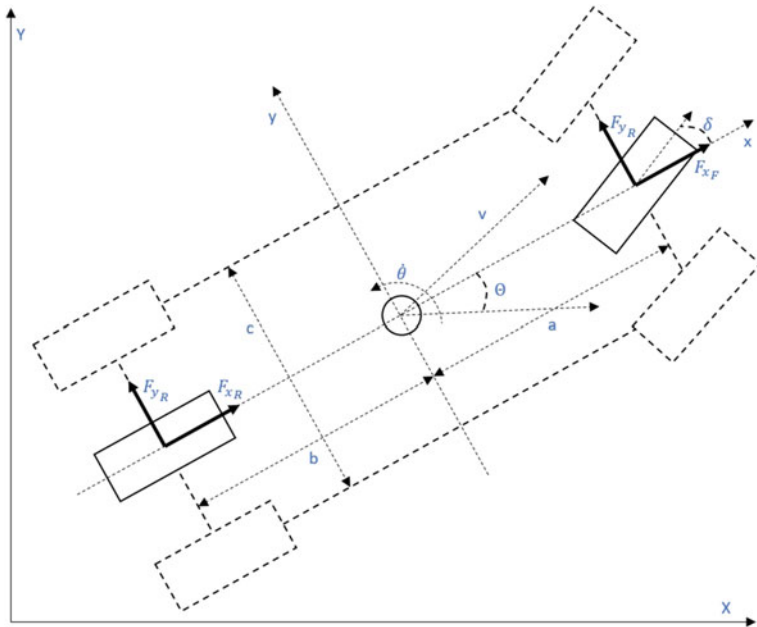


Fig. 6 Vehicle 2D model and coordinates

$$m\ddot{y} = -m\dot{x}\dot{\theta} + F_{y_F} + F_{y_R}, \quad (1b)$$

$$I\ddot{\theta} = aF_{y_F} - bF_{y_R} + c(-F_{x_{F,l}} + F_{x_{F,r}} - F_{x_{R,l}} + F_{x_{R,r}}), \quad (1c)$$

where I is the inertia moment, m is the vehicle mass, and F_x and F_y are the forces in x and y directions, and the subscripts r and l indicates the force direction compound. Finally, the kinematic model, translated to X and Y coordinates, can be described as:

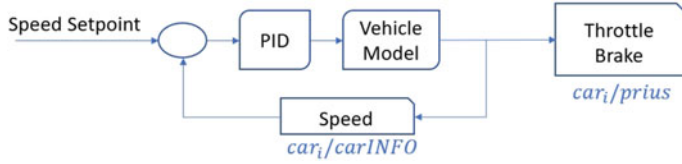
$$\dot{X} = \dot{x} \cos \Theta - \dot{y} \sin \Theta, \quad (2a)$$

$$\dot{Y} = \dot{x} \sin \Theta - \dot{y} \cos \Theta, \quad (2b)$$

$$\dot{\Theta} = \dot{\theta}. \quad (2c)$$

3.2 Cruise Controller (CC)

Like an actual vehicle, the Prius model does not allow direct speed control but only throttle and brake adjustments. So, this simulator adopts a Proportional Integral

**Fig. 7** PID CC

Derivative (PID) strategy to the vehicle speed controller. Although this controller is quite simple, it will help the student to develop basic control skills and move towards other implementations, including several autopilot strategies and tuning models [47]. In this way, the Cruise Controller (CC) will be responsible for keeping the vehicle constant speed during the vehicle's movement and adjusting it when necessary, changing the brake and the throttle pedals, through the *car_i/prius* topic. The PID equation is defined as follows:

$$\alpha(t) = K_P * \varepsilon^\sigma(t) + K_I * \int \varepsilon^\sigma(t) dt + K_D * \frac{\Delta \varepsilon^\sigma(t)}{dt}, \quad (3)$$

where K_P , K_I , and K_D denote the Proportional, Integral, and Derivative gain constants respectively, $\varepsilon^\sigma(t)$ is the speed error, measured by the difference between the current speed value and the desired one and α is the desired system acceleration. The α is then normalized to a value between $-1 \dots 1$, representing the Throttle and Brake pedals usage. A positive value indicates that the Throttle pedal has been used while the Brake is free. Conversely, the Brake is pressed for a α negative value, and the Throttle pedal is free. The complete controller is illustrated in Fig. 7, where it is assumed that the time constant of the actuator is much bigger than the motor one, and the CC algorithm is summarized in Algorithm 1.

Algorithm 1 Cruise Controller Algorithm

Input: Speed Set Point, Current Speed
Output: Throttle and Brake percentage

- 1: $\varepsilon^\sigma \leftarrow \text{speed_set_point} - \text{current_speed}$
- 2: $\alpha \leftarrow \text{PID}(\varepsilon^\sigma)$
- 3: $\alpha_{control} \leftarrow \text{Normalized}[-1 \dots 1](\alpha)$
- 4: **if** $\alpha_{control} \geq 0$ **then**
- 5: $\text{throttle} \leftarrow \alpha_{control}$
- 6: $\text{brake} \leftarrow 0$
- 7: **else**
- 8: $\text{throttle} \leftarrow 0$
- 9: $\text{brake} \leftarrow \alpha_{control}$
- 10: **end if**

3.3 Line Follower

In this work, the vehicle will simulate a standard trajectory path following method, using a road line [48]. The simulated car has several cameras, and one of them is used to identify the road line and follow it with real-time detection. The Line Follower (LF) algorithm processes the captured image and delivers information regarding the line position to the controller. The vehicle's controller will keep its center over the line with a second PID controller. The implemented algorithm is similar to the one proposed in [49]. Nevertheless, as Gazebo provides a realistic camera view, it is possible to implement algorithms without a real one, changing the image coordinates, frame rate, data size, among other image capture characteristics, and evaluate the changes' impact over the controller.

An OpenCV node was implemented to read the data from the onboard front camera. This node subscribes to the topic *car_i/front_camera* and virtually receives all the images from the camera in an 800×800 pixels frame. Then, the LF algorithm filters the image to find a vertical line in the track, and the detection is performed using the Progressive Probabilistic Hough Transform (HT) [50]. This method is commonly used in image processing and can help detect any shape if it can be represented in mathematical form.

The Line Detection (LD) algorithm is illustrated in three frames of Fig. 8. The first one, in Fig. 8a shows the vehicle camera simulated view. The LD algorithm applies a mask over this image to filter it, highlighting a particular color. This color can be adjusted following the Red Green Blue (RGB) model. The filtered image is then converted to a greyscale picture, as presented in Fig. 8b, allowing the edges detection using the Canny Edge detection [51], using vectors with Cartesian coordinates. Finally, these edges are integrated with the HT, defining a *most probably* line to be followed, as demonstrated in Fig. 8c.

The line coordinates are published in *car_i/line_data* topic and can be used by the LF controller module. This module is called *controller* and is responsible for the vehicle's motion controller. The vehicle heading error (ε^θ) related to the line reference

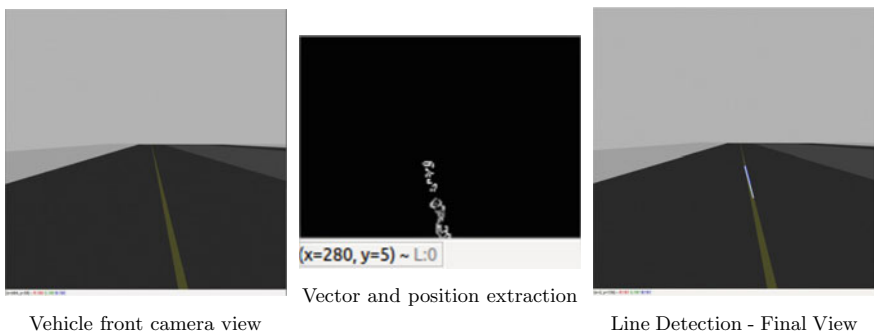
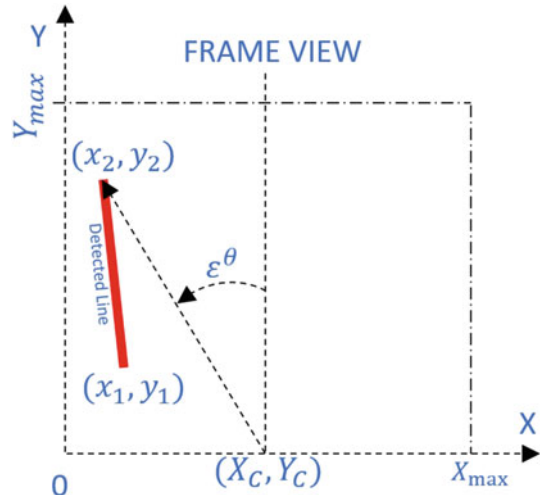


Fig. 8 Line detection process

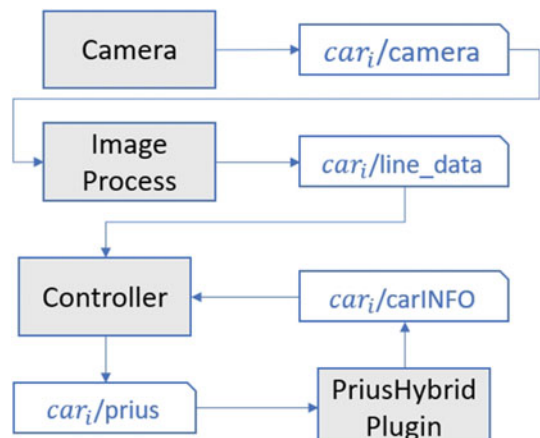
Fig. 9 Vehicle heading error (ε^θ)



is defined as a relative measurement, using the center of the image frame as illustrated in Fig. 9. In this figure, the *Detected Line* is the output of the LD algorithm, with (x_1, y_1) and (x_2, y_2) respectively the initial and the final coordinates. The X_{max} and Y_{max} represent the frame limits and X_C is the frame center point in X axis. The ε^θ is defined as the angular difference between the X_C and the (x_2, y_2) coordinates, given by Eq. 4. Finally, the *controller* calculates the car's *Steering Wheel Angle*, using the PID control action presented in Eq. 5.

$$\varepsilon^\theta(t) = \arcsin \frac{X_C - x_2}{y_2 - Y_C} \quad (4)$$

Fig. 10 Line detection and driving controller



$$\theta_{wheels}(t) = K_P^\theta * \varepsilon^\theta(t) + K_I^\theta * \int \varepsilon^\theta dt + K_D^\theta * \frac{\Delta \varepsilon^\theta(t)}{dt}, \quad (5)$$

where K_P^θ , K_I^θ and K_D^θ denote the Proportional, Integrator, and Derivative gain constants, and θ_{wheels} is the *Steering Wheel Angle* to be applied to the vehicle. Figure 10 shows the general LF flowchart, including the controller action, while the complete LF algorithm can be observed in Algorithm 2.

Algorithm 2 Line Follower Algorithm

Input: Image Frame

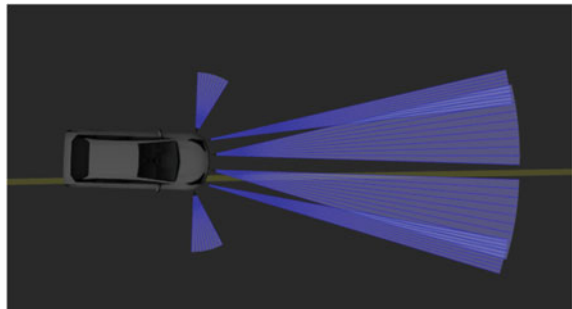
Output: Steering Angle

- 1: Mask image to find Vertical Lines
 - 2: Filter image to obtain Data Vectors
 - 3: $Line_Vectors \leftarrow Hough_Line_Transform$
 - 4: $Line_Coordinates \leftarrow MERGE(Line_Vectors)$
 - 5: $\varepsilon^\theta \leftarrow Eq. 4$
 - 6: $\theta_{wheels} \leftarrow PID(\varepsilon^\theta)$
-

3.4 Obstacle Detection and Avoidance

Obstacle detection and avoidance is one of the most common autonomous vehicular application, given the demanded safety conditions. So, in this simulator demonstration, sonars are used to detect and avoid unpredicted obstacles and help the vehicles to keep the LF algorithm. The car_i will use six sonars: four in the car's front and one on each side of it, as seen in Fig. 11. The simulator allows the user to change the sonar's positions and ranges and add or remove them in *prius.urdf* file. This simulator assumes that the obstacles are positioned near the reference line and have the same lateral size as the vehicles.

Fig. 11 Sonar visualization



Algorithm 3 Line Follower with Detection and Avoidance Algorithm**Input:** Sonars Info, Image Frame**Output:** Steering Angle

```

1: while Object_Detected do
2:   if Right_Object_Detected then
3:      $\theta_{wheels} \leftarrow Left\_Deviation$ 
4:   else if Left_Object_Detected then
5:      $\theta_{wheels} \leftarrow Right\_Deviation$ 
6:   end if
7: end while
8: Line_Follower_Algorithm (Algorithm 2)

```

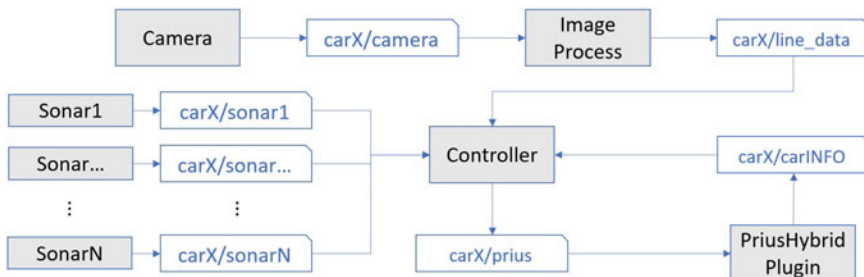


Fig. 12 General vehicle architecture, with line detection and detection and avoidance modules

The sonars are used together with the LF algorithm. However, as the Detection and Avoidance (DA) algorithm has priority over the LF, it assumes the vehicle controller until the obstacle is out of view and the LF is reactivated. So, the algorithm 3 is an extension of the LF algorithm. When the sonars detect an obstacle, the DA controller turns the vehicle in the opposite direction, within a fixed θ_{wheels} value. This heading adjustment is continued until the four front sonars stop detecting the obstacle. Then, the lateral sonars avoid the vehicle trying to return to the line before it overtakes the obstacle. Finally, the LF algorithm uses the last information about the detected line to return to the desired trajectory. The DA block diagram is presented in Fig. 12.

4 Experimental Validation

A control simulation environment should present several controller tools to the student. This section will introduce three main tools developed in RosDrive that allow the student to analyze the vehicle's controller performance and elaborate on different strategies to guarantee its safety. The vehicle's controller performance can be defined in several ways, including fuel consumption, final speed, acceleration, among others. In this chapter, the performance is measured by the vehicle's capacity to track the setpoint, both in speed and heading adjustments.

Table 1 Cruise Controller PID Settings

CC	K_P	K_I	K_D
PID1	10.8	0.0	0.0
PID2	10.8	2.16	0.270
PID3	10.8	4.32	0.135
PID4	10.8	2.16	0.135

4.1 Cruise Controller Implementation

The CC was developed as an independent module. So, it works as a black box implementation, where the inputs are the setpoint and current vehicle's speed, and the outputs are the throttle and brake percentage, while the controller parameters are adjusted inside the module. This architecture choice increases the simulator's flexibility, allowing the user to replace the controller and adjust its parameters.

Taking into account Fig. 3, the straight line between the points 7 and 1, without obstacles, was used to evaluate the CC and check how does the vehicle behaves with several accelerations and decelerations. In this scenario, the vehicle speed setpoint was changed from 20.0, to 14.0, 16.0, 12.0 m/s and finally 0.0 m/s. All the speed settings are defined in the *controller.py* file in the parameters section. They are related to the vehicle's current position on the track.

The controller parameters K_P , K_I , and K_D were defined with the Ziegler Nichols (ZN) empirical method [52]. The vehicle was accelerated from a rest position until it reached the first setpoint speed in the proposed scenario. Increasing K_P until the system oscillation limit, it was possible to determine the ultimate gain (K_u), at 18, with a period of 0.1 ms. These values show how the vehicle's actuator has a rapid response since the oscillation period is fast. In this test, the Ziegler Nichols Tuning parameters are $K_P = 10.8$, $K_I = 2.16$, and $K_D = 0.135$. The system's response is presented in Fig. 13.

As described above, the RosDrive was designed so that the student can change the system's characteristics and observe the impact on the vehicle's response. In addition to changing the controller model, the change of control parameters already implies different responses to be analyzed, providing the user with a practical study of the characteristics of each one of them. Three variations of the parameters obtained with ZN are proposed to exemplify their impacts on the vehicle's control action. These parameters are shown on the Table 1, where *PID1* is a proportional-only controller, *PID2* increases the derivative component, *PID3* enforces the integrator component, and finally *PID4* shows the parameters obtained by the method ZN.

Figure 13a and b show in detail the impact of controller changes on the system response, and in Fig. 13b it is possible to observe that the control proportional-only (*PID1*) presents a more significant oscillation and that the increase of the derivative component (*PID2*) makes the response slower, but with a smaller overlap. On the other hand, the increase in the integrator component (*PID3*) makes the system faster

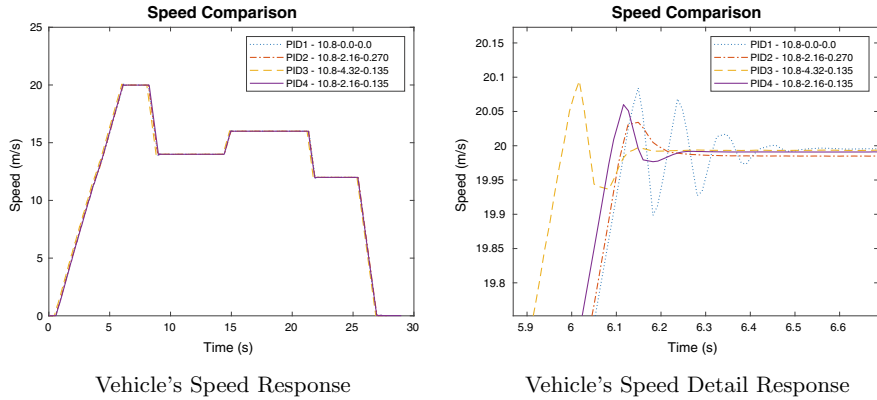


Fig. 13 Vehicle speed response to different PID parameters

but with a greater overshoot on the setpoint. In this scenario, the parameters obtained by ZN show a better response as they are at an intermediate point of response time and overshoot. In all models presented, the controller error was minimal with a maximum steady-state value lower than 0.006 m/s.

The PID CC example shows the student the basic vehicle controller models. It translates the conceptual controller view to a practical application, reducing the gap between the theoretical aspects and the implementation one, allowing the development of active skills and opening the doors to the student's creativity. A shortly CC RosDrive demonstrator is presented in <https://youtu.be/QFVwgFyhaF4>. All the video demonstrators links are presented in Sect. 5.

4.2 Line Follower (LF) Controller

The LF controller is responsible for the vehicle's heading adjustment, performed by the Heading Controller (HC). This control ensures that the vehicle safely makes the circuit curves, preventing accidents. As can be seen in Fig. 3, in this scenario, tighter curves were chosen, allowing the student to analyze more complex situations, such as car skidding. Under these conditions, the vehicle's controller is adjusted in one curve and then evaluated its performance on the whole circuit.

Initially, the circuit's curves radius were analyzed to define the maximum speed that would prevent the vehicle from going off at the curve's tangent. The maximum speed (v_{out}) is given by $|v_{out}| = \sqrt{\mu \cdot |g| \cdot R}$, where μ is the friction's coefficient, $|g|$ is the gravity acceleration and R is the curvature ray. In the proposed scenario, it is defined that $\mu = 0.9$, $g = -9.8 \text{ m/s}$, and $R = 18.38 \text{ m}$, which means that $v_{out} = 13.34 \text{ m/s}$.

Table 2 HC PID parameters

HC	Speed (m/s)	K_P^θ	K_I^θ	K_D^θ	HC	Speed (m/s)	K_P^θ	K_I^θ	K_D^θ
<i>REF</i>	13	10.0	0.0	0.5	<i>PID8</i>	15	10.0	1.0	1.0
<i>PID5</i>	15	10.0	0.0	0.5	<i>PID9</i>	15	10.0	0.5	0.0
<i>PID6</i>	15	10.0	0.0	1.0	<i>PID10</i>	15	10.0	0.5	0.5
<i>PID7</i>	15	10.0	0.0	1.0	<i>PID11</i>	15	10.0	1.0	0.0

The heading controller has a different evaluation in comparison with the CC. In the CC, the setpoints are defined through a step function, while in the HC, the setpoints function follows the curve design, with a long transition phase. It means that the system's response should be evaluated after the desired heading is constant. Due to this condition, a more complex scenario is proposed to evaluate the system's response in adversarial conditions. Initially, the vehicle's trajectory was fixed with v_{out} as the heading reference. Then, the objective was to find the most suitable HC PID parameters for the system with $v = 15$ m/s. It means that the HC will suffer from skidding. In this scenario, the student's experience determining the best HC PID parameters will be necessary since the ideal conditions presented in theory are not present. Furthermore, it will increase the student's perception of the problem and stimulate creative new solutions since the vehicle's speed increase will increase the skidding, compromising the system's stability. It is also important to highlight that the user can set up any speed and check its response.

The HC PID parameters were obtained initially in curve 7 given the long straight lines before and after. The obtained parameters are presented in Table 2. Figure 14a presents the vehicle's trajectory on curve 7, while Fig. 14b perform an in-depth view of the same curve. Both figures illustrate how the reference HC has a smoother trajectory, with no skidding. As expected, there is some skidding in all the HC PID configurations, with a speed setpoint of 15 m/s. However, these figures analysis allow the identification of the best controller performance, even on these conditions. So, in the proposed scenario, the *PID7* presents a better response due to the derivative action, avoiding extreme adjusts keeping the vehicle's trajectory near to the *REF* trajectory. On the other hand, the integral action presented in *PID8* and *PID11* configurations produces more oscillation and increases the distance between the *REF* and the performed trajectory due to the skidding.

Figure 15 presents the vehicle's heading error (ε^θ), due to the different HC PID parameters. As expected, while the LF reference adjusts the heading setpoint, the vehicle's heading suffers from much oscillation, trying to respond to the new conditions. However, the system's response can be better studied after the transition, when the LF algorithm sets the new line. This situation can be observed in Fig. 14b. This figure highlights the smooth response of *PID7*, with little oscillation above the *REF* response. Nevertheless, the systems' response with *PID8* and *PID11* have a considerable overshoot and take much more time until the stabilization.

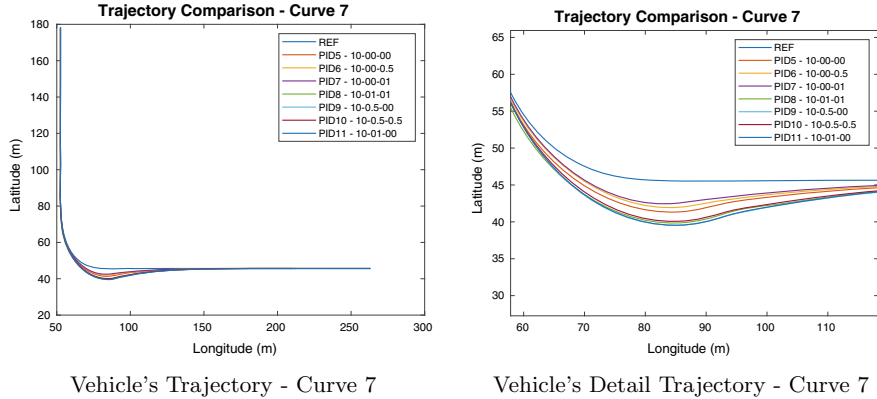


Fig. 14 Vehicle trajectory analysis (curve 7) under different HC PID settings

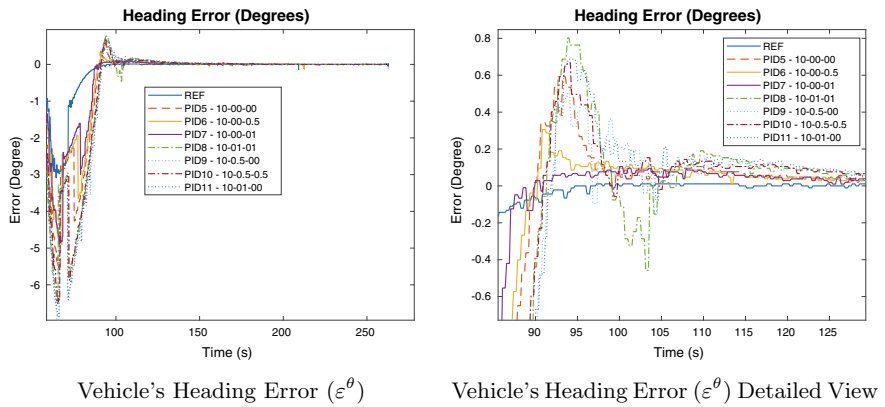


Fig. 15 Vehicle heading error(ε^θ) at curve 7 under different HC PID settings

The HC PID response analysis can be extended to the entire circuit. Looking at the heading error (ε^θ) presented in Fig. 15, the best controllers response were performed by the PD configurations, namely the *PID6* and *PID7*. Furthermore, a full lap was performed to evaluate the vehicle's heading controller, comparing its trajectory and the general ε^θ . Figure 16a present the vehicle's trajectory comparison in the full lap. It shows the vehicle's skidding in all the curves and the most distinguished one in curve 4. Thus, Fig. 16b highlight the vehicle's trajectory in this curve, showing that although all the HC PID configurations suffer from high skidding on this curve, the *PID7* configuration provides a smaller skidding and is the faster one to stabilize the system after the curve. Finally, the Fig. 16c shows a comparison between the general ε^θ during the full lap. It demonstrates that the *REF* configuration has the smallest error variation during the circuit and that the *PID7* error response is the most approximate to it.

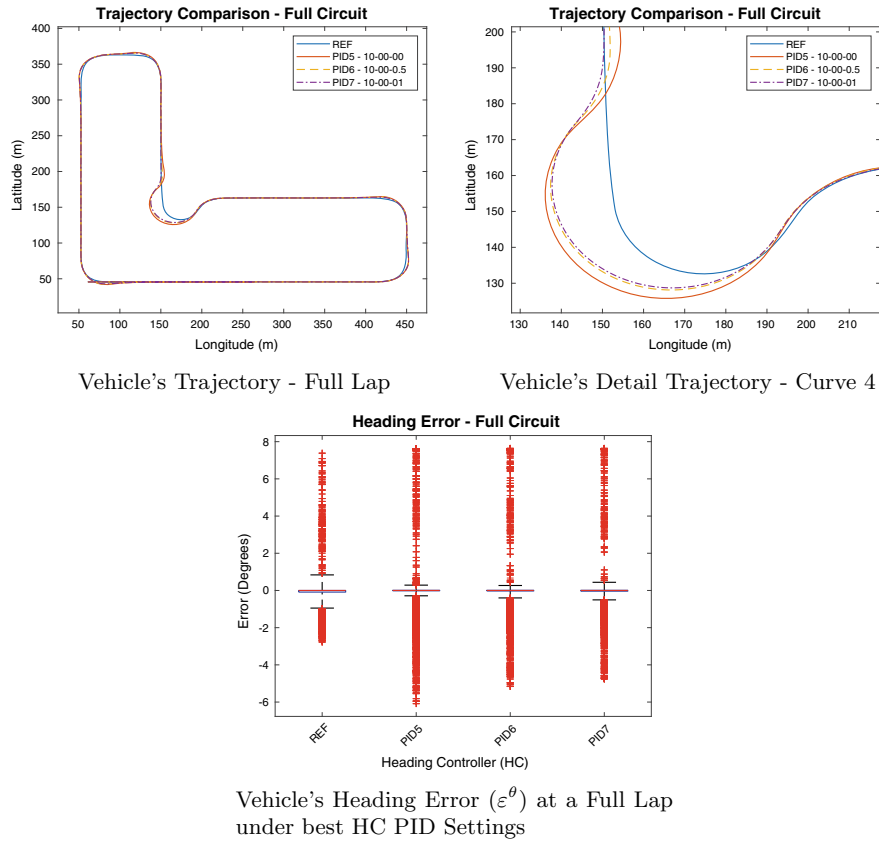


Fig. 16 Vehicle trajectory analysis (Full Lap) under different HC PID settings

This scenario was built to illustrate the simulator's flexibility, merging the LF algorithm with the HC method under an adversarial context. In this way, the student will be able to extend its capabilities, changing the controller's parameters and checking the system's response, proposing new situations, and evaluating them. Furthermore, it will help students build and reinforce their capabilities and skills without damaging any equipment by extrapolating the commonly encountered theoretical conditions.

4.3 *Obstacle Detection and Avoidance*

In addition to the analysis of the CC and HC controllers on the vehicle's performance in isolated scenarios, RosDrive allows the analysis of its interaction with other vehicles, whether static or dynamic.

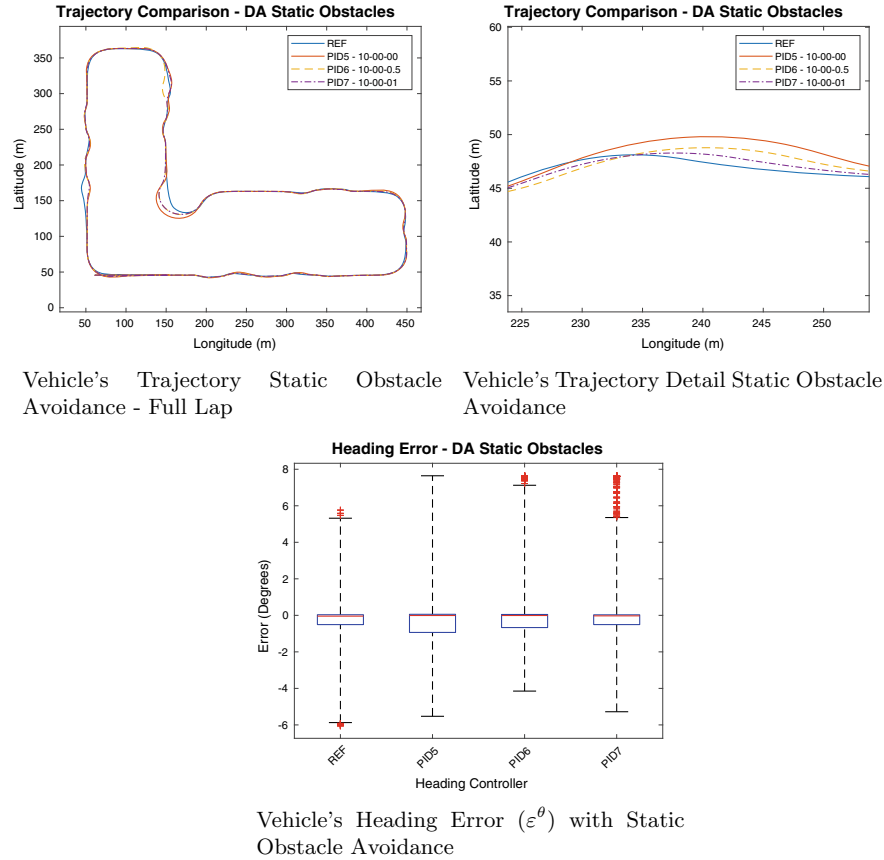


Fig. 17 Vehicle trajectory analysis (static obstacle avoidance) under different HC PID settings

4.3.1 Static Obstacle Detection and Avoidance

The vehicle's ability to perform a trajectory avoiding several close obstacles was initially analyzed, comparing the heading error (ϵ^θ) given the HC parameters changes. The 19 static obstacles are illustrated in Fig. 3 and are modeled as Pickup vehicles. These obstacles are positioned on the straight circuit lines avoiding curves overtaking. Again, the *REF* vehicle running with a 13.0 m/s speed was presented against the *PID5*, *PID6*, and *PID7* HC configuration, running at 15.0 m/s. The vehicle's trajectory is presented in Fig. 17a, illustrating that the skidding is still present, mostly in curve 4.

Furthermore, the vehicles do not necessarily follow the same trajectory to avoid obstacles. This situation is illustrated in the straight line between curves 4 and 5, where the vehicle with the HC *PID6* avoids the last obstacle with a left turn and the others perform a right curve. This obstacle avoidance action responds to the first

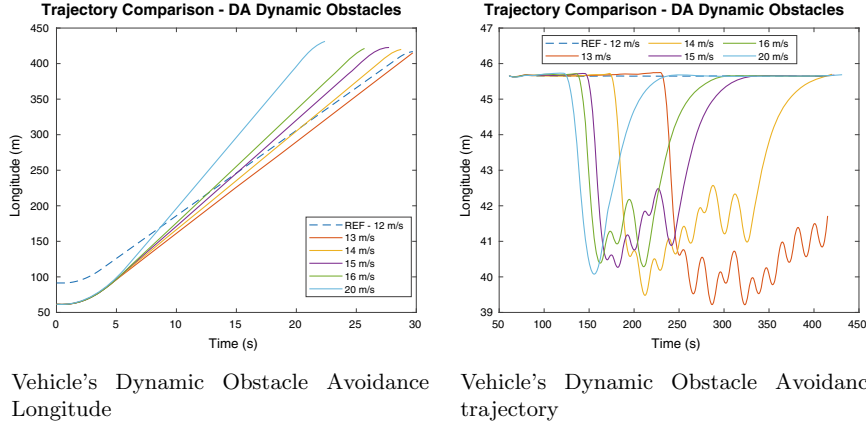


Fig. 18 Vehicle trajectory analysis (dynamic obstacle avoidance)

sonar activated in the vehicle. As the vehicle's trajectories are slightly different due to the HC response, the car's angular position at that point is not the same for all the configurations, providing different sonar activation. The same situation is observed in the last obstacle between curve 7 with all the HC PID configurations compared with the *REF*.

To compare the HC PID's performance in a static detection and avoidance condition, Fig. 17b emphasize the vehicle's movement over the second track obstacle. It is possible to observe that the HC PID performance follows the model presented in the LF algorithm, with *PID7* providing the best system's response in comparison with *REF*. However, the ε^θ 's variation between *REF*, *PID6*, and *PID7* is similar, given the rapid heading transitions triggered by the ODA and the LF algorithms, as presented in Fig. 17c. On the other hand, the boxplots of *PID7* ε^θ in both Figs. 16c and 17c show that although the maximum variation is similar, these errors appear more frequently, no longer presenting themselves as outliers but as values that are repeatedly perceived. These errors happen due to several obstacles and the constant need to adjust the vehicle's position caused by the HC action.

4.3.2 Dynamic Obstacle Detection and Avoidance

RosDrive's flexibility allows different control models, algorithms, and movement strategies. Thus, it is possible to evaluate strategies for overtaking vehicles in motion, observing how the fastest vehicle behaves and if it can perform the maneuver safely. To conduct this demonstration, the *car₁* and *car₂*, with $v_1(t) > v_2(t)$ were defined, with $x_2(0) = x_1(0) + 30\text{ m}$. This way, *car₁* has time to reach its maximum speed before the sonar detects the presence of *car₂* and only then starts the overdrive process.

The *vehicles.launch* allows the setup and launches of the necessary vehicles, with no additional development. In this file, the vehicle models, their initial positions, and the algorithms to be used are instantiated. Initially car_1 (*REF*) and car_2 are defined with the same CC and HC parameters as *PID4* and *PID7*. In the same file, the car_2 sonars are deactivated, avoiding its reaction to car_1 presence. So, car_1 accelerates, detects the presence of car_2 and performs the overtake action. As the same ODA strategy presented in Sect. 3.4 is applied, after the obstacle detection, car_1 will return to the line only after overtaking the obstacle, when the lateral sonars indicate that there are no more obstacles there.

In this scenario, v_2 was defined as 13.0, 14.0, 15.0, 16.0, and 20.0 m/s and $v_1 = 12$ m/s, while the front sonar's ranges are set to 20 m and the lateral ones are 2 m.

When theoretically studying physical systems, it is common to analyze that vehicles are points in space and that overtaking, for example, is just a matter of validating the relationship between space traveled in time, having as reference the speed of the two points. However, in a realistic simulator, vehicles cannot be treated as points in space but as bodies that can collide and must avoid this to remain safe. Thus, the overtaking process begins with detecting the body ahead, followed by a diversion action and consequent movement.

This controller action of car_1 is illustrated in Fig. 18. Figure 18a illustrates a more simplified view of the system, indicating the longitudinal trajectory of car_1 and car_2 under all different velocity conditions of car_1 . It is important to note that the movement of car_2 is the same in all scenarios, as its speed is constant, and its movement is not affected by car_1 . In this figure, it is possible to observe the crossing point when the curve referring to car_1 crosses the curve of car_2 . Thus, it is seen that the speed of 13.0 m/s, car_1 is not able to exceed car_2 on the desired route, indicating an unsafe maneuver.

However, extending this view to a 2D dimension, as presented in Fig. 18b, it is possible to analyze how does the overtake movement is performed. Under the proposed conditions, only the vehicle with a 20 m/s speed has overtaken car_2 with no oscillatory movement. With other speeds, car_1 lateral sonar detects car_2 presence, and adjust car_1 heading position, avoiding a collision. This figure illustrates how car_1 with a 13.0 m/s speed cannot overtake car_2 in the desired time and finally, how the same movement with 14.0 m/s is dangerous since the overtaken process ends just at the limit of the desired trajectory.

In this way, the student has more information to check how the movement was performed and propose different safety strategies. In addition, this scenario allows the student to create new sonars detection algorithms, different controller strategies, and some intelligent systems to increase the system's safety.

5 Conclusions and Future Works

This chapter presents RosDrive, an open-source simulator for developing the study of vehicle control techniques in a realistic way. It presents the conditions that make this simulator able to bring together the students' theoretical lessons with their practical implementation, reducing gaps in their training. By using ROS as a development platform, RosDrive is compatible with the most diverse Linux systems and has continuous support. In addition, its wide adoption by the community allows for the rapid introduction of new sensors and components and integration with other platforms.

Scenarios were developed to evaluate vehicle speed and heading control models using systems similar to actual vehicles. These systems use acceleration and braking variation and cameras to analyze the environment and take action. Furthermore, algorithms were introduced to avoid collisions between controlled vehicles and static or dynamic obstacles, providing different analyzes and conditions for different control and security systems.

For this, RosDrive features a modular architecture based on a flexible set of easily adjustable and interchangeable control tools to assist in the extrapolations imagined by students and teachers who will use the tool. With this, we firmly believe that active learning can be reinforced in classrooms, introducing low-cost dynamic models that mimic reality, increasing the applicability of knowledge, and consolidating the skills necessary for the formation of the control engineer.

Shortly, we hope to develop communication between vehicles, enabling the exchange of information between them, simulating scenarios referring to the ITS models. We also hope to extend the configuration modules for more intuitive platforms using windows that facilitate the user's vision. Finally, we plan to introduce the use of RosDrive in a classroom context, visualizing the difficulties of students and teachers and analyzing the impacts of its adoption in teaching control systems.

Supplementary Material: Simulator Installation and Execution Instructions

This section presents the main requirements for installing and configuring RosDrive Simulator. Furthermore, it summarizes the prerequisites and indicates the current repository for downloading the necessary files.

5.1 Main Code Repository

- The complete code can be found at: <https://github.com/enioprates/rosdrive>

5.2 Main Requirements

- Operating System: Ubuntu 18.04
- ROS Distribution: Melodic
- Gazebo: 9 or above
- Python: 2.7 or above
- GCC: 7.3 or above

5.3 Setup Project

1. Install ROS Melodic following the instructions of:
<http://wiki.ros.org/melodic/Installation/Ubuntu>.
2. Download files from Github RosDrive Simulator:
<https://github.com/enioprates/rosdrive>
3. RosDrive Setup
 - **RosDrive Simulator**
 - (a) Open a new terminal inside .../CISTER_car_simulator
 - (b) Type: catkin_make
 - **RosDrive Simulator Controllers**
 - (a) Open a new terminal inside .../CISTER_image_processing
 - (b) Type: catkin_make

5.4 How to Run RosDrive Simulator

1. Run the simulator:
 - (a) Open a new terminal inside .../CISTER_car_simulator
 - (b) Type: source devel/setup.launch
 - (c) Type: roslaunch car_demo demo_t.launch

The GAZEBO should open on your screen with the vehicle in the position defined in *cars_t_curve_2.launch*. The vehicle will remain stopped until the Vehicle Controller is turned on.

2. PAUSE the simulation and reset the time!
3. Starting the Vehicle Controllers:

- (a) Open a new terminal inside .../CISTER_image_processing
- (b) Type: source devel/setup.launch
- (c) Type: roslaunch image_processing vehicle.launch

This launcher file will start the vehicle's Line Follower Detection and the Vehicle's movement controller, respectively with the nodes *lane_lines_detection.py* and *simulation_connector.py*.

4. Start the Gazebo simulation

5.5 Optional Configuration

1. Speed PID Configuration
 - (a) Open/CISTER_image_processing/src/scripts/simulation_connector.py
 - (b) Find #Speed PID
 - (c) Adjust $K_P \rightarrow kp_vel$, $K_I \rightarrow ki_vel$, and $K_D \rightarrow kd_vel$
2. Heading PID Configuration
 - (a) Open/CISTER_image_processing/src/scripts/simulation_connector.py
 - (b) Find #Steering PID
 - (c) Adjust $K_P^\theta \rightarrow kp_steer_l$, $K_I^\theta \rightarrow ki_steer_l$, and $K_D^\theta \rightarrow kd_steer_l$

5.6 RosDrive Video Demonstrations

1. Cruise Controller demonstrator:
<https://youtu.be/QFVwgFyhaF4>.
2. Line Follower demonstrator:
<https://youtu.be/sRlXk2KIJc>
3. Static Obstacle Detection and Avoidance demonstrator:
<https://youtu.be/YEoO2CQUiKc>
4. Dynamic Obstacle Detection and Avoidance demonstrator:
<https://youtu.be/5135G3aafLw>

Acknowledgements This work was partially supported by National Funds through FCT/MCTES (Portuguese Foundation for Science and Technology), within the CISTER Research Unit (UIDP/UIDB/04234/2020); also by the FCT and the EU ECSEL JU under the H2020 Framework Programme, within project(s) ECSEL/0010/2019, JU grant nr. 876019 (ADACORSA). Disclaimer: This document reflects only the author's view and the Commission is not responsible for any use that may be made of the information it contains.

References

1. Simonsen, B., Fairbanks, S., Briesch, A., Myers, D., Sugai, G.: Evidence-based practices in classroom management: considerations for research to practice. *Educ. Treat. Child.* **31**(1), 351–380 (2008)
2. Maciejewski, A.A., Chen, T.W., Byrne, Z.S., De Miranda, M.A., Mcmeeking, L.B.S., Notaros, B.M., Pezeshki, A., Roy, S., Leland, A.M., Reese, M.D., Rosales, A.H., Siller, T.J., Toftness, R.F., Notaros, O.: A holistic approach to transforming undergraduate electrical engineering education. *IEEE Access* **5**, 8148–8161 (2017)
3. Jamison, A., Kolmos, A., Holgaard, J.E.: Hybrid learning: an integrative approach to engineering education. *J. Eng. Educ.* **103**, 253–273 (2014)
4. McKenna, A.F.: Educating engineers: designing for the future of the field. *J. Higher Educ.* **81**, 717–719 (2010)
5. Shooter, S., Mcneill, M.: Interdisciplinary collaborative learning in mechatronics at Bucknell University. *J. Eng. Educ.* **91**, 339–344 (2002)
6. Xie, Y., Fang, M., Shauman, K.: STEM education. *Ann. Rev. Sociol.* **41**, 331–357 (2015)
7. WEG: Learning workbenches for training. Teaching Equipment. Teaching Equipment. Electric Panels. WEG - Products, May 2020. Library Catalog: <https://www.weg.net/>
8. Nulle, L.: Lucas Nülle - Lucas-Nuelle Training Systems for vocational training and didactic (2020)
9. Feedback PLC: Welcome to Feedback plc (2020). Library Catalog: <https://fbkmed.com/>
10. Galadima, A.A.: Arduino as a learning tool. In: 2014 11th International Conference on Electronics, Computer and Computation (ICECCO), pp. 1–4 (2014)
11. Chancharoen, R., Sripakagorn, A., Maneeratana, K.: An Arduino kit for learning mechatronics and its scalability in semester projects. In: 2014 IEEE International Conference on Teaching, Assessment and Learning for Engineering (TALE), pp. 505–510 (2014)
12. Omar, H.M.: Enhancing automatic control learning through Arduino-based projects. *Eur. J. Eng. Educ.* **43**, 652–663 (2018)
13. Gonçalves, J., Pinto, V.H., Costa, P.: A line follower educational mobile robot performance robustness increase using a competition as benchmark. In: 2019 6th International Conference on Control, Decision and Information Technologies (CoDIT), pp. 934–939 (2019). ISSN: 2576-3555
14. Serrano Pérez, E., Juárez López, F.: An ultra-low cost line follower robot as educational tool for teaching programming and circuit's foundations. *Comput. Appl. Eng. Educ.* **27**, 288–302 (2019)
15. Cruz-Martín, A., Fernández-Madrigal, J., Galindo, C., González-Jiménez, J., Stockmans-Daou, C., Blanco-Claraco, J.: A LEGO mindstorms NXT approach for teaching at data acquisition, control systems engineering and real-time systems undergraduate courses. *Comput. & Educ.* **59**, 974–988 (2012)
16. Leonard, M., Morgan, J., Coffelt, J.P.: Digital systems teaching and research (dstr) robot: a flexible platform for education and applied research. In: Proceedings of the 2018 ASEE Gulf-Southwest Section Annual Conference. The University of Texas at Austin, p. 5, ASEE (2018)
17. Staranowicz, A., Mariottini, G.L.: A survey and comparison of commercial and open-source robotic simulator software. In: Proceedings of the 4th International Conference on PErvasive Technologies Related to Assistive Environments - PETRA '11, Heraklion, Crete, Greece, p. 1. ACM Press (2011)
18. Michel, O.: Webots: professional mobile robot simulation. *Int. J. Adv. Rob. Syst.* **1**, 5 (2004)
19. Open Source Robotic Foundation: ROS/Introduction (2018)
20. Suwasono, S., Prihanto, D., Dwi Wahyono, I., Nafalski, A.: Virtual laboratory for line follower robot competition. *Int. J. Electr. Comput. Eng. (IJECE)* **7**, 2253 (2017)
21. Dosovitskiy, A., Ros, G., Codevilla, F., Lopez, A., Koltun, V.: CARLA: An Open Urban Driving Simulator (2017). [arXiv:1711.03938 \[cs\]](https://arxiv.org/abs/1711.03938)
22. Costa, V., Rossetti, R., Sousa, A.: Simulator for teaching robotics, ROS and autonomous driving in a competitive mindset. *Int. J. Technol. Human Interact.* **13**, 19–32 (2017)

23. Grover, R., Krishnan, S., Shoup, T., Khanbaghi, M.: A competition-based approach for undergraduate mechatronics education using the arduino platform. In: Fourth Interdisciplinary Engineering Design Education Conference, pp. 78–83 (2014). ISSN: 2161-5330
24. Reguera, L.M., Verdu, E., Munoz, M.F., Perez, M.A., de Castro, J.P., Verdu, M.J.: Effects of competitive E-learning tools on higher education students: a case study. *IEEE Trans. Educ.* **52**, 279–285 (2009). Conference Name: IEEE Transactions on Education
25. Tully Foote: Demo of Prius in ROS/GAZEBO (2017). https://github.com/osrf/car_demo
26. Vieira, B., Severino, R., Filho, E.V., Koubaa, A., Tovar, E.: COPADRIVE - a realistic simulation framework for cooperative autonomous driving applications. In: IEEE International Conference on Connected Vehicles and Expo - ICCVE 2019, Graz, Austria, pp. 1–6. IEEE (2019)
27. Filho, E.V., Severino, R., Rodrigues, J., Gonçalves, B., Koubaa, A., Tovar, E.: CopaDrive: an integrated ROS cooperative driving test and validation framework. In: Robot Operating System (ROS), vol. 962, pp. 121–174. Springer International Publishing (2021). Series Title: Studies in Computational Intelligence
28. Filho, E.V., Guedes, N., Vieira, B., Mestre, M., Severino, R., Gonçalves, B., Koubaa, A., Tovar, E.: Towards a cooperative robotic platooning testbed. In: IEEE International Conference on Autonomous Robot Systems and Competitions (ICARSC), Ponta Delgada, Portugal, pp. 332–337. IEEE (2020)
29. Rivera, Z.B., De Simone, M.C., Guida, D.: Unmanned ground vehicle modelling in gazebo/ROS-based environments. *Machines* **7**, 42 (2019)
30. Furrer, F., Burri, M., Achtelik, M., Siegwart, R.: Rotors—A Modular Gazebo MAV Simulator Framework, pp. 595–625. Springer International Publishing, Cham (2016)
31. Vaz, F.C., Portugal, D., Araújo, A., Couceiro, M.S., Rocha, R.P.: A localization approach for autonomous underwater vehicles: a ros-gazebo framework (2018)
32. Kim, M.S., Delgado, R., Choi, B.-W.: Comparative study of ros on embedded system for a mobile robot. *J. Autom. Mob. Robotics Intell. Syst.* **12**, 61–67 (2018)
33. Kuosa, K., Distant, D., Tervakari, A., Cerulo, L., Fernández, A., Koro, J., Kailanto, M.: Interactive visualization tools to improve learning and teaching in online learning environments. *Int. J. Distance Educ. Technol.* **14**, 1–21 (2016)
34. Meyer, J., Sendobry, A., Kohlbrecher, S., Klingauf, U., von Stryk, O.: Comprehensive simulation of quadrotor UAVs using ROS and gazebo. In: Simulation, Modeling, and Programming for Autonomous Robots, vol. 7628, pp. 400–411. Springer, Berlin, Heidelberg (2012)
35. Feng, H., Wong, C., Liu, C., Xiao, S.: ROS-based humanoid robot pose control system design. In: 2018 IEEE International Conference on Systems, Man, and Cybernetics (SMC), Miyazaki, Japan, pp. 4089–4093 (2018)
36. Hambuchen, K.A., Roman, M.C., Sivak, A., Herblet, A., Koenig, N., Newmyer, D., Ambrose, R.: NASA's space robotics challenge: advancing robotics for future exploration missions. In: AIAA SPACE and Astronautics Forum and Exposition, Orlando, FL. American Institute of Aeronautics and Astronautics (2017)
37. NIST: Agile Robotics for Industrial Automation Competition (2020). <https://www.nist.gov/el/intelligent-systems-division-73500/agile-robotics-industrial-automation-competition>. Last Modified: 2020-07-09T09:19-04:00
38. Open Source Robotics Foundation: Prius Challenge (2017)
39. Sherman, M., Eastman, P.: Simtk - simbody: Multibody physics api
40. PyBullet: Bullet real-time physics simulation
41. Smith, R.: Ode - open dynamics engine
42. Lab, G., Lab, H.R.: Dynamic animation and robotics toolkit - dart
43. Hussein, A., García, F., Olaverri-Monreal, C.: Ros and unity based framework for intelligent vehicles control and simulation. In: 2018 IEEE International Conference on Vehicular Electronics and Safety (ICVES), pp. 1–6 (2018)
44. Robotics, C.: Coppelia robotics
45. Rizzato, C., Katyara, S., Fernandes, M., Chen, F.: The importance and the limitations of sim2real for robotic manipulation in precision agriculture (2020)

46. Attia, R., Orjuela, R., Bassett, M.: Combined longitudinal and lateral control for automated vehicle guidance. *Veh. Syst. Dyn.* **52**, 261–279 (2014)
47. Vartika, V., Singh, S., Das, S., Mishra, S.K., Sahu, S.S.: A review on intelligent pid controllers in autonomous vehicle. In: Reddy, M.J.B., Mohanta, D.K., Kumar, D., Ghosh, D. (eds.) *Advances in Smart Grid Automation and Industry 4.0* (Singapore), pp. 391–399. Springer Singapore (2021)
48. Tesla: Transitioning to Tesla Vision (2021)
49. Kondakor, A., Torcsvari, Z., Nagy, A., Vajk, I.: A line tracking algorithm based on image processing. In: 2018 IEEE 12th International Symposium on Applied Computational Intelligence and Informatics (SACI), Timisoara, pp. 000039–000044. IEEE (2018)
50. OpenCV: Hough Line Transform (2019)
51. OpenCV: Canny Edge Detection (2022)
52. Kobatake, K., Okazaki, T., Arima, M.: Study on optimal tuning of pid autopilot for autonomous surface vehicle. *IFAC-PapersOnLine* **52**(21), 335–340 (2019). 12th IFAC Conference on Control Applications in Marine Systems, Robotics, and Vehicles CAMS 2019



Enio Vasconcelos Filho is currently Assistant Professor at the Federal Institute of Goias (IFG). Since 2018, he has been carrying out his Ph.D. in Electrical and Computer Engineering at the University of Porto (FEUP), Portugal. He joined the CISTER Research Unit in 2018, working with Cyber-Physical Cooperative Systems, notably in vehicular communications. He has a BSc degree in Automation and Control (2006) and an M.Sc. degree in Mechatronics Systems (2012), both from Universidade de Brasília (UnB). His most significant interests are autonomous vehicles, communication networks, and artificial intelligence in real-time applications.



Jones Yudi is a Professor at the University of Brasília since 2010, in the area of Industrial Automation. Doctor in Electrical Engineering & Information Technology from Ruhr-Universität Bochum (2018), Master in Mechatronic Systems from the University of Brasília (2010), with a degree in Control and Automation Engineering (Mechatronics) from the same University (2007). Specialist in the design of hardware/software architectures for high-performance embedded systems, focusing on image and signal processing, instrumentation and control. Experience in distributed systems, sensor networks, ubiquitous computing, Industrial Internet of Things and Industry 4.0.



Mohamed Abdelkader is currently an Assistant Professor at Prince Sultan University, Riyadh, KSA, where he leads multiple R&D projects related to autonomous delivery drone system, and autonomous drone hunting system, in the Robotics and Internet of Things lab. Abdelkader obtained his Ph.D. in Mechanical Engineering from King Abdullah University of Science Technology (KAUST) working with real-time distributed autonomous multi-robot systems for pursuit-evasion applications. His main research works are in the development of AI-powered swarm robotic systems, and safe autonomous navigation. He is a technical team lead at Systemtrio, Abu Dhabi, UAE, developing autonomous robotics solutions including a UAV swarm system for security and surveillance, affiliated with the IEEE Robotics and Automation Society, and a reviewer in several robotics conferences and journals including ICUAS, IROS, and JINT.



Anis Koubaa is a Professor in Computer Science, Advisor to the Rector of Research Governance, Director of the Research and Initiatives Center, and Director of the Robotics and Internet of Things Research Lab, in Prince Sultan University. He is also a Senior Researcher in CISTER/INESC TEC and ISEP-IPP, Porto, Portugal. He is also a Senior Fellow of the Higher Education Academy (HEA) in the UK. He received several distinctions and awards including the Rector Research Award in 2010 at Al-Imam Mohamed bin Saud University and the Rector Teaching Award in 2016 at Prince Sultan University. He is on the list of top 2.



Eduardo Tovar received the Licentiate, M.Sc. and Ph.D. degrees in electrical and computer engineering from the University of Porto, Porto, Portugal, in 1990, 1995 and 1999, respectively. Currently he is a Professor in the Computer Engineering Department at the School of Engineering (ISEP) of Polytechnic Institute of Porto (P. Porto), where he is also engaged in research on real-time distributed systems, wireless sensor networks, multiprocessor systems, cyber-physical systems and industrial communication systems. He heads the CISTER Labs, an internationally renowned research centre focusing on RTD in real-time and embedded computing systems. He is currently the Vice-chair of ACM SIGBED and is member of the Executive Committee of the IEEE Technical Committee on Real-Time Systems (TC-RTS). He is currently deeply involved in the core team setting up a Collaborative (industry-academic) Lab on Cyber-Physical Systems and Cyber-Security Systems.

Autonomous Laser-Induced Breakdown Spectroscopy System for Chemical and Mineralogical Designation of Interplanetary Materials



George Stavrinos, Elias Chatzitheodoridis, and Olga Sykioti

Abstract The invention of the laser has pushed the boundaries of technological advancements with its variety of uses. This use case chapter analyses the implementation of an Autonomous Laser-Induced Breakdown Spectroscopy System for Chemical and Mineralogical Designation of Interplanetary Materials. In more detail, it highlights all the major components of the development of an autonomous system that maps the material composition of a meteorite sample using the Laser-Induced Breakdown Spectroscopy method. In the first chapter all key concepts are presented while offering a short literature survey regarding (calibration-free) Laser-Induced Breakdown Spectroscopy. It also highlights the use of the Robot Operating System (ROS) as a tool for the implementation of hardware drivers and autonomy components. Continuing with the details of the implementation, the manuscript focuses on the reference and description of all major hardware components. In the third chapter, the software components of the implementation are discussed. These components include hardware drivers, autonomy capabilities, data visualisation and user interfacing. For interested readers, chapter four offers a quick tutorial on compiling, configuring and running the implemented software. Chapter five summarises the experimental setup and presents results. Finally, this chapter concludes with a quick summary and an overview of the limitations of the implementation along with future work.

Keywords Laser-Induced Breakdown Spectroscopy · LIBS · Mineralogy

G. Stavrinos (✉) · E. Chatzitheodoridis · O. Sykioti

National Observatory of Athens and National Technical University of Athens, Athens, Greece

e-mail: gstavrinos@protonmail.com

URL: <https://gstavrinos.github.io/>

E. Chatzitheodoridis

e-mail: eliasch@central.ntua.gr

URL: <https://www.eliasch.gr/>

O. Sykioti

e-mail: sykioi@noa.gr

URL: <https://members.noa.gr/sykioi/>

1 Introduction

From the invention of the laser in 1959 by Gordon Gould [17], there have been a lot of studies on how to exploit its capabilities. One of the most significant observations was that a concentrated pulsing laser beam could generate radiating plasma on specific materials. This discovery was of major importance since it could potentially be used in the field of spectrochemistry.

1.1 *Laser-Induced Breakdown Spectroscopy*

Laser-Induced Breakdown Spectroscopy (*LIBS*), sometimes mentioned as Laser-Induced Plasma Spectroscopy (*LIPS*), is based on the high photon density laser pulses, which when reacting with a material's surface they create plasma. In the last forty years, LIBS has been flourishing as a technique to qualitatively and quantitatively analyse sample materials.

The main principle of the LIBS technique is to extract the emission spectrum from a spot of a material, in order to acquire its elemental composition. This seemingly simple procedure can lead to extraordinary results and can be applied to a wide variety of applications [21]. Some applications include analysis of cultural heritage items [1] and archaeological conservation state [30], to meteorite samples [14] and interplanetary soil [24].

A typical LIBS setup includes a pulsed laser system that is controlled by a pulse generator. The pulsing laser beam is focused on a sample (in this case a meteorite), on which the high density of photons induces radiation from the generated plasma. This radiation is received by an optical fiber which is connected to a spectrograph. The whole spectra acquisition procedure is driven by a computer system, which also performs all data processing and storage.

Once the spectra data are acquired on the computer, a wide variety of elemental analysis can be conducted on various materials, from molten steel [36] and glass [34] to jewellery [16] and meteorites [12].

A typical setup of a LIBS system is shown in Fig. 1 in the form of a flow diagram.

The importance of a pulse generator lies on the fact that the spectrograph needs to acquire the spectrum after a very strict time frame (of about $1\ \mu\text{s}$). This delay is required because the pulsed laser system during plasma generation creates other physical phenomena like fluorescence that have a strong effect on the acquisition data. Thus, in order to minimise their effects, the pulse generator induces a precise delay between the laser pulse and the spectrograph acquisition.

The above is demonstrated on Fig. 2 as presented in [11]. Initially, and immediately together with the pulse we have a strong signal from the plasma continuum. When plasma cools, then this diminishes/reduces and then we can open the spectrograph (gate) for acquisition. Then the characteristic element excitation is clearly

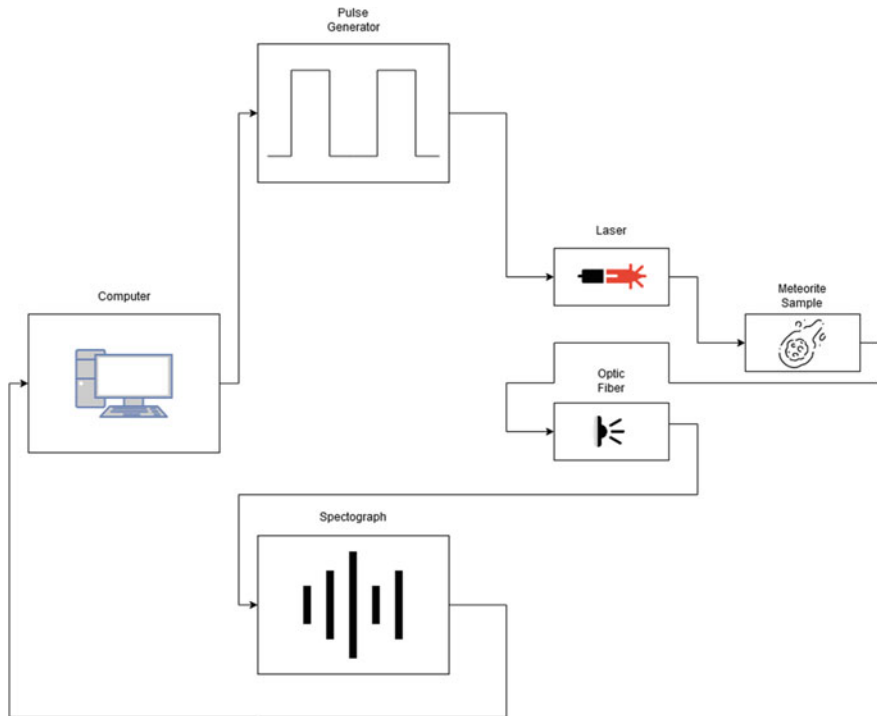


Fig. 1 A typical Laser-Induced Breakdown Spectroscopy setup

visible compared to the reduced plasma continuum (see inserts left top without the delayed gating, and top right the same material with delayed gating of the acquisition spectrograph).

1.2 LIBS Advantages and Disadvantages

The LIBS technique has been extensively studied and already there is an extensive number of publications [15, 19, 37] through which major advantages over other techniques are reported as well as some limitations.

One of the most important advantages is that the LIBS experimental apparatus is very simple to setup and use. Additionally, it can be highly miniaturised to allow fieldwork or to be employed as payload of a mission to another planet [10, 27, 43].

Another important advantage of the LIBS technique is its ability to analyse any type of material, being gas [40], liquid [32] or solid [26]. This makes it very versatile and allows for a variety of experiments without the need to change the apparatus setup or prepare the sample. Additionally, it can analyse the very light and heavy elements.

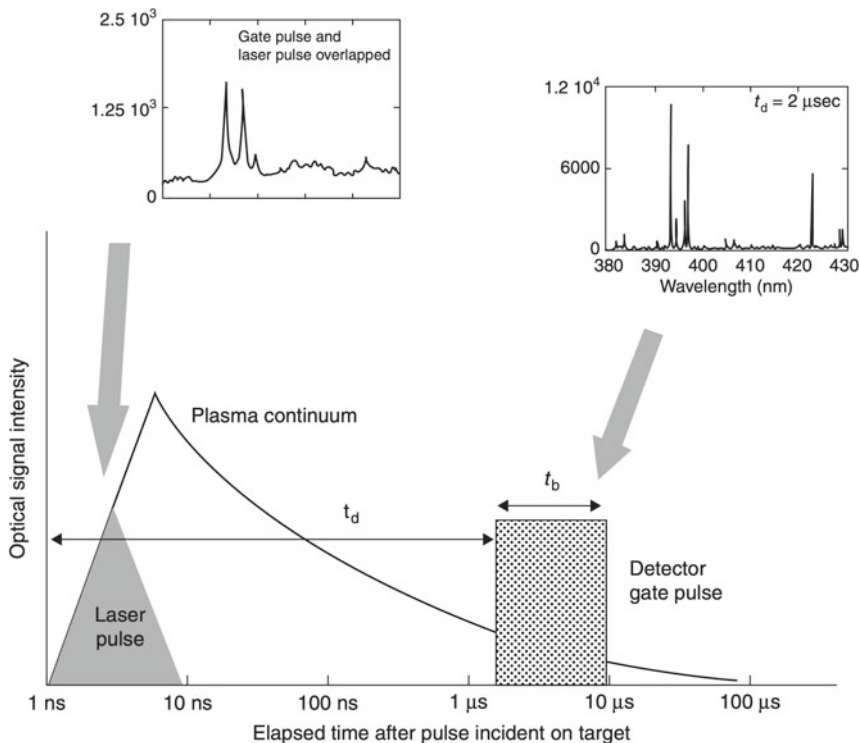


Fig. 2 A schematic overview of the temporal history of a LIBS plasma. The gate delay and window are shown. Inserts illustrate the kind of spectra one might observe at the different times

The results of the LIBS analytical technique are available instantly after each laser pulse. This makes its application extremely useful for in-situ and real-time scenarios.

The limitations of the LIBS are the matrix interference, the requirement for post-processing techniques and the bad repeatability of the measurement that does not allow easy quantification.

The most important one could be interference (matrix) effects during the excitation of the material and the generation of radiating plasma. The presence of the matrix effects is due to the LIBS technique itself. With LIBS, in order to analyse a sample, plasma needs to be created. This generation of plasma involves the ablation of the prototype material, which leads to fluctuation of the expected result. This fluctuation is mainly due to the fluorescence of the plasma generation procedure. In addition to the ablation of the sample, the plasma generation also produces free electrons which can falsely be read by the spectrograph as part of the sample. The plasma that is generated by the pulsing laser beam can also absorb part of the beam itself while cooling, leading, again, to inaccurate results. All of these constitute the matrix effects that can greatly affect the quality of the acquisition results.

Table 1 LIBS advantages and disadvantages summarising table

Advantage	Disadvantage
Simple apparatus	Matrix noise effects
Works with any material	Need for post-processing
Detects all elements even the light ones	Fewer research resources
Instant results	Setup-dependent precision
In-situ and real-time applications	

The generated noise leads us to the next disadvantage of LIBS, which is the need for post-processing filtering techniques. Post-processing techniques can vary from simple averaging of multiple acquisitions to more complicated LIBS dedicated methods [21] like calibration-free LIBS [8].

Another disadvantage that has been in the centre of research using the LIBS technique is the poor precision values and the precision dependence on a variety of experimental setup factors (i.e. sample composition) [5].

LIBS is still a technique under development and the even increasing bibliography and its technical advancements are expected to bring it to the required maturity, especially in performing quantitative measurements.

Table 1 summarises the advantages and disadvantages of the LIBS technique.

1.3 Calibration-Free LIBS

Studying the disadvantages of the LIBS method, a major observation arises; even though the qualitative results of the technique are instant and easy to acquire, they lack the accuracy found in other methods, such as the acquisition using a scanning electron microscope (SEM), for quantitative analyses, and thus require corrections during post-processing that is performed through the comparison with standards of similar chemical matrix or calibration curves. This process can prove very time-consuming, and this is why researchers have worked into implementing a new method of LIBS called Calibration-Free Laser-Induced Breakdown Spectroscopy (*CF-LIBS*) [8].

With traditional LIBS, as stated earlier, the matrix effects must be reported and documented as accurately as possible in order to subtract them from the result of the experiment. CF-LIBS avoids this last step, nullifying the need for intricate matrix databases.

In short, the CF-LIBS technique tries to bypass the problem of matrix noise effects by incorporating the matrix itself into the problem of analysing the sample materials. These changes in the matrix itself could be studied in order to derive information about the underlying material composition.

In order for this hypothesis to be valid and dependable, a series of assumptions need to be adopted (as seen in [42]):

- The plasma composition is representative of the unperturbed target composition. This means simply that there are no probabilistic models behind each plasma reading.
- The generated plasma is in Local Thermodynamic Equilibrium (LTE) in the temporal and spatial sampling window. This means that ionisation states are modelled based on the Saha-Boltzmann equilibrium equation. Practically (and simplified) this means that the plasma composition is considered uniform and stable for the duration of acquisition.
- The plasma can be modelled as a spatially homogeneous source.
- The spectral lines included in the calculation are optically thin.

These assumptions are very difficult to satisfy in most experiments. This is the reason why CF-LIBS often presents divergence from the expected/desired results.

The work of Tognoni et al. [42] on the state of the art of CF-LIBS allows for an in-depth analysis of the method which are out of the scope of this study.

1.4 LIBS Applications

LIBS applications include tests on analysing various materials, but also LIBS exploitation for other multi-disciplinary problems.

All applications discussed in this section, have been implemented using either the base LIBS method or the calibration-free one.

As a start, the wide variety of materials analysed using the (CF-)LIBS method should be highlighted. As stated earlier, the LIBS methods have been used on molten steel [36], glass [34], jewellery [16], meteorites [12], gases [40], water and ice [2] and bacteria [33].

The LIBS technique offers only one type of information: the spectrum of each laser pulse. This fact has not discouraged researchers to use it for an immensely wide variety of applications. Using the materials discussed earlier as an example, researchers can characterise (and even appraise) jewellery [16]. Another example is the identification of bacteria [33] under different condition that enhances biologists' understanding on bacteria discrimination based on different experimental environments.

Another very interesting field of LIBS application is interplanetary materials. Many studies have been conducted in various materials, with the ultimate goals to either understand the composition of a meteor from far away [12] or analyse the surface of a planet with instrument payloads on rovers, such as the Curiosity rover on Mars [33]. These studies can surely enhance our knowledge of our outer-Earth environment. They can also provide vital information on habitable worlds and exploitation techniques for interplanetary resource acquisition.

1.5 The Focus of This Study

A topic that a lot of studies have been conducted on, is the process of mapping sample materials [3, 20, 23, 41]. This, in short, means that researchers are not only interested in getting a single spot measurement from a sample, but rather scan it for a series of matrix-like measurements to produce a material composition map. This can be extended to different modes of analyses, such as line and depth profiles, along the surface of the sample and vertical to it inside the sample, or three-dimensional (3D) maps, taking advantage of the destructive character of the technique (i.e., removal of material with ablation and crater formation).

In general, mapping is achieved by moving the sample material (or, in cases, the focus point of a beam) in a two-dimensional plane while reading data from the pulsing laser beam in each individual position of the spatial array. This can be achieved by an X-Y moving plate like those found in 3D printers and CNC machines. Figure 3 shows a typical LIBS mapping setup as found in [4].

The autonomous mapping process is the main goal of this work. In order to achieve such a task, precise control of the XY plate is required, as well as constant knowledge of the position of the plate. With a robust control method, elemental mapping can be achieved by introducing the LIBS technique.

The final product of this manuscript aims to be a basis of a complete autonomous LIBS mapping system that could be used in the future for quantitative analyses using the calibration-free LIBS method.

The steps required to create such a system include the design, collection and construction of the mechanical/hardware part i.e. the laser system, the spectrograph, the kinematic stage etc. Apart from the hardware, complementary software needs to be developed in order to drive (control) each hardware component and also integrate

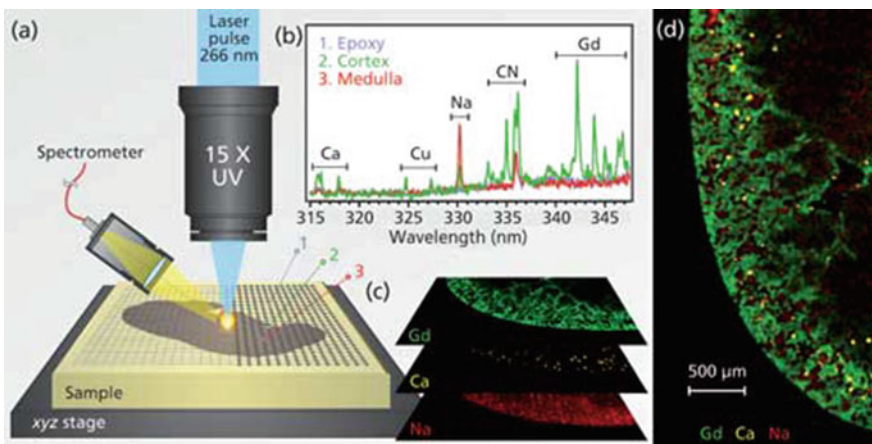


Fig. 3 A typical Laser-Induced Breakdown Spectroscopy mapping setup as presented in [4]

it into a single, seamless pipeline. The software implementation is extremely vital for this custom setup, since it is the basis of all the features and capabilities of the system. In addition, it should be implemented in a way that offers plug-and-play hardware functionality, for easier component upgrade and swapping.

It has to be noted that this study focuses on the analysis of interplanetary materials and more specifically meteorite samples. With that in mind, the system is focused on geological/geochemical and mineralogical analyses of such samples and aims to offer the base tools for easier interpretation of the results.

1.6 *The Robot Operating System*

Mapping the LIBS technique requires interfacing, visualising and planning the mapping process as a different challenge. In order to effectively tackle the mobility, positioning and generally the automation tasks, the *Robot Operating System (ROS)* [31] middleware was selected to be used. Among a variety of robotics and automation frameworks, ROS has the largest community of users and available (open source) software packages.

ROS is a set of software packages that offer interfaces for hardware abstraction and almost plug-and-play autonomy capabilities. It is built around the philosophy that each process, called node, runs in a distributed environment, allowing for easy scalability and transferability of software. Even though it is oriented around robotic platforms being wheeled or legged, the overall value of its already implemented packages remains for the autonomous LIBS mapping implementation. More specifically, this study uses the `ros_control` [7] package and implements the robot hardware interface (`RobotHW`) that allows for hardware abstraction, use of multiple input commands, integration with planners etc. Details on the implementation of the ROS software and its integration with the rest of the system is discussed later in this manuscript.

2 In-Depth LIBS Instrumentation

2.1 *Concept*

As discussed in the introductory chapter, an autonomous LIBS mapping and analysis system consists of a group of interconnected devices. Those devices, as shown in Figs. 1 and 3, are the following:

- A computer (mainly) for control automation and data processing.
- A pulse generator with at least two transistor-transistor logic (TTL) digital outputs to trigger for both the laser beam and the spectrograph.

- A pulsed laser, such as the commonly used solid state Nd:YAG (neodymium-doped yttrium aluminum garnet) laser.
- A kinematic stage capable of moving on an X-Y plane, and in cases vertically to it (Z direction).
- A sample material (in the case of this study, a meteorite sample), which is preferably cut to a flat polished surface.
- An optical fiber to collect the radiation from the cooling plasma. It can be adapted with a focusing lens in the entry side of the fiber and this focus point should be positioned in the volume of the plasma.
- A spectrograph to analyse the spectra collected by the optical fiber.

The rest of this chapter is dedicated to reference and analyse each of the hardware components used in this study. It has to be noted that the optical fibre and the meteorite samples are not discussed in this chapter due to their simplicity and variety respectively. The software side of the implementation and its usage are introduced in the next chapters.

2.2 *Instrumentation*

All of the hardware equipment used for this study along with the facilities of the experiments are located in Prof. Elias Chatzitheodoridis' lab [6] in the School of Mining and Metallurgical Engineering of the National Technical University of Athens, Greece.

2.2.1 **Instrumentation Summary**

This chapter focuses on the hardware side of the autonomous LIBS mapping system. The information circle that starts and ends on the computer is analysed. This circle includes apart from the processing unit, the pulse generator, the laser device, the XY plate movement system and the spectrograph. Figure 4 shows the complete setup used for the work of this chapter. In addition, Table 2 summarises all the hardware components of the setup.

Complementary to the hardware components of the LIBS system, is the software. Software includes hardware drivers, communication protocols, autonomy, visualisation and user interface. All of these software components are discussed in detail in the next chapter.

2.2.2 **The Processing Unit**

It would be rightful to report on the processing unit of the autonomous LIBS system first. In the LIBS system of this use case chapter, the computer is the easiest to acquire

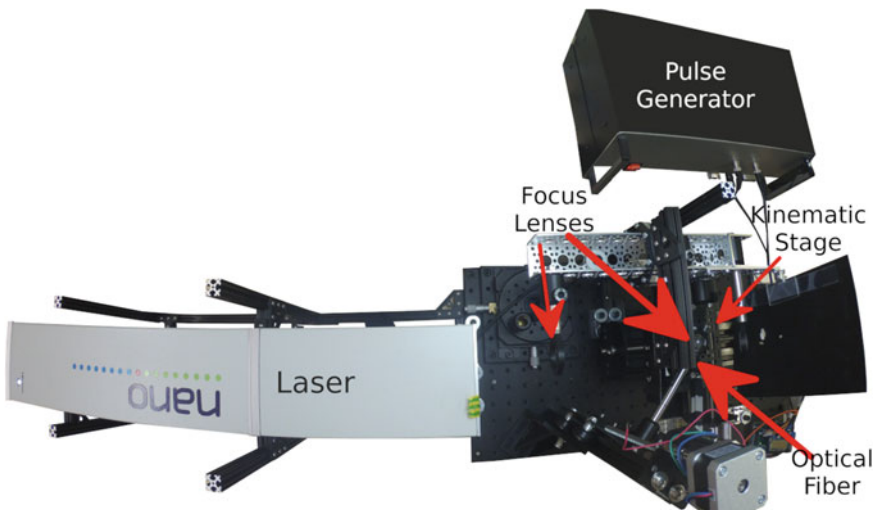


Fig. 4 The top view of the autonomous LIBS mapping setup of this study

Table 2 Hardware setup summary of this study

Computer	Lenovo B50-80
Pulse generator	BNC 588-OEM-1ns
Laser	Litron Nano LG 250-20
Movement system motors	Wantai 57BYGH420
Spectrograph	Ocean optics USB4000

Table 3 Laptop specifications

Manufacturer	Lenovo
Model	B50-80
CPU	i7-5500U
RAM	8 GB (DDR3)
GPU	AMD Radeon R5 M330
VRAM	2 GB
Storage	1 TB (HDD)

and integrate with the rest of the components. Thus, the processing takes place in a consumer grade laptop. Table 3 summarises the specifications of the processing unit that has been used for development. It has to be noted that the implemented LIBS system did not introduce any hard constraints on the required computer hardware. Information regarding the software that was run on this laptop is discussed in the next chapter.

2.2.3 The Pulse Generator

After the processing unit, the flow of information of a LIBS system leads to the pulse generator. As stated earlier, the pulse generator is responsible for generating the required TTL 5 volt signals for triggering a laser pulse from the laser system in order to irradiate a sample and generate plasma on the meteorite sample.

The pulse generator used in this study is the Berkeley Nucleonics Corp (BNC) Model 588-OEM-1ns. This model is a board level, digital pulse generator. These specifications are important in order for the device to generate accurate time gaps in the range of several μ s between triggering signals. Table 4 presents the specifications regarding the model used for this manuscript. The given specifications are not exhaustive for the system; only the most important are included which were used for the development and operation of the newly setup LIBS system. Figure 5 shows the pulse generator as seen by the original website of the company [9].

The pulse generator is connected to the main computer over a USB serial link. Through this link, a set of commands are uploaded to the system with which the two pulse channels would produce two consequent pulses. The code used is included in the first annex of the chapter.

Table 4 Pulse generator specifications

Manufacturer	Berkeley nucleonics corp
Model	588-OEM-1ns
Channel modes	Single shot, burst, normal, duty cycle
Delay	0–1000 s
Pulse width	10 ns–1000 s
Resolution	1 ns
Accuracy	1.5 ns + 0.0001 delay
Time base	50 MHz, 25 PPM crystal oscillator

Fig. 5 The BNC 588-OEM-1ns pulse generator



2.2.4 The Laser

The signals generated by the pulse generator are relayed to the power, control and cooling unit of the laser system. The laser device used in this study is the Litron Nano LG 250-20. Table 5 highlights the basic specifications of this laser device. It should be noted that not all details have been included, but rather only those of interest for the current study. Figure 6 shows the laser device as seen by the original website of the company [25].

Table 5 Laser specifications

Manufacturer	Litron
Model	Nano LG 250-20
Laser type	Solid State Nd:YAG, multimode, Q-switched
Max repetition rate	20 Hz
Max output energy @ 1064 nm/20 Hz	260 mJ
Max output energy @ 532 nm/20 Hz	139 mJ
Max output energy @ 266 nm/20 Hz	34 mJ
Beam diameter	About 5 mm
Beam divergence	<0.8 mrad
Pulse length @ 1064 nm	7–11 ns
Resonator type	Telescopic
Timing jitter	<0.5 ns



Fig. 6 The Litron Nano LG 250-20

2.2.5 The XY Plate Movement System

The XY plate is one of the moving parts of the LIBS analytical system of this study, and this should carry the sample as well i.e. it is responsible for moving the flat surface of the meteorite sample along the laser beam in a controlled way, in order to generate plasma at certain points on the surface of the sample and acquire spectra. It is a custom-made build, based on OpenBuilds [28] parts and Wantai [44] Nema 23 stepper motors. The hardware and the overall setup are based on concepts made for CNC machines that offer high accuracy in movement. Table 6 presents the specification of the movement system of the LIBS setup. Figure 7 shows a photograph of the XY plate when it was disconnected from the other part of the setup for testing purposes.

2.2.6 The Spectrograph

The final component of any LIBS system is the spectrograph that performs the data acquisition, i.e. this device is responsible for reading the emitted radiation from the generated plasma and create spectrum graphs. The spectrograph used in this study is the Ocean Optics (Ocean Insight) USB4000. As its name suggests, it is can be interfaced via USB, allowing for easy connection to any computing machine. Table 7 presents the specifications of the spectrograph. Figure 8 shows the device itself as seen on the official website of the company [29].

Apart from the USB port, the USB400 spectrograph has a 22-pin connect for external to external hardware for control and automation. From the 22 pins of the connector, only two will be used in our setup, which are:

- The pin Nr 6, which is the electrical ground
- The pin Nr 7, which is the external trigger pin which receives TTL signals to trigger acquisition. All other acquisition parameters are set by the software on the computer through the USB port.

Figure 9 shows the 22-pin connector.

Table 6 XY plate movement system specifications

Motors manufacturer	Wantai
Motors model	57BYGH420
Motors form factor	Nema 23
Motors driving modes	Single, double, interleaved, microstepping
Motors step accuracy	$\pm 5\%$
Motors step angle	1.8 degrees
X max travel	12.9 cm
Y max travel	17.8 cm
Resolution	250 μ m

Fig. 7 The XY plate movement system



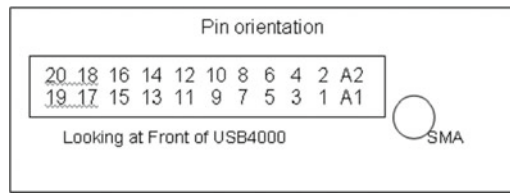
Table 7 Ocean optics USB4000 spectrograph specifications

Manufacturer	Ocean optics
Model	USB4000
Detector sensor	Toshiba TCD1304AP linear CCD array
No. of elements	3648 pixels
Pixel size	8 $\mu\text{m} \times 200 \mu\text{m}$
Detector range	200–1100 nm
A/D resolution	16bit
Entrance aperture	100 μm

Fig. 8 The Ocean Optics USB4000 spectrograph



Fig. 9 The 22-pin connector of the Ocean Optics USB4000 spectrograph



3 LIBS System Software

The software components of the implemented autonomous LIBS mapping system include custom device drivers and libraries already developed by the hardware provider and software that was developed for the current LIBS system. The software can be classified in the following four main categories:

- Hardware drivers, which mainly includes the software that controls the motors and also the communication between the various nodes of the system.
- Autonomy, which mainly includes the planning and mapping procedures.
- Visualisation, which mainly includes code that generates ROS-compatible messages that can be visualised using the main ROS visualisation utility called RViz [22].
- User Interface, which mainly includes user-oriented software that aims to simplify the parameter configuration process, by providing graphical interface methods to interact with the whole system.

The implemented software is open source and available through a github repository [38]. It consists of a variety of ROS packages each with its own nodes and configuration files. The implemented ROS packages are:

- auto_libs_msgs: This package contains the custom ROS Services used for the autonomous LIBS mapping system.
- auto_libs_description: This package contains the physical description of the XY moving platform for visualisation, control and planning purposes.
- auto_libs_control: This package contains hardware drivers, laser/spectrograph control software and movement-related configuration files.
- auto_libs_navigation: This package includes the planning software along with the navigation control graphical user interface application and related configuration files.

This chapter analyses all of the above components and offers a detailed description of all the capabilities of the autonomous LIBS mapping system for meteorite samples. This chapter focuses solely on the details of the implementation and not the usage or the configurability. The latter are topics that are discussed in the next tutorial chapter.

3.1 Hardware Drivers

The XY kinematic stage is the piece of hardware that was implemented from ground up. Other hardware components already came with their own factory-implemented drivers like the Litron Nano LG 250-20 laser module and the BNC 588-OEM-1ns pulse generator. These devices have either hardware interfaces or communicate with other systems over serial ports and implement an internal command language set. The Ocean Optics USB4000 spectrograph came with both proprietary and open source drivers.

The XY kinematic stage driver software had to be implemented from scratch, since it consisted of general purpose devices (CNC and 3D printing oriented), such as the Wantai Nema-23 type motors, and a series of linear movement hardware components. The specifications of the XY movement system have already been provided in the previous chapter.

The Wantai motors are driven using an Arduino Mega. The Arduino is responsible to send to the computer and also receive from it messages that allow the integration with the rest of the software components in a distributed manner. In short, distributed computing relies on a variety of machines and/or processes that simultaneously work towards the solution of a problem while updating the required components with their status.

The Arduino code, uploaded to the Arduino over its serial port and permanently running when it is on power, follows the ROS communication protocol. This communication protocol has the rationale of “talkers” and “listeners”. Talkers (publishers in the ROS language) send data to other software components and listeners (subscribers in the ROS language) receive data and process them. Table 8 summarises the input and output data of the XY movement system node.

With the data exchange in mind, it should be clear that the motor controlling software receives commands either in the form of velocity or position and acts based on that. As an output, the drivers only report the status of the system and also provide feedback for debugging purposes.

The motor controlling software itself consists of a small set of functions that include:

- The setup function.
- The motor controlling function.
- The velocity commands receiver function.
- The goal position receiver function.

Table 8 XY movement system drivers inputs and outputs

Input	Output
Velocity commands	Movement system status
Goal position	Debugging info

- The movement system status reporting function.
- The main loop.

In the setup function, all the objects and variables are initialised including position loggers and communication objects (publishers and subscribers). Most importantly, in this function the movement system is self-calibrated. This is achieved by driving the movement plate to the maximum X and Y positions and then recentering the plate while also resetting the recorded position variables. This self-calibration takes place when the device (Arduino) is powered on, when a new serial device is connected to it and also per user request.

The motor controlling function implements the main capabilities of the motor driver (Adafruit hardware integrated on the Arduino) by sending the appropriate current to the stepper motors. As discussed in the previous chapter, the motors used in this setup are also capable of performing multiple stepping modes apart from single stepping.

The ‘interleaved’ and ‘microstepping’ modes are of major importance for the autonomous LIBS mapping system. They provide double and quadruple stepping accuracy respectively compared to the single stepping mode. The motor controlling function exploits all three stepping modes in order to provide accurate and fast control. More specifically, the motor controller always tries to maximise the step distance, based on the absolute distance between the desired and the current position. Figure 10 shows the motor stepping mode selection process in the form of a decision tree diagram.

The velocity commands receiver function is the next motor controlling driver function that should be discussed. This function is a simple ROS subscriber callback. This means that it is triggered only when a new velocity command is sent (published) by another node. The callback simply receives the commanded velocity and translates it to a desired position based on the Eqs. 1 and 2.

In Eqs. 1 and 2, and considering that i represents either the x or the y movement direction, p_i is the desired position, i is the current position, vel_i is the commanded velocity, s_i are the motor steps per centimeter and k_i is a constant multiplier.

$$p_x = x + vel_x \times s_x \times 100 \times k_x, vel_x \in [-1.0, 1.0] \quad (1)$$

$$p_y = y + vel_y \times s_y \times 100 \times k_y, vel_y \in [-1.0, 1.0] \quad (2)$$

Following the same rationale, the goal position receiver function is triggered only when a goal position message is published by another node. The callback receives a two-dimensional position and translates it to motor steps, while respecting hardware limitations. In the case of the autonomous LIBS mapping system, these limitations refer to the X and Y movement limits of the platform. Equations 3 and 4 show the calculations required for the conversion from real world coordinates to motor step positions. In Eqs. 3 and 4, and again i is replaced by axes x and y, p_i is the desired position, g_i is the input position, and t_i is the maximum travel in cm.

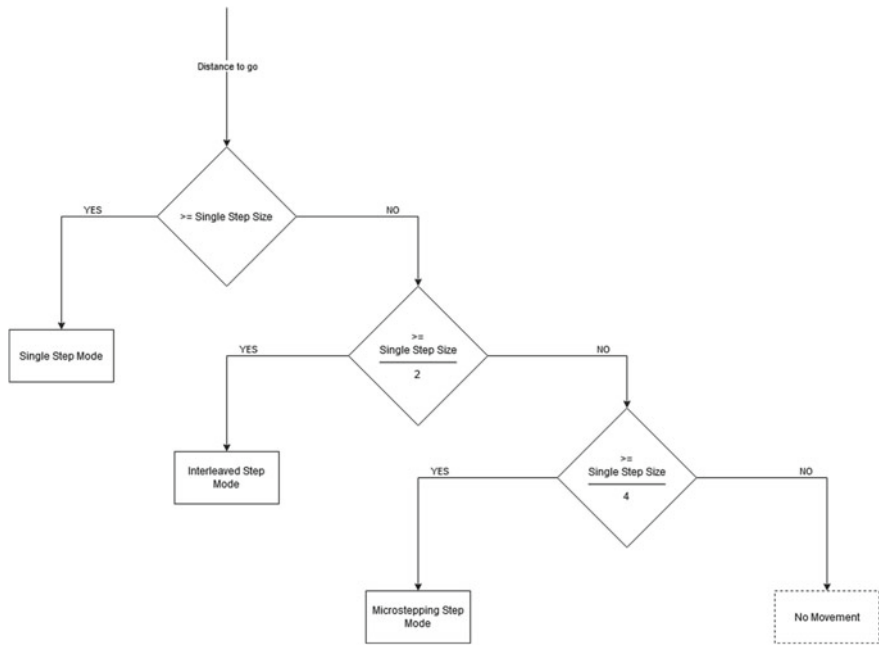


Fig. 10 The motor controller decision tree diagram

$$p_x = \left(g_x \times 100 + \frac{t_x}{2} \right) \times s_x, g_x \in \left[\frac{-t_x}{2}, \frac{t_x}{2} \right] \quad (3)$$

$$p_y = \left(g_y \times 100 + \frac{t_y}{2} \right) \times s_y, g_y \in \left[\frac{-t_y}{2}, \frac{t_y}{2} \right] \quad (4)$$

The movement system status reporting function is a message publishing routine. It is constantly called to report the position of the XY movement platform. This function does not make any calculations. It just generates the appropriate message for the Arduino complementary code. This complementary code is discussed later in this section.

Finally, the motor controlling driver utilises the main loop function. The main loop is responsible for making the appropriate calls to other functions in order to ensure the normal driver operation. This infinite loop calls the motor controlling function that was discussed earlier first. After successfully returning from that function, it calls the status reporting function to update the corresponding subscribed nodes. Finally, it calls the spin() function included in the main ROS library, in order to poll for incoming messages.

Now that all of the Arduino code has been covered, another part of the motor controlling driver should be referenced. As mentioned in the description of the status reporting function, there is also complementary code for the Arduino part of the

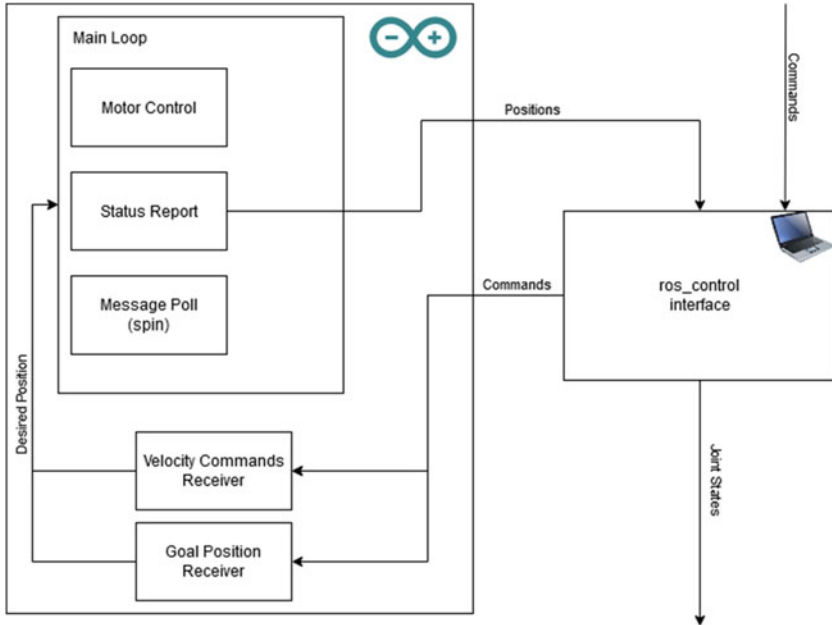


Fig. 11 The complete hardware driver flowchart diagram

driver. This code consumes the status messages generated from the Arduino code, and updates the platform’s “joints”. In the case of the autonomous LIBS mapping system, the joints refer to the X and Y positions of the moving plate. In more complicated setups, the joints could refer to actual robot arm/legs joints, or other physically moving parts. The complementary code was developed in order to offer full ROS integration by implementing the `ros_control` [7] interface. The complete list of advantages of implementing the `ros_control` interface is out of the scope of this chapter, but parts of it will be apparent in the following sections.

Figure 11 shows a complete diagram of the software threads connected in the hardware driver implementation.

3.2 Autonomy

The ability to effectively control the moving parts of the hardware, allows for a wide variety of additional capabilities and features, including autonomy. In the autonomous LIBS mapping system, autonomy refers to the ability of the system to plan, move, generate plasma, acquisition and data storage without requiring external (human) input.

With this definition of autonomy in mind, this section discusses the following software components:

- Planning software.
- Laser control.
- Sampling/acquisition.
- Saving data.

The list of software components is not exhaustive. Other minor parts were developed which will be discussed later in this section.

In order to achieve robust autonomy, the architecture of the software relies on a highly distributed architecture, following the ROS rationale. More specifically, all of the different software components send and receive messages that work either as triggers or as input data for calculations. Figure 12 shows the architecture of the autonomy software components. Additionally, Table 9 summarises the inputs and outputs of the autonomy software components. It should be noted that the rows of the table are not directly related. Interested readers should continue reading for a detailed analysis of each software component.

Starting with the planning software component of the autonomy package, the main purpose of this node is to create a valid plan for the moving platform to follow. In order to achieve such task, the planner needs a series of parameters that discretise the search space. For the purpose of this chapter, the two-dimensional space is discretised into an XY grid.

Apart from space discretisation, the implemented software allows for half stepping and goal tolerance configuration. Goal tolerance refers to the maximum distance the platform can be away from the goal in order to be considered as correctly positioned. Half stepping enables double resolution by configuring the planner to generate paths that pass twice from each grid cell. The planner has a series of other parameters that can be set either on initialisation or dynamically during run time. Details on the parameters are discussed in the next chapter.

With the LIBS meteorite sample mapping as a goal, the planning software generates paths that require the moving platform to pass through all of the configured grid cells, based on a (user) defined resolution. The paths generated are optimal, meaning that the required displacement of the platform from one position to the next is always minimum. This optimality does not include the first position of the plan. It is always the top left corner of the sample, regardless of the current position of the platform. Figure 13 shows the base rationale for all planning procedures.

The planner keeps track of the moving platform's position. This allows it to discriminate between a goal in progress and an achieved goal position, based on a (user) defined goal tolerance. When a goal position is reached, the planner pauses, and send a fire trigger to the laser controller.

The laser controller, when a fire signal is received, fires the pulsed laser into the sample, based on (user) defined parameters. At the same time, the laser controller enables the spectrograph's optical fibre and samples/acquires the radiating plasma on the meteorite sample. When the sampling/acquisition process is over, the data

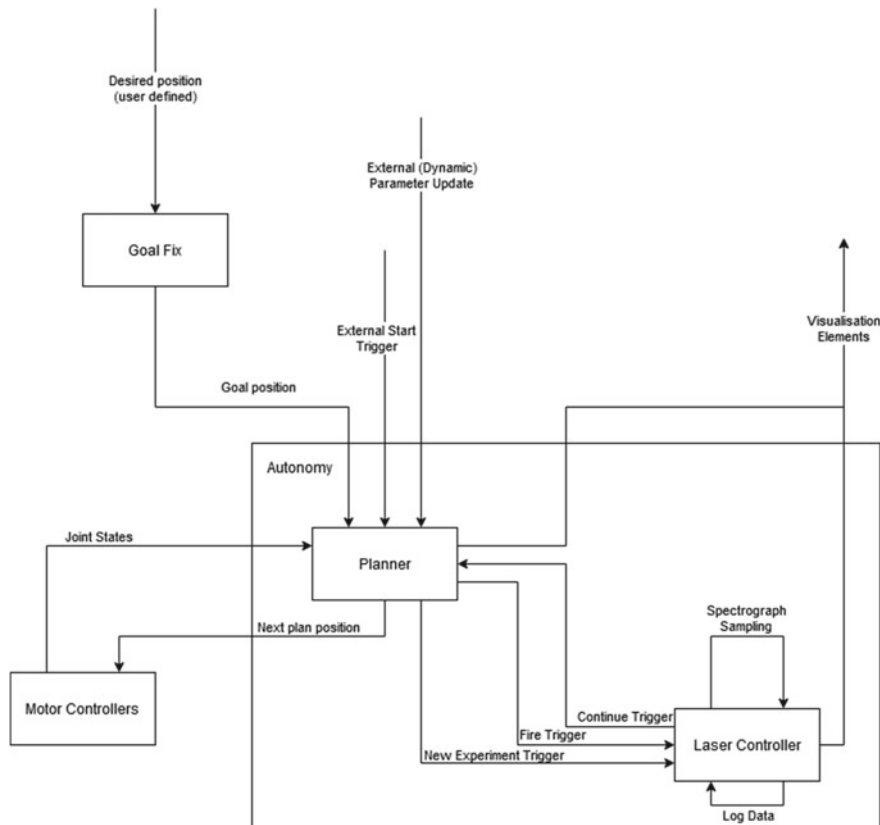


Fig. 12 The architecture of the autonomy software components

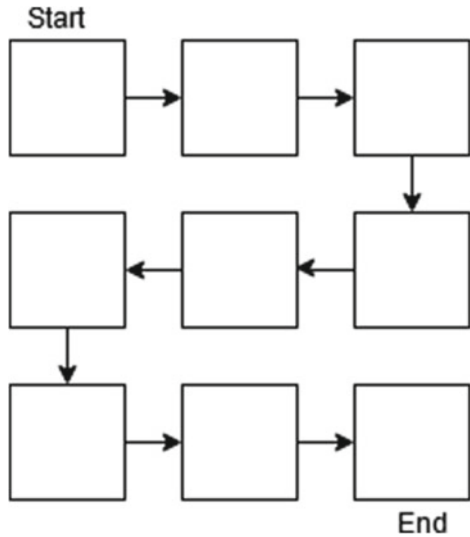
Table 9 Autonomy software inputs and outputs

Input	Output
External goal position	Next plan position
External start trigger	Visualisation elements
External dynamic parameter update	
Joint States	

collected is saved into the hard disk and the laser controller sends a continue trigger to the planner. At that point, the planner sends the next goal position to the motor controller. This vicious circle continues until all planned positions have been reached and spectra from the radiating meteorite plasma have been collected.

It should be highlighted that the spectra acquisition procedure includes a dark current noise [18] (also referred to as instrument signature) removal based on a typical baseline subtraction and the spectrograph manufacturer's available dark cur-

Fig. 13 The grid planning rationale



rent specifications that are available at runtime. More specifically, the dark current removal procedure can be described with Eq. 5. In Eq. 5, I'_s is the new intensity, I_s is the intensity that includes the dark current noise, k is the number of spectra values and d_k is dark current baseline noise provided by the manufacturer.

$$I'_s = I_s - \left(\frac{1}{k} \times \sum_0^k d_k \right), \forall s \in [0, k], k = No.spectra \quad (5)$$

In the autonomy software components architecture diagram, there is a node outside the main autonomy package called ‘Goal Fix’. This is a simple ROS node that translates all input goal position to the correct reference frames for the moving platform. This offers seamless integration between a variety of different input methods. Since the autonomy code itself has reference frame awareness (contradictory to humans), the goal fix node is only used for human interfacing.

3.3 Visualisation

The core functionality of the autonomous LIBS mapping system would not be complete without the appropriate software components for visualisation/debugging tools. This section discusses all the visualisation capabilities of the implemented software.

The visualisation software components are majorly based on RViz, the main Robot Operating System visualisation tool. Visualisation capabilities include:

- Moving platform position visualisation. (in RViz)

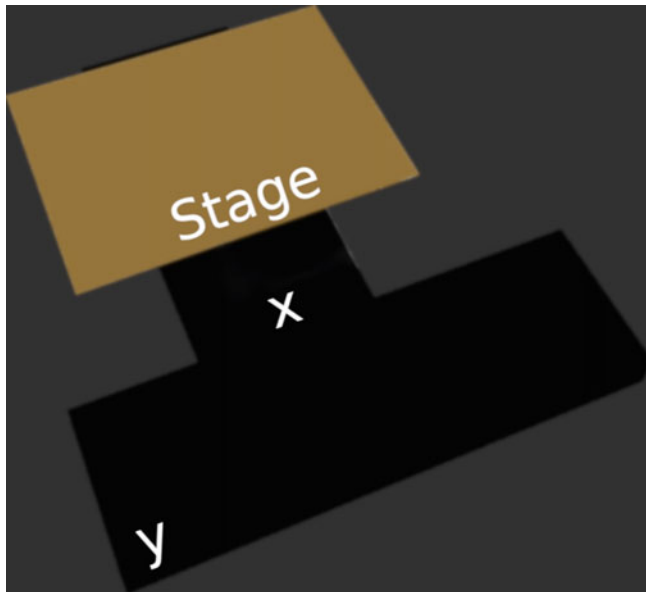


Fig. 14 The movement system real time visualisation in RViz

- Generated plan visualisation. (in RViz)
- Planning grid visualisation. (in RViz)
- Laser beam firing visualisation. (in RViz)
- Spectrograph sampling visualisation.

The above list of visualisation capabilities offers a complete reference for humans to follow and understand the progress of the autonomous LIBS mapping process.

The moving platform position visualisation appears inside in a three-dimensional window (in RViz) the current state of the moving plate. It follows the movement of the plate in real time, based on the reported joint states of the ros_control interface of the hardware driver. Figure 14 shows a screenshot with the three-dimensional state of the movement system.

The visualisation of the generated plan (path) consists of a series of connected straight lines. These lines connect the positions that constitute the whole navigation plan. As stated earlier, the generated plan is based on a specified grid that needs to be covered. The visualisation of the planning grid offers allows humans to quickly evaluate the coverage of the generated plan. Figure 15 shows a plan on top of the planning grid. The thin green line is the generated plan, and the blue layer below it is the planning grid. Again, the visualisation is integrated into RViz, using the appropriate message types, for real time updates. The real time aspect of the planning phase, involves the removal of already visited positions of the plan.

Another part of the visual software components is the visualisation of the laser beam. Enabling the capability for humans to see the laser beam in RViz, allows for

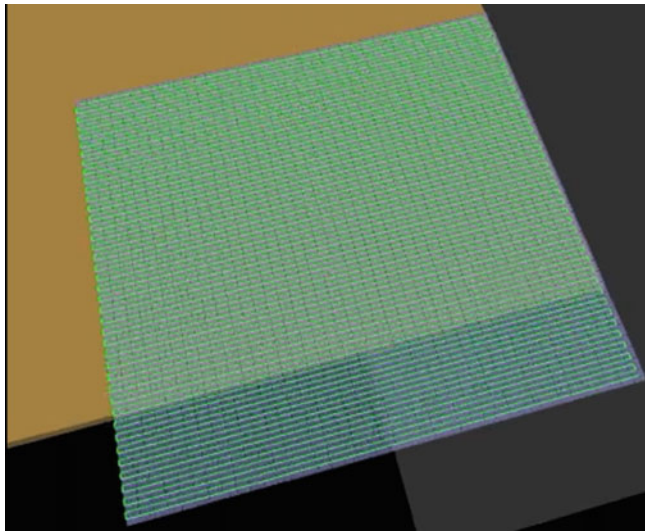


Fig. 15 The generated plan and grid real time visualisation in RViz

better understanding of the autonomous LIBS mapping process. This involves the appearance and disappearance of a red line whenever the laser controller is pulsing a beam or not respectively. Figure 16 shows a complete visualisation screenshot from RViz, while the laser controller is firing a beam.

Finally, the spectrograph sampling visualisation tool is an external application designed to read and visualise the log files generated during the acquisition process from the laser controller. The interface consists of five components. The grid cell selector, the spectrum visualiser and its visualisation toolbar as well as the elemental map and its visualisation toolbar.

The grid cell selector shows a grid that users can click on to choose a cell for which the spectrum will be visualised. The selected grid cell is highlighted to offer an enhanced user experience. The spectrum visualiser is the plot itself, while the toolbar consists of tool to configure a series of parameters of the plot visualisation. The last feature of the spectrograph sampling visualisation tool is the elemental map along with its toolbar. Located in the top left corner of the application, the elemental map is populated based on the currently selected spectrum limits. This means that users can alter the area of interest by zooming in an intensity of interest in the spectrum visualiser, and thus generate and elemental map based on a spectrum of choice. The corresponding elemental map toolbar allows users to zoom and pan on the map for thorough inspection. Finally, to offer easier spectrum investigation, a ' $\Sigma(x)$ ' has been included that selects all grid cells for an overall sum of intensities.

Figure 17 shows a screenshot from the spectrograph's sampling visualisation tool.

It should be noted that an extra random synthetic dataset generator has been script implemented for instant log access. The random generation script populates a log

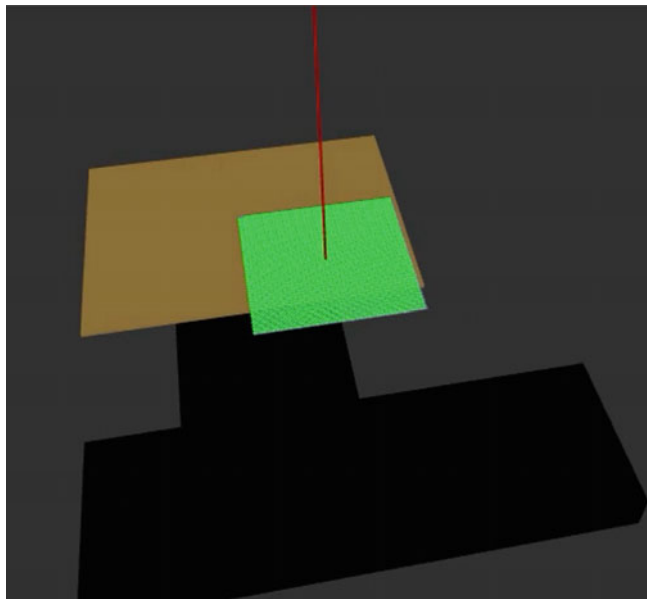


Fig. 16 Screenshot from RViz showing the complete visualisation capabilities of the system, including position and laser beam states, generated plan and the planning grid

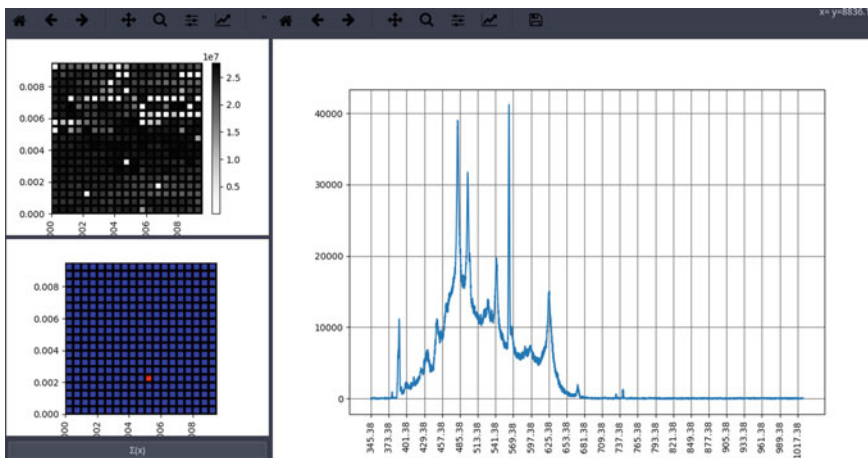


Fig. 17 Screenshot from the spectrograph sampling visualisation tool

file with random intensities in the range of zero (0) to one (1). The probability for an intensity value to be higher than 0.2 is 5% or 0.05. This probability tries to (very) roughly simulate the output of the spectrograph sampling procedure.

3.4 User Interface

In order to offer a complete autonomous LIBS mapping solution, a number of ways are required for humans to interface to the system. For this purpose three ways were integrated into the system, that are listed below from the simplest to the most complicated:

- Sending a single goal position through RViz
- Teleoperating the moving platform with a joystick
- Configuring and controlling the planning process through a graphical user interface.

Starting with the simplest, the goal position button (called “2D Nav Goal”) that is part of the RViz tools was integrated. It is of vital importance to offer to the user a robust and transparent to the user way to send navigation goals. For this purpose, the goal fix node consumes (receives) the goal position before actually sending it to the rest of the system. As discussed earlier, this procedure ensures reference frame stability.

The process of sending a navigation goal using the RViz goal position button is simple. The user first has to select the goal position tool from the RViz top tool panel. Then the user needs to click anywhere inside the main RViz screen where the state of the moving platform is visualised. As soon as the mouse click is released, a message is sent to the goal fix node in order for it to translate the point to the correct reference frame and relay it to the rest of the autonomy pipeline.

The second way for users to interact with the LIBS mapping system, is to use a joystick (gamepad) to teleoperate the moving platform. This process is quite straight forward, since users do not have to do anything other than use the analogue sticks of an ordinary wired or wireless gamepad. As a reference, two gamepads were used as a test, a Logitech F710 (wireless) and a Logitech F340 (wired). In order to achieve this seamless integration of the gamepad, the ROS joystick driver [35] is used. The joystick driver sends commands directly to the moving platform drivers where the commanded velocity is handled accordingly.

The last user interaction method is through a graphical user interface (GUI). This application allows users to configure and control the autonomous planning routine as well as monitor the spectra acquisition process. Figure 18 shows a screenshot of the navigation control application.

In order to make the application even more user friendly, a USB camera was added to the hardware setup. The camera integration allows users to draw a rectangle in its image. This rectangle specifies the planning grid limits.

The navigation control GUI allows users to configure a series of planning parameters:

- The planning grid cell size (equivalent to the laser spot size, depending on the magnification of the objective lens). This parameter indirectly sets the number of cells of the grid, by trying to fit the cells inside the user defined grid rectangle.

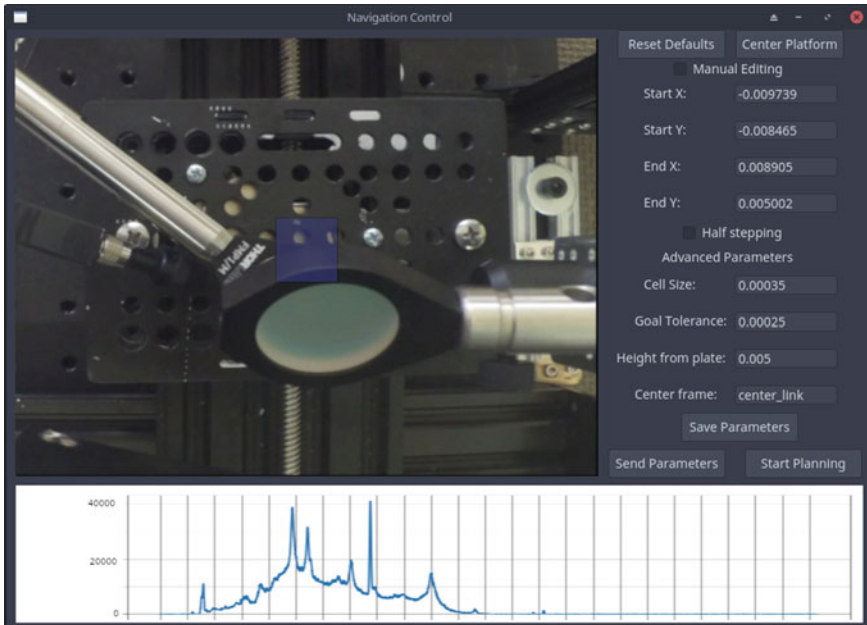


Fig. 18 Screenshot of the navigation control application

This is a simple division calculation after having set up the optical microscopic configuration of the system and having measured the spot size.

- The goal tolerance. This parameter sets the minimum distance that the platform needs to be away from a goal position in order to be considered as reached by the planner.
- The camera height from the plate. This parameter is only used for visualisation purposes. It sets the z-axis distance that the grid and the plan will be drawn with the plate as the origin.
- The centre frame. This is a highly advanced parameter that allows users to change the reference frame of the centre of the platform. It is included in the case of application to a different setup.
- Half stepping toggle mode. This boolean parameters sets the planner's half stepping mode. Half stepping was discussed in a previous chapter. In short, when enabled, it doubles the control points of the planning function.

As stated earlier, apart from parameter configuration, the navigation control application also allows for easy selection of a part of the sample to be analysed. This can be achieved with two different methods.

The first method involves the camera image. It allows users to draw a rectangle with the mouse, which specifies the limits of the analysis rectangle. This rectangle pixels are translated into real world coordinates, based on the fact that the camera height from the moving plate is known and constant.

The second method requires the “Manual Editing” option to be enabled. It allows users to specify the exact limits of the analysis rectangle by typing in the appropriate boxes.

It should be clear that even though the first method is far more intuitive for humans, it is less accurate. The second method was implemented to offer a less user friendly but precise implementation.

As highlighted earlier, the navigation control application also offers a live spectra acquisition visualisation. It is located at the bottom of the window and offers a rough estimate of the current sampling intensity.

4 Software Tutorial

Before moving on to the experimental setup and the final results of this chapter, a proper tutorial should be included for interested readers. This chapter contains information regarding on how to compile and run the implemented software. Additionally, detailed description of all configuration parameters and files are provided.

4.1 *Compiling the Software*

The compilation section of this chapter considers ROS already installed. The process of installing ROS is out of scope of this chapter. Minor familiarity with the ROS ecosystem is also assumed.

The first step in order for users to be able to use the implemented software is to download the required code. The whole implementation is open source and available on github. It consists of the main autonomous LIBS mapping implementation [38] and also a fork [39] of the unofficial open source Ocean Optics spectrograph device driver [13].

Before describing all of the compilation details, it should be noted that the software was tested under MX Linux 18.1 (Debian 9 based Linux distribution). The software is not Debian or even Linux specific, so users of other operating systems should not have any major problems compiling (Windows or Mac).

The seabreeze fork does not include any major changes over the official release, apart of modernised CMake changes for instant compilation on more recent C++ compilers. The compilation process of the spectrograph device driver follows the typical CMake based compilation procedure. The following commands allow users to download, compile and install the seabreeze device driver as a system library. It should be highlighted again, that the process was tested in a Debian based Linux distribution.

- Download: `git clone https://github.com/gstavrinos/seabreeze`
- Compile:

Table 10 Software dependencies

Messages/services	Functionality packages
nav_msgs	tf
std_srvs	roscpp
sensor_msgs	roserial
geometry_msgs	roserial_arduino
visualization_msgs	controller_manager
	Joy
	usb_cam
	hardware_interface

- `mkdir seabreeze/SeaBreeze/build`
- `cd seabreeze/SeaBreeze/build`
- `cmake ..`
- `make`
- `cd ../../`

– Install: `sh install_seabreeze.sh`

With the spectrograph device driver compiled and installed, users should be able to compile and use the main software implementation.

Before compiling the ROS package, users should make sure that all ROS dependencies are installed on their system. The ROS dependencies of the auto_libs package are summarised in Table 10.

With all the dependencies in Table 10 satisfied, users can normally compile the auto_libs related packages, using the catkin_make tool. The following commands allow users to download and compile the implemented packages:

– Download:

- `cd <catkin workspace location>/src`
- `git clone https://github.com/gstavrinos/auto_libs`
- `cd ..`

– Compile: `catkin_make`

With all software compiled and installed, users should be ready to configure and run the whole autonomous LIBS mapping implementation. These tasks are discussed in the following sections of this chapter.

4.2 Configuring the Software

As discussed in the previous chapter, the configuration of the whole autonomous LIBS pipeline, can be achieved in two ways. The first one involves editing configuration files. The second one, allows only a portion of parameters to be configured and can be done via a graphical user interface.

All of the available parameters are presented in Table 11. For the sake of simplicity, only the equivalent ROS package for each parameter has been included in the table. Interested readers should refer to the referenced packages in order to note on which node each one refers to.

Configuration files are an established way to experiment with parameters in the ROS community. They are deterministic and precise. Even though configuration files are an effective way to set parameters for the autonomous LIBS mapping system, they also have a series of flaws. These include lack of simplicity, since they require users to search through files and edit them, but also lack of dynamic configuration capabilities.

The disadvantages of configuration files are tackled by the second configuration method, that involves a graphical user interface. As discussed in the previous chapter, the graphical user interface allows user to set a large subset of the parameters of system while offering user friendly interaction and dynamic reconfiguration capabilities. Figure 18 from the previous chapter, shows a screenshot of the navigation control application.

4.3 Running the Software

Since the implemented software could rely on configuration files to initialise some parameters, the need for a way to execute the system combined with the appropriate configuration files is needed. Luckily, ROS offers an easy way to achieve this.

Batch execution (“launch”) of ROS nodes along with their configuration files can be done using an XML file with the *.launch* extension. This XML file specifies exactly which nodes should be run and where the appropriate parameter can be found.

For the implemented autonomous LIBS mapping system, a single launch file has been included that executes everything needed to control and visualise the planning and sampling autonomous procedure.

In order to execute the whole autonomous LIBS mapping pipeline, users have to run:

```
roslaunch auto_libs_navigation auto_libs_complete.launch
```

The *auto_libs_complete.launch* file runs the following software:

- The XY moving platform hardware driver.
- The laser/spectrograph controller.
- The USB camera hardware driver.
- The goal fix node for reference frame abstraction.

Table 11 Software Configuration Parameters

Name	Description	Package
teleop_twist_joy	This is a set of parameters that allows for sensitivity setting of the joystick commands	auto_libs_control
cell_size	This parameter allows for planning grid cell size configuration (in meters)	auto_libs_navigation
half_cell_step	This parameter enables or disables the half stepping mode of the planner that allows for double planning resolution by visiting each cell on its edges instead of its centre.	auto_libs_navigation
goal_tolerance	This parameter configures the minimum distance between the moving platform and a goal point in order for the later to be considered reached (in meters)	auto_libs_navigation
boundaries	This parameter configures the rectangle of interest for which the planner will generate a path for the moving platform to follow	auto_libs_navigation
visualise_beam	This parameter enables or disables the visualisation of the laser beam	auto_libs_control
center_link	This parameter sets the name of the reference frame for the centre of the XY axes of movement	auto_libs_control
laser_link	This parameter sets the name of the reference frame for the (vertical) source of the laser beam	auto_libs_control

- The autonomous LIBS mapping planner.
- An instance of RViz for visualisation.
- The navigation control graphical user interface application.

The only part of the implementation that is not run using the auto_libs_complete.launch file, is the teleoperation node. The teleoperation software has been isolated in a dedicated launch file, since it is not part of the standard autonomous LIBS mapping procedure. Users that need to execute the teleoperation node, should run:

```
roslaunch auto_libs_control teleop.launch
```

The teleop.launch executes the appropriate joystick hardware drivers along with the required button mappings and configurations. It also run a velocity command multiplexer that manages simultaneous inputs based on a predefined multiplexing logic.

Figure 19 shows the complete graph of nodes when running both the auto_libs_complete.launch and teleop.launch files. It should be noted that some nodes that appear unconnected user ROS Services to communicate, which is not visible in the graph due to its on-demand nature.

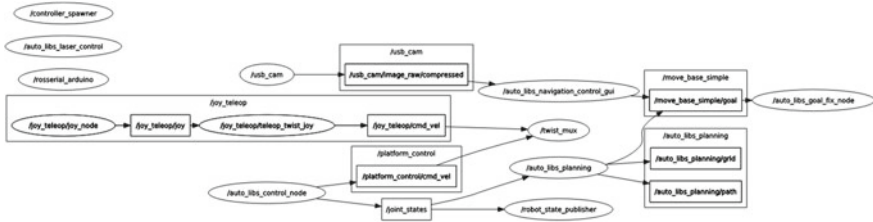


Fig. 19 The complete ROS node graph

5 Experiments and Results

The experimental and validation setup of the autonomous LIBS mapping implementation precedes a preliminary test phase. This test phase includes the execution of the whole elemental mapping pipeline in synthetic samples that could easily offer a first impression of the overall validity of the acquisition/mapping results.

For the testing phase two synthetic samples were prepared and used. Both of them consisted of an aluminium (Al) plate as a substrate and smaller copper (Cu) details on it, formed or having specific shapes, in order to be easily identifiable during LIBS analysis.

Single spot analyses from these materials (Cu and Al) have been acquired, as well as two spectra from atmospheric air (Fig. 20). Table 12 contains spectral lines from

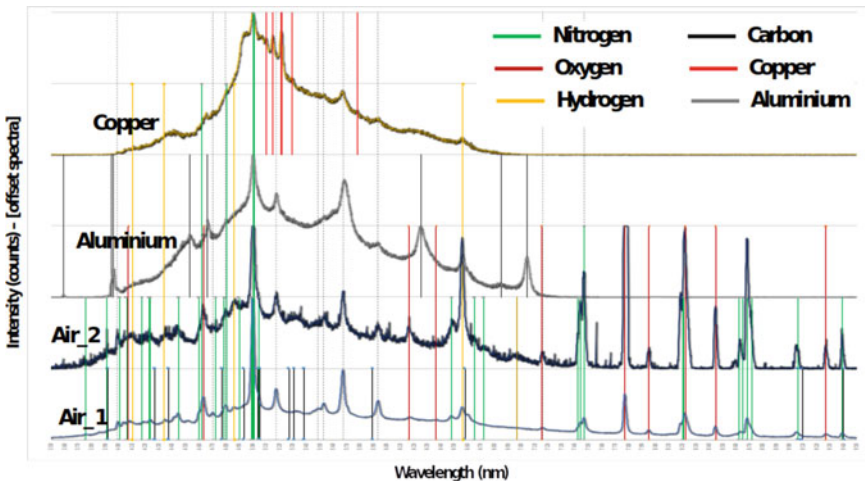


Fig. 20 Reference spectra from pure metals of copper (first from the top) and of aluminium (second from the top), as well as two analyses from atmospheric air (two lower spectra). Few unidentifiable peaks belong to the air analysed with the solid materials

Table 12 Spectral lines of reference materials used in this study

Element	Wavelength (nm)	Element	Wavelength (nm)
Al	358.7	N	375.54
Al	394.4	N	391.4
Al	396.2	N	400.5
Al	453	N	405.94
Al	466.3	N	417.6
Al	625	N	422.8
Al	685	N	423.5
Al	704	N	444.7
Ar	696.5	N	460
C	392.03	N	462.1
C	426.87	N	472.35
C	437.14	N	478.8
C	477.18	N	480.3
C	493.2	N	489.5
C	504.01	N	498.7
C	505	N	499.4
C	505.24	N	500.1
C	526.91	N	500.7
C	530.65	N	504.5
C	538.02	N	648
C	589.07	N	665
C	658	N	672
C	906	N	742.4
C	909	N	744.2
C	940	N	746.8
Cu	510	N	820
Cu	515	N	821
Cu	521	N	862
Cu	522	N	865
Cu	529	N	868
Cu	578	N	872
H	410	N	906
H	434	N	939
H	486.1	O	407

(continued)

Table 12 (continued)

Element	Wavelength (nm)	Element	Wavelength (nm)
H	656.33	O	463
		O	616
		O	636
		O	715
		O	777.2
		O	795
		O	822
		O	844.7
		O	929.6

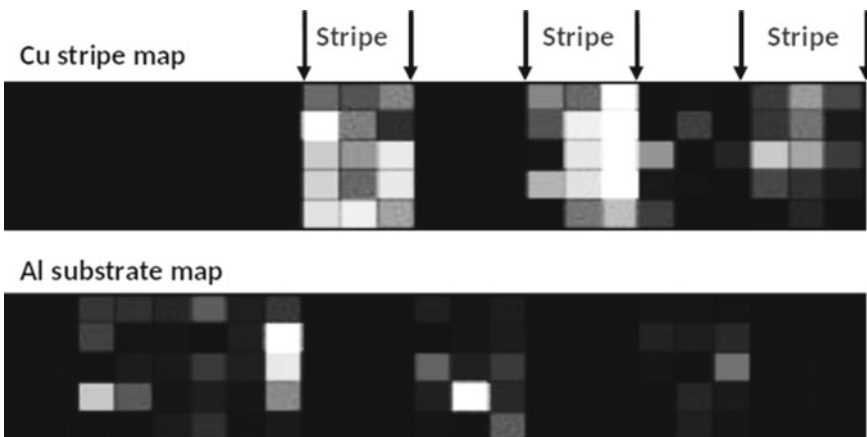


Fig. 21 Elemental maps performed during the first test of the experimentation process to discriminate between different materials, i.e., Cu strips (top map) on an Aluminum substrate (bottom map). Each map is formed by extracting the intensity of a characteristic peak from each material

the materials in Fig. 20. These should be used as a reference for interpreting results from the following studies.

The first synthetic sample had long parallel stripes of a Cu foil, each of about 1 mm width and 1 mm spacing from each other. The result of this first test is shown in Fig. 21, which show two elemental maps, extracted from the spectra from representative spectral lines for Cu (top elemental map) and for Al (bottom elemental map).

The second test consisted of a copper (Cu) ring on top of an aluminium (Al) plate/substrate. Such rings are specially fabricated by lithographic processes and are used in microscopy to calibrate the instruments or as a scale reference since they are very precise in shape and sizes. In our experiment, the ring's outer diameter was 3 mm and its inner hole diameter was 1 mm. The results of this second test are shown in Fig. 22. The figure shows two elemental maps (top images), each of different selected

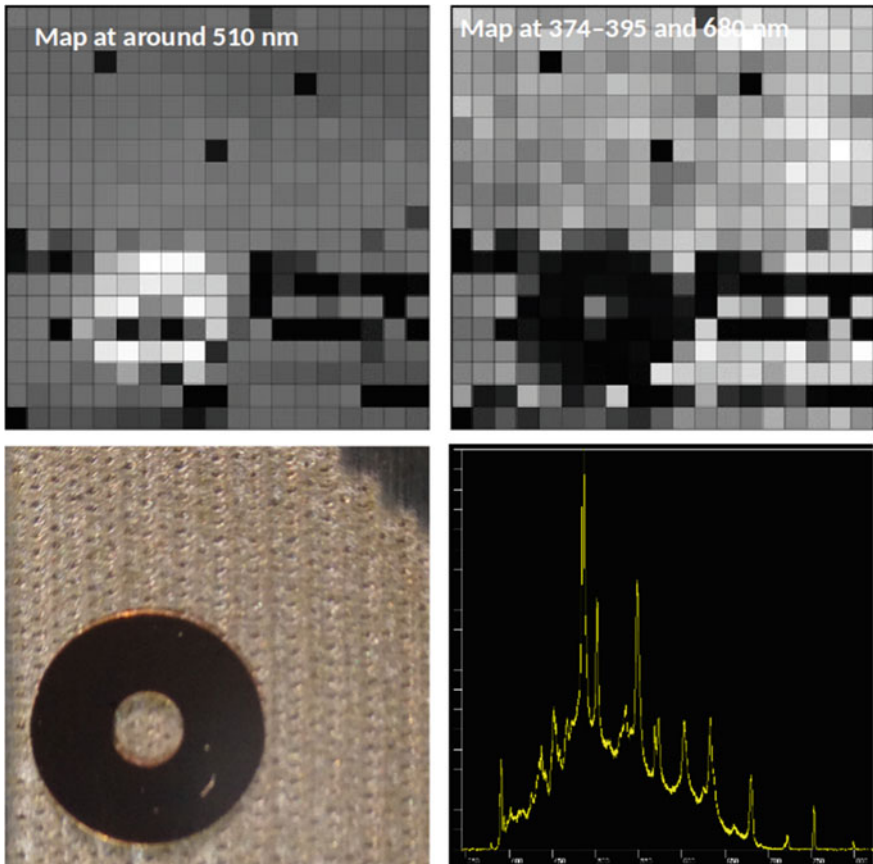


Fig. 22 The second test of the experimentation process that included Cu rings (spectral line at 510 nm) on a Al substrate (spectral lines at between 374 and 395 nm, and at 680 nm)—see top images. On the bottom left is an optical microscope image showing the copper ring positioned on an already irradiated area. On the bottom right the total spectrum is shown of the current experiment, contained characteristic peaks from each element and from the surrounding environment (atmospheric air)

spectral line, that leads to the designation of the two materials, for copper (top left image; peak at 510 nm) and aluminium (top right image; mapping range between 374 and 395 nm—the same image is acquired when the 680 nm line is used). Figure 23 shows spectra from points on the Cu ring and on the Al substrate. Furthermore, to better demonstrate the geometrical characteristics of the laser stops, Fig. 24 shows this synthetic sample in scale with magnification of x200 (optical microscope objective lens of 20x magnification). The craters on the aluminium substrate created formed by the pulsed laser pulses are now clearly visible and have an elliptical shape of $110 \times 200 \mu\text{m}$ (top image); one crater is further magnified using the microscope objective of 50x (bottom image).

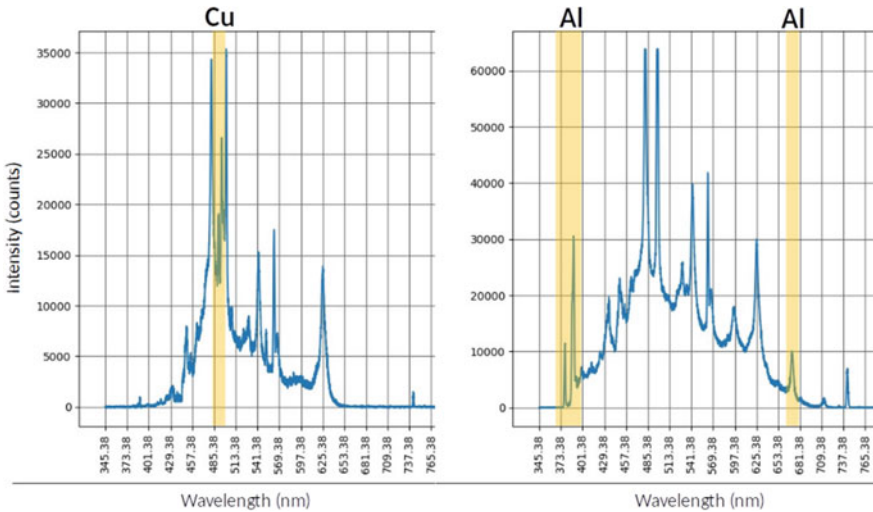


Fig. 23 Spectra from spots on the Cu ring (left) and on the Al substrate (right). The other peaks are characteristic of the air composition

The visibility (under a microscope) of the craters created from the laser pulses offers a chance to evaluate the precision of the kinematic plate (motors and mechanical linear movement axes). While testing the autonomous LIBS mappings system, during the second test a drift of the motors was noticed in the microscopic level. Figure 25 shows a plain aluminium plate scanned by the implemented autonomous LIBS system in a resolution of a quarter of a millimetre (0.25 mm). The image in the figure is acquired with a microscope with 10x objective lens. It should be noted that the sampled area is not a rectangle as expected. The drift displacement is around half a millimetre (0.5 mm) which is not acceptable for the use case of a LIBS elemental mapper.

Experimentation with different motor step values for the implemented autonomous LIBS mapping system led to the conclusion that the minimum robust value is around a third of a millimetre (0.3 mm). This realisation made the experimentation process more robust and the elemental maps generated during the following experiments of better quality. Figure 26 shows the precision of the system magnified with 20x objective lens on the microscope, both on the Al substrate and on a meteorite sample, the NWA 3118, a CV3 chondrite. The constant distance between laser pulse craters is clearly demonstrated on the Al sample, but it is also discernible on the meteorite sample.

It should be mentioned that further results on the NWA 3118 CV3 chondrite (meteorite) sample have been to the current stage omitted, due to their polymorphic nature of the sample, i.e., mineral phases smaller than the spot and step size of the LIBS system, as well as the topography of the surface of the sample (not a polished section) do not produce recognisable patterns. To achieve this, a high caliber kine-

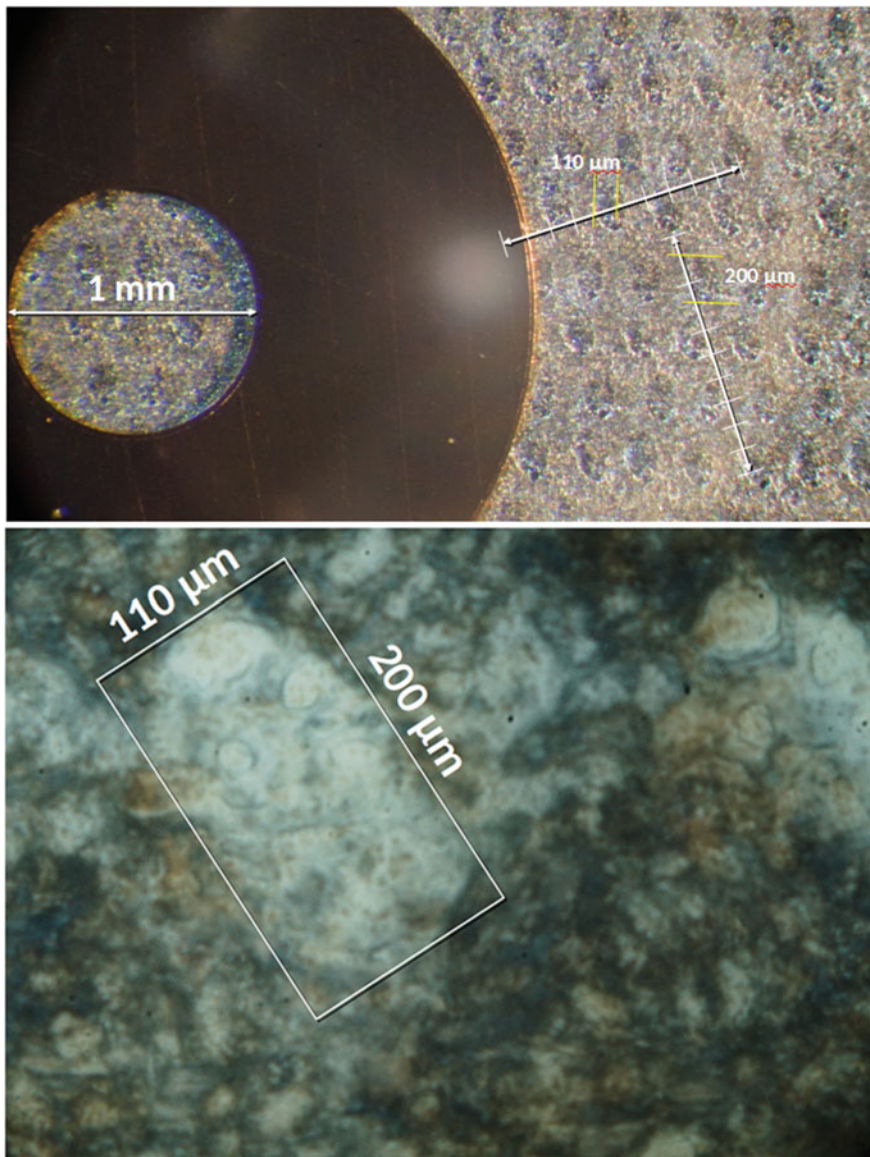


Fig. 24 Optical microscopic images of the synthetic sample of the second test of the experimentation process. It is composed of a 3 mm copper ring with a 1 mm hole, placed on an aluminium substrate (top image). Scales show the copper ring opening and the laser crater size ($110 \times 200 \mu\text{m}$) which is magnified in the bottom image with an objective lens of x50



Fig. 25 Observation of motor/kinematic stage drifting during the second test phase in a microscopic level

matic motor stage is required as well as a high magnification microscope objective instead of the 1 inch objective used in our LIBS system.

The final experiment using the implemented autonomous LIBS mapping system was conducted on an iron-nickel alloy (NeFi) meteorite, the Gebel Kamil ataxite meteorite containing a characteristic iron-nickel phosphate mineral phase, the schreibersite mineral with formula $(\text{Fe}, \text{Ni})_3\text{P}$. This meteorite also contains traces of Rare Earth Elements (REEs), observed as grain accumulations, often occurring close to schreibersite. Figure 27 shows a backscatter electron image of the schreibersite phase, which we mapped with LIBS. This image shows the schreibersite core, which is the brightest of all phases in BSE, then around it the kamacite phase, and finally the plessite matrix in which it resides. Figure 28 shows X-ray Energy Dispersion (EDX) spectra from the two major phases, schreibersite and kamacite. Kamacite is composed of iron and minor nickel, while schreibersite is also composed of iron, together with nickel and phosphorus (see mineral formula above). During LIBS mapping it is expected that Fe will show less intense signal in schreibersite than kamacite. This is true if we look at the LIBS elemental map at the top right of Fig. 29. There are some points at the rim of the mineral inclusion that show brighter colours, and these are clearly located in the Kamacite zone surrounding the iron nickel phosphate (schreibersite mineral phase). In the same Figure, the top right optical image demonstrates that enough spots exist inside schreibersite to resolve it in the map. The optical images of Fig. 31 have been acquired under a petrographic optical microscope just before irradiation with the laser (Fig. 29).

Before we proceed to any interpretation, we have assembled a graph (Fig. 30) of the major elements we expect to detect in Gebel Kamil meteorite, i.e., Fe, Ni, and P. From the reference spectra it is clear that the major characteristic peaks of

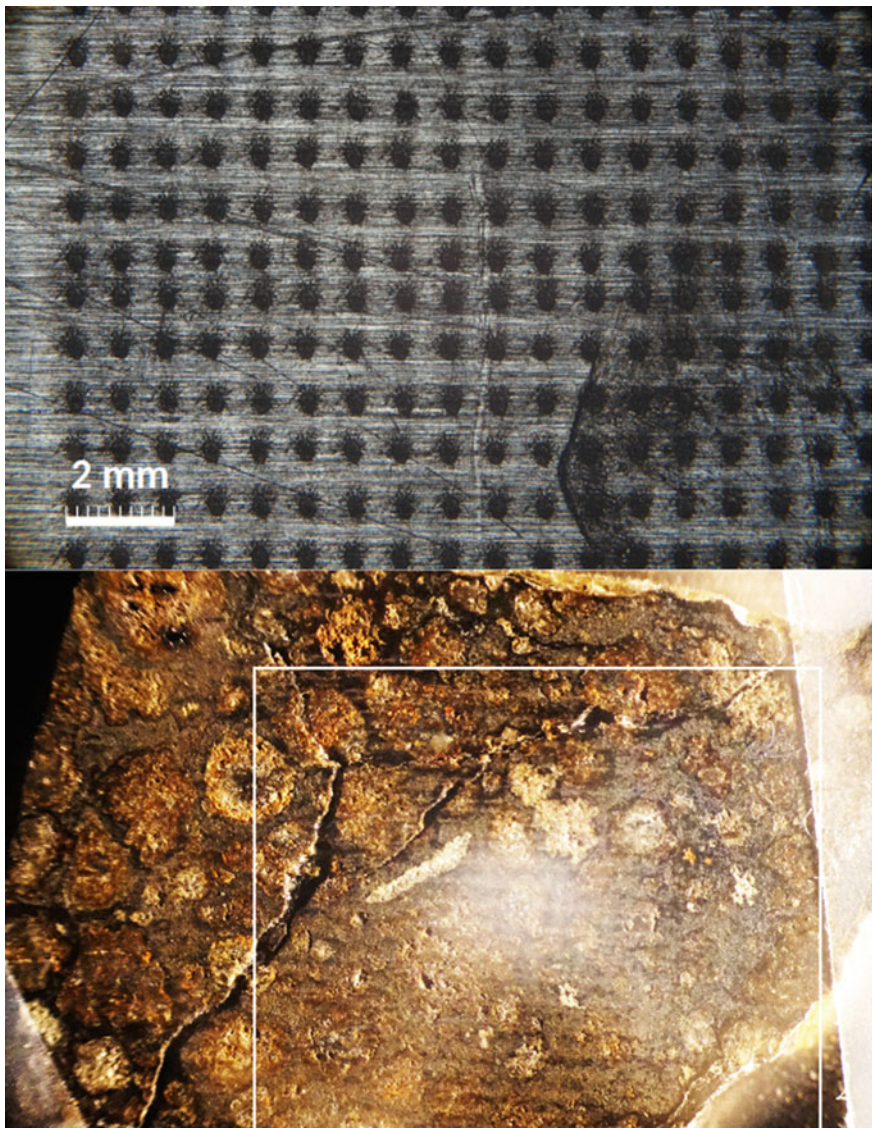


Fig. 26 Precise laser pulse craters spacing on an aluminium substrate (top) and on NWA 3118-CV3 Chondrite (meteorite) sample (bottom). The chondrite laser ablation spot pattern has a horizontal arrangement; it is discernible, although with some difficulty. Scale is the same for both images

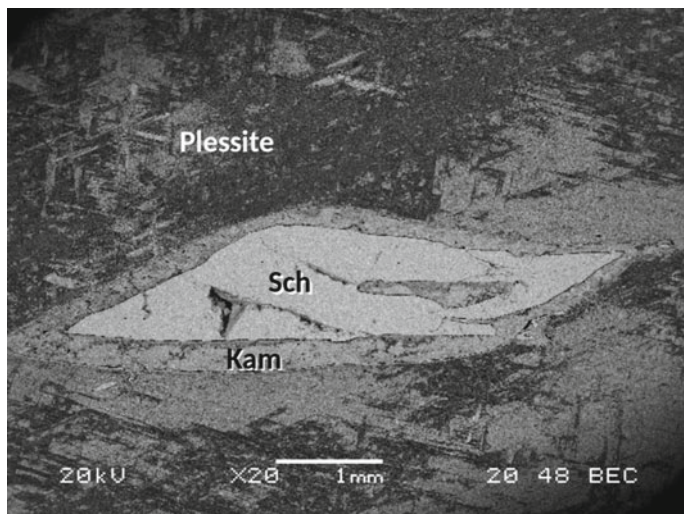


Fig. 27 Backscatter electron image (BSE) of the LIBS mapped schreibersite phase in the Gebel Kamil meteorite. Sch = schreibersite, Kam = Kamacite, and Plessite, which is a fine-grained mixture between Kamacite and Taenite

these elements are not visible by our spectrometer. This spectrometer is tuned to work mostly with light elements and a new spectrometer is required, tuned to view wavelengths starting as low as 200 nm to detect metals. This is a current hardware restriction, and consequently, we do not expect that we will acquire characteristic maps for these elements. However, we will investigate if we can detect minor peaks of the elements and extract some information. As from Fig. 30, minor peaks of the elements occur within the range covered by our spectrometer.

The elemental maps of Fig. 30 (top row) are extracted from the spectra at lines 568.6 and 510.1 nm (left and right map, respectively). The map of the 568.6 nm line should represent the Fe-Ni matrix, where the schreibersite inclusion appears dark due to lower contents of both elements relative to the matrix. We also produced the graphs in Fig. 32 to demonstrate the difference of the spectra between schreibersite (yellow trace) and kamacite (green trace). The absolute value of the difference between these spectra is shown with a blue trace. It is clear that the largest difference between the two spectra is visible at the 568.6 nm peak, as well as the 582 nm peak. Similarly, a large difference is observed at 451.7 nm, however it is not easily visible because the peak is small.

The 510.1 nm element map is expected to demonstrate the P-rich area, revealing the schreibersite inclusion. On the other hand, the 568.6 nm peak should demonstrate the Fe peak, because it is dark in schreibersite, brighter in Kamacite, and intermediate in plessite, as expected from their chemistries. The demonstrated contrast is realistic; however, we could not identify from the literature and from the NIST database any

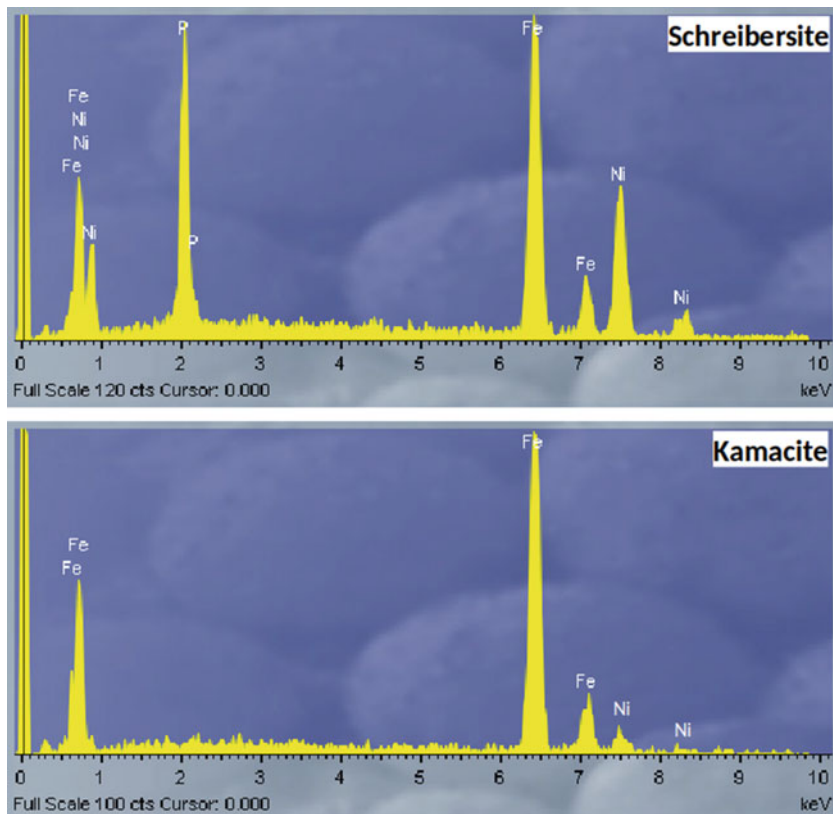


Fig. 28 EDX (X-ray electron dispersion) spectra of schreibersite and kamacite phases. Schreibersite has a phosphor peak, while this element is totally missing from Kamacite

plasma emission lines of the three major elements to fit those peaks. At the same time, these peaks are not identifiable in the spectra taken from atmospheric air (Fig. 20).

The bottom images of Fig. 30 are optical microscopy images of schreibersite, before irradiation (bottom left image) and after irradiation (bottom right image) demonstrating the laser spot sizes. A number of spots are discernible to occur inside schreibersite, suggesting that the spectra from its matrix are representative. We require hardware upgrades in order to pursue this work further.

6 Conclusion

In this use case chapter an Autonomous LIBS Mapping System for Chemical and Mineralogical Designation of Interplanetary Materials was implemented. The implementation includes hardware design and setup, as well software for device drivers,

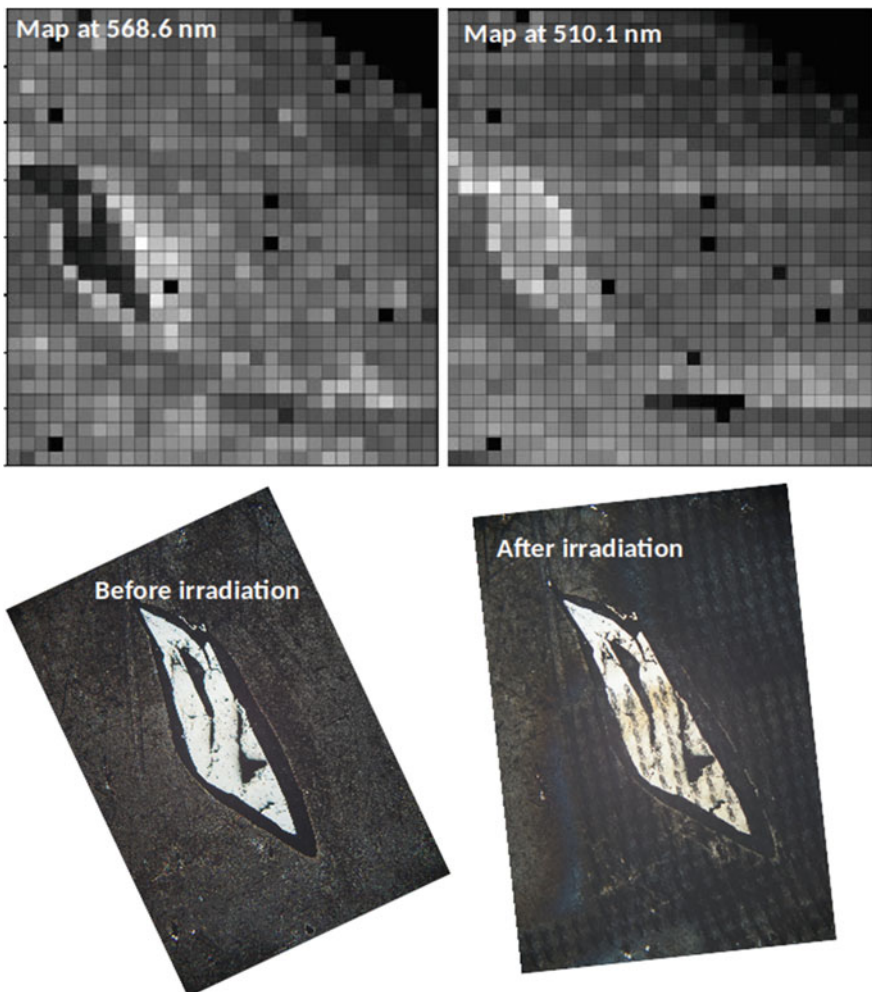


Fig. 29 Schreibersite, $(\text{Fe}, \text{Ni})_3\text{P}$, mineral inclusion (bright area) in the Gebel Kamil FeNi meteorite (Egypt, 2009–2010). The surrounding matrix (dark area) is the kamacite FeNi alloy, common to iron meteorites. Elemental maps (top images) show different images (opposite) if two different wavelengths are selected

control and planning, in addition to graphical user interfacing applications. It is then demonstrated on different synthetic samples, as well as two meteorites.

The implemented system offers a complete solution to the autonomous LIBS mapping problem, but not without its limitations. From the hardware point of view, and as seen in the previous chapter regarding the experiments and results of the implemented system, a major drawback was the lack of high precision movement under resolution requirements of equal or lower than a quarter of a millimetre (0.25 mm).

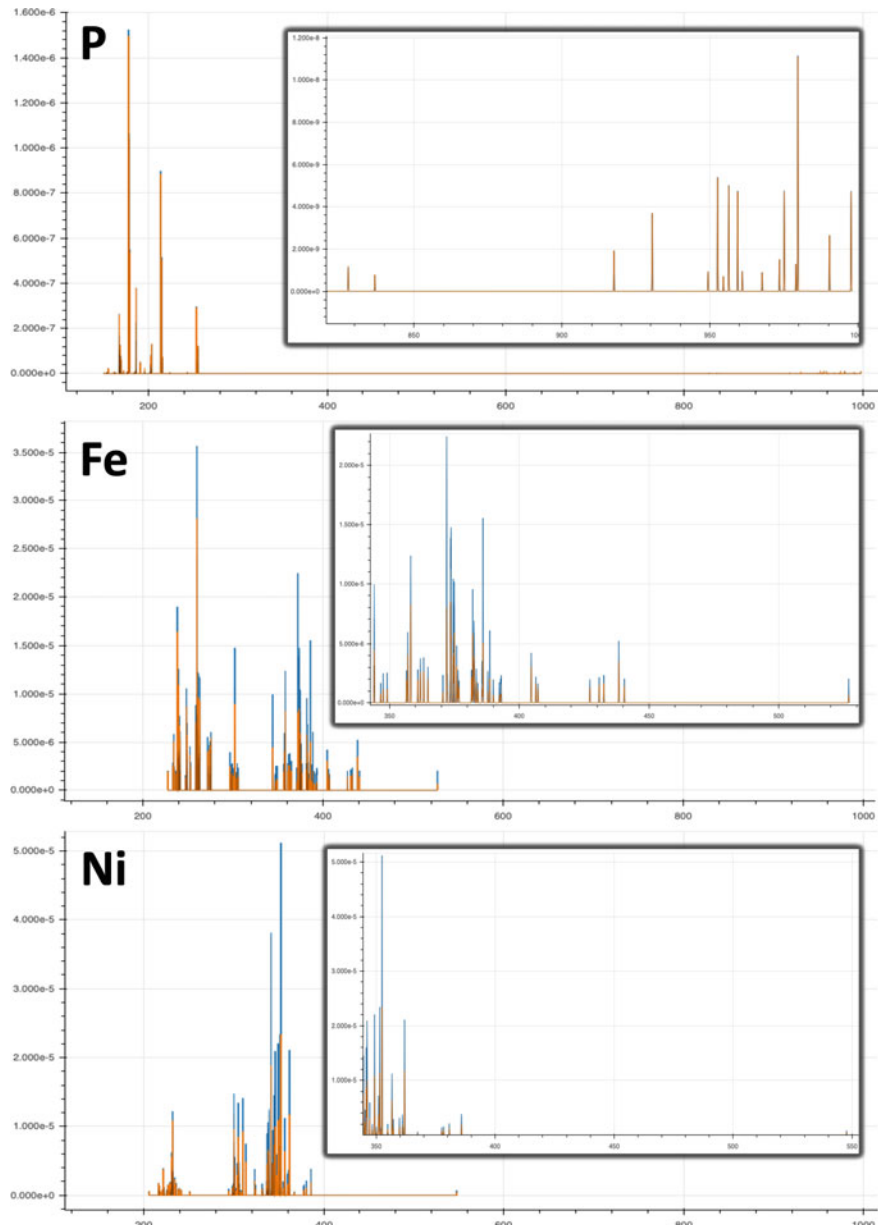


Fig. 30 The simulated spectra of the most important elements of the sample, those of Fe, Ni, and P, calculated from the NIST database. Insets represent the wavelength range that our spectrometer can view

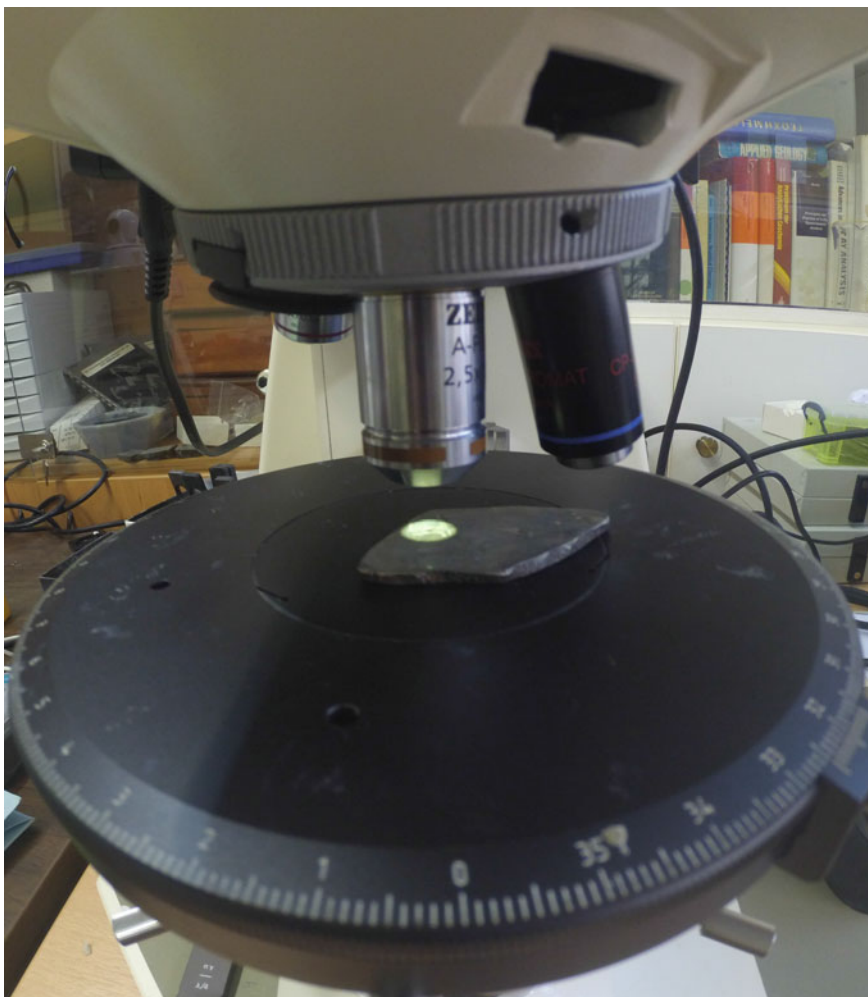


Fig. 31 The iron-nickel alloy (NeFi) meteorite sample under the microscope with a 2.5x zoom lens

This is not adequate also for the current laser spot size which is smaller (0.20 mm in its larger axis of the ellipsis, improved to a circular spot of about 0.1 mm diameter when a better focusing is performed and a smaller aperture is used). Since the linear movement mechanism along with the power source for the motors and the motors themselves were hobbyist-level products, it was to be expected. Luckily, the hardware abstraction offered by the software should make a future upgrade of the linear movement system a straight forward task. Another hardware limitation was the spectrometer. Its spectral range is between 340 and 1040 nm, which is appropriate for light elements (i.e., gases) but not for the heavy elements (i.e., metals) which emit

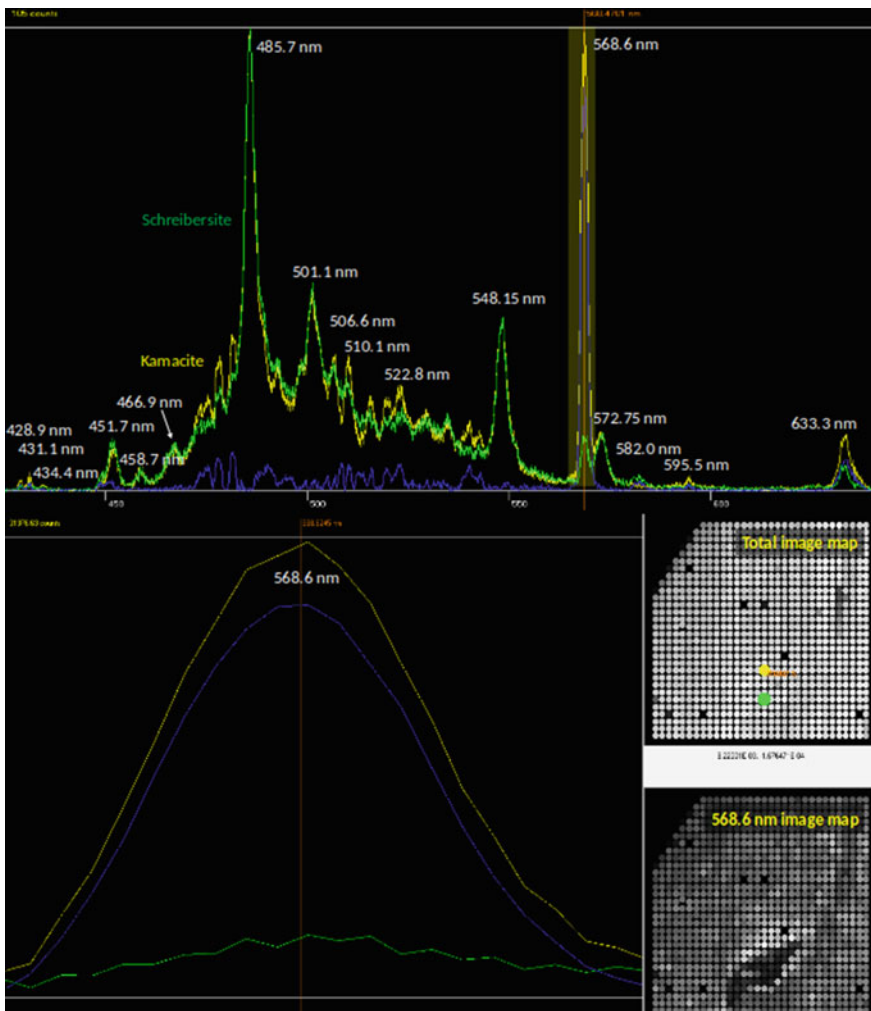


Fig. 32 Spectra difference between schreibersite and kamacite (top spectrum) and zoom in at 568.6 nm peak (bottom spectrum). On the right of the bottom spectrum, the total elemental distribution map is shown (top) and the elemental map extracted from the 568.5 nm peak

their characteristic major lines in the UV region. An upgrade of the spectrometer with a properly selected grating would solve this problem. Moreover, the spectrometer should contain faster electronics to allow precise control for delayed gating during acquisition in order, for example, to reduce background due to luminescence. With the current spectrometer acquisition was delayed by a variable unknown time interval after triggering, degrading the elemental maps.

Apart from hardware limitations, this implementation was planned to reach only certain specifications which have to do with the automation and usability of the technique. Acquisition currently includes only the subtraction of the dark current noise, but additional post-processing procedures would enhance the functionality of the system and the analytical results. For example, calibration-free LIBS integration to the already implemented system is a short-term goal that would greatly enhance acquisition performance in respect to interpretation. Future work could also ideally include more robust and sophisticated sample processing methods using machine learning techniques.

To conclude, this chapter focused on the development of an Autonomous LIBS Mapping System for Chemical and Mineralogical Designation of Interplanetary Materials. The implementation includes the hardware design and setup as well as all software components required for complete autonomy and user interfacing. The implementation did not come without a set of drawbacks though, which can be potentially be the focus of future work.

Annex A: Pulse Generator Configuration Commands

*RST

```
:PULS0:MOD SING  
:PULS1:POL NORM  
:PULS2:POL NORM  
:PULS1:OUTP:MOD ADJ  
:PULS2:OUTP:MOD ADJ  
:PULS2:OUTP:AMPL 5  
:PULS1:OUTP:AMPL 5  
:PULS1:DEL 0  
:PULS2:DEL 0  
:PULS1:WIDT 100E-3  
:PULS2:WIDT 100E-3
```

The command “RST” resets the system. Command ‘:PULS0’ and subcommands refer to general settings of the pulse generator. The commands ‘PULS1’ and ‘PULS2’ pass parameters to the two individual channels, such as time delay (‘DEL’) and pulse duration (‘WIDT’).

References

1. Anglos, D.: Shedding light on the past: optical technologies applied to cultural heritage (2017)
2. Arp, Z.A., Cremers, D.A., Wiens, R.C., Wayne, D.M., Sallé, B., Maurice, S.: Analysis of water ice and water ice/soil mixtures using laser-induced breakdown spectroscopy: application to mars polar exploration. *Appl. Spectrosc.* **58**(8), 897–909 (2004)
3. Bonta, M., Gonzalez, J.J., Quarles, C.D., Russo, R.E., Hegedus, B., Limbeck, A.: Elemental mapping of biological samples by the combined use of libis and la-icp-ms. *J. Anal. At. Spectrom.* **31**(1), 252–258 (2016)
4. Bush, L.: Biological mapping with libis. *Spectroscopy* 26–31 (2016)
5. Castle, B.C., Talabardon, K., Smith, B.W., Winefordner, J.D.: Variables influencing the precision of laser-induced breakdown spectroscopy measurements. *Appl. Spectrosc.* **52**(5), 649–657 (1998)
6. Chatzitheodoridis, E.: Lab (2021). <http://minpetlab.metal.ntua.gr/>
7. Chitta, S., Marder-Eppstein, E., Meeussen, W., Pradeep, V., Rodríguez Tsouroukdessian, A., Bohren, J., Coleman, D., Magyar, B., Raiola, G., Lüdtke, M., Fernández Perdomo, E.: ros_control: a generic and simple control framework for ros. *J. Open Source Softw.* (2017). <https://doi.org/10.21105/joss.00456>. <http://www.theoj.org/joss-papers/joss.00456/10.21105.joss.00456.pdf>
8. Ciucci, A., Corsi, M., Palleschi, V., Rastelli, S., Salvetti, A., Tognoni, E.: New procedure for quantitative elemental analysis by laser-induced plasma spectroscopy. *Appl. Spectrosc.* **53**(8), 960–964 (1999)
9. Corporation, B.N.: Bnc website (2021). <https://www.berkeleynucleonics.com/>
10. Cousin, A., Meslin, P., Wiens, R., Rapin, W., Mangold, N., Fabre, C., Gasnault, O., Forni, O., Tokar, R., Ollila, A., et al.: Compositions of coarse and fine particles in martian soils at gale: a window into the production of soils. *Icarus* **249**, 22–42 (2015)
11. Cremers, D.A., Radziemski, L.J.: *Handbook of Laser-Induced Breakdown Spectroscopy*. Wiley, New York (2013)
12. De Giacomo, A., Dell'Aglio, M., De Pascale, O., Longo, S., Capitelli, M.: Laser induced breakdown spectroscopy on meteorites. *Spectrochim. Acta Part B* **62**(12), 1606–1611 (2007)
13. K. C. et al.: Seabreeze (2021). <https://sourceforge.net/projects/seabreeze/>
14. Ferus, M., Koukal, J., Lenza, L., Srba, J., Kubelik, P., Laitl, V., Zanozina, E.M., Vana, P., Kaiserova, T., Knizek, A., Rimmer, P., Chatzitheodoridis, E., Civis, S.: Calibration-free quantitative elemental analysis of meteor plasma using reference laser-induced breakdown spectroscopy of meteorite samples. *A&A* **610**, A73 (2018). <https://doi.org/10.1051/0004-6361/201629950>. <https://doi.org/10.1051/0004-6361/201629950>
15. Fichet, P., Tabarant, M., Salle, B., Gautier, C.: Comparisons between libis and icp/oes. *Anal. Bioanal. Chem.* **385**(2), 338–344 (2006)
16. García-Ayuso, L., Amador-Hernández, J., Fernández-Romero, J., De Castro, M.L.: Characterization of jewellery products by laser-induced breakdown spectroscopy. *Anal. Chim. Acta* **457**(2), 247–256 (2002)
17. Gould, R.G. et al.: The laser, light amplification by stimulated emission of radiation. In: *The Ann Arbor Conference on Optical Pumping*, vol. 15, p. 92. The University of Michigan (1959)
18. Hagins, W., Penn, R., Yoshikami, S.: Dark current and photocurrent in retinal rods. *Biophys. J.* **10**(5), 380–412 (1970)
19. Hou, X., Jones, B.T.: Field instrumentation in atomic spectroscopy. *Microchem. J.* **66**(1–3), 115–145 (2000)
20. Ilhardt, P.D., Nuñez, J.R., Denis, E.H., Rosnow, J.J., Krogstad, E.J., Renslow, R.S., Moran, J.J.: High-resolution elemental mapping of the root-rhizosphere-soil continuum using laser-induced breakdown spectroscopy (libis). *Soil Biol. Biochem.* **131**, 119–132 (2019)
21. Jolivet, L., Leprince, M., Moncayo, S., Sorbier, L., Liemann, C.-P., Motto-Ros, V.: Review of the recent advances and applications of libis-based imaging. *Spectrochim. Acta Part B* **151**, 41–53 (2019)

22. Kam, H.R., Lee, S.-H., Park, T., Kim, C.-H.: Rviz: a toolkit for real domain data visualization. *Telecommun. Syst.* **60**(2), 337–345 (2015)
23. Kim, T., Lin, C., Yoon, Y.: Compositional mapping by laser-induced breakdown spectroscopy. *J. Phys. Chem. B* **102**(22), 4284–4287 (1998)
24. Knight, A.K., Scherbarth, N.L., Cremers, D.A., Ferris, M.J.: Characterization of laser-induced breakdown spectroscopy (libs) for application to space exploration. *Appl. Spectrosc.* **54**(3), 331–340 (2000)
25. Lasers, L.: Litron website (2021). <https://litron.co.uk/>
26. Lasheras, R., Bello-Galvez, C., Rodriguez-Celis, E., Anzano, J.: Discrimination of organic solid materials by libs using methods of correlation and normalized coordinates. *J. Hazard. Mater.* **192**(2), 704–713 (2011)
27. Neuland, M.B., Meyer, S., Mezger, K., Riedo, A., Tulej, M., Wurz, P.: Probing the allende meteorite with a miniature laser-ablation mass analyser for space application. *Planet. Space Sci.* **101**, 196–209 (2014)
28. OpenBuilds: Openbuilds website (2021). <https://openbuilds.com/>
29. Optics, O.: Ocean optics website (2021). <https://www.oceaninsight.com/>
30. Pagnotta, S., Lezzarini, M., Ripoll-Seguer, L., Hidalgo, M., Grifoni, E., Legnaioli, S., Lorenzetti, G., Poggialini, F., Palleschi, V.: Micro-laser-induced breakdown spectroscopy (micro-libs) study on ancient roman mortars. *Appl. Spectrosc.* **71**(4), 721–727 (2017)
31. Quigley, M., Conley, K., Gerkey, B., Faust, J., Foote, T., Leibs, J., Wheeler, R., Ng, A.Y.: Ros: an open-source robot operating system. In: ICRA Workshop on Open Source Software, vol. 3, p. 5. Kobe, Japan (2009)
32. Rai, N.K., Rai, A.: Libs-an efficient approach for the determination of cr in industrial wastewater. *J. Hazard. Mater.* **150**(3), 835–838 (2008)
33. Rehse, S.J., Diedrich, J., Palchaudhuri, S.: Identification and discrimination of pseudomonas aeruginosa bacteria grown in blood and bile by laser-induced breakdown spectroscopy. *Spectrochim. Acta Part B* **62**(10), 1169–1176 (2007)
34. Rodriguez-Celis, E., Gornushkin, I., Heitmann, U., Almirall, J., Smith, B., Winefordner, J., Omenetto, N.: Laser induced breakdown spectroscopy as a tool for discrimination of glass for forensic applications. *Anal. Bioanal. Chem.* **391**(5), 1961 (2008)
35. ROS: joystick_drivers (2021). https://wiki.ros.org/joystick_drivers
36. Sattmann, R., Sturm, V., Noll, R.: Laser-induced breakdown spectroscopy of steel samples using multiple q-switched: Yag laser pulses. *J. Phys. D Appl. Phys.* **28**(10), 2181 (1995)
37. Senesi, G.S.: Laser-induced breakdown spectroscopy (libs) applied to terrestrial and extraterrestrial analogue geomaterials with emphasis to minerals and rocks. *Earth Sci. Rev.* **139**, 231–267 (2014)
38. Stavrinos, G.: auto_libs (2021). <https://github.com/gstavrinos/auto-libs>
39. Stavrinos, G.: seabreeze fork (2021). <https://github.com/gstavrinos/seabreeze>
40. Sturm, V., Noll, R.: Laser-induced breakdown spectroscopy of gas mixtures of air, co₂, n₂, and c₃h₈ for simultaneous c, h, o, and n measurement. *Appl. Opt.* **42**(30), 6221–6225 (2003)
41. Taschuk, M., Tsui, Y., Fedosejevs, R.: Detection and mapping of latent fingerprints by laser-induced breakdown spectroscopy. *Appl. Spectrosc.* **60**(11), 1322–1327 (2006)
42. Tognoni, E., Cristoforetti, G., Legnaioli, S., Palleschi, V.: Calibration-free laser-induced breakdown spectroscopy: state of the art. *Spectrochim. Acta Part B* **65**(1), 1–14 (2010)
43. Wang, W., Li, S., Qi, H., Ayhan, B., Kwan, C., Vance, S.: Revisiting the preprocessing procedures for elemental concentration estimation based on chemcam libs on mars rover. In: 2014 6th Workshop on Hyperspectral Image and Signal Processing: Evolution in Remote Sensing (WHISPERS), pp. 1–4. IEEE (2014)
44. Wantai: Wantai website (2021). <https://wantmotor.com/>

George Stavrinos received a B.Sc. degree in Computer Science from the Athens University of Economics and Business in 2014 and a M.Sc. in Intelligent Systems and Robotics from De Montfort University in 2018. In 2020, he received his second M.Sc. in Space Science, Technologies and Applications from the National Observatory of Athens. He is currently working as

a researcher in RoboSKEL Lab in the National Centre of Scientific Research “Demokritos” in Athens, Greece. His main research interests are robots under zero-gravity (microgravity) conditions (rovers or humanoids), autonomous spacecraft, flying robots (autonomous UAVs), navigation autonomy, dynamics and kinematics analysis and motion planning.

Elias Chatzitheodoridis is Professor of Mineralogy-Petrology at the National Technical University of Athens (NTUA), and Director of the Laboratory of Mineralogy, Petrology, and Economic Geology. He studied Geology at the National and Kapodistrian University of Athens and acquired his M.Sc. and Ph.D. degrees from the University of Manchester, UK. He worked at the Foundation for Research and Technology—Hellas (FORTH) in Heraklion, Crete, at the Technical University of Vienna (TUWien), and at the high-tech private company Austria Technologie and Systemtechnik AG (AT&S AG) at Leoben-Hinterberg, Austria. His research interests are in astrochemistry, astrobiology, and planetary sciences. He has also a strong applied research background on photonic technologies, micro- and nanotechnologies, lithography, microsystems (MEMS), and on the development of analytical instruments. He is President of the ‘Stellar Discoveries’ network, CEO of the ‘Network of Researchers on the Chemical Evolution of Life’ (NorCEL), and Council Member of the ‘European Astrobiology Network Association’ (EANA). He has published more than a hundred peer reviewed scientific and technological papers, and he organised conferences in astrobiology and planetary sciences.

Olga A. Sykioti is Senior Researcher at the Institute of Astronomy, Astrophysics, Space Applications and Remote Sensing of the National Observatory of Athens. She obtained her B.S. in Geology from the National and Kapodistrian University of Athens, her M.S. degrees in Remote Sensing and in Hydrology, Geostatistics and Geochemistry as well as her Ph.D. in Geosciences and Remote Sensing from Pierre and Marie Curie University (Paris, France). Her research interests include imaging spectroscopy and machine learning applications in Geosciences with emphasis on mineral/chemical exploration and geological mapping of terrestrial surfaces. She is President of the Remote Sensing and Space Applications Committee of the Geological Society of Greece. In 2009, she was awarded with a Fulbright Scholar fellowship. She has published more than fifty peer reviewed papers in high-ranked scientific journals and international conference proceedings and she has participated in more than thirty international, European, European Space Agency (ESA) and national funded research projects.

High Fidelity IMU and Wheel Encoder Models for ROS Based AGV Simulations



Emre Ozdemir, Hakan Gokoglu, M. Koray Yilmaz, Umut Dumandag,
Ismail Hakki Savci, and Haluk Bayram

Abstract In this research chapter, we study the problem of how automated guided vehicles (AGVs) are simulated considering the realistic settings in their sensors. Wheel encoders and inertial measurement units (IMUs) are two fundamental sensors in AGVs. These sensors are prone to error due to internal or environmental disturbances and noises. To have a better representation of a robot in simulation environments, these disturbances/noises should also be modeled. However, since simulators have the simplified or idealized version of sensors, the high fidelity models of the sensors are usually ignored, which leads to simulation results inconsistent with the real-life scenarios. In this chapter, we develop related ROS nodes and Gazebo plugins to incorporate the disturbance/noise into the sensors and model the error occurrences using Poisson distribution. We validate the approach through Gazebo simulations using an AGV model. The source codes and installation details are provided via a public repository.

1 Introduction

Industry 4.0 requires smart factories with automated guided vehicles (AGVs) [7]. AGVs have a growing usage in factories, warehouses and other areas. These robots can autonomously navigate around their environments by using magnetic tapes, reflector systems, rails or natural navigation and can carry out their assigned tasks

E. Ozdemir · H. Gokoglu · I. H. Savci
Light Mobility Laboratory, Ford Otosan Kocaeli Plant, Kocaeli, Turkey
e-mail: ozdemi8@ford.com.tr

H. Gokoglu
e-mail: hgokoglu@ford.com.tr

I. H. Savci
e-mail: isavci@ford.com.tr

M. K. Yilmaz · U. Dumandag · H. Bayram (✉)
Field Robotics Laboratory, BILTAM, Istanbul Medeniyet University, Istanbul, Turkey
e-mail: haluk.bayram@medeniyet.edu.tr

[16]. Natural navigation is one of the preferred ways for AGV localization and navigation as it provides better flexibility and requires almost no infrastructure change, such as placing artificial landmarks to the environment.

To expedite the development process of mobile robots, various framework and simulations, such as ROS and Gazebo, have been developed. ROS and Gazebo frameworks allow users to develop algorithms and quickly validate the system performance using simulations. High fidelity sensor models have a profound effect on this performance. For instance, localization task is commonly handled by reading various sensor inputs (LiDAR, wheel encoder and IMU) and fusing them in real time. One drawback in performing this task in simulators is the lack of disturbance or noise in the wheel encoder and IMU models as often these have an important effect on the localization performance.

In the literature, there has been a large body of studies on the noise/disturbance/inaccuracies in wheel encoder and IMU sensors. In these studies, the sources of inaccuracies and how to deal with them are examined. For wheel encoder sensors, these sources are given as in [15]: (1) wheel slips, (2) uneven surfaces, (3) skidding, (4) variations in wheel diameter due to environmental changes (temperature) and physical factors (pressure, speed), (5) irregularities in wheel diameters and wheel configuration, (6) limitations (resolution, sample rate) of the wheel encoders. In addition, the work in [12] states that although the scale factor of wheel encoders is considered noised constants, the error characteristics of the measurements taken from

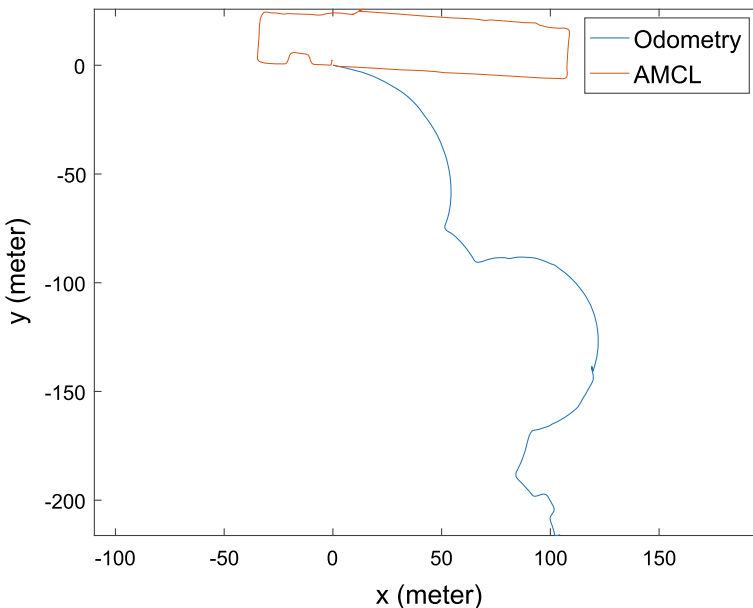


Fig. 1 Odometry drift vs. localization (amcl package) from our field experiments in Ford Otosan Yenikoy Plant, Istanbul, Turkey

wheel encoders are “unknown and largely unstable”. As to IMU sensors, the sources of errors can be listed in [1, 2, 15, 17] as follows: (1) biases, (2) scale factors, (3) nonlinearities, (4) environmental effects (varying temperature, humidity, vibrations, non-rigid mounting). In the simulations of robotic systems, these errors are generally either ignored or characterized by a known distribution with fixed parameters.

In this work, we developed an approach to provide a more realistic simulation environment by considering real life events such as wheel encoder uncertainties (due to wheel slip) and IMU noise/disturbance. In doing so, Poisson distribution is used to model the undesirable events, such as wheel slips. One example from a real industrial scenario is given in Fig. 1 where the red trajectory shows the robot localization using the ROS package amcl whereas the blue trajectory shows the odometry drift occurring mostly due to wheel slips and mechanical coupling problems.

2 High Fidelity Wheel Encoder and IMU Models in ROS and Gazebo

In this section, we show how to improve the fidelity level of the existing wheel encoder and IMU models by incorporating uncertainties/disturbances using Poisson distribution. All the source codes are accessible via the public repository [3].

2.1 Run-Time Adjustable Noise in Gazebo Wheel Encoder

The differential drive models developed for Gazebo, such as DiffDrivePlugin [10] and gazebo_ros_diff_drive [8], do not have noise support. For instance, this can be seen in the following code fragment (lines 377–378) in the original source codes from the plugin gazebo_ros_diff_drive:

```
double sl = vl*(wheel_diameter_/.2.0)*seconds_since_last_update;
double sr = vr*(wheel_diameter_/.2.0)*seconds_since_last_update;
```

Here, the displacements of the left and right wheels are calculated using the perfect knowledge of the wheels’ linear velocities. In the rest of the code, the current robot pose is computed from the previous pose and the odometric integration according to the following equation [14]:

$$\begin{bmatrix} x_k \\ y_k \\ \theta_k \end{bmatrix} = \begin{bmatrix} x_{k-1} \\ y_{k-1} \\ \theta_{k-1} \end{bmatrix} + \begin{bmatrix} \frac{s_r+s_l}{2} \cos(\theta_{k-1} + \frac{s_r-s_l}{2b}) \\ \frac{s_r+s_l}{2} \sin(\theta_{k-1} + \frac{s_r-s_l}{2b}) \\ \frac{s_r-s_l}{2b} \end{bmatrix} \quad (1)$$

where b is the distance between the two wheels, and s_r and s_l denote the displacement of the left and right wheels, respectively. The Gazebo differential drive model makes use of this pose update equation. As can be seen in Eq. 1, the odometry

update does not contain any noise term. However, since the odometry is required to provide the corresponding 6×6 covariance matrix, the fixed variances (small variances for the diagonals related to x , y and rotation about Z axis, and large variances for the diagonals related to z , rotation about X axis, rotation about Y axis) are assigned to the diagonals of the matrix¹ (between the lines 482–487 in the plugin `gazebo_ros_diff_drive`).

As a result, by using this kind of idealized model in mapping, localization, or navigation tasks, the odometry is calculated from noiseless and perfect encoder data. Since the noiseless encoder does not model the real-life conditions (i.e. wheel slips), the simulations cannot be used effectively to verify the developed algorithms before they are deployed in the field tests. Therefore, the plugin `gazebo_ros_diff_drive` was modified to incorporate the noise. For this purpose, the function `UpdateOdometryEncoder` is modified such that the noise is added to s_r and s_l (lines 430–431):

```
double sl = vl*(wheel_diameter_/_2.0)*seconds_since_last_update
+ GaussianKernel(0,diffd_gaussian_noise.data.at(0))
*diffd_noise_on_off.data.at(0);
double sr = vr*(wheel_diameter_/_2.0)*seconds_since_last_update
+ GaussianKernel(0,diffd_gaussian_noise.data.at(1))
*diffd_noise_on_off.data.at(1);
```

where the noise is Gaussian noise $\mathcal{N}(0, \sigma^2)$ with zero mean and σ standard deviation which can be set via a ROS topic. To generate a random number from $\mathcal{N}(0, \sigma^2)$, a function called `GaussianKernel` (lines 231–243) is added.

In order to be able to change the noise related parameters in the model, we add two new subscribers (lines 180–183 and lines 185–188) to the plugin `gazebo_ros_diff_drive`. As a result, the plugin subscribes to the following ROS topics: `/diff_drive/noise_on_off` and `/diff_drive/set_noise`. We also add the associated callback functions `CallbackNoiseOnOff` (lines 215–221) and `CallbackNoise` (lines 223–229) in order to set the variables `diffd_gaussian_noise` and `diffd_noise_on_off` in the calculation of the wheel displacements. In the original version of the plugin, the diagonals of the covariance matrix related to the odometry are set to fixed values and cannot be changed during the simulation. These values in the modified version (lines 535–541) depend on the noise standard deviation which can be set by the user while the simulation is running.

All the changes were made in the following source files [4]: `noisy_diff_drive.h` and `noisy_diff_drive.cpp`. With these changes, the user can enable or disable the noise in the wheel encoders via the topic `/diff_drive/noise_on_off`, and change the noise standard deviation via the topic `/diff_drive/set_noise`.

¹ The diagonals of the odometry covariance matrix correspond to x , y , z , rotation about X axis, rotation about Y axis, rotation about Z axis [11].

2.2 Run-Time Adjustable Noise in Gazebo IMU Sensor

The Gazebo IMU sensor plugin `gazebo_ros_imu_sensor` includes Gaussian noise as a plugin parameter [13]. However, this noise parameter can be set only through xacro file. Therefore once the simulation starts running, this parameter cannot be changed. To change the noise level at run-time, all the additions and modifications were made in the following source files [5]: `noisy_imu_sensor.h` and `noisy_imu_noise.cpp`.

The published IMU data has three main fields: orientation, linear acceleration, angular velocity. Since the orientation is in quaternion form, it has four sub-fields: x, y, z, w . On the other hand, the linear acceleration and angular velocity fields have three sub-fields: x, y, z . The code from the function `UpdateChild` in the modified IMU plugin (lines 126–128) for the linear acceleration is as follows:

```
imu_msg.linear_acceleration.x = accelerometer_data.X()
+GaussianKernel(0,imu_gaussian_noise.data.at(7))
* imu_noise_on_off.data.at(7);
imu_msg.linear_acceleration.y = accelerometer_data.Y()
+ GaussianKernel(0,imu_gaussian_noise.data.at(8))
* imu_noise_on_off.data.at(8);
imu_msg.linear_acceleration.z = accelerometer_data.Z()
+ GaussianKernel(0,imu_gaussian_noise.data.at(9))
* imu_noise_on_off.data.at(9);
```

The similar code is added for the orientation and angular velocity. The variables `imu_gaussian_noise` and `imu_noise_on_off` are set through the ROS topics `/imu/set_noise` and `/imu/noise_onoff`. These variables are 10 dimensional arrays in which the first four elements of these arrays are dedicated for the orientation's sub-fields, the next three elements for the angular velocity's sub-fields, the last three elements for the linear acceleration's sub-fields. Since the plugin needs to subscribe to these ROS topics, two additional subscribers (lines 74–78) and their associated callback functions (lines 85–92 and lines 94–101) are added to the modified plugin. Hence, the user can activate or deactivate the noise and change the standard deviation of Gaussian noise in the IMU sensor through these topics.

2.3 Modeling Sensor Uncertainties/Disturbances Using Poisson Distribution

While AGVs are operating in their workspace, unexpected events may occur (as discussed in Section 1), thereby increasing sensor uncertainty in wheel encoders and IMU sensors. These unexpected events need to be integrated into the simulations, as well. For this purpose, a ROS node called `sensor_uncertainty` was developed in which Poisson distribution is used to decide when an unexpected event occurs [6]. The probability mass function for Poisson distribution is given as:

$$f(k; \lambda) = \frac{\lambda^{k-1} e^{-\lambda}}{k!} \quad (2)$$

where the parameter λ is the expected separation (interval) within which k events occur. The reason why the Poisson distribution was chosen is that the Poisson distribution gives the probability of a given number of unexpected events occurring in a fixed amount of time. By using this distribution, we can determine how many unexpected events will occur within a certain period of time and how long they will last. Therefore, we have an opportunity to test our algorithms, such as localization and mapping algorithms, under varying noise settings. Here, the unexpected events can be thought of as the changes in the noise level.

To simulate the errors (unexpected events) occurring in wheel encoder and IMU sensors (the plugins `gazebo_ros_diff_drive` and `gazebo_ros_imu_sensor`), we need to determine when these events occur. For this purpose, we make use of NumPy library in Python to generate random numbers from the Poisson distribution. The following code (lines 22–34) from the ROS node `sensor_uncertainty` is used to change the noise level between low and high noises for the IMU plugin:

```
while rospy.is_shutdown():
    imu_poisson=poisson(imu_num_of_error_occurrences/time_interval)
    if imu_poisson >= 1:
        publisher.publish(high_msg)
        start_time = counter

    if (counter - start_time) == imu_noise_duration:
        publisher.publish(low_msg)

    rate.sleep()
    counter += 1
```

Here we can define the number of error (unexpected event) occurrences (the variable `imu_num_of_error_occurrences`) within a given time interval (the variable `time_interval`) in seconds and the duration of how long the high noise level stays active in seconds (the variable `imu_noise_duration`). If the random number generated from the Poisson distribution is greater than or equal to 1, the noise level is changed from low to high and kept high for `imu_noise_duration`. When the time runs out, the noise level is changed from high to low. The same principle is applied for the wheel encoders (lines 48–60).

The ROS node interacts with wheel encoder (`noisy_diff_drive`) and IMU (`noisy_imu_sensor`) plugins through topics. This interaction can be seen in Fig. 2. The node can enable or disable the noise in the wheel encoders and IMU via the topics `/diff_drive/noise_on_off` and `/imu/noise_on_off`, and change the noise standard deviations via the topics `/diff_drive/set_noise` and `/imu/set_noise`.

We can specify all the necessary parameters for each sensor in the configuration file `sensor_uncertainty_config.json`. There are three main fields for the IMU sensor: orientation, angular velocity and linear acceleration. Each of these

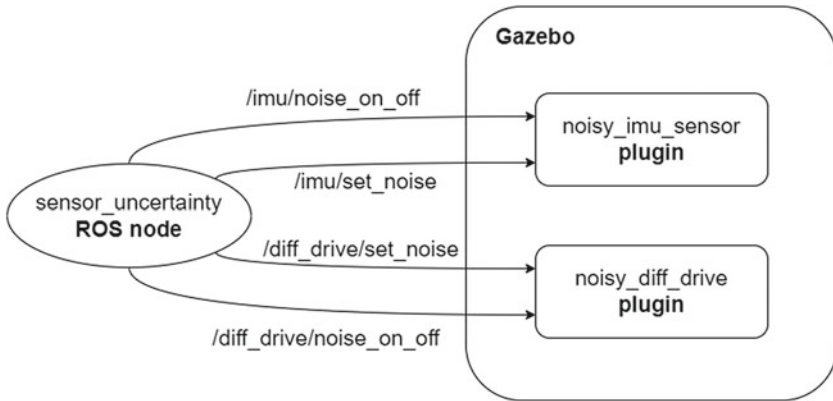


Fig. 2 The relationship between the `sensor_uncertainty` ROS node and the modified Gazebo plugins

fields has sub-fields: x, y, z for angular velocity and linear acceleration, and x, y, z, w for orientation. Each sub-field is defined to have the standard deviations of low and high noises. Therefore, there are the following 20 parameters in total for the IMU sensor: `imu_angular_velocity_[x/y/z]_[low/high]_noise` in rad/s, `imu_linear_acceleration_[x/y/z]_[low/high]_noise` in m/s², and `imu_orientation_[x/y/z/w]_[low/high]_noise` in quaternion form. As to the wheel encoders, there are two fields (left and right) each of which has the standard deviations of low and high noises. Therefore, there are four parameters for the wheel encoder: `diff_drive_[left/right]_wheel_[low/high]_noise` in meters. We can activate or deactivate the noises using the following parameters taking the values of “True” or “False”: `imu` and `diff_drive`. We have also some parameters used in modeling the sensor uncertainties. The parameters `[imu/diff_drive]_num_of_error_occurrences` denote the expected number of error occurrences for the IMU and wheel encoder sensors within a certain time interval defined by `time_interval` in seconds. `[imu/diff_drive]_noise_duration` gives the duration of how long the high noise level stays active in seconds.

3 Simulation Studies

In this section, we aim to demonstrate the effect of the sensor plugins and explain how to use them briefly. The details regarding the installation and usage of the plugins can be found in the repository [3].

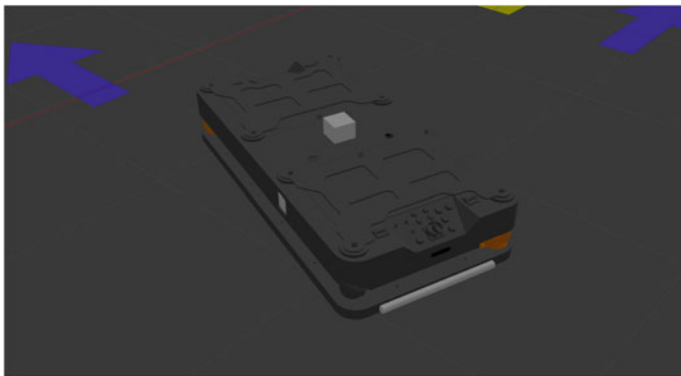


Fig. 3 AGV Gazebo model

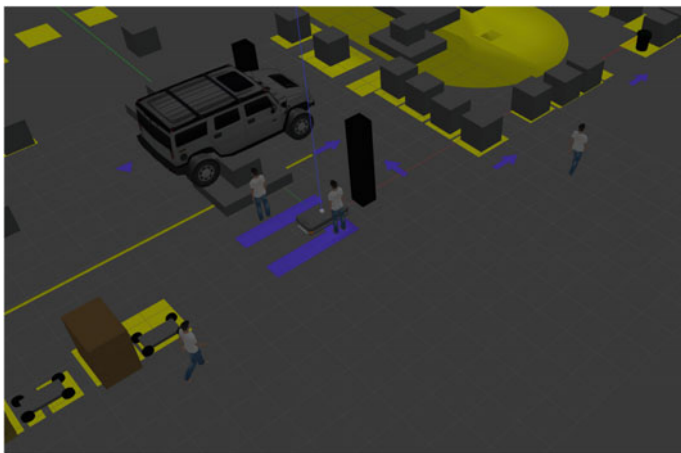


Fig. 4 Gazebo factory environment used in the simulations

In order to test the sensor noise models, a realistic AGV model is created in Gazebo environment. A differential drive based AGV dynamic model integrated with an IMU sensor is generated via Solidworks URDF Export tool from CAD model. Its wheelbase and wheel diameters are 0.51 m and 0.25 m, respectively. The physical dimension of the AGV is 0.95 m (L) \times 0.45 m (W) \times 0.40 m (H). It can travel at a maximum speed of 1 m/s. The Gazebo model of the AGV is shown in Fig. 3. The AGV operates in the Gazebo factory environment as shown in Fig. 4.

Odometry calculation is done with the modified version of the plugin `gazebo_ros_diff_drive` and fused with IMU measurements using `robot_pose_ekf` package [9] to improve the pose estimation.

Under the robot description package directory, “plugins” and “scripts” folders were created. The files listed below are located in the “plugins” directory:

- `gazebo_ros_utils.h` and `gazebo_ros_utils.cpp`
- `noisy_diff_drive.h` and `noisy_diff_drive.cpp`
- `noisy_imu_sensor.h` and `noisy_imu_sensor.cpp`

The following files are located in the “scripts” directory:

- `sensor_uncertainty_generator.py`
- `sensor_uncertainty_config.json`

In order to use the noisy plugins, the libraries `libnoisy_diff_drive.so` and `libnoisy_imu_sensor.so` are selected in the robot description `.xacro` file. For these simulations, `p3d_base_controller - libgazebo_ros_p3d.so` plugin is also activated in order to compare the results with ground truth.

After setting up the robot description package, we spawned a robot in Gazebo environment. Due to its real time capability, the sensor noise can be enabled or disabled without restarting the simulation.

The file `sensor_uncertainty_config.json` is used to characterize the Poisson distribution and sensor noise. This configuration file is used by the Python script `sensor_uncertainty_generator.py` which is a ROS node changing noise parameters in `libnoisy_diff_drive` and `libnoisy_imu_sensor` plugins. During the simulation, the noise parameters can be changed to test localization or mapping algorithms using varying sensor dynamics.

The simulations are conducted for the following two manoeuvres with the noisy plugins activated:

- 3 m × 3 m square route
- Circular route with 1 m turning radius.

3.1 Square Route Test

The AGV is spawned at the pose (0, 0, 0) and moves 3 m forward and then turns left with 90 degrees until it arrives its starting position. At the beginning of the simulation, the noise is activated in the modified version of `gazebo_ros_diff_drive` with the following settings:

- “time_interval”:10,
- “diff_drive_num_of_error_occurrences”:1,
- “rate”: 1,
- “imu”:“False”,
- “diff_drive”:“True”,
- “diff_drive_noise_duration”:0.5,
- “diff_drive_left_wheel_low_noise”:0.001,
- “diff_drive_right_wheel_low_noise”:0,

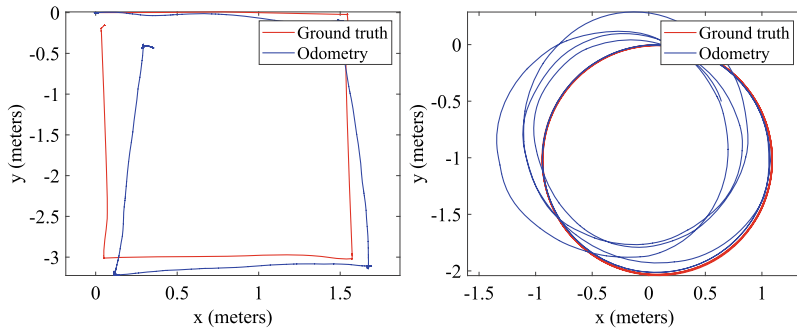


Fig. 5 Wheel odometry for square and circular routes without (red) and with noise (blue)

- “diff_drive_left_wheel_high_noise”:5.0,
- “diff_drive_right_wheel_high_noise”:0

In this configuration file, the left wheel encoder is intentionally set to be worse compared to right wheel encoder. Since the route is a square, the odometry pose should end up where it started. However some pose drifts as well as a distorted square shape instead of a perfect square are observed. The trajectories for the ground truth and the odometry can be seen in Fig. 5(left).

3.2 Circular Route Test

The AGV is located at (0, 0, 0) and the following message is published to /cmd_vel topic to obtain a circular trajectory:

- linear x = 0.5
- angular z = -0.5

The parameters in the configuration file `sensor_uncertainty_config.json` are set as follows:

- “time_interval”:10,
- “imu_num_of_error_occurrences”:3,
- “diff_drive_num_of_error_occurrences”:1,
- “rate”: 1,
- “imu”:“True”,
- “diff_drive”:“True”,
- “imu_noise_duration”:0.5,
- “diff_drive_noise_duration”:0.2,
- “imu_orientation_x_low_noise”: 0.1,
- “imu_orientation_y_low_noise”: 0.1,
- “imu_orientation_z_low_noise”: 0.1,

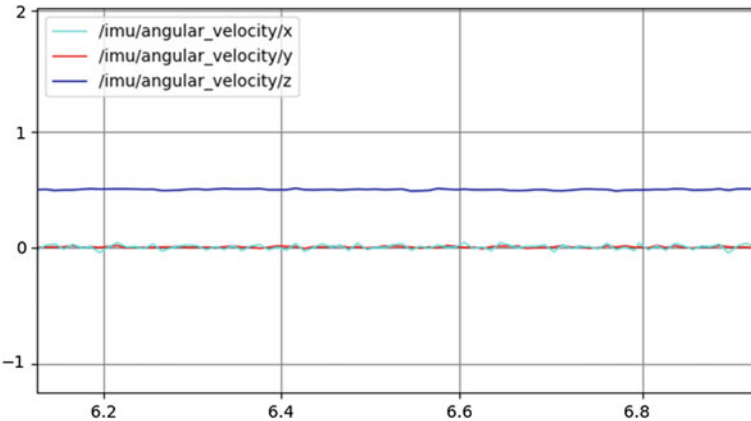


Fig. 6 IMU angular velocity output without noise

- “imu_orientation_w_low_noise”: 0.1,
- “imu_angular_velocity_x_low_noise”:0.1,
- “imu_angular_velocity_y_low_noise”:0.1,
- “imu_angular_velocity_z_low_noise”:0.1,
- “imu_linear_acceleration_x_low_noise”: 0.1,
- “imu_linear_acceleration_y_low_noise”: 0.1,
- “imu_linear_acceleration_z_low_noise”: 0.1,
- “imu_orientation_x_high_noise”: 0.5,
- “imu_orientation_y_high_noise”: 0.5,
- “imu_orientation_z_high_noise”: 0.5,
- “imu_orientation_w_high_noise”: 0.5,
- “imu_angular_velocity_x_high_noise”:0.5,
- “imu_angular_velocity_y_high_noise”:0.5,
- “imu_angular_velocity_z_high_noise”:0.5,
- “imu_linear_acceleration_x_high_noise”: 0.5,
- “imu_linear_acceleration_y_high_noise”: 0.5,
- “imu_linear_acceleration_z_high_noise”: 0.5,
- “diff_drive_left_wheel_low_noise”:0.001,
- “diff_drive_right_wheel_low_noise”:0.001,
- “diff_drive_left_wheel_high_noise”:0.3,
- “diff_drive_right_wheel_high_noise”:0.3

In this configuration file, the odometry and IMU noise levels are set to be medium based on the field experience. From the simulation results shown in Fig. 5(right), the odometry error accumulation is observed in negative x and positive y directions. Similarly, the effect of noise on IMU measurements can be seen in Figs. 6 and 7.

The same test is conducted again in order to see the noise effect on localization performance. For localization task, noisy odometry and IMU data are fused in the

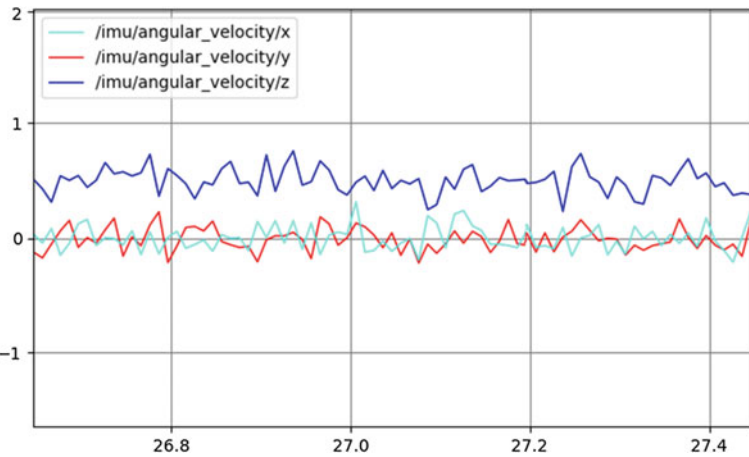


Fig. 7 IMU angular velocity output under noise

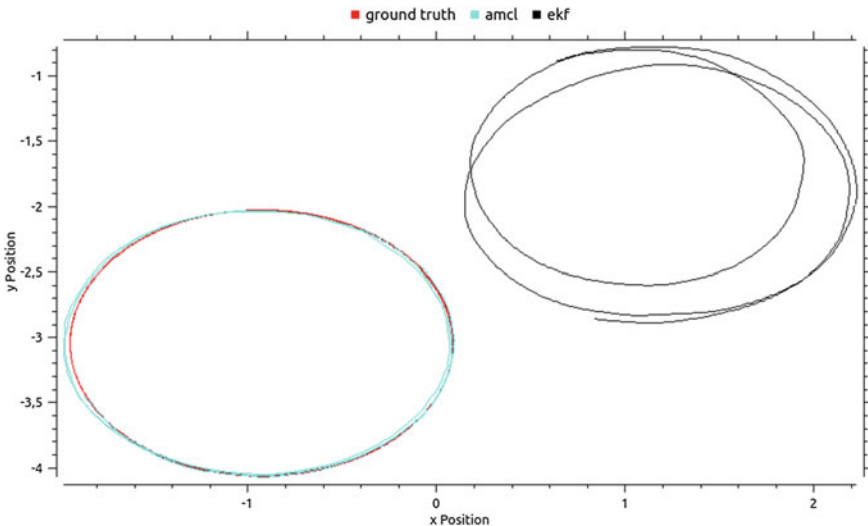


Fig. 8 Effects of noisy odometry and IMU data on the localization using EKF and AMCL

robot_pose_ekf package. Then 2D laser scanner data and EKF output are fed into Adaptive Monte Carlo Localization (AMCL) algorithm. Figure 8 shows the effect of noise on Extended Kalman Filter and AMCL particle filter. The ground truth position data is also plotted as a reference. It can be seen that noisy IMU and wheel encoder measurements cause both distortion and shift on EKF output. However, this effect is mostly corrected by the particle filter because `odom_alpha` values are set to low values (0.15 for this case).

4 Conclusion

In this chapter, we consider the problem of how AGVs are simulated considering realistic disturbances and noises in their sensors. These disturbances or noises on wheel encoder and IMU sensors are modeled to have simulation results consistent with the real-life scenarios. Hence, we develop a ROS node and Gazebo plugins to incorporate the disturbance/noise into the sensors and model the error occurrences using Poisson distribution. The proposed method is tested in Gazebo environment with two different routes. The internal or environmental effects like wheel slip, encoder mechanical coupling problems, uneven encoder counting issues cause errors or sudden drifts on odometry calculation, which is a significant problem for localization tasks. This effect is demonstrated on Extended Kalman Filter and Adaptive Monte Carlo Localization algorithms. Using the proposed methodology, these effects can be simulated in the Gazebo environment.

References

1. Amirsadri, A., Kim, J., Petersson, L., Trumpf, J.: Practical considerations in precise calibration of a low-cost mems imu for road-mapping applications. In: American Control Conference (ACC), pp. 881–888 (2012)
2. Barreda Pupo, L.: Characterization of errors and noises in MEMS inertial sensors using Allan variance method. Master's Thesis, Universitat Politècnica de Catalunya (2016)
3. Bayram, H.: High Fidelity Sensor Models (2021). <https://github.com/hlkbyrm/HighFidelitySensorModels>
4. Bayram, H.: The modified version of DiffDrivePlugin (2021). https://github.com/hlkbyrm/HighFidelitySensorModels/blob/main/turtlebot3_highfidelityWheelEncoderIMU/plugins/noisy_diff_drive.cpp
5. Bayram, H.: The modified version of Gazebo IMU Sensor plugin (2021). https://github.com/hlkbyrm/HighFidelitySensorModels/tree/main/turtlebot3_highfidelityWheelEncoderIMU/plugins
6. Bayram, H., Bozma, H.I.: Assistance networks for dynamic multirobot tasks. Auton. Robots **40**(4), 615–630 (2016)
7. Goel, R., Gupta, P.: Robotics and industry 4.0. In: A Roadmap to Industry 4.0: Smart Production, Sharp Business and Sustainable Development, pp. 157–169. Springer (2020)
8. Hsu, J., Koenig, N., Coleman, D.: gazebo_ros_pkgs - gazebo_rosv_diff_drive. https://github.com/ros-simulation/gazebo_ros_pkgs/blob/kinetic-devel/gazebo_plugins/src/gazebo_ros_diff_drive.cpp (2019 - commit c89b250)
9. Meeussen, W.: robot_pose_ekf. https://github.com/ros-planning/robot_pose_ekf (2021 - commit fd6cef3)
10. Open Source Robotics Foundation: DiffDrivePlugin. <https://github.com/osrf/gazebo/blob/gazebo11/plugins/DiffDrivePlugin.cc> (2020 - commit 3e5ffc9)
11. Open Source Robotics Foundation: geometry_msgs/PoseWithCovariance Message (2021). https://docs.ros.org/en/melodic/api/geometry_msgs/html/msg/PoseWithCovariance.html
12. Ouyang, W., Wu, Y., Chen, H.: INS/odometer land navigation by accurate measurement modeling and multiple-model adaptive estimation. IEEE Trans. Aerosp. Electron. Syst. **57**(1), 245–262 (2020)
13. Settimi, A.: gazebo_ros_imu_sensor in Simulation Tools In ROS. https://github.com/ros-simulation/gazebo_ros_pkgs/tree/noetic-devel/gazebo_plugins/src/gazebo_ros_imu_sensor.cpp (2020 - commit 05d6cb4)

14. Siegwart, R., Nourbakhsh, I.R., Scaramuzza, D.: *Introduction to Autonomous Mobile Robots*, 2nd edn. MIT Press, Cambridge (2011)
15. Skog, I., Handel, P.: In-car positioning and navigation technologies - a survey. *IEEE Trans. Intell. Trans. Syst.* **10**(1), 4–21 (2009)
16. Ullrich, G.: *Automated Guided Vehicle Systems*, 1st edn. Springer, Berlin (2015)
17. Yang, Y., Geneva, P., Zuo, X., Huang, G.: Online IMU intrinsic calibration: is it necessary? In: *Proceedings of Robotics: Science and Systems (RSS)* (2020)

Emre Ozdemir is an Autonomous Mobile Robots Development Engineer at Ford Otosan, Turkey for 7 years where he focuses on dynamic simulation, control system design and path tracking algorithms. He is a Ph.D. student at Yildiz Technical University, focusing on Advanced Robust Control Systems.

Hakan Gokoglu is an Autonomous Mobile Robots Development Engineer at Ford Otosan, Turkey. He worked as an Engine Test Engineer at dynamometers for 9 years, focusing on engine testing and automated component test rig real time controller design and development. For two years, he focuses on autonomous mobile robot control systems design and software development.

M. Koray Yilmaz received the B.Sc. degree in Electrical and Electronics Engineering from Sakarya University, Sakarya, Turkey, in 2011. He is currently a graduate student at Istanbul Medeniyet University, Istanbul, Turkey. He is a member of Field Robotics Laboratory. His research interests include aerial robots and target localization.

Umut Dumandag is an undergraduate student in Electrical and Electronics Engineering, Istanbul Medeniyet University. He is also a member of Field Robotics Laboratory. His research focus is on robotic simulations and aerial robots.

Ismail Hakkı Savci received the Ph.D. degree in mechanical engineering from Marmara University, Istanbul, Turkey in 2015. He is a technical manager at Ford Otosan for 13 years. He specializes internal combustion engines, experimental studies and mobile robot applications.

Haluk Bayram received the Ph.D. degree in electrical and electronics engineering from Bogazici University, Istanbul, Turkey in 2013. He was a Post-Doctoral Associate at Robotic Sensor Networks Laboratory, Department of Computer Science and Engineering, University of Minnesota between 2014 and 2017. He is an Assistant Professor with Istanbul Medeniyet University, Istanbul, Turkey. He is also the director of Field Robotics Laboratory. His research interests include target localization and tracking, field robotics, aerial and surface robotics, and automated guided vehicles.